The Study of MBE-Grown Type III Superlattices for Very Long Wavelength Infrared nBn Detectors

BY

PEIHONG MAN

B.S., Nanjing University, Nanjing, China 2012
M.S. in Physics, University of Illinois at Chicago, Chicago, 2014
M.S. in Computer Science, University of Illinois at Chicago, Chicago, 2020

THESIS

Submitted in partial fulfillment of the requirements
for the degree of Doctor of Philosophy in Physics
in the Graduate College of the
University of Illinois at Chicago, 2021

Chicago, Illinois

Defense Committee:

Dr. Sivalingam Sivananthan, Chair and Advisor
Dr. Christoph Grein, Physics
Dr. Robert Klie, Physics
Dr. Srini Krishnamurthy, Physics
Dr. Paul Boieriu, EPIR Technologies.
Dr. Jonathan Art, Anatomy and Cell Biology

To my wife, Carla Li,

my parents, Baoyuan Man and Aihua Liu,

and my daughters, Ellie Man and Arya Man,

for nursing me with affections and love

and their dedicated partnership for success in my life.

ACKNOWLEDGMENTS

I would like to thank my advisor, Dr. Sivalingam Sivananthan, for his continuous guidance and support, not only in my research, but also in my life. He invited me to Microphysics Laboratory and provided me with the opportunities to learn and use some of the most advanced lab equipment, especially Molecular Beam Epitaxy. And I will never forget his help during the hard times of my Ph.D. study, like a father and like a friend.

My sincere thanks go Professor Christoph Grein and Dr. Srini Krishnamurthy, for their insightful comments and advice. Their knowledge and brilliance inspired and motivated me through the whole time of my Ph.D. study.

I would also like to thank other members in the Microphysics Laboratory: Ryan Sellers and Eranjan Bandara Kandegedara Rathnayake Mudiyanselage, who went through the Ph.D. with me here at MPL, and Xin Zheng, who motivated me to keep going. Special thanks to Dr. Suk-Ryong Hahn, who offers great help in the lab. And many thanks to Thomas Mlynarski, Brian good and Mahisha Amarasinghe for their company.

I am also thankful toward other members of my final thesis and preliminary exam committee: Dr. Robert Klie, Dr. Silviu Velicu, Dr. Paul Boieriu, Dr. Jonathan Art and Dr. Gregory Brill-- for their unwavering support and genuine comments. And many thanks to Cynthia Deters for helping me coordinate the defense time.

ACKNOWLEDGMENTS (continued)

I would also like to acknowledge Ehsan Nahvi for his help in theoretical modeling. Special thanks to Professor David Smith's group from Arizona State University, for providing TEM measurements and elaborate discussions. Many thanks to Professor M. E. Flatté's group at the University of Iowa for providing essential modeling tools, which is important to my thesis.

I am also grateful to Zahira El Khalidi and Zaheer Ahmad, who freed me from lab works when I am writing this thesis.

Last but not least, I would like to thank my family, especially my parents-in-law, Yi Li and Lizhen Qin, who offer selfless help during the pandemic. Thanks to my wife for giving me two lovely daughters, and my parents, without whom none of this would indeed be possible.

Peihong Man

Table of Contents

PART I: 1

Very Long Wavelength Infrared Type III Superlattices 1

1 INTRODUCTION 2

1.1 Infrared Detection 2
1.1.1 Infrared radiation 2
1.1.2 Infrared detection applications 5
1.1.3 Infrared detectors 7

1.2 Mercury Cadmium Telluride 10

1.3 Superlattice 12

1.4 Type-III Superlattice 16
1.4.1 History 16
1.4.2 Band Alignment 16
1.4.3 T3SL Compared to HgCdTe Alloy 19
1.4.4 T3SL Compared to T2SL 22

1.5 Thesis Motivation 23
1.5.1 Why We Care About T3SL Now 24
1.5.2 Why We Care About VLWIR 25

1.6 Summary and chapter arrangement 27

2 DESIGN AND MODELING 28

2.1 T3SL Band Structure 28

2.2 K·p Method 32
2.2.1 K·p method for bulk material 32
2.2.2 K·p method for superlattices 37

2.3 Modeling Details 40

2.4 Calculated band structure 42

3 MOLECULAR BEAM EPITAXY GROWTH OF TYPE-III SUPERLATTICE 49

3.1 A Brief Introduction to MBE 49

3.2 MBE 32p System 51

3.3 Customized Mercury Cell: A Key to Successful Growth 54
3.3.1 Motivation 54
3.3.2 Previous and Existing Mercury Cell Design 57
3.3.3 Newest Mercury Cell Design 59

3.4 MBE Temperature Control 64

3.5 Growing T3SL Using MBE 67

4 CHARACTERIZATION 71

4.1 MBE *In-situ* Growth Characterization 71
4.1.1 Reflection High Energy Electron Diffraction 71
4.1.2 Ellipsometry 76

4.2 MBE *Ex-situ* Growth Characterization 82
4.2.1 Overview 82
4.2.2 Microscope and Nomarski 84
4.2.3 Scanning Electron Microscopy 87
4.2.4 Transmission Electron Microscopy 91
4.2.5 X-ray Diffraction 100
5 ABSORPTION STUDY 112
5.1 Absorption and Absorption Coefficient 112
5.2 Fourier-transform Infrared Spectroscopy 114
5.2.1 Overview 114
5.2.2 FTIR Analysis of MCT Samples 115
5.2.3 FTIR Data Analysis Using Multi-Layer Thin-film Model 118
5.3 Absorption Behavior of T3SL 129
5.4 Temperature-dependent Absorption Study of T3SL 133
5.5 Determination of T3SL Interband Transition Energies 138
6 SUMMARY AND ISSUES WITH T3SL 143
6.1 Summary 143
6.2 The Major Challenge of T3SL Infrared Photodetectors 144
PART II: 148
nBn Devices using Type III Superlattices 148
7 INTRODUCTION TO NBN DEVICES 149
7.1 Overview 149
7.2 Dark Current Suppression in nBn Devices 151
7.3 Valence Band Offset 152
8 DESIGN AND MODELING OF NBN DEVICE 155
8.1 nBn Device with Bulk (***n*** and ***p***-type) Barrier 155
8.1.1 nBn Device with ***n***-type Barrier 155
8.1.2 nBn Device with ***p***-type Barrier 157
8.2 nBn Device with T3SL Barrier 160
9 MBE GROWTH AND CHARACTERIZATION OF NBN DEVICE 164
9.1 nBn Samples Grown with MBE and Their Characterization Results 164
9.2 Methods to Measure Valence Band Offset 169
10 NBN DEVICE WITH T3SL ABSORBER AND 2-COLOR NBN 171
10.1 Introduction 171
10.2 Design and Modeling 175
10.3 Result and Discussion 179
11 SUMMARY AND FUTURE WORK 192

REFERENCES 195

LIST OF TABLES

Table 1 Division of Infrared Radiation [1]. 4

Table 2 Band structure parameters for HgTe and CdTe at T = 0 K employed in the 8×8 Kane model 36

Table 3 Band structure parameters for HgTe and CdTe at T = 300 K employed in the 14-band k·p calculations 42

Table 4 The designed number of periods, HgTe well layer thickness, and CdTe barrier layer thickness of the inverted band structure superlattice samples 68

Table 5 The designed number of periods, HgTe well layer thickness, and CdTe barrier layer thickness of three representing normal band structure superlattice samples. 70

Table 6 The designed number of periods and well/barrier thicknesses of three T3SL samples used in TEM characterization 93

Table 7 The designed number of periods, well thicknesses dw, barrier thicknesses db, and SL period dSL (dSL = dw + db) of selected T3SL samples used in XRD characterization. 107

Table 8 Calculated pseudo x value, well thickness dw, barrier thickness db and SL period dSL of sample hct15048 and hct15051 from XRD ω-2θ scan. 108

Table 9 The designed and calculated thicknesses, along with FWHM of the peak associated with superlattice of the three selected samples for XRD measurement 110

Table 10 A comparison between the substrate peak FWHM and SL Peak FWHM of the selected three samples. 111

Table 11 The growth temperatures, absorber compositions, absorber thicknesses, superlattice barrier thicknesses, and the growth time of each superlattice period of the three HgCdTe-based nBn structure with HgTe/CdTe superlattice barrier. 165

LIST OF FIGURES

Figure 1 The electromagnetic spectrum (https://en.wikipedia.org/wiki/Electromagnetic_spectrum) 3

Figure 2 Blackbody radiation (https://en.wikipedia.org/wiki/Black-body_radiation) 3

Figure 3 atmospheric transmittance in the infrared region (https://en.wikipedia.org/wiki/Infrared) 4

Figure 4 VLWIR infrared, visible and a hybrid image of M31, the Andromeda galaxy, taken with the Spitzer Space Telescope. (Credit: NASA/JPL–Caltech/K. Gordon, University of Arizona)....6

Figure 5 A zincblende unit cell (https://en.wikipedia.org/wiki/Cubic_crystal_system#Zincblende_structure).....11

Figure 6 The bandgap energy (at room temperature) and the lattice constant ao of a few common semiconductor compounds with zincblende structure[10]. Three pairs of materials are chosen and circled in red as examples of widely used superlattices: AlAs/GaAs, InAs/GaSb, and HgTe/CdTe. 14

Figure 7 Band alignment of three types of superlattices. The three representing examples shown here are the band structures of GaAs/Ga1-xAlxAs, InAs/GaSb, and HgTe/CdTe SL, respectively. 14

Figure 8 The band structure of HgTe (left) and CdTe(right) at room temperature[15]. 17

Figure 9 A comparison of the band structure of HgTe/CdTe superlattice with different well thickness d_w[10].....18

Figure 10 Band gap energy of HgTe/HgCdTe superlattice as a function of well thickness d_w at T=5K.....19

Figure 11 The cut-off wavelength for $Hg_{1-x}Cd_xTe$ as a function of composition, x, as given by Hansen's equation. The four major infrared subbands are also shown, along with the ranges of x values that correspond to a cut-off wavelength within these bands [16].....20

Figure 12 The cut-off wavelength as a function of composition x for HgCdTe (Left), Normal band structure T3SL (Middle), and Inverted band structure T3SL (Right) at various temperatures. The blue dash lines show the range of $\lambda_{cutoff} = 17.0 \pm 1.0$ μm @ 40K, and the corresponding x values/well layer thicknesses for HgCdTe and T3SL separately[17].....21

Figure 13 An illustration of band diagrams about the zone center (k = 0) for CdTe and HgTe at 0 K. 28

Figure 14 Superlattice minibands formed from wavefunction overlap [31]. 30

Figure 15 The 14 bulk bands considered in our 14-band k.p calculations and their important band structure parameters for unstrained (left) and strained (right) cases [42].....36

Figure 16 Modeled band structure of MCT with x=0.3. 43

Figure 17 Modeled band structure for (a) inverted and (b) normal HgTe/CdTe SL. 45

Figure 18 3D graph of bandgap vs. numbers of HgTe/CdTe monolayers (ML). The number of ML range from 1 to 31, which corresponding to 3.24 Å to 100.44 Å. The red curve corresponds to where the bandgap Eg = 0. 46
Figure 19 The Fermi level energy (meV) as a function of the number of CdTe ML layers at different numbers of HgTe ML layers and different doping levels at 80K. 48
Figure 20 The major components of a general MBE growth chamber. 52
Figure 21 MBE 32p system in Microphysics Laboratory at the University of Illinois at Chicago 54
Figure 22 An effusion cell. 56
Figure 23 A continuous feed mercury source. (K. A. Harris, et al., 1986). 58
Figure 24 RIBER VHG500 Mercury cell (500 cc) 58
Figure 25 RIBER MCL Mercury cell (1100cc) 59
Figure 26 A picture of the new Mercury cell installed on the MBE 32p chamber (left), and a sketch of the Mercury cell's major components (right). 59
Figure 27 The upper part of the Hg cell. The feedthrough is connected to the cell port inside the chamber. And a glass tube is connected to the feedthrough to monitor the mercury level inside the cell port closely. 61
Figure 28 The glass tube used to monitor the mercury level 62
Figure 29 Mercury cell flux calibration on two different days showing good run-to-run flux stability 62
Figure 30 A sketch of mercury cell port. 63
Figure 31 An illustration of PID control loop 65
Figure 32 A temperature ramping profile using PID control 65
Figure 33 The structure of the inverted band SL samples. The insert shows one period of the SL layer. 68
Figure 34 The structure of the normal band SL samples. The insert shows one period of the SL layer. 69
Figure 35 An illustration of an RHEED system. (https://en.wikipedia.org/wiki/Reflection_high-energy_electron_diffraction) 71
Figure 36 This diffraction condition of RHEED 73
Figure 37 RHEED images of a typical HgTe/CdTe SL growth. (Left) HgTe well (Right) CdTe barrier 73
Figure 38 RHEED patterns associated with problems during the growth. (Left) 3D growth on the samples surface usually resulting from multiple crystalline phases; (Right) Twinning dots due to short streaks from (111) twin plane adjacent to the primary reflection. 75
Figure 39 An illustration of an Ellipsometry system (https://en.wikipedia.org/wiki/Ellipsometry) 76

Figure 40 An example of fitted ellipsometry data. ψ and Δ are plotted as a function of light energy. The data is from a single timestamp during the HgTe/CdTe superlattice growth, and the fitted model is a HgTe model based on experimental data. 78

Figure 41 Ellipsometry data during one MWIR DLPH growth. Surface roughness and Hg1-xCdxTe composition are plotted as a function of time into the growth process. SWIR buffer layer, MWIR absorber layer, and the HgCdTe cap layer corresponds to different regions on the composition vs. time curve. 79

Figure 42 Ellipsometry parameter ψ as a function of time for light sampled at different energies. The curves oscillate at the beginning of the growth due to interference between reflected lights. The effect disappears after 30min into the growth. The data is fitted using interference theory. Note that the time starts at a non-zero position because ellipsometry and the growth were started at different times. 80

Figure 43 Ellipsometry being used to calibrate HgTe growth rate. A HgTe layer is grown on CdTe on Si sample for 15 minutes. The thickness of the layer as a function of time is plotted using the fitted data. The growth rate can then be extracted from the slope of the linear fit. 81

Figure 44 A few examples of the RHEED pattern and the ellipsometry surface roughness of MWIR single layer HgCdTe samples. A strong correlation between the ellipsometry surface roughness and RHEED patterns can be observed. 81

Figure 45 An example of ellipsometry data got from superlattice growth. Because the HgTe well and barrier layers are relatively thin, ellipsometry does not have enough layer thickness to build up stable polarization information. 82

Figure 46 A picture of as-grown HgTe/CdTe superlattice sample on CdZnTe (211)B substrate. 83

Figure 47 A picture taken with a whole wafer imaging system of as-grown 25mmx25mm HgTe/CdTe superlattice sample on CdZnTe (211)B substrate 84

Figure 48 Microscope imaging of the surface of three HgTe/CdTe superlattice samples: (a) a defect-free surface (b) a surface full of triangle void defects (c)a micro-defects rich surface. 85

Figure 49 A Nomarski microscopic image of an as-grown HgTe/CdTe superlattice sample on CdTe (211)B on Si substrate. 86

Figure 51 Nomarski imaging of (a) a void defect under 1000x magnification. The triangle void defect sits on a crater (b) a needle defects rich surface under 500x magnification. 87

Figure 52 An illustration of a Scanning electron microscope. (Source: Encyclopædia Britannica, https://www.britannica.com/technology/scanning-electron-microscope) 88

Figure 53 SEM imaging of the cross-section of a HgTe/CdTe superlattice sample grown on CdTe (211)B on Si substrate at (a) 162× magnification (b) 5570× magnification (c) 12850× magnification 89

Figure 54 SEM imaging of the cross-section of a HgTe/CdTe superlattice sample grown on CdTe (211)B on Si substrate made with a dicing saw. 91

Figure 55 An illustration of transmission electron microscope 92

Figure 56 SEM Imaging of the cross-section of the FIB lift-out sample 94

Figure 57 A low magnification (10k×) XTEM image of sample hct16003 95

Figure 58 A medium magnification XTEM image of sample hct16003 96

Figure 59 high magnification XTEM images of sample hct16003 prepared with (a) FIB (b) Ar-ion milling at liquid nitrogen temperature. 97

Figure 60 High magnification XTEM images of all three samples mentioned in Table 6. The average thicknesses of HgTe well layers and CdTe barrier layers are also given on the images. 98

Figure 61 HgTe error percentage (left) and CdTe error percentage (right) as a function of sample index since the start of this batch of HgTe/CdTe superlattice growths. The blue and red straight lines are the linear fit of the three TEM characterized samples. 99

Figure 62 Examples of irregularity observed from XTEM. (a) Superlattice pattern becomes wavy near the sample surface, and Te Precipitates are observed. (b) An extra thick CdTe barrier layer was created shortly after the SL growth started due to Tellurium shutter malfunction. 99

Figure 63 Rotation angles of the XRD sample stage. (https://www.semanticscholar.org/paper/Determination-of-residual-stresses-by-X-ray-Fitzpatrick-Fry/ecbaba17e7e95806ab701cefab1fd50781adc2b6#paper-header).....101

Figure 64 The basic setup of the XRD system at Microphysics Laboratory of the University of Illinois at Chicago.....102

Figure 65 Two beams scattered off atoms in two different planes in a Bragg diffraction situation. (https://en.wikipedia.org/wiki/Bragg%27s_law).....103

Figure 66 A ω-2θ scan of the (422) reflection of two SL samples with inverted band structure, hct15048 (left) and hc15051(right). Diffraction peaks associated with the substrate (S), superlattice (L), and satellite fringes (F) are labeled on the figure.....108

Figure 67 ω-2θ scan of the (422) reflection of sample SL_CZT (left), sample SL_CdTe/Si_1 and SL_CdTe/Si_2 (right). Diffraction peaks associated with the substrate (S), superlattice (L), HgCdTe cap layer (C), and satellite fringes (F) are labeled on the figure. 109

Figure 68 A schematic diagram of a Michelson interferometer configured for FTIR (https://en.wikipedia.org/wiki/Fourier-transform_infrared_spectroscopy).....115

Figure 69 An example of the transmission spectrum of a HgCdTe MWIR DLPH heterostructure obtained from FTIR measurement.....116

Figure 70 Typical intrinsic absorption spectra of $Hg_{1-x}Cd_xTe$ with x=0.0030 at temperatures from 4.2 to 300K [92]. 125

Figure 71 The experimental (blue) and fitted (red) transmission spectrum of an MBE-grown HgCdTe MWIR DPLH layer.....128

Figure 72 The transmission and the absorption coefficient of two HgTe/CdTe superlattice samples as a function of wavenumber at room temperature. The two samples are (a)sample hct15055 with inverted band structure, 200 periods of 67 Å HgTe/44 Å CdTe (b)sample SL_CZT with normal band structure, 500 periods of 50 Å HgTe/50 Å CdTe. The transmission (solid blue line), the absorption (solid red line), the theoretical transmission (dashed blue line), and the theoretical absorption (dashed red line) are shown.....130

Figure 73 The transmission spectra of two HgTe/CdTe superlattice samples SL_CdTe/Si_0 (green) and SL_CdTe/Si_1 (orange) as a function of wavenumber at room temperature. The two samples were both designed to have 52 Å HgTe well and 54 Å CdTe barrier.The difference is that SL_CdTe/Si_0 has 150 periods while SL_CdTe/Si_1 has 500 periods. 131

Figure 74 The room temperature transmission spectra of SL_CZT (blue), SL_CdTe/Si_1(orange) and SL_CdTe/Si_2 (red) as a function of wavenumber and photon energy. The sharp absorption edge, two obvious absorption stages are labeled on the full spectral range graph (left). The absorption peak associated with Si is labeled on the "Zoom in for the 1st transition" graph(right). 132

Figure 75 The calculated absorption coefficients of SL_CZT (blue) and SL_CdTe/Si_2 (red). 133

Figure 76 20 to 296 K transmission curves of a 50Å HgTe/50Å CdTe HgTe/CdTe superlattice sample measured using FTIR. At 40 K, 50% of the maximum transmission is at 613 cm-1, which corresponds to 76 meV in energy and 16 μm in wavelength. 134

Figure 77 20 to 296 K temperature-dependent absorption coefficients extracted from transmission measurements of sample SL_CZT. They are plotted as a function of infrared photon wavenumbers and energies. 135

Figure 78 The experimentally extracted absorption coefficients of sample SL_CZT compared with theoretical predictions at three doping levels, at two temperatures, 40K and 296K (indicated by arrows in the figure). 136

Figure 79 Comparing the measured absorption coefficient of sample SL_CZT with the calculated absorption spectrum of a HgCdTe alloy with a similar cut-off at 40K. 137

Figure 80 The calculated absorption spectra for InAs/$In_xGa_{1-x}Sb$ SLs with various indium content. 138

Figure 81 The absorption coefficient extracted from transmission spectrum(solid green line) and its first derivative(blue circles), the theoretically calculated absorption coefficient(solid black line) and its first derivative (dashed black line), the ratio of transmission at 60K and 20K (red circles) are shown in Figure 84. The two major peaks shown in the first derivatives and the transmission ratio curve are fitted using the Gaussian function. The Physics meaning of the two peaks is marked with arrows. 139

Figure 82 Experimental HH1-C1 and LH1-C1 intersubband transition energies and their difference (H1-L1) are plotted as a function of temperature. Two methods are used to determine these energies, namely dα/dE (empty squares) and the transmission ratio (filled squares). 140

Figure 83 The first transition energy of sample SL_CZT as a function of temperature computed using dα/dE (empty blue square), the ratio of transmission (solid blue square), 50% transmission cut-off (green square), 500cm^{-1} absorption coefficient cutoff (yellow square) and 1000cm^{-1} absorption coefficient cutoff (pink square). The first transition energy of two HgCdTe alloys with similar cutoff wavelength as a function of temperature is also shown (green and red dashed line). 142

Figure 84 Annealing process shifts the cutoff edge of T3SL samples [105]. 145

Figure 85 XTEM images of T3SL sample annealed (a) 30 min at 225°C and (b) 30 min at 250°C [105]. 146

Figure 86 Band diagram of an InAs-based nBn structure [109]. 149

Figure 87 Band alignment for nBn detectors under reverse bias: (a) with significant VBO (b) zero VBO [54]. 153

Figure 88 The cross-sectional device structure and structural parameters of an nBn device with a n-type barrier. The red arrows indicate the light incident direction. 156

Figure 89 Modeled energy band diagrams of HgCdTe nBn photodetector with an n-type barrier (a) at equilibrium (b) under 600mV reverse bias (c) under 600 mV forward bias. 157

Figure 90 The cross-sectional device structure and structural parameters of an nBn device with a p-type barrier. The red arrows indicate the light incident direction. 158

Figure 91 Modeled energy band diagrams of HgCdTe nBn photodetector with an p-type barrier (a) at equilibrium (b) under 600mV reverse bias (c) under 600 mV forward bias. 159

Figure 92 Calculated space-charge regions in an MWIR HgCdTe nBn detector with a p-type barrier. 160

Figure 93 The cross-sectional device structure and structural parameters of an nBn device with HgTe/CdTe SL barrier. The red arrows indicate the light incident direction. 162

Figure 94 Modeled energy band diagrams of HgCdTe nBn photodetector with HgTe/CdTe superlattice barrier at equilibrium. 163

Figure 95 Screenshots of RHEED pattern at different stages of the MBE growth of an nBn structure with HgTe/CdTe superlattice barrier. (a) Absorber (b) CdTe barrier in SL (c) HgTe well in SL 166

Figure 96 The ellipsometry data of one full MBE growth of nBn structure with HgTe/CdTe superlattice barrier. Composition (green) and surface roughness (red) as a function of time are plotted. 167

Figure 97 The transmission spectra as a function of the wavenumber of the three nBn samples mentioned in Table 11. 168

Figure 98 Nomarski imaging of nBn sample hct18001 at (a) 100x magnification (b) 500x magnification 168

Figure 99 The computed HgCdTe alloy detector band profiles with the LWIR layer under (a) +0.2 V (b) -0.2V bias relative to the VLWIR layer. The arrow shows the motion of photo holes generated in the activate absorber region [123]. 173

Figure 100 (a) Schematic of a two-color type-II InAs/GaSb superlattice-based pBp photodetector. (b) Band alignment under forward and reverse biases, where the bias is applied on the top electrode of the detector [127]. 174

Figure 101 Calculated band structure of HgTe/CdTe superlattices at 100K. (a) 55 Å HgTe/55 Å CdTe SL. (b) 26 Å HgTe/90 Å CdTe SL (c) 45 Å HgTe/55 Å CdTe SL. 176

Figure 102 The cross-sectional device structure and structural parameters of an nBn device designed for the VLWIR region with all superlattice layers except the substrate. The red arrows indicate the light incident direction. 176

Figure 103 The cross-sectional device structure and structural parameters of a 2-color nBn device designed for VLWIR and LWIR absorption with all superlattice layers except the substrate. The red arrows indicate the light incident direction. 177

Figure 104 Schematic illustration of the predicted band alignment under (a) forward and (b) reverse biases for a 2-color nBn device designed for VLWIR and LWIR absorption. The forward bias means a positive polarity applied on the LWIR absorber side (bottom side) of the detector. The optical transitions contributing to photocurrents are also shown in the figure. 178

Figure 105 The calculated energy band diagrams of an nBn device designed for the VLWIR region with HgTe/CdTe superlattice absorber and barrier (device structure shown in Figure 102) (top) at equilibrium (middle) under forward bias $\mathrm{Vbias} = 0.1\mathrm{V}$ (bottom) under reverse bias $\mathrm{Vbias} = -0.1\mathrm{V}$. 180

Figure 106 The simulated I-V characteristics of an nBn device designed for the VLWIR region with HgTe/CdTe superlattice absorber and barrier (device structure shown in Figure 102). 0.5μm (solid blue line) or 5 μm (dashed red line) contact layer is used in the simulation. 182

Figure 107 The calculated energy band diagrams of a two-color nBn device designed for VLWIR/LWIR region with HgTe/CdTe superlattice absorbers and barrier (device structure shown in Figure 103) (top) at equilibrium (middle) under forward bias $\mathrm{Vbias} = 0.1\mathrm{V}$ (bottom) under reverse bias $\mathrm{Vbias} = -0.1\mathrm{V}$. 183

Figure 108 The simulated I-V characteristics of a two-color nBn device designed for VLWIR/LWIR region with HgTe/CdTe superlattice absorbers and barrier (device structure is shown in Figure 103). 185

Figure 109 The simulated I-V characteristics of a two-color nBn device with increased absorber thicknesses (15 μm of VLWIR absorber and 10 μm of LWIR absorber) compared to Rule 07. 186

Figure 110 The calculated energy band diagrams of a two-color nBn device with the VLWIR absorber doped at a higher level ($8 \times 1016\ \mathrm{cm} - 3$) (top) at equilibrium (middle) under forward bias $\mathrm{Vbias} = 0.1\mathrm{V}$ (bottom) under reverse bias $\mathrm{Vbias} = -0.1\mathrm{V}$. 187

Figure 111 The simulated I-V characteristics of the second design of two-color VLWIR/LWIR nBn. 188

Figure 112 The simulated I-V characteristics of the second design of two-color VLWIR/LWIR nBn with increased absorber thicknesses (15 μm of VLWIR absorber and 10 μm of LWIR absorber) compared to Rule 07. 189

Figure 113 The calculated energy band diagrams of a two-color $\mathrm{nB_pn}$ device with $1 \times 1016\ \mathrm{cm} - 3$ p-type doped barrier (top) at equilibrium (middle) under forward bias $\mathrm{Vbias} = 0.1\mathrm{V}$ (bottom) under reverse bias $\mathrm{Vbias} = -0.1\mathrm{V}$. 190

LIST OF ABBREVIATIONS

MBE	Molecular beam epitaxy
SL	Superlattice
T1SL	Type-I superlattice
T2SL	Type-II superlattice
T3SL	Type-III superlattice
IR	Infrared
NIR	Near infrared
SWIR	Short-wavelength infrared
MWIR	Mid-wavelength infrared
LWIR	Long-wavelength infrared
VLWIR	Very-long-wavelength infrared
FIR	Far infrared
subMM	Submillimeter
MCT	Mercury cadmium telluride
RHEED	Reflection high-energy electron diffraction
SE	Spectroscopic ellipsometry
FTIR	Fourier-transform infrared spectroscopy
SEM	Scanning electron microscopy
TEM	Transmission electron microscopy
XRD	X-ray diffraction
FWHM	Full width at half maximum

LIST OF ABBREVIATIONS (continued)

FIB	Focused ion beam
IPE	Internal photoemission
UHV	Ultra High Vacuum
I-V	Current-voltage
1D	One dimensional
2D	Two dimensional
MLTF	Multi-layer thin film
ML	Monolayer
MPL	Microphysics Laboratory
UIC	University of Illinois at Chicago

SUMMARY

Potentials possessed by type-III superlattices in theory were not realized in practice, despite relatively comprehensive research efforts in the 1990s. Those efforts predict its several advantages relative to HgCdTe alloys, namely longer Auger lifetime, lower tunneling currents, sharper absorption onset, and more uniform and easier-to-control cutoff wavelength, especially in the very long wavelength infrared (VLWIR) region. Molecular beam epitaxy (MBE) was relatively new at that time, and the growth of HgCdTe-based materials was in its infancy. Lack of computer-controlled shutters and consistently reliable substrates made high-quality T3SL samples in high demand yet hard to find. However, MBE technology is mature now, and all the difficulties mentioned above can be conquered. It is time to revisit T3SL and fully utilize its potentials as an infrared detection material.

In this thesis, T3SLs designed for VLWIR absorption were grown using molecular beam epitaxy (MBE) with precise layer thickness control. *In-situ* and *ex-situ* characterization methods like reflection high-energy electron diffraction (RHEED), spectroscopic ellipsometry (SE), Nomarski microscope, Fourier-transform infrared spectroscopy (FTIR), transmission electron microscopy (TEM), and x-ray diffraction (XRD) were used to evaluate as-grown samples. The measured temperature-dependent infrared absorption spectra of the T3SL samples exhibit sharp and strong absorption onsets, which agree very well with our values calculated using the 14-band superlattice k.p method.

However, T3SL's significant interdiffusion under elevated temperatures during the annealing process after p-type ion implantation shifts the absorption edge to higher energies and

even makes the SL characters disappear. This critical disadvantage makes T3SL unsuitable for photovoltaic photodetector applications.

To fully exploit T3SL's potential as an infrared detection material working in the VLWIR region and circumvent the need for p-type doping followed by high-temperature annealing, an nBn architecture based on HgTe/CdTe T3SL absorber and barrier that works in the VLWIR region is proposed for the first time. The T3SL barrier layer can be engineered to eliminate valence band offset (VBO), an essential requirement for an efficient nBn structure. Additionally, a bias-selective two-color nBn with two absorbers working in VLWIR and long-wavelength infrared (LWIR) region is proposed. A detailed and integrated design is presented, and the dark current-voltage characteristics of the modeled device are evaluated. Near-zero valence band offset can be achieved with various doping levels. The simulated dark current densities are comparable to those given by "Rule 07", a heuristic predictor of the state-of-the-art HgCdTe photodiode performance.

PART I:
Very Long Wavelength Infrared Type III Superlattices

1 INTRODUCTION

1.1 Infrared Detection

1.1.1 Infrared radiation

This research's primary motivation is developing and characterizing novel techniques and material systems for infrared detection. Infrared detectors have a wide range of applications, including but not limited to astronomy, military, medical treatment, industrial and environmental safety, and remote sensing. The electromagnetic spectrum (Figure 1) is classified into several regions (bands) due to radiation of different wavelengths. Ranking the wavelength from short to long (frequency from high to low), the electromagnetic spectrum includes gamma-rays, X-rays, ultraviolet, visible light, infrared, microwave, and radio waves. Infrared (IR) radiation encompass wavelengths from 700nm, which is the red edge of the visible light, to 1 mm, which is called far-infrared (FIR). Our interest falls into this infrared wavelength region, particularly an even smaller wavelength range covering 1μm to 25 μm. Any matter above absolute zero temperature emits IR radiation. The relationship between the object's temperature and the wavelength of maximum emission that it emitted is shown in Figure 2. It shows that as the temperature decreases, the emitted radiation curve moves to lower intensities and longer wavelengths. For various critical applications involving object detection, the maximum emission wavelength is in the 1μm to 25 μm range.

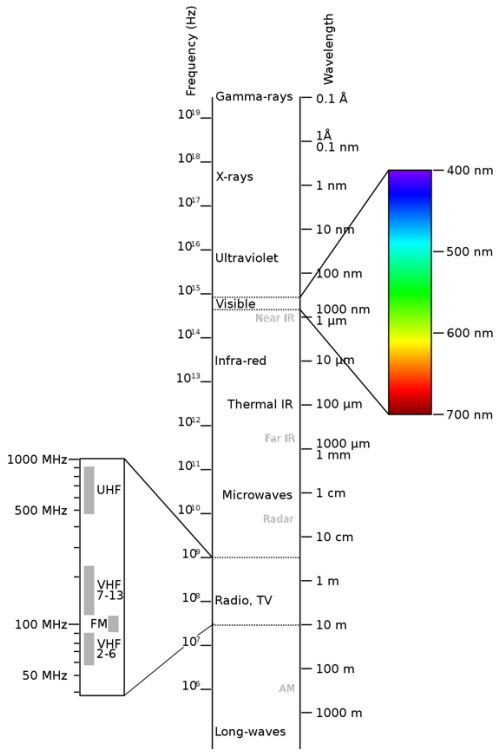

Figure 1 The electromagnetic spectrum (https://en.wikipedia.org/wiki/Electromagnetic_spectrum)

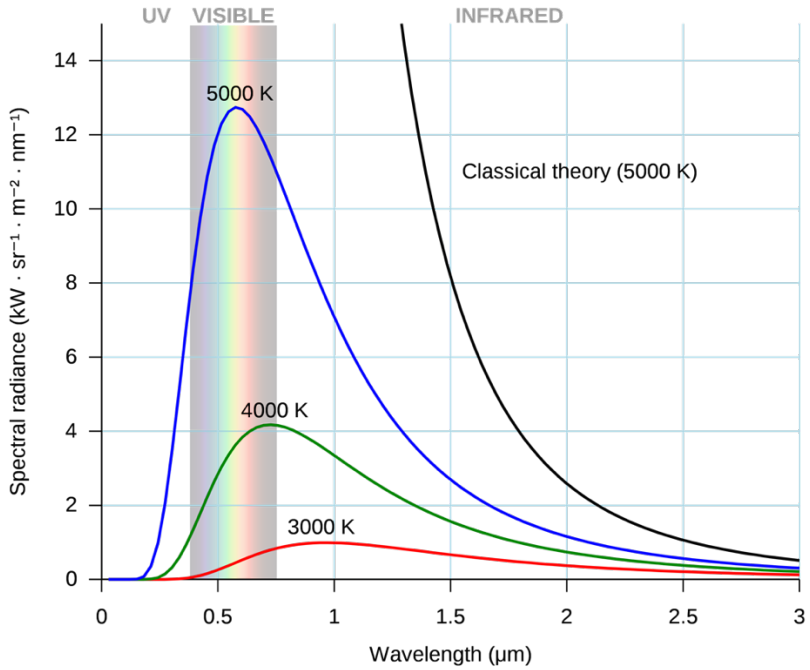

Figure 2 Blackbody radiation (https://en.wikipedia.org/wiki/Black-body_radiation)

The infrared band is often subdivided into smaller sections, based on the atmosphere's natural absorption majorly from carbon dioxide and water vapor (Figure 3). The naming of the subsections and their corresponding wavelength range is given in Table 1.

Region (Abbreviation)	Wavelength Range (μm)
Near infrared (NIR)	0.78-1
Short wavelength IR (SWIR)	1-3
Medium wavelength IR (MWIR)	3-6
Long wavelength IR (LWIR)	6-15
Very long wavelength IR (VLWIR)	15-30
Far infrared (FIR)	30-100
Submillimeter (subMM)	100-1000

Table 1 Division of Infrared Radiation [1].

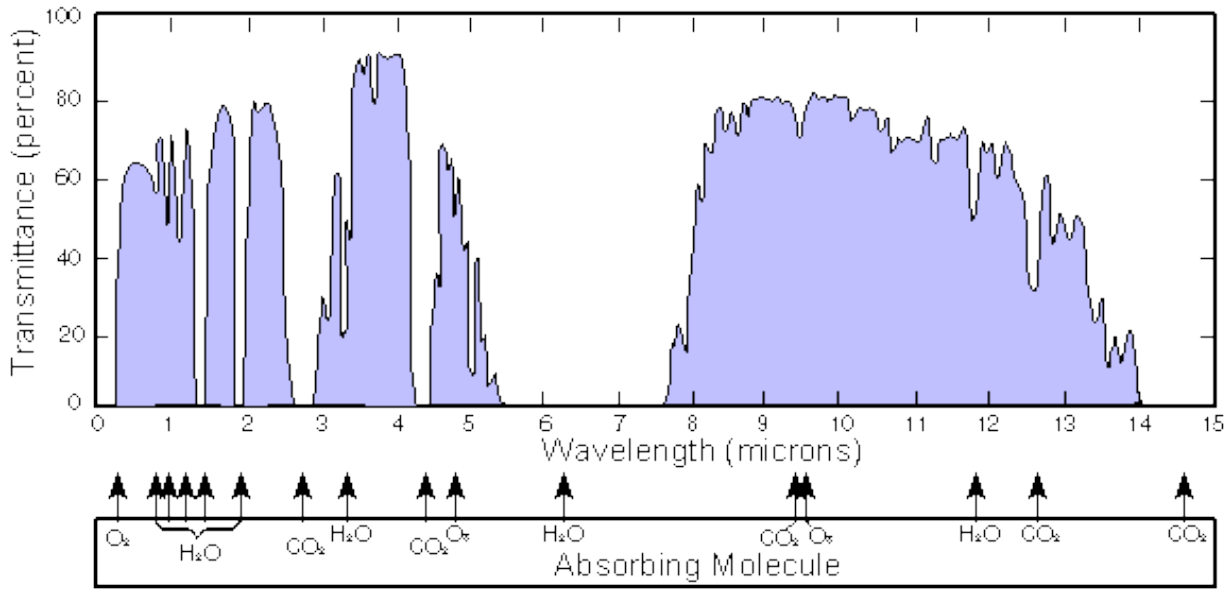

Figure 3 atmospheric transmittance in the infrared region (https://en.wikipedia.org/wiki/Infrared)

1.1.2 Infrared detection applications

The uniqueness of radiation of infrared light from any objects above 0K brings us to the most prominent advantage of IR detection. IR detectors can observe targets that cannot be seen by human eyes. One is that objects that are relatively far or too cold emit infrared light that can be captured by IR detectors, though they do not emit visible light. This feature has proven useful in Astronomy. It has been used to discover previously unseen objects such as comets, stars, planets and to observe the dust particles and gas molecules around the planets in the galaxy and interstellar medium to determine their chemical structure. Typical infrared images obtained from the telescope are shown in Figure 4.

The second is that a longer wavelength of IR radiation enables it to be less likely to scatter than visible light due to diffraction. Gas molecules and dust particles can absorb or reflect visible light, whereas infrared light with a longer wavelength can move around those small obstacles and "penetrate" through gas and dust. Due to this feature, IR detection is widely useful in the military for observing objects whose visible light is concealed by dust and gas particles in the path. Night vision, target cognition, and missile detection are typical military applications of infrared systems.

Thermal imaging is another critical application of infrared detection. In some medical treatments, thermal imaging offers a quick and non-evasive process replacing the need for surgery. Thermal imaging can show localized blood flow rate changes under the skin by detecting temperature changes, which can help diagnose inflammation, circulation disorders, and skin diseases like skin cancer.

Non-contact monitoring using infrared detection technologies finds extensive application in the industry. Pyrometry, which measures the surface temperature by the characteristics of the infrared radiation emitted, is widely used in many high-temperature industrial processes, where direct-contact temperature measurement is impractical. Infrared imaging is also advantageous to monitor a large area in the industry. For example, it can be used to detect high-temperature gas leaks on pipes. Fault detection in electrical systems is another application of infrared imaging whereby problems can be identified without power down the system.

Infrared detection is commonly used in remote sensing systems. Global weather satellite systems monitor the earth's atmosphere and surface over several infrared bands, which provides critical information for weather prediction models. Infrared remote sensing can also provide important metrological and environmental information on land and water surface temperature measurements, hurricane tracking, earthquake prediction, and bushfire detection.

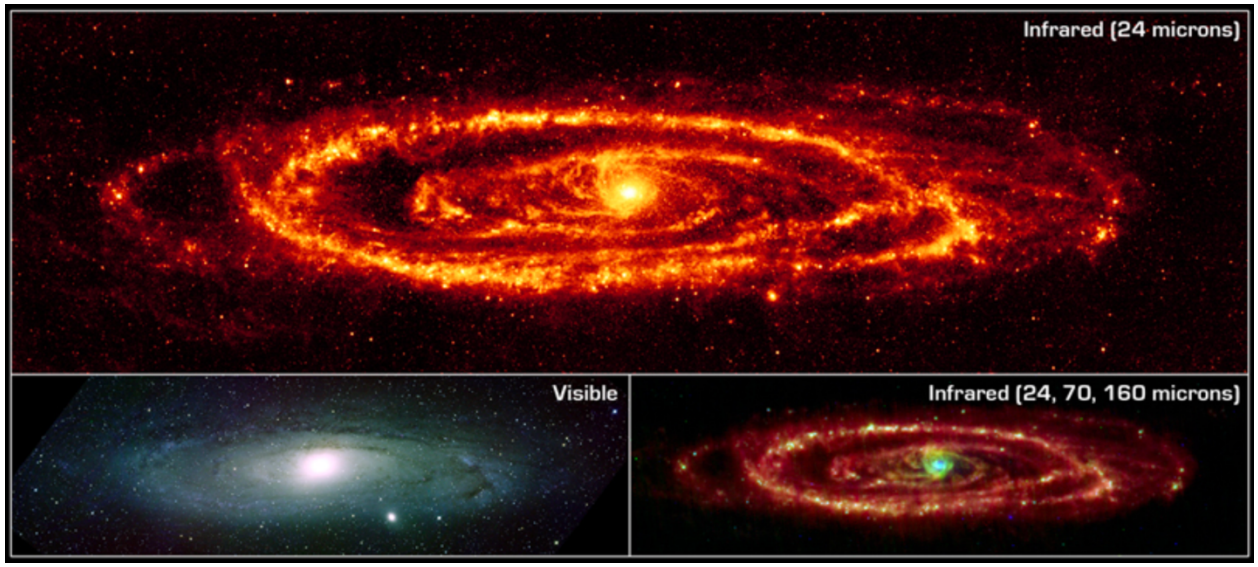

Figure 4 VLWIR infrared, visible and a hybrid image of M31, the Andromeda galaxy, taken with the Spitzer Space Telescope. (Credit: NASA/JPL–Caltech/K. Gordon, University of Arizona).

1.1.3 Infrared detectors

There are several criteria to measure the performance or the overall efficiency of infrared detectors used for imaging and sensing, namely response wavelength range, sensitivity, response times, and overall production cost. Depends on the specific application, requirements for infrared detectors vary considerably. There is usually a tradeoff between these criteria, and each infrared detection system has its advantages. For example, Focal plane arrays (FPA) are employed for infrared imaging thanks to their great sensitivity and response time, but they are costly to make. On the other side, infrared sensing can be implemented using relatively simple single-element detectors.

In general, there are two types of infrared detectors, thermal and photonic (photodetectors) [2]–[4].

Thermal detectors are usually more cost-efficient than photodetectors. They rely on the measurement of a material property, which changes with the temperature change of the element through the absorption of electromagnetic radiation. Two common types of thermal detectors are pyroelectric detectors and bolometers. Pyroelectric detectors measure the temperature-dependent changes in the electric polarization of the absorbing material. Bolometers measure the power of incident infrared light via detecting the heating of a temperature-dependent electrical resistance material. While thermal detectors are relatively cheap to make, they suffer from a few drawbacks: 1) Thermal detectors detect all lights incident into the detectors. They generally cannot be tuned to specific wavelengths without external filtering. 2) Sensitivity is low, and response time is high compared to photodetectors. 3) It is not suitable for rapid sensing due to its long recovery time.

Recent advances in microfabrication of silicon-based structures have led to the exciting area of micro-bolometers, which can measure changes of 0.1°C from a power input as small as 10 nW. Micro-bolometers are an array of bolometers fabricated directly on a silicon readout circuit. One of the significant advantages of micro-bolometers is that they can operate near room temperature. Compared to other sophisticated photodetectors, micro-bolometers do not need bulky and expensive housings to accommodate ultra-high vacuum and cryogenically cooled operation. However, their detection capability is still much less than that of photon detectors due to their fundamental working mechanism, although micro-bolometers' performance is significantly improved over bolometers.

On the other hand, photodetectors [5]–[7] have a faster response time, higher sensitivity compared to thermal detectors. And most importantly, photodetectors made with semiconductor alloys and superlattices can be tuned only to detect infrared light at a specific wavelength. Photodetectors are based on the conversion of photons of light directly into free current carriers. Photodetectors are usually made from semiconductors, where a non-zero bandgap is present. Electrons are photo-excited across the energy gap from the valence band to the conduction band, which generates a current, voltage, or resistance that gives rise to an observable electrical signal. Electrons can only be excited when the incident photons have energies larger than the energy gap of the material, E_g:

$$E_{photon} = \frac{hc}{\lambda} > E_g \tag{1.1}$$

The longest wavelength, which satisfies Equation (1.1), is designated the cut-off wavelength of the material, λ_c. And the electrons with wavelength λ_c has the cut-off energy E_c. We will discuss later that the definition of cut-off energy E_c varies.

Photodetectors have much higher sensitivity and faster response time compared to thermal detectors. Moreover, because the bandgap of semiconductor materials can be tuned in several ways, these photodetectors can be engineered to absorb specific wavelength ranges, for example, SWIR, MWIR, and LWIR that we mentioned in 1.1.1.

Other than photons, phonons can also transfer energy to electrons and excite electrons across the bandgap. This mechanism generates noise in our signal. Therefore, photodetectors must be cooled down to low temperatures to reduce the number of thermally generated carriers across the bandgap. Cooling requires expensive housing, which makes photodetectors bulky and expensive. This drawback of photodetectors has driven intensive research to raise the operating temperature while achieving good performance.

The two most widely used modes of photodetectors are photoconductive (PC) and photovoltaic (PV). Photovoltaic detectors are based on P-N junctions. An electron-hole pair is generated when a photon with the energy greater than the energy bandgap is absorbed. The generated electron and hole are separated by the built-in potential barrier of the PN junction and diffuse in opposite directions to the contacts. A photocurrent (a signal) is created, and it is measured by an external circuit.

Photoconductive (PC) detectors, unlike photovoltaic detectors, do not have PN junctions and build-in potential. Photoconductive detectors need to operate under a constant bias. A

conductance change in the PC device is caused by the free carriers generated by the incident photons. Under a constantly applied bias, the incident flux of photons produces a proportional level of the current increase in the detectors. Like photovoltaic detectors, the photons can only be absorbed when the photons' energy is greater than the energy gap. The energy gap corresponds to the direct bandgap of the material, except for extrinsic semiconductors. Extrinsic semiconductors are usually heavily doped, and the majority carriers are being excited from the doping level to the conduction band (n-type) or the valence band (p-type). Extrinsic semiconductors are out of the scope of this work, though we will briefly mention its application in VLWIR region in Section 1.5.2.

Several materials have emerged over time for photodetection applications in the wavelength regions of interest, such as MWIR and LWIR. The following sections, 1.2 & 1.3 gives a brief overview of the competing materials used in today's infrared photon detectors.

1.2 Mercury Cadmium Telluride

At present Mercury Cadmium Telluride (MCT) is the most widely used variable gap semiconductor for infrared (IR) photodetection applications [8]. MCT, or HgCdTe, is a ternary alloy made of Hg and Cd as Cation, and Te as Anion. It remains the material of choice for the majority of SWIR, MWIR, and LWIR infrared applications due to its high absorption coefficient and long carrier lifetimes, and it can be optimized for operation at temperatures ranging from that of liquid helium to room temperature. HgCdTe can be used for detectors operated at various modes like photoconductors and photodiodes (photovoltaic), though it is commonly seen in photodiodes.

Single crystal HgCdTe has a zincblende crystal structure (Figure 5), similar to most II-VI semiconductor binary compounds. Zincblende is a cubic lattice with two face-centered cubic sublattices, bonded tetragonally and separated by a quarter of a lattice constant. HgCdTe has two Cations, Hg and Cd, occupying the same positions in the zincblende lattice. The ratio of Cd and Hg is described by composition, where the composition of Cd is *x,* and the composition of Hg is *1-x*. We write the ternary alloy as $Hg_{1-x}Cd_xTe$.

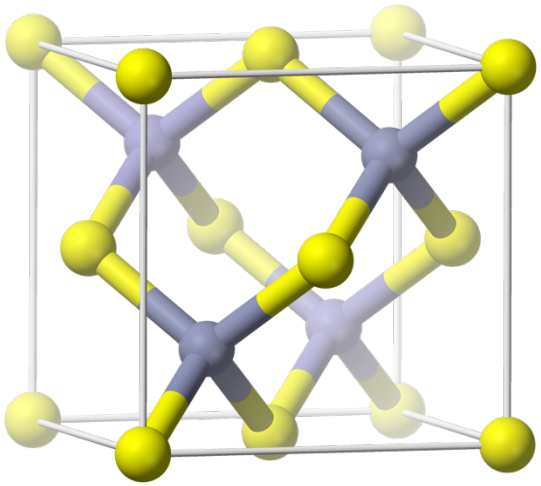

Figure 5 A zincblende unit cell
(https://en.wikipedia.org/wiki/Cubic_crystal_system#Zincblende_structure)

When $x = 1$, we have Cadmium Telluride (CdTe). CdTe is a direct-bandgap material with a bandgap energy of about 1.45 eV at room temperature. CdTe is the second most common PV solar cell technology globally after crystalline silicon. CdTe is also used as a substrate for crystal growth. When x=0, we have Mercury Telluride (HgTe). Despite HgTe and CdTe have a common anion, they have significantly different properties. HgTe is a direct-bandgap material with a so-called "zero" bandgap, which makes it a semimetal. By tuning the composition between 0 to 1, $Hg_{1-x}Cd_xTe$ offers a tunable bandgap between 0-1.45eV. An empirical expression

for the bandgap E_g of $Hg_{1-x}Cd_xTe$ as a function of composition x and temperature T, is first given by Hansen [9]:

$$E_g(x,T) = -0.302 + 1.93x + 5.35 \times 10^{-4}T(1-2x) - 0.810x^2 + 0.832x^3 \qquad (1.2)$$

This tailorable bandgap allows direct band-to-band absorption of infrared light covering the infrared range of 1-25μm that we are interested in. This is one of the most significant advantages of HgCdTe as an infrared material. Other advantages of HgCdTe are 1) Sharp optical absorption that enables high quantum efficiency; 2) Long minority carrier lifetime and high electron mobilities leads to good quantum efficiency even at high operating temperature. All these advantages are related to the electronic band structure of HgCdTe, which we will discuss in detail in Section 2.1.

1.3 Superlattice

Superlattice (SL) is a periodic structure (heterojunctions) of layers of two (or more) materials. One of the most significant advantages of superlattices is that they have multiple design degrees of freedom: the number of substances used in SL, choice of substances, thicknesses of each layer in one period, all of which gives more possibility to obtain desirable electronic /phonon /structural properties. Superlattices can be active layers in IR devices like photoconductive devices or nBn as direct replacements for bulk materials. They also have great potential in multicolor detectors and High Operating Temperature (HOT) detectors. The most common superlattices are the periodic structure of two layers *A* and *B*.

The materials of layer *A* and *B* are carefully chosen to provide the desired physics properties. First of all, superlattices made for infrared detectors require high quality to provide the best performance. Superlattices being a single crystal is a must, then the local defect density has to be controlled to improve minority carrier lifetime and reduce noise. Growing a single crystal of one material on top of another is challenging. First, the two materials need to have the same lattice structure. The semiconductors that we are focusing on here are those with zincblende structure. Second, the lattice mismatch between the lattices of different materials made heterojunctions hard to make. Luckily, Epitaxy technologies like Molecular Beam Epitaxy (MBE) are capable to grow lattice-matched semiconductor materials on top of one another. Still, lattice constant difference between the two materials causes strain, which is usually unwanted because it could generate more defects. As a result, one of the fundamental principles of a successful superlattice design is to have layer *A* and *B* lattice matched as much as possible. Another fundamental principle is to have layer *A* and *B* have different bandgap energies. This will give us the capability to adjust the bandgap of the superlattice based on the specific application. Figure 6 shows the bandgap energy (at room temperature) and the lattice constant a_o of a few common semiconductor compounds with zincblende structure. Three pairs of materials are chosen and circle in red as examples of widely used superlattices: AlAs/GaAs, InAs/GaSb, and HgTe/CdTe. They all consist of two semiconductor compounds with the same zincblende lattice structure, similar lattice constant, and different bandgap energies.

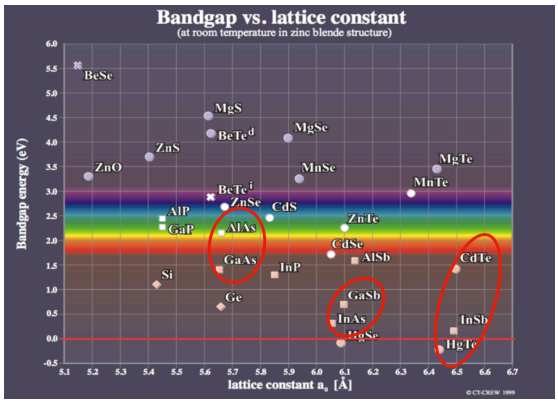

Figure 6 The bandgap energy (at room temperature) and the lattice constant a_o of a few common semiconductor compounds with zincblende structure[10]. Three pairs of materials are chosen and circled in red as examples of widely used superlattices: AlAs/GaAs, InAs/GaSb, and HgTe/CdTe.

Superlattices are classified into three types, based on the conduction and valence band alignments of *A* and *B* layers. Three types of SL are illustrated in Figure 7. Type-I Superlattice (T1SL)and Type-II Superlattice (T2SL) are the most common types. They are majorly based on III-V semiconductor materials. The difference between T1SL and T2SL is that the electrons and holes are localized in different layers. For T1SL, the conduction minimum and valence band maximum lie within the same layer (layer *A* shown here); In T2SL, however, the electrons and holes are localized in different layers (electrons in layer A and holes in layer B as shown here). Usually, we define the layer confining electrons as the "well" layer and the other layer as the "barrier" layer.

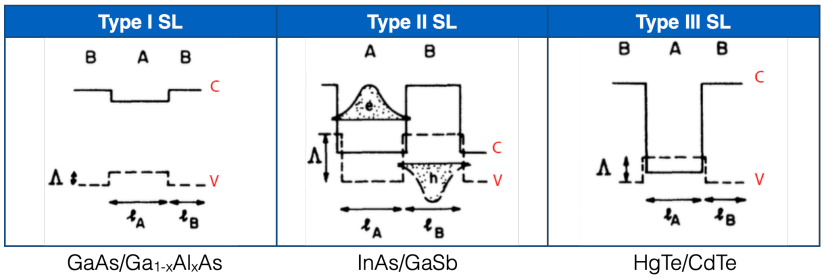

Figure 7 Band alignment of three types of superlattices. The three representing examples shown here are the band structures of GaAs/Ga1-xAlxAs, InAs/GaSb, and HgTe/CdTe SL, respectively.

T2SL based infrared detector technology is undergoing rapid development as a potential alternative to traditional HgCdTe. T2SL has the advantages of superlattices. The band structure and absorption cutoff are tuned by chancing substances in each layer and changing the layer thicknesses, which offers more degrees of freedom compared HgCdTe. During the past decade, there has been a rapid increase in innovative T2SL designs. FPA based on antimonide materials has achieved closer-to-HgCdTe performance, which is a promising achievement in a short time. However, T2SL based detector technology is still in infancy. The potential of T2SL has not been fully realized.

Type-III superlattice (T3SL) is one of a kind due to the inversion of the conduction and valence bands in the well material. Same as T1SL, T3SL has electrons and holes localized in the same layer. However, the band alignment of T3SL is very different from T1SL's and T2SL's. T3SL usually uses HgTe as the well material to provide the inverted band structure.

HgTe/CdTe superlattices are the central focus of this thesis. We use CdTe as the barrier in our modeling. However, a $Hg_{1-x}Cd_xTe$ barrier with a high Cadmium composition is grown in our lab due to a natural mercury vapor background during the MBE growth. We will use HgTe/CdTe superlattice and T3SL interchangeably throughout this thesis, considering their physics properties are majorly decided by the HgTe well, and HgTe/CdTe superlattices are the primary representative of T3SL. We will briefly introduce T3SL in section 1.4, and then discuss it in great detail in section 2.1.

1.4 Type-III Superlattice

1.4.1 History

The HgTe-CdTe superlattice was first suggested as a potential infrared material by Schulman and McGill in 1979 [11]. This is the first reveal of a superlattice with a type-III band alignment due to the introduction of HgTe, a symmetry-induced semimetal.

The first HgTe/CdTe superlattice was grown by Faurie, Million, and Piaguet in 1982 using MBE [12]. Extensive research on T3SL, including theoretical modeling, MBE growth, and characterization, continued throughout the 1980s until the mid-nineties. Then for a decade, there was an industry-wide suspension of efforts to develop HgTe/CdTe superlattice infrared detectors due to the rising of HgCdTe and a lack of research funding. It is quite interesting that HgCdTe started from HgTe/CdTe superlattice. The first MCT layer was created by annealing a HgTe/CdTe superlattice to make HgTe and CdTe interdiffuse. Later researchers have shown that a SL buffer layer can improve the quality of HgCdTe absorber layer [13]. In the last couple of years, even though HgCdTe is dominating the infrared detection world, there has been renewed industry-based interest in HgTe/CdTe superlattice infrared applications, particularly in the VLWIR and FIR regions. We will discuss this in detail in the next two sections.

1.4.2 Band Alignment

This section will briefly discuss the band alignment of Type III Superlattices and why it is different from Type-I and Type-II band alignment.

Take a HgTe/CdTe superlattice as an example. The band structure of HgTe and CdTe at room temperature is shown in Figure 8. HgTe is a semimetal and has an inverted band structure [14], [15]. It means that the p-symmetry band Γ_8 is above the s-symmetry band Γ_6, which is usually the opposite in other direct bandgap semiconductors like CdTe.

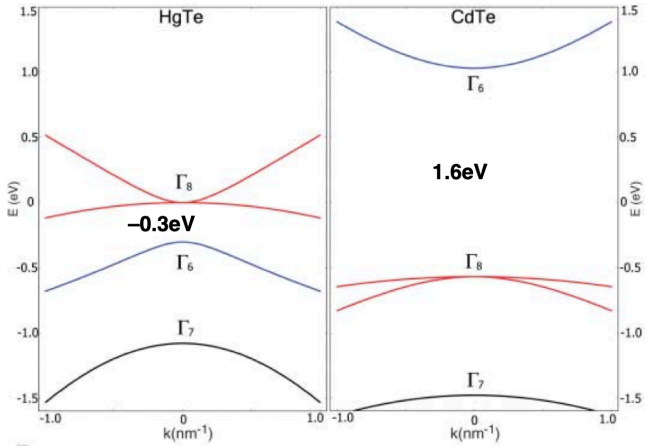

Figure 8 The band structure of HgTe (left) and CdTe(right) at room temperature[15].

A Type-III band alignment with HgTe and CdTe makes the electrons and holes localized in the HgTe well layers. Due to quantum confinement, the energy separation between the first electron subband (E1) and the first two hole subbands, namely heavy hole subband (H1) and light hole subband (L1), is decided by the thickness of the HgTe well layer. The minimum allowed optical transition energy, the bandgap energy E_g, corresponds to the superlattice's H1-E1 transition. It turns out that the HgTe/CdTe Superlattice can have an inverted band structure just like HgTe when the thickness of the HgTe well layer d_w is bigger than the critical thickness $d_c = 6.3\ nm$. When $d_w < d_c$, however, HgTe/CdTe superlattice will have a normal band structure like CdTe. A comparison of the band structure of HgTe/CdTe superlattice with different well thickness d_w is shown in Figure 9.

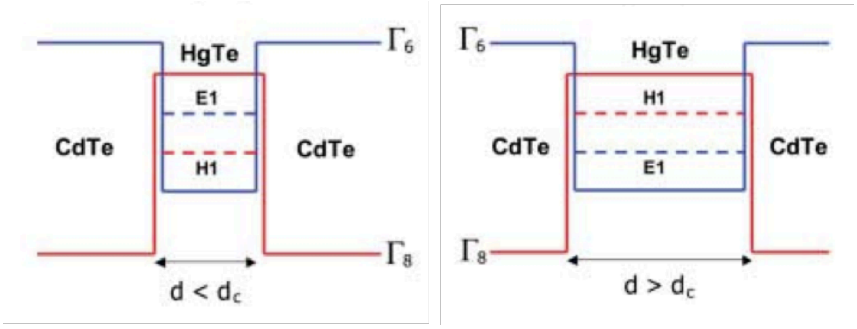

Figure 9 A comparison of the band structure of HgTe/CdTe superlattice with different well thickness d_w[10].

For any HgTe/CdTe superlattice, the bandgap energy E_g is decided by the HgTe well layer thickness. As an example, the bandgap energy of HgTe/HgCdTe superlattice as a function of well thickness d_w at $T = 5K$ is shown in Figure 10. It can be seen that bandgap energy between 0 and 600meV can be achieved by tuning the HgTe layer thickness. The quantum confinement effect on the superlattice energy bands is similar to the effect that variation of composition has on the energy bands of $Hg_{1-x}Cd_xTe$ alloy. So T3SL can be designed to detect a specific wavelength just like HgCdTe. However, for bandgap energy that is smaller than 100meV, one can find two d_w that gives the same bandgap energy, one corresponding to normal band structure superlattice, the other one corresponding to inverted band structure superlattice. Both seem to work as Infrared detector for light with small energies, but we use the one with normal band structure in reality. We will discuss this in more detail in section 2.1.

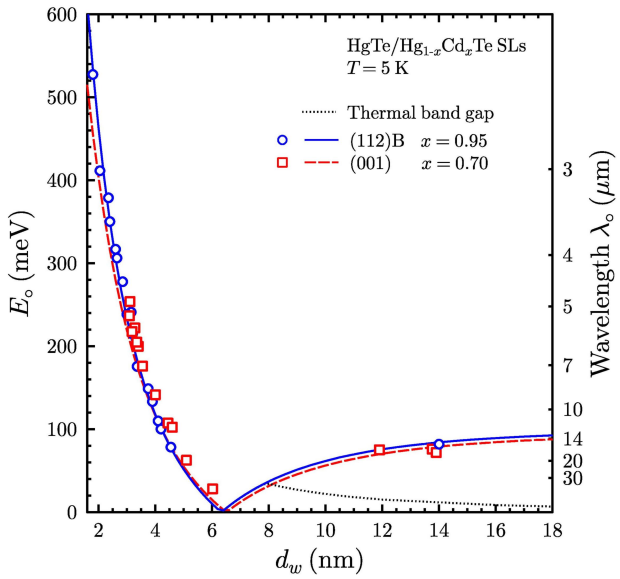

Figure 10 Band gap energy of HgTe/HgCdTe superlattice as a function of well thickness d_w at T=5K.

We will compare T3SL to the two most popular Infrared detector materials, HgCdTe and T2SL, in the next two sections.

1.4.3 T3SL Compared to HgCdTe Alloy

Back in the 1980s and 1990s, after Schulman and McGill first published on HgTe/CdTe superlattice in 1979, researchers including Schulman and McGill suggested that this novel material would have several advantages over the HgCdTe alloy. Nowadays, the spotlight of infrared detection is still on MCT, but all the potentials T3SL possesses still hold.

The most critical advantage of T3SL over HgCdTe is that the cut-off wavelength would be easier to control than the alloy, especially at longer wavelengths. The cutoff of T3SL is controlled by the well layer thickness, while the cutoff of $Hg_{1-x}Cd_xTe$ alloy is controlled by

composition *x*. During the fabrication of these materials in the lab, the layer thickness is much easier to control than the composition. Besides that, the cutoff is less sensitive on layer thicknesses, especially in the very long wavelength infrared region. In comparison, controlling the cutoff of HgCdTe in the VLWIR region is problematic. The relationship between the cutoff wavelength and the composition *x* of $Hg_{1-x}Cd_xTe$ can be plotted based on Hansen's equation. The result is shown in Figure 11 [16]. One can see that in the longer wavelength regime, a small change in composition leads to a significant change in the cutoff wavelength. Especially in the very long wavelength infrared region, a 1% change in composition would result in a 7.5% change in cutoff wavelength, which is not ideal for precise Infrared detection. Comparing the acceptance range of composition/layer thickness for $Hg_{1-x}Cd_xTe$ and HgTe/CdTe superlattice separately for a target cutoff wavelength of 17.0 ± 1.0 μm at 40K [17], it is quite evident that superlattices can control the cutoff much easier than HgCdTe (Figure 12).

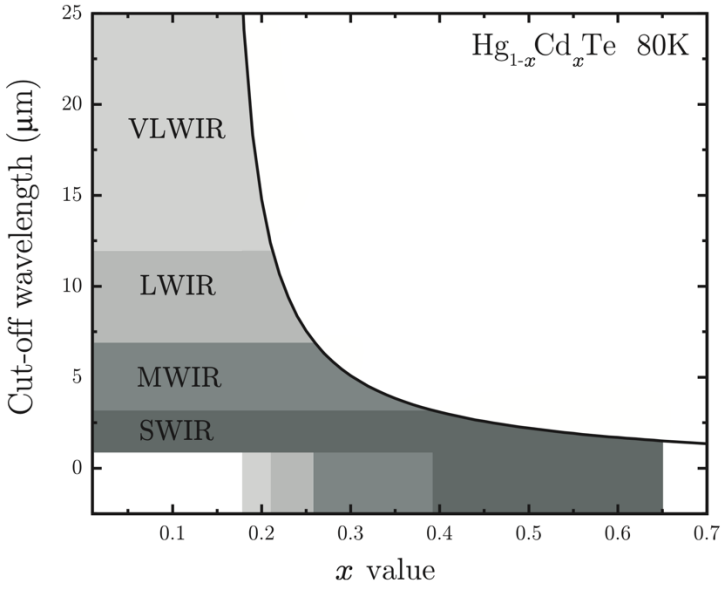

Figure 11 The cut-off wavelength for $Hg_{1-x}Cd_xTe$ as a function of composition, x, as given by Hansen's equation. The four major infrared subbands are also shown, along with the ranges of x values that correspond to a cut-off wavelength within these bands [16].

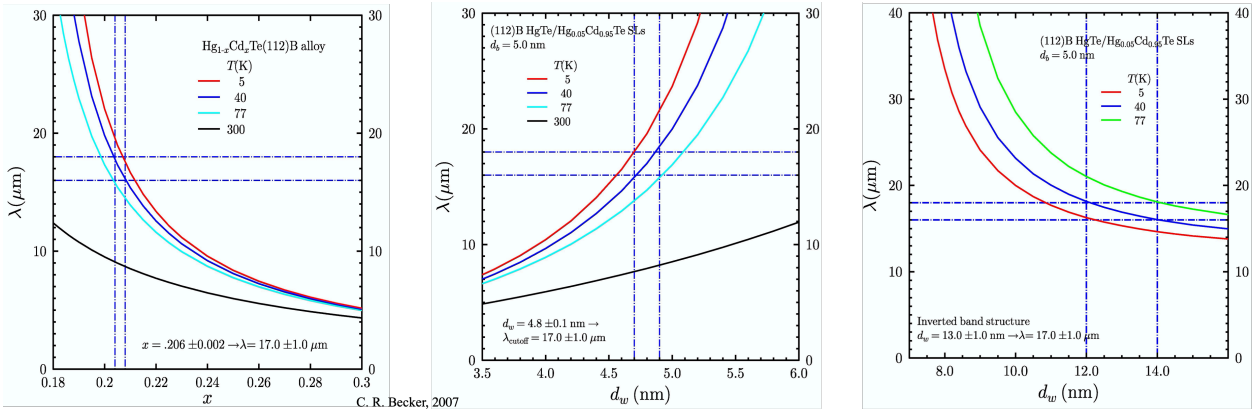

Figure 12 The cut-off wavelength as a function of composition x for HgCdTe (Left), Normal band structure T3SL (Middle), and Inverted band structure T3SL (Right) at various temperatures. The blue dash lines show the range of λ_{cutoff} = 17.0 ± 1.0 μm @ 40K, and the corresponding x values/well layer thicknesses for HgCdTe and T3SL separately[17].

For HgCdTe, not only controlling the cutoff in the very long wavelength infrared region is not ideal, but the uniformity is also a problem. During the Molecular Beam Epitaxy growth, Hg and Cd occupy the lattice cation positions randomly, which means that Hg and Cd's distribution in HgCdTe alloy could be non-uniform. Moreover, even though MBE produces very uniform flux from sources, there could be Hg or Cd clusters formed on the surface. These factors cause composition inconsistency in the alloy, which then leads to cutoff non-uniformity. On the other hand, HgTe/CdTe superlattices do not have this issue because they rely on layer thicknesses instead of the composition to control the cutoff.

T3SL also has a sharper optical absorption onset due to carrier confinement and the high density of states near the band edge. The higher absorption coefficient of T3SL is crucial as it allows thinner absorber layers to be used while maintaining enough optical absorption and high quantum efficiency. More details about absorption in T3SL will be discussed in chapter 0. Thinner layers are more cost-effective from the MBE growth perspective, as thicker layers require more time and more materials to grow. High-quality thinner layers are also easier to grow

than thicker layers, as the defects propagate from the bottom to the top of the layers. Besides, thinner layers have smaller thermal generation volumes and lower diffusion dark currents.

Another advantage of T3SL is that it has lower tunneling currents due to greater effective masses in the growth-axis direction. Tunneling currents prevalent in HgCdTe would be vastly reduced, and infrared detectors working in the VLWIR region can achieve better performance at higher temperatures.

Auger lifetimes are believed to be longer in T3SL compared to HgCdTe. Auger recombination can be suppressed via electronic band structure engineering of the superlattice. However, Type-II superlattice has more advantage on Auger lifetime compared to Type-III superlattice due to strain effect.

1.4.4 T3SL Compared to T2SL

In this section, we compare a Type-III superlattice to a Type-II superlattice. T2SL based infrared detector technology is undergoing rapid development as a potential alternative to traditional HgCdTe.

Both T2SL and T3SL have the advantages of superlattices. With certain substances for each layer, the band structure and absorption cutoff are tuned by changing the layer thicknesses, which offers more degrees of design freedom, more controllable, and more uniform cutoff wavelength compared HgCdTe. However, T3SL has a highly tunable band gap range due to the unique band character of the HgTe well, which makes T3SL more suitable for longer wavelength applications.

T3SLs have stronger optical absorption coefficients, especially in the VLWIR region due to a Type-III band alignment, where electrons and holes are localized in the same layer[18]. While with type-II band alignment, electrons and holes reside in different layers, which leads to a reduction in the optical matrix element for the optical transitions and hence a smaller absorption coefficient.

T3SLs are measured to have longer Shockley-Read-Hall (SRH) lifetimes of up to 20 μs [19] compared to T2SL highest reported lifetime of about 10 μs [20]. Another source reported much shorter lifetime of 0.07 μs [21].

T2SL has a few advantages over T3SL [18]. Auger suppression is stronger in T2SLs due to stronger strain. It has been shown that the degree of Auger suppression is strongly strain-dependent [22]. Moreover, T3SL is less suitable for light-emitting diode and laser applications due to the low thermal conductivity of T3SL. More research and development efforts and funds are effectively capitalized in multiple application areas for T2SL.

1.5 Thesis Motivation

The history of Type-III superlattice research mentioned in section 1.4.1 seems to suggest that Type-III superlattice had its time. Now HgCdTe is the most competitive infrared material, and Type-II superlattice is the second best and can get-close-to HgCdTe performance. However, we have seen the potentials of T3SL and all the advantages it has over HgCdTe and T2SL, especially in the VLWIR region. This work aims to bring T3SL back to the game, and the reasons will be explained in the next two subsections.

1.5.1 Why We Care About T3SL Now

Research on Type-III superlattice, majorly HgTe/CdTe superlattice, peaked in the late 1980s and very early 1990s. Advantages possessed by type-III superlattices in theory were not realized in practice at that time, despite relatively comprehensive research efforts.

MBE itself was relatively new at that time. The growth of HgCdTe-based materials was in its infancy. High-quality superlattice samples are not widely available. Many advantages of T3SL promised by theoretical modeling were not achieved in the lab. MBE technologies, especially growing HgCdTe-based materials, have been improved significantly since then. Optimized growth condition control is tricky, but several growth temperature control techniques have been developed. Nowadays, the yield of MBE growth is much higher due to years of historical data.

The successful growth of the HgTe layer requires stable, uniform, and high Hg flux. Unmatured designs of Hg cells at that time was another challenge to grow high-quality T3SLs. Hg cell design has been polished and gone through several generations in the past few decades. The Hg cell in our lab was redesigned in recent years. *In-situ* characterizations have also been improved to aid MBE growth. Reflection high-energy electron diffraction (RHEED) and Ellipsometry are proved to be reliable characterization tools to perfect MBE growth.

The absence of computer-controlled shutters on the MBE system is another challenge. Superlattice usually contains hundreds of layers. We have mentioned that the HgTe layer's thickness determines the cutoff wavelengths of HgTe/CdTe superlattices. The thickness of each layer is determined by the growth time, which is controlled by shutters. Manually controlled

shutters cannot open or close for the same amount of time for each layer, which would result in layer thickness non-uniformity. Modern MBE systems are controlled by computer. The growth programs or recipes control the growth time of each layer precisely.

Consistently high-quality substrates are one of the fundamental requirements to successful MBE growth. Defects from the substrates can propagate through the layers grown on top and affect the overall layer quality. Today high-quality lattice matched CdZnTe substrates and CdTe substrates with low defect levels are widely available, which is not the case in the 1990s.

In summary, MBE technology is now mature and suitable for growing high-quality superlattices. MBE can offer low-temperature growth with a slow growth rate, providing precise layer thickness control and thin layer interfaces. There is a big chance that we can finally realize all the potential advantages of T3SL.

1.5.2 Why We Care About VLWIR

Infrared detection is extensively used in medical diagnostics, telecommunications, military, and astronomical applications. Many of these applications use infrared light in the VLWIR region. Objects that are relatively far or too cold to discharge visible light emit VLWIR infrared light that IR detectors can capture. In astronomy, it has been used to discover previously unseen objects and to observe dust particles and gas. Besides, a longer wavelength of IR radiation enables it to be less likely to scatter than visible light. Hence VLWIR is very useful in remote sensing applications, where infrared light with a longer wavelength can move around

small obstacles and "penetrate" through gas and dust. Infrared remote sensing provides important metrological and environmental information on land and water surface temperature measurements, hurricane tracking, earthquake prediction, and bushfire detection.

Despite the broad applications of VLWIR detection, there are few infrared materials developed to match this wavelength region. A. Rogalski has reviewed and compared commercially available infrared detectors [1]. Only a few infrared detectors can detect light in the VLWIR region ($\lambda > 15\mu m$), and most of them are thermal detectors and lack the wavelength selectivity. There are two among these VLWIR detectors, namely Ge:Zn(PC) and Si:As(PC) working at 4.2K, are designed to detect VLWIR light. These are extrinsically doped photodetectors that require high-level doping. The detectivity and signal-to-noise ratio of extrinsic photodetectors cannot match intrinsic photodetectors like HgCdTe or superlattices. Besides, these extrinsic photodetectors requires extreme cooling, which reflect in the size and weight of these detectors. As a result, intrinsic photodetectors designed especially for the VLWIR region are in high demand.

Recent publications show that T2SL can be used in VLWIR intrinsic photodetectors via careful selection of SL materials and their alloy compositions [23]–[25]. However, the absorption coefficient is fundamental limited due to the separation of electron and hole carriers in a Type-II band alignment.

Our focus is to design, grow, and characterize high-quality Type-III superlattice materials aimed at VLIWR detection. In this work, various HgTe/CdTe superlattices and device structures using HgTe/CdTe superlattice will be proposed and discussed.

1.6 Summary and chapter arrangement

In the first chapter, we discussed the importance of Infrared detection and gave a brief introduction to mainstream Infrared detectors. This work's focus, Type-III superlattice, is compared to two other competitive Infrared detecting materials, namely HgCdTe and Type-II superlattice. While there are not many photodetectors designed to detect VLWIR light, T3SL shows unmatched potential in VLWIR detection.

Part I of this thesis is focused on realizing the potential of T3SL as VLWIR detecting material. In Chapter 2, we will discuss the design and modeling of T3SL aiming at VLWIR absorption. In Chapter 3, the MBE growth of T3SL is carried out, and great details of successful growths are discussed. The characterization results of T3SL samples are given in Chapter 0. The absorption properties of the grown samples are discussed in chapter 5. Then in Chapter 6, we discuss the significant drawbacks of T3SL as an infrared detection material.

Part 2 of this thesis is focused on the solution to the problem brought up in Chapter 6. A unique nBn device structure is proposed to eliminate the problem. An introduction of nBn devices is given in Chapter 7. Then in Chapter 8, we talked about designs of nBn devices. A few nBn layers are successfully grown, and the result is shown in Chapter 9. Finally, the design to eliminate the problem with T3SL is proposed, and the modeling result is also shown in Chapter 10.

2 DESIGN AND MODELING

2.1 T3SL Band Structure

In this section, we briefly discuss the characteristics of the T3SL band structure.

Superlattices are usually made of periods of 2 layers. In a HgTe/CdTe superlattice, HgTe is the well layer, and CdTe is the barrier layer. The HgTe/CdTe superlattice band structure is decided by CdTe and HgTe (Figure 13). Both CdTe and HgTe are direct bandgap semiconductors, and their conduction band/valence band extremes are all at the Γ point, which is the zone center in the Brillouin zone (where $k = 0$). For CdTe, which is a normal bandgap semiconductor, the electron band Γ_6 is the conduction band, while hole band Γ_8 is the valence band. Hole band Γ_8 actually contains two bands, namely the heavy hole band Γ_8^{hh} and the light hole band Γ_8^{lh}. There is another split-off band Γ_7 right below the two Γ_8 bands. The bandgap energy E_g is defined as the energy difference between Γ_6 and Γ_8 at Γ ($k = 0$) point. For CdTe, $E_g = 1.6\ eV\ @\ 0\ K$.

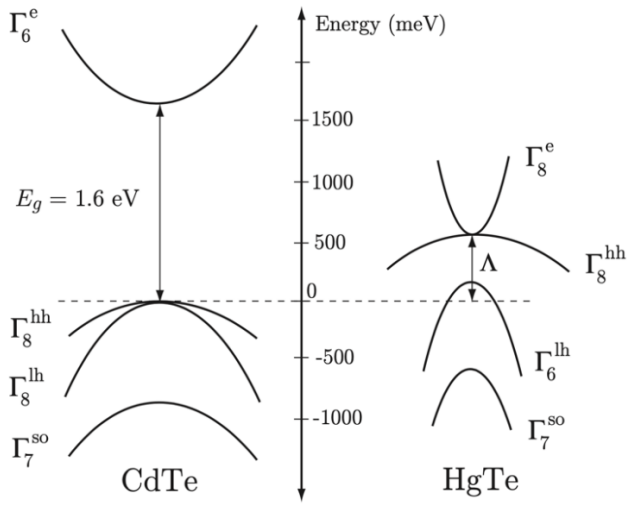

Figure 13 An illustration of band diagrams about the zone center (k = 0) for CdTe and HgTe at 0 K.

The band structure for HgTe is quite different from that for CdTe. The Γ_6 and Γ_8^{lh} are inverted. Γ_6 is now below Γ_8 bands and hence HgTe is sometimes referred to as having a "negative" bandgap. But in reality, the Γ_8^{l} band now becomes an electron band and the Γ_6 band now becomes a light hole band. Since Γ_8^{l} is still in touch with Γ_8^{hh} at the Γ point, HgTe has a zero bandgap, and hence called semimetal.

When HgTe and CdTe are put together to form HgTe/CdTe superlattice, the bands' relative position can be described by valence band offset (VBO). VBO, shown as Λ in Figure 13, is the energy difference between the valence bands of two constituent materials, which in this case are HgTe and CdTe. The valence band offset is an essential parameter of superlattices upon which many optical and electronic properties depend significantly. The value of VBO between HgTe and CdTe has been the subject of controversy [17], [26], [27]. In our modeling, we use a 40K valence band offset of 554 meV [27]. The HgTe/CdTe superlattices have a type-III band alignment, which means both the maximum of valence band and the minimum of conduction band lies within the HgTe well layer.

The well layer creates quantum confinement effects for both electrons and holes. The energy levels inside the well are defined by the eigenstates solved from the Schrödinger's equation. Since the barrier, the CdTe layer, has finite height, the corresponding wavefunctions leak to the barrier, i.e., some carriers can tunnel through the barrier into adjacent wells. The thickness of the barrier is relatively thin, so the overlap between wavefunctions is non-trivial. This is the fundamental difference between superlattices and multiple quantum wells (MQW). In MQW, the barriers are thick enough, and the wavefunction is confined in the wells. The carriers do not interact between adjacent wells; the bands become dispersionless in the growth direction.

A three-dimensional quantum well is called a quantum dot. Both Quantum wells and quantum dots are infrared detection materials [28]–[30] for different applications. The discussion of quantum well and quantum dots is out of the scope of this thesis.

Since the wavefunctions of each HgTe well overlap in the HgTe/CdTe superlattice, the energy levels will have to split in order to satisfy Pauli's exclusion principle. There are many wells in a superlattice so that each discrete energy level will split into energy bands with some width. Each energy band consists of many levels that are very close to each other. These energy bands are known as minibands, and they are uniform across the whole superlattice. The minibands of superlattice need to be distinguished from the bands of HgTe and CdTe. Energy levels of superlattice minibands are the same across the superlattice, while HgTe and CdTe bands form the jagged band alignment. An illustration of superlattice minibands is shown in Figure 14 [31].

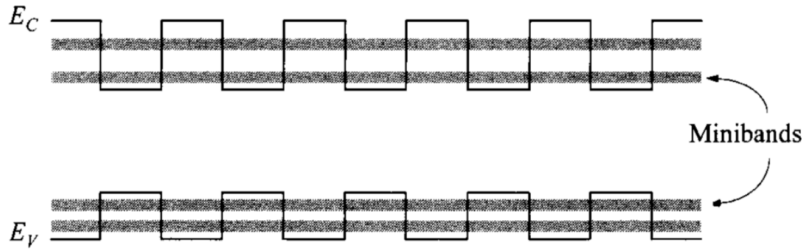

Figure 14 Superlattice minibands formed from wavefunction overlap [31].

The energy separation between the first electron subband (E1) and the first two hole subbands, namely heavy hole subband (H1) and light hole subband (L1), is decided by the thickness of the HgTe well layer. The minimum allowed optical transition energy, the bandgap energy E_g, corresponds to the superlattice's H1-E1 transition. It turns out that the H1 can go

above E1, and hence the HgTe/CdTe Superlattice has an inverted band structure just like HgTe when the thickness of the HgTe well layer d_w is bigger than the critical thickness d_c:

$$d_w > d_c = 6.3\ nm$$

When $d_w < d_c$, however, HgTe/CdTe superlattice will have a normal band structure like CdTe, and E1 is above H1. The situation becomes complicated when the thickness of the HgTe well passes 8nm. H2 goes between E1 and H1, and now the H2-H1 transition is smaller than the optical bandgap. H2-H1 transition is optically forbidden, but carriers can still be thermally generated from H2 to H1. Inverted band structure HgTe/CdTe superlattices were once thought to be excellent IR absorber, considering their outstanding bandgap control at larger HgTe well thickness. However, the H2-H1 electric gap precludes the use of them as an infrared photodetector. As a result, we will focus on normal band structure superlattices ($d_w < d_c = 6.3\ nm$).

The CdTe barrier layer thickness has a significant influence on dispersion in the growth direction and the growth direction effective masses. The CdTe barrier layer thickness also affects the miniband width. When the barrier layers are thick enough ($d_b \geq 10\ nm$), there is no overlap between carrier wavefunctions from adjacent wells. The material becomes a multi-quantum-well structure, and electrons and holes are confined in the HgTe wells. So CdTe layer thickness offers another degree of freedom for band-engineering when designing a superlattice.

2.2 K·p Method

2.2.1 K·p method for bulk material

In order to calculate band structure and hence get absorption characteristics of T3SL, we need to calculate the band structure of HgTe and CdTe first.

Both CdTe and HgTe are direct bandgap semiconductors, and their conduction band/valence band extremes are all at the Γ point, which is the zone center in the Brillouin zone (where $k = 0$). "In most semiconductors, the most populated electron and hole states lie within a fraction of an eV from the band edges" [32]. As a result, only the band structure near the Brillouin Zone center is needed for our application.

k·p method is a semi-empirical method that calculates band structure near the center of Brillouin Zone [33]–[39],. It starts with the Schrödinger equation, using the Bloch theorem to represent the periodic electron wave functions under periodic lattice potential. The accuracy of the band structure is increased if we include more bands in the calculation. 8-band **k·p** method is widely used to calculate band structure for HgCdTe. 8-band **k·p** method includes the two spin states of the conduction band (C), heavy hole band (HH), light hole band (LH), and split-off band (SO) in the calculation. Here we give a brief introduction of the 8-band **k·p** method for bulk materials, majorly based on the seminal papers of Kane [34],and Luttinger and Kohn [40].

Single crystal bulk HgCdTe has a Zincblende crystal structure. The moving carriers experience a periodic potential from the lattice. Bloch's theorem states that solutions to the

Schrödinger equation in a periodic potential, electrons moving in a crystal lattice for instance, has the form of a periodic function multiply by a plane wave:

$$\phi_k(r) = u_k(r) \exp(ik \cdot r) \tag{2.1}$$

where r is the position, ϕ is the wave function, u is a periodic function with the same periodicity as the crystal, the wave vector k is the crystal momentum vector.

The periodic function u satisfy the periodicity equation:

$$u_k(r) = u_k(r + R) \tag{2.2}$$

where

$$R = C \cdot d$$

C is an integer, and d is the spacing between parallel planes within a crystal. Plug (2.2) back into (2.1) we can get:

$$\phi_k(r + R) = \exp(ik \cdot R)\, \phi_k(r) \tag{2.3}$$

We need to solve the Schrödinger equation:

$$H(r)\phi_k(r) = E\phi_k(r) \tag{2.4}$$

$H(r)$ is the Hamiltonian for an electron in a periodic lattice, and it can be written as:

$$H(r) = \frac{\mathbf{p}^2}{2m} + V(r) + \frac{\hbar}{2m^2c^2}[\vec{\sigma} \times \nabla V(r)] \cdot \mathbf{p}. \tag{2.5}$$

where $\mathbf{p}$ is the momentum operator, $V(r)$ is the periodic potential of the lattice, and the last term describes the spin-orbit coupling with $\vec{\sigma}$ which represents the vector of the three Pauli matrices.

By expanding the general form of the Schrödinger equation (2.4) and extracting the $\exp(ik \cdot r)$ plane wave dependence, it can be written as:

$$\left(H_0 + H_{\mathbf{k}\cdot\mathbf{p}}\right)u_{n\mathbf{k}}(r) = \varepsilon_n(\mathbf{k})u_{n\mathbf{k}}(r) \tag{2.6}$$

where

$$H_0 = \frac{\hat{\mathbf{p}}^2}{2m_0} + V(r) + \frac{\hbar^2\mathbf{k}^2}{2m_0} \tag{2.7}$$

$$H_{\mathbf{k}\cdot\mathbf{p}} = \frac{\hbar}{m_0}\mathbf{k} \cdot \hat{\mathbf{p}} + \frac{\hbar}{4m_0^2c^2}\nabla V(r) \times \hat{\mathbf{p}} \cdot \vec{\sigma} \tag{2.8}$$

The k · p method got its name from the $\mathbf{k} \cdot \mathbf{p}$ term in the equation above. And $u_{n\mathbf{k}}(r)$ are the eigenstates of band n at wavevector $\mathbf{k}$ near the Γ point. Eight bands are being considered here as mentioned before, which includes the spin up and spin down conduction band s-orbitals $|S\rangle$ and three valence band p-orbitals $|X\rangle$, $|Y\rangle$ and $|Z\rangle$. In a three-dimensional periodical lattice, spin-orbit coupling splits the valence band states' six-fold degeneracy into four-fold degeneracy with $J = 3/2$ states at E_v and two-fold degeneracy with $J = 1/2$ split-off states at $E_v - \Delta_{\mathrm{so}}$. This is the primary approach of the 8-band Kane model.

Equation (2.6) is solved at **k**=0. Then, $u_{n\mathbf{0}}(r)$ form a complete set of functions, and $\varepsilon_n(0)$, the energy levels at **k**=0, are used as basis states to expand the solutions for other values of **k**. Equation (2.6) is then treated as an 8×8 matrix problem, and the elements of the Hamiltonian matrix are:

$$H_{ij} = \left[\varepsilon_i(0) + \frac{\hbar^2\mathbf{k}^2}{2m_0}\right]\delta_{ij} + \langle u_{i0}\left|H_{\mathbf{k}\cdot\mathbf{p}}\right|u_{j0}\rangle \tag{2.9}$$

The second term gives the non-diagonal term with coupling between s-orbitals and p-orbitals:

$$\langle S|\mathbf{k}\cdot\mathbf{p}|X\rangle = k_x\langle S|P_x|X\rangle = k_xP \tag{2.10}$$

$$\langle S|\mathbf{k}\cdot\mathbf{p}|Y\rangle = k_y\langle S\left|P_y\right|Y\rangle = k_yP \tag{2.11}$$

$$\langle S|\mathbf{k}\cdot\mathbf{p}|Z\rangle = k_z\langle S|P_z|Z\rangle = k_zP \tag{2.12}$$

where P is the inter-band momentum matrix element. The full matrix is expressed in terms of the band-edge energies E_g, split-off energy Δ_{so} relative to the valence band edge, the Luttinger parameters γ_1, γ_2, γ_3, and the Kane parameter F. Band structure parameters for HgTe and CdTe at T = 0 K employed in the 8×8 Kane model is shown in Table 2. The full 8x8 Kane Hamiltonian can be found in the paper from L. R. Ram-Mohan, K. H. Yoo, and R. L. Aggarwal [41]. The band structure parameters used in Ram-Mohan's paper are slightly different from the ones in Table 2.

	HgTe	CdTe
E_g (eV)	-0.303	1.606
Δ_{so} (eV)	1.08	0.91
E_p (eV)	18.8	18.8
γ_1	4.1	1.47
γ_2	0.5	-0.28
γ_3	1.3	0.03
F	0	-0.09

Table 2 Band structure parameters for HgTe and CdTe at T = 0 K employed in the 8×8 Kane model

For $Hg_{1-x}Cd_xTe$ alloy, we can simply assume the change of each parameter is linear with the composition. The band structure of HgCdTe calculated from the 8-band k · p method is reasonably accurate at the zone center and is in good agreement with the experiment. In order to increase the accuracy of the band structure at higher **k** values, more bands need to be included in the calculation. A fourteen band k · p method is implemented to include the higher-lying antibonding p states perturbatively [42]. Other than the six valence (bonding) p states and two conduction (antibonding) s states ($\bar{s}$), the most important previously neglected six antibonding p states ($\bar{p}$) are added. The schematic of 14 bulk bands and the most important band structure parameters are shown in Figure 15. P_0, P_1 and Q are the interband momentum matrix elements.

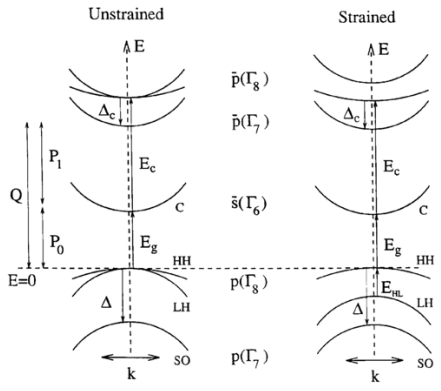

Figure 15 The 14 bulk bands considered in our 14-band k.p calculations and their important band structure parameters for unstrained (left) and strained (right) cases [42].

2.2.2 K·p method for superlattices

Extending this k·p formalism from bulk to the superlattice structure is done by introducing an envelope function that varies along the growth direction[36], [43]–[46]. This approach is used to express superlattice quantities in terms of bulk electronic structure parameters of HgTe and CdTe. Here we give a brief introduction of calculating superlattice band structure using the 14-band k·p method and envelope function approach. This part is based mainly on the paper by Wayne H. Lau, J. T. Olesberg, and Michael E. Flatté [47].

Superlattices have a periodicity on the scales larger than the bulk lattice constant. This periodicity exists only in the superlattice growth direction, which is taken to be the $\hat{z}$ direction. The Schrödinger equation for superlattices is written as [47]:

$$\widehat{H}^{SL}\langle \mathbf{r}|\mathcal{L},\mathcal{S},\mathbf{K}\rangle = E_{\mathcal{L}\mathcal{S}}(\mathbf{K})\langle \mathbf{r}|\mathcal{L},\mathcal{S},\mathbf{K}\rangle \tag{2.13}$$

where $\widehat{H}^{SL}$ is the superlattice Hamiltonian, and can be written as the sum of the crystal Hamiltonian of all layers:

$$\widehat{H}^{SL} = \sum_{i=1}^{N_{layer}} \widehat{H}_i \theta_i(\mathbf{r}) \tag{2.14}$$

$$\theta_i(\mathbf{r}) = \begin{cases} 1 & \text{if } \mathbf{r} \in i\text{th layer} \\ 0 & \text{if } \mathbf{r} \notin i\text{th layer} \end{cases} \tag{2.15}$$

Here $\widehat{H}_i$ is the crystal Hamiltonian of the *i*th layer given in Equation (2.7) and (2.8). N_{layer} is the number of layers in the superlattice unit cell, which equals 2 in a HgTe/CdTe superlattice. $|\mathcal{L},\mathcal{S},\mathbf{K}\rangle$ is the superlattice eigenstate for a carrier with wavevector $\mathbf{K}$ and spin $\mathcal{S}$, in

the $\mathcal{L}$th band. The corresponding eigenenergy is $E_{\mathcal{L}S}(\mathbf{K})$. Similar to the bulk case, we first solve the Schrödinger equation at the zone center where $\mathbf{K} = 0$.

The zone-center superlattice wavefunction is expressed in terms of bulk electronic structure parameters:

$$\langle \mathbf{r}|N, S, \mathbf{0}\rangle = \sum_{n\sigma} F_{NSn\sigma}(r)\, \langle \mathbf{r}|n, \sigma, \mathbf{0}\rangle \tag{2.16}$$

where $|n, \sigma, \mathbf{0}\rangle$ are the corresponding zone-center Bloch states of the constituent bulk compounds. $F_{NSn\sigma}(r)$ are envelope functions that are slowly varying. They are on the scale of the constituent bulk semiconductor lattice constant. Here, for convenience, we adopt the convention that lower and upper cases represent bulk and superlattice states, respectively.

Substitute Equation (2.16) into Equation (2.13), multiply from the left-hand side of the resulting equation by the corresponding wavefunction $\langle n, \sigma, \mathbf{0}|\mathbf{r}\rangle$ of the zone-center Bloch state and integrate over a unit cell of the constituent bulk semiconductor, we obtain the zone-center Schrödinger equation:

$$\sum_{n'\sigma'} \widehat{H}^{ZC}_{n\sigma n'\sigma'}(\mathbf{r}) F_{NSn'\sigma'}(\mathbf{r}) = E_{NS}(\mathbf{0}) F_{NSn\sigma}(\mathbf{r}) \tag{2.17}$$

where

$$\widehat{H}^{ZC}_{n\sigma n'\sigma'}(\mathbf{r}) \equiv \frac{\widehat{\mathbf{p}}^2}{2m_e}\delta_{nn'}\delta_{\sigma\sigma'} + E^{Bulk}_{n\sigma n'\sigma'}(\mathbf{r}) + \frac{\hbar}{m_e}\widehat{\mathbf{p}} \cdot \mathbf{P}^{Bulk}_{n\sigma n'\sigma'}(\mathbf{r}) \tag{2.18}$$

with

$$\mathbf{P}^{Bulk}_{n\sigma n'\sigma'}(\mathbf{r}) \equiv \langle n, \sigma, \mathbf{0}|\hat{\mathbf{p}}|n', \sigma', \mathbf{0}\rangle \tag{2.19}$$

$$E^{Bulk}_{n\sigma n'\sigma'}(\mathbf{r}) \equiv \left\langle n, \sigma, \mathbf{0}\middle|\widehat{H}\middle|n', \sigma', \mathbf{0}\right\rangle \tag{2.20}$$

The bulk energy $E^{Bulk}(\mathbf{r})$ is a diagonal matrix whose diagonal terms are the eigenenergies of the bulk states at zone center:

$$E^{Bulk}_{n\sigma n'\sigma'}(\mathbf{r}) = E^{Bulk}_{n\sigma}(\mathbf{r})\delta_{nn'}\delta_{\sigma\sigma'} \tag{2.21}$$

Note that the opposite-spin eigenstates of the constituent bulk states at the zone center are two-fold degenerate. The zone-center eigenvalue problem (2.17) is solved in Fourier space:

$$\widehat{H}^{ZC}_{n\sigma n'\sigma'}(z) = \sum_{\mu=-\infty}^{\infty} \widetilde{\widehat{H}}^{ZC}_{n\sigma n'\sigma'\mu}\exp\left(i\mu qz\right) \tag{2.22}$$

$$F_{NSn'\sigma'}(z) = \sum_{\mu=-\infty}^{\infty} \tilde{F}_{NSn\sigma\mu}\exp\left(i\mu qz\right) \tag{2.23}$$

where $q \equiv \frac{2\pi}{D_{SL}}$. D_{SL} is the thickness of one period in the superlattice. Substituting Equation (2.22) and (2.23) into (2.17), multiplying from the left-hand side of the resulting equation by $exp(-i2\pi\nu qz)$, and integrating over the superlattice period, we obtain the zone-center superlattice eigenvalue equation in Fourier space as

$$\sum_{n'\sigma'\mu} \widetilde{H}^{ZC}_{n\sigma n'\sigma'(\nu-\mu)} \tilde{F}_{NSn'\sigma'\mu} = E_{NS}(\mathbf{0}) \tilde{F}_{NSn\sigma\nu} \tag{2.24}$$

where

$$\widetilde{H}^{ZC}_{n\sigma n'\sigma'\mu} = \int_{D_{SL}} dz\, \widehat{H}^{ZC}_{n\sigma n'\sigma'}(\mathrm{z}) \exp(-i\mu q z) \tag{2.25}$$

Diagonalizing the matrix $\widetilde{H}^{ZC}$ in Equation (2.24) gives us the zone-center eigenvalues and eigenvectors. Once the zone-center superlattice eigenstates and eigenenergies have been determined, $\mathbf{K} \neq 0$ eigenstates can be obtained by applying superlattice k·p theory [45].

2.3 Modeling Details

All calculations in this thesis were performed using the code and software developed by Professor M. E. Flatté's group at the University of Iowa and employ an envelope function implementation of a 14-band k·p method.

For HgTe/CdTe superlattices, the most critical parameters are thicknesses of HgTe and CdTe layers. We need to calculate the band structure of HgTe/CdTe superlattices with various well/barrier thicknesses. The energy band gap is tailored by varying the layer thicknesses of the HgTe well to achieve cutoff wavelengths in the VLWIR ranges. Moreover, the CdTe well thickness is used to adjust effective masses and miniband widths. Because the energy of VLWIR radiation is small, we can achieve the same cutoff with both normal band structure SL and inverted band structure SL. As mentioned in section 2.1, the H2-H1 electric gap precludes using

inverted band structure SL as an infrared photodetector. Still, here we calculated the band structure of both normal and inverted for comparison.

HgTe and CdTe's bandgap energy used in our calculation is based on the bandgap energy of $Hg_{1-x}Cd_xTe$ $E_g(x,T)$. The equation for $E_g(x,T)$ we used is slightly different from the Hansen equation (1.2) and is updated to match with the sample data [27]:

$$E_g(x,T) = -303(1-x) + 1606x - 132x(1-x)$$
$$+ [4.95(1-x) + 3.25x - 3.93x(1-x)] \times \frac{0.1T^2}{[11(1-x) + 78.7x + T]} \qquad (2.26)$$

The unit is meV. We adjusted the number 4.95 in Equation (2.26) to 7.80 later to match our simulation with other theoretical modeling result [27], [44], [48] and the absorption data we got in the lab.

	HgTe	CdTe
a_0 (Å)	6.462	6.482
Δ_{so} (eV)	1.06	0.93
C-band mass	0.12	0.12
HH-band mass	0.40	0.90
LH-band mass	0.18	0.18
c_{11} $(10^{11}\ dyn/cm^2)$	5.97	5.62
c_{12} $(10^{11}\ dyn/cm^2)$	4.15	3.94
c_{44} $(10^{11}\ dyn/cm^2)$	2.26	2.06
E_v (eV)	0	-0.554
E_c (eV)	6.50	5.36
Δ_c (eV)	0.24	0.25
E_{P_0} (eV)	23.13	23.13
E_{P_1} (eV)	0.05	0.05
E_Q (eV)	13.03	13.03
V_a (eV)	-4.48	-4.52

V_b (eV)	-1.15	-1.10

Table 3 Band structure parameters for HgTe and CdTe at T = 300 K employed in the 14-band k·p calculations

The effect of strain due to lattice mismatch between HgTe and CdTe layers can be readily incorporated into our band structure calculation. Split-off energies Δ_{so} of HgTe and CdTe that we used in the 14-band k·p calculations are slightly different from the ones in Table 2. Δ_{so} along with other important band parameters are shown in Table 3.

Most of the parameters listed in Table 3 have been illustrated in Figure 15. E_v is the valence band offset compared to HgTe.

2.4 Calculated band structure

The calculated band structure of $Hg_{1-x}Cd_xTe$ with composition x=0.3 is shown in Figure 16. Four major bands can be seen near the zone center, namely the conduction band (Γ_6), the heavy hole band (Γ_8^{hh}), the light hole band (Γ_8^{lh}) and the split-off band (Γ_7). The band structure agrees well with the modeling result from the previous paper published by our fellow researchers [49].

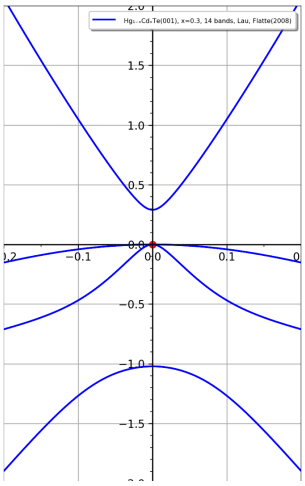

Figure 16 Modeled band structure of MCT with x=0.3.

The curvature of the light hold band away from the zone center is the unique result for 14-band k·p calculations. The Kane model [34] is commonly used to describe the band structure near the Γ point. The band structure near the zone center has a hyperbolic form. For example, the energy-momentum relationship of the conduction band ($E_c(k)$) can be written as:

$$E_c(k) = \sqrt{s^2k^2 + b^2} - b + E_g \tag{2.27}$$

where $b = E_g/2$, and $s^2 = 2P^2/3$, P is the momentum matrix element with a value of $(8.0 - 8.5) \times 10^{-8}$eV cm [50], [51]. It has been shown that 14-band k·p calculations gives similar hyperbolas describing E_c or E_{lh} dispersions [52]. At small values of k, however, the lowest order of a Taylor series of Equation (2.27) gives us a reasonable approximation of the band dispersion with a parabolic shape:

$$E_c = E_g + \frac{s^2}{2b}k^2 \tag{2.28}$$

Hence the electron effective mass can be obtained from

$$\frac{m_e^*}{m_0} = \frac{\hbar^2 b}{s^2 m_0}$$

where m_0 is the free electron mass.

After we finished and checked our modeled band structure of HgCdTe, we moved on to HgTe/CdTe superlattice. Our 14-band k·p calculations use an envelope function implementation, and all SL band structure calculations were performed using the code and software developed by Professor M. E. Flatté's group at the University of Iowa.

Figure 17 shows a comparison of modeled band structure for inverted (left) and normal (right) band structure HgTe/CdTe superlattices. They look reasonably similar, but the nature of the bands is quite different. In both band structures shown, the valence band edge at the zone center is taken as the zero-energy reference point. In the normal band structure band structure SL, the conduction band is the E1 electron band, and the valence band is the H1 heavy hole band. Below the valence band, we have the H2 heavy hold band and the L1 light hole band. In the inverted band structure SL, however, the conduction band is the H1 heavy hole band, and the valence band is the H2 heavy hole band. The E1 electron band goes under the H2 band. Because the optical transition between H2 and H1 is forbidden, the electric bandgap H2-H1 is smaller than the optical gap E1-H1. This is the primary reason we use superlattice with a normal band structure as our candidate for VLWIR absorption.

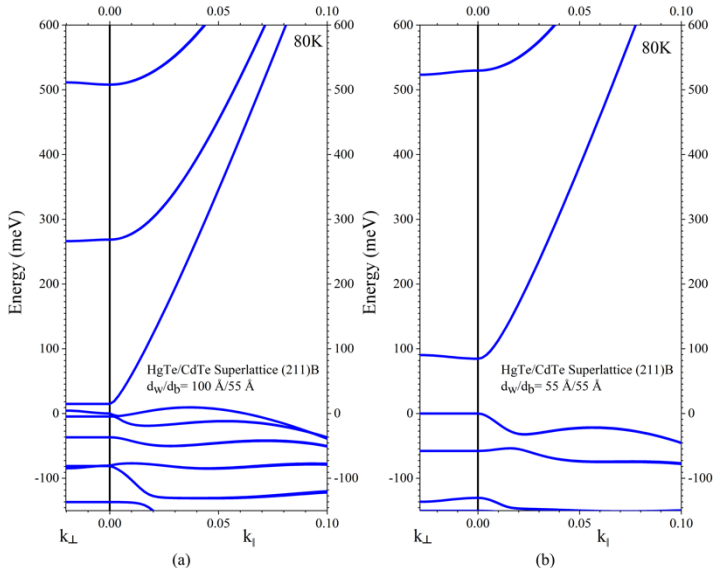

Figure 17 Modeled band structure for (a) inverted and (b) normal HgTe/CdTe SL.

Figure 17 shows k values in different directions. $k_\perp$ includes k vectors along the superlattice growth direction, which is usually labeled as z-direction; $k_\parallel$ includes k vectors parallel to the SL plane, the x-y plane. Note that the k values shown in Figure 17 have different ranges to $k_\perp$ and $k_\parallel$ directions, due to the periodicity of superlattices. The first Brillouin zone is a reciprocal space (or k-space) primitive cell. For a semiconductor with lattice constant a, the corresponding values of k in the first Brillouin zone should be in $(-\pi/a, \pi/a)$. Other than the periodicity of the lattice, superlattice introduces a new periodicity. Superlattices under consideration in this thesis have a period thickness d in the order of 100 Å, which has a much bigger scale than the crystal lattice constant, which is around 6.5 Å. This results in a much smaller k range in the reciprocal space for the first Brillouin zone. With period thickness d replacing lattice constant a, we have the corresponding values of k in the reciprocal space in $(-\pi/d, \pi/d)$. This explains the band structure shown above, which has $k \in (0, \pi/a)$ along $k_\parallel$ direction and $k \in (0, \pi/d)$ along $k_\perp$direction.

We note that the band structures of T3SLs disperse much less along the z-direction compared to xy-direction. Due to the superlattice periodicity, the first Brillouin zone shrinks down to a much smaller value along the z-direction. The energy bands have to fold back to the small Brillouin zone, which results in superlattice minibands. Besides that, the degeneracy of bands at the Brillouin zone edge and center opens up gaps due to Bragg diffraction. As a result of this reduced Brillouin zone, the band dispersion is significantly reduced and the growth-axis effective masses are much larger than SL in-plane effective masses and bulk effective masses, which suppresses band-to-band and trap-assisted tunneling and can reduce dark currents [53].

An automation program is written to calculate HgTe/CdTe superlattices' bandgap as a function of HgTe and CdTe thicknesses. The result is shown in Figure 18. The thicknesses of the layers are in the unit of monolayers (ML). For a (211) grown HgTe/CdTe superlattice, the thickness of a single ML is approximately 3.24 Å [54].

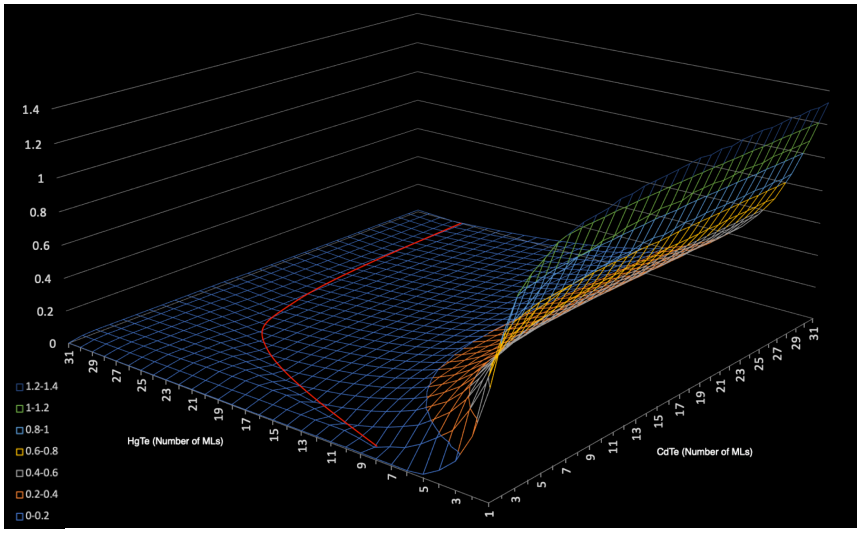

Figure 18 3D graph of bandgap vs. numbers of HgTe/CdTe monolayers (ML). The number of ML range from 1 to 31, which corresponding to 3.24 Å to 100.44 Å. The red curve corresponds to where the bandgap $E_g = 0$.

The red curve shown in Figure 18 corresponds to the data points where $E_g = 0$. Increasing the HgTe thickness beyond the red curve generates SL with an inverted band structure; Decreasing the HgTe thickness below the red curve generates SL with a normal band structure. While the HgTe layer thickness is the deciding factor of the bandgap energy, the CdTe layer thickness also has a non-trivial effect on E_g. For a specific HgTe layer thickness, the bandgap energy decreases with the CdTe layer thickness. This effect is not obvious when CdTe is more than 15 ML (48.5 Å) thick. However, when CdTe is extremely thin, the wavefunction overlap between each HgTe well becomes significant; hence the SL miniband width increases, and the bandgap energy becomes smaller.

The Fermi level energy is also inspected. Figure 19 shows the Fermi level energy as a function of the number of CdTe ML layers at different numbers of HgTe ML layers and different n-type doping levels at 80K. For a fixed combination of HgTe and CdTe layer thickness, increasing n-type doping would increase the Fermi level energy, though the change is relatively small. CdTe layer thickness plays a vital role in Fermi level energy. This can again be explained by the significant wavefunction overlap between each HgTe well when the CdTe layer is thin. SL miniband width increases and the bandgap energy becomes smaller. Besides, the valence band's effective mass decreases with CdTe layer thickness, which leads to the decrease of valance band density of states. As a result, the Fermi level decreases with the CdTe layer thickness when the SL is n-type doped.

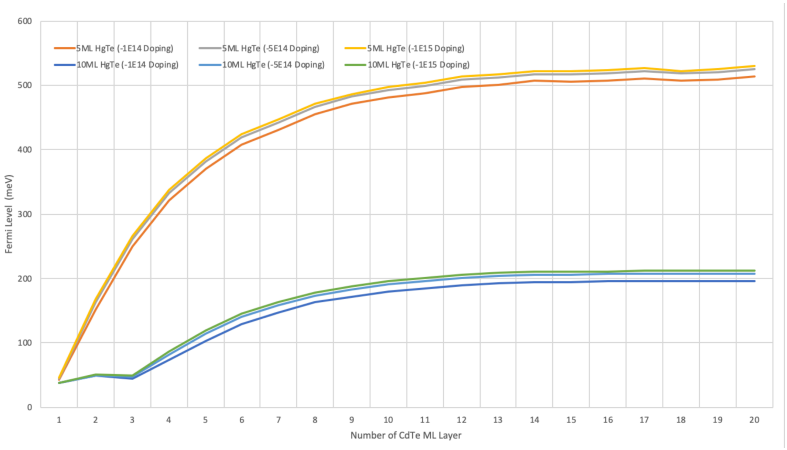

Figure 19 The Fermi level energy (meV) as a function of the number of CdTe ML layers at different numbers of HgTe ML layers and different doping levels at 80K.

3 MOLECULAR BEAM EPITAXY GROWTH OF TYPE-III SUPERLATTICE

3.1 A Brief Introduction to MBE

Molecular beam epitaxy (MBE) is a mature growth technique widely recognized as capable of growing sophisticated semiconductor multilayer materials [12], [19], [55]–[77].

In the 1970s, researchers realized that binary compounds could be used for Infrared applications that require optimum performance at a specific wavelength range corresponding to the materials' bandgap. However, no compound is known to have a bandgap in the LWIR range. Therefore, the use of high-quality tunable bandgap ternary materials is necessary for many IR detector applications. Alloy materials, including II-VI and III-V materials, came to the game with their advantages of tunable and direct bandgaps, which cover a wide range of infrared spectra with high quantum efficiency.

These needs stimulated the industry, and several material growth technologies were developed. MBE is one of the greatest crystal growth technique whereby single crystal monolayers are grown upon a substrate under ultra-high vacuum (UHV). Ultra-high purity source materials thermally evaporate molecules and form molecular beams with extensive mean free paths, traveling and interacting with the temperature-controlled substrate. MBE has the unmatched ability to grow layer-by-layer in a 2D growth mode under the right conditions, which is ideal for growing high-quality heterostructures with HgCdTe alloys and superlattices with precise layer thickness requirements. Combining with its low-temperature growth conditions, MBE is the best when it comes to growing II-VI heterostructures with Hg involved due to the significant interdiffusion of Hg at higher temperatures.

A successful MBE growth requires precise control of substrate temperature and molecular beam fluxes. This is especially the case for growing HgCdTe-based heterostructures. The "growth window," which is defined as the optimized growth temperature range for a successful single-crystal MBE growth, is absurdly small. One explanation is that the bond strength of Hg-Te is very weak compared to Cd-Te bond. The heat of formation of HgTe and CdTe, which gives a good indication of the bond strengths, are -7.6 kcal/mol and -24.1 kcal/mol, respectively [78]. The weak Hg-Te bond has a number of ramifications affecting the growth of HgTe-related materials like HgCdTe and HgTe/CdTe superlattices. For $Hg_{1-x}Cd_xTe$ with a composition in the range of 0.2-0.3, the growth window can be as little as 3°C. Besides that, stable source beam flux is crucial to the uniform composition and correct layer thickness. Luckily, we have PID controlled power supplies to control the cell and substrate temperatures within $\pm 0.1°C$.

MBE has a few drawbacks. It is a sophisticated and complicated system that requires materials, physics, chemistry, mechanical and electronic engineering skills to master the growth and maintain the MBE chamber. The learning curve is steep and sometimes quite frustrating, even for experienced growers. The cost of building a chamber is high, so does the growth and maintenance. The high cost of MBE growth limits its application to high-end Infrared detection systems, majorly military and astronomy, where performance outweighs the cost. Still, MBE is an excellent crystal growth technique for research, considering its ability to realize all different kinds of material design. All superlattice samples we used in this research are grown by MBE. In the next section, we will discuss the major component of the RIBER 32p MBE system at our Microphysics Laboratory.

3.2 MBE 32p System

A typical MBE system usually has three UHV chambers: The loading chamber to load substrates into the system and unload the samples from the system, the growth/main chamber to perform MBE growth, and the transfer/buffer chamber to connect the loading chamber and the growth chamber. The loading chamber needs to be constantly exposed to the atmosphere. The transfer chamber is necessary to keep the growth chamber clean and to maintain the UHV condition.

The growth chamber, where the MBE growth happens, is depicted in Figure 20. The substrate is mounted on a moly holder, loaded and transferred to the growth chamber, then mounted onto the manipulator using the transfer arm. The manipulator can rotate freely inside the main chamber so that the substrate can be adjusted to face the source materials directly. All effusion cells, including In, CdTe, and Te cells, and special designed Hg cell are designed so that the molecular fluxes come out of the cells converge to one point – the center of the substrate. These cells' geometry shape can ensure the flux is uniformly covering the substrate up to 3 inches.

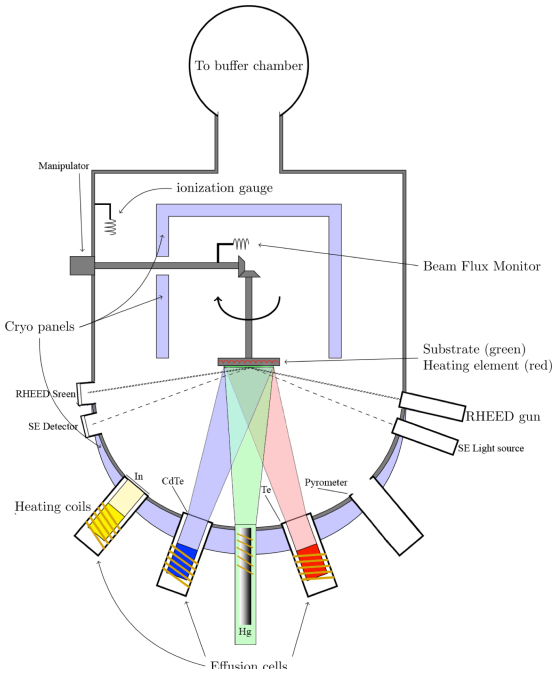

Figure 20 The major components of a general MBE growth chamber.

The manipulator has heating elements that sit right behind the substrate holder and heat it to a constant temperature during the MBE growth. Thermal couples and PID systems are employed to perform precise temperature control of both material sources and the substrate. Three ion gauges at different positions inside the chamber monitor the vacuum status and the material fluxes during the growth. One of the ion gauges is installed directly onto the manipulator for flux calibration. MBE systems have cryo panels surrounding the inside of the chamber. A constant flow of liquid nitrogen (LN2) through the cryo panels helps to maintain the UHV and collect unused molecules from the cells and other contaminations consist of small amounts of water vapor, carbon monoxide, and hydrogen. This prevents molecules other than those from the sources from hitting the surface of the substrate during the growth, which ensures the grown samples have high quality and purity.

Different pumps are used to pump the three chambers. The transfer chamber is relatively light duty, so an ion pump is used to main UHV. The ion pump is not suitable for the main chamber and loading chamber because the ion pump's pumping rate is low, and sudden exposure to high pressure may damage the ion pump. Cryopumps, on the other hand, are very good at handling relatively high fluxes. Hence, they are used on the growth chamber and the loading chamber. Cryopumps trap gases and vapors by condensing them on a cold surface. The cold head inside the pump is cooled by compressed helium coming from the compressor. Cryopump is the only choice for growing II-VI heterostructures because the Hg vapor pressure during the growth can be as high as 10^{-4} Torr. Only cryopumps can handle such a significant flux in a UHV chamber. Other than the cryopump used on the loading chamber to keep it under UHV when connecting to the transfer chamber, an oil-free diaphragm pump and a turbopump are used for different pumping stages when the substrate is being loaded.

The growths can be monitored with a few *in-situ* characterization techniques. We use a pyrometer to remotely measure the substrate surface temperature during the growth. Reflection high-energy electron diffraction (RHEED) and Spectroscopic ellipsometry (SE) are used to closely monitor the growth condition, surface roughness, and compositions. A detailed discussion on RHEED and SE can be found in section 4.1. A residual gas analyzer (RGA) allows real-time monitoring of gas residue species present in the chamber, which helps leak detections.

Figure 21 shows the top view of the MBE 32p system in Microphysics Laboratory (MPL) at the University of Illinois at Chicago (UIC). The chamber is specially designed with all-metal seals. The yellowish color of the chamber body is due to the special annealing treatment at

RIBER to reduce the outgassing from the metal inside the chamber. This is very important to keeping the UHV condition and also reducing the contamination to the samples.

Figure 21 MBE 32p system in Microphysics Laboratory at the University of Illinois at Chicago

3.3 Customized Mercury Cell: A Key to Successful Growth

3.3.1 Motivation

Mercury (Hg) is a heavy, silvery element with an atomic number of 80. It remains liquid form at standard temperature and pressure conditions. This unique mercury character is why people use it widely in thermometers, sphygmomanometers, and many other medical applications, fluorescent lamps, and other devices. The concerns about Hg's toxicity have led to thermometers and sphygmomanometers using Hg being mostly phased out. For example, alcohol-based thermometers are more common nowadays.

As an inevitable element in our lab, mercury needs to be carefully handled. Mercury waste from MBE growth is collected using a cold trap near the cryopump. Then the mercury waste is carefully removed and move to a mercury waste bottle. Researchers are required to wear

respirators when the chamber is opened and exposed to the air, during which the mercury vapor level in the air is believed to rise quickly.

The fact that mercury is liquid even at room temperature makes the mercury cell design differs from other cells. CdTe cell and Te cell, for example, use metal ingots as source materials. The most common system for these source materials is the effusion cell (Thermal Evaporation Sources or K-cells) (Figure 20). The solid ingots are inserted into the PBN crucible. The crucible is surrounded by a heating assembly, which usually contains heating filaments and thermocouples. To prevent uneven heat of the crucible, which could lead to a material condensation at the crucible lip, most of these effusion cells also feature a dual-filament design. The temperature gradient over the crucible length varies to accentuate either a "hot lip" or "cold lip" type behavior. These effusion cells are widely used and can produce stable and reproducible flux with the help of PID control.

Most MBE chambers are designed in the way that most, if not all, effusion cells are facing up at an angle, so the material inside the crucible will not drop or slide out due to gravity. This design consideration makes these effusion cells even able to handle liquid source materials. For example, in our MBE 32p system, Indium, the n-type doping material, is loaded into an effusion cell. Indium melts at 156.6^{o}C and remains in the liquid phase during the operation of MBE growth. However, these effusion cells are not suitable for mercury, even though mercury remains in the liquid phase for our application.

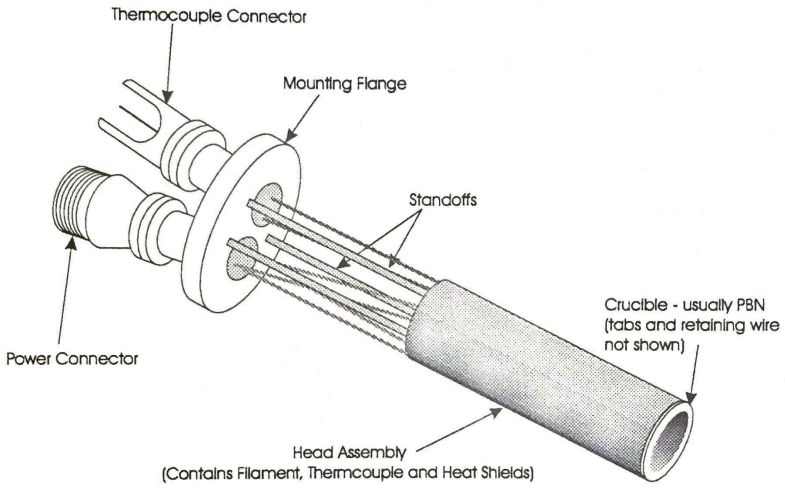

Figure 22 An effusion cell.

The effusion cell is not suitable for mercury for several reasons. We first need to explain how mercury is used in MCT growth. Mercury evaporates much faster compared to other source materials, even at room temperature. At growth temperature (around 130^{o}C for mercury), the Hg vapor pressure is about 10^{-3} Torr, which is much larger than that of CdTe (10^{-6} Torr at 600 ^{o}C) and Te (10^{-6} Torr at 400 ^{o}C). Since mercury atom and Te atom form HgTe molecule, the ratio of these atoms deposited onto the sample during the MBE growth should be 1:1. In reality, mercury has a much smaller sticking coefficient than Te; that is why the mercury pressure should be much higher than the Te pressure. Higher pressure means that there are many more atoms emitted into the MBE chamber in a unit of time. As a result, the mercury source material dissipates very fast. An effusion cell can only hold a minimal amount of source material; And it is impossible to refill the crucible without bringing the chamber to the atmosphere, remove and reinstall the cell. Not only could this cause much trouble, but also it interrupts the growth champaign and potentially contaminate the chamber by frequently opening the chamber. A unique design for the mercury cell is needed to provide continuous mercury flux during the growth.

3.3.2 Previous and Existing Mercury Cell Design

A previous mercury cell design we used at Microphysics Laboratory is shown in Figure 23. It consists of an internal reservoir to store mercury, an external reservoir, a valve to refill the internal reservoir, a mercury vapor feedthrough, a valve to control mercury vapor flux, heating elements, and thermometers to monitor the operating temperature of the inner reservoir and mercury vapor. During the growth, the internal reservoir is heated up to 350 ^{o}C. The vapor flows into the chamber via the feedthrough. A needle valve controls the flux. This design has four major flaws: 1) The needle valve can be clogged with accumulated mercury and other contamination sources from the chamber, eventually affecting the run-to-run consistency of mercury flux and the purity of mercury flux; 2) The feedthrough and the needle valve cannot be cleaned without dissembling; 3) It is challenging for this cell to achieve high mercury flux because the source mercury is stored in an internal reservoir which is far from the end of the feedthrough inside the chamber; 4) The mercury reservoir is usually small because it is directly attached to the MBE chamber; 5) Because the mercury is heated up to a high temperature during the growth (about 300 ^{o}C), there is a big chance the impurities from mercury will incident into the chamber. We can achieve an operational pressure (flux) around low 10^{-4} Torr with this design. A similar design is from RIBER (Figure 24), who manufactured our MBE 32p system. This model VHG500 valved mercury cell shares a very similar design to ours, and the performance should be comparable.

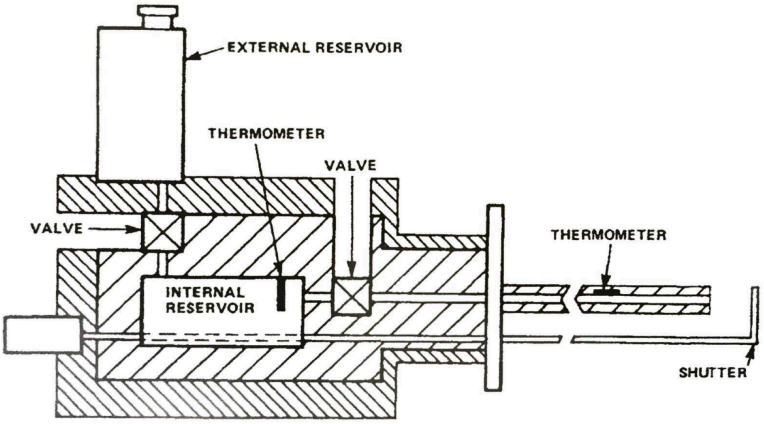

Figure 23 A continuous feed mercury source. (K. A. Harris, et al., 1986).

Figure 24 RIBER VHG500 Mercury cell (500 cc)

Another popular mercury cell design by RIBER is shown in Figure 25. It has a reservoir that is separate from the feedthrough and the valve. The significant difference between this design and the previous designs is that it raises the mercury liquid level into the feedthrough, using the principle of communicating vessels. Hence, the liquid surface is much closer to the cell port. As a result, the maximum flux can be one order of magnitude higher than that of the previous design. This design is the closest one to our new mercury cell design. Still, it has two issues worth mentioning: One is that it is not convenient to adjust the mercury level by raising and lowering the mercury reservoir; Two is that it has a needle valve that can be clogged and contaminated with accumulated mercury and other source materials from the chamber.

We will show how we overcome all of these issues with our new mercury cell design.

Figure 25 RIBER MCL Mercury cell (1100cc)

3.3.3 Newest Mercury Cell Design

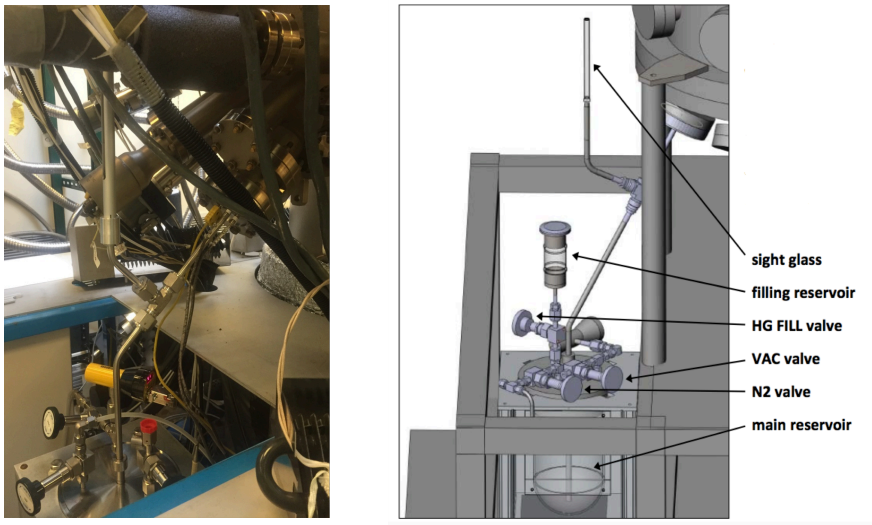

Figure 26 A picture of the new Mercury cell installed on the MBE 32p chamber (left), and a sketch of the Mercury cell's major components (right).

To overcome all the issues and concerns we mentioned in 3.3.2, we keep improving our design, and the newest designed mercury cell is shown in Figure 26. It raises the mercury liquid

level into the feedthrough, so the liquid surface is much closer to the cell port compared to other designs. This feature is essential to provide a high and stable mercury flux at a much lower operating temperature.

The way the mercury liquid is raised is significantly different from RIBER's design (Figure 25). In our design, the mercury liquid level is controlled by adjusting the mercury reservoir pressure $P_{reservoir}$. With high enough surface pressure, mercury can be pumped up to the cell port inside the chamber. The pumping mechanism uses the concept of a U-shaped tube filled with liquid. When the surface pressure is the same on two sides of the tube, the liquid level is also the same on the two sides. When there is a pressure difference between the two sides, the liquid will start moving from the higher-pressure side to the lower-pressure side through the tube. In our mercury cell, we do not have a perfect U-shape tube. Instead, we have the feedthrough tube sticking inside the mercury liquid, coated with unique materials to avoid mercury and stainless-steel reactions. $P_{feedthrough}$, the mercury liquid surface pressure inside the feedthrough, is always close to zero, because it is directly connected to the ultra-high-vacuum MBE chamber. When the mercury cell is at standby, we keep the inside of the mercury reservoir under vacuum, so $P_{reservoir} \approx P_{feedthrough} \approx 0$. The mercury liquid stays inside the reservoir. At the beginning of an MBE growth, we vent the mercury reservoir with high purity nitrogen gas. The difference between $P_{reservoir}$ and $P_{feedthrough}$ becomes significant. $h_{mercury}$, the height difference between the liquid level inside the feedthrough and that in the mercury reservoir, is determined by $P_{reservoir}$ and $P_{feedthrough}$ using Hydrostatic pressure formula:

$$P_{reservoir} - P_{feedthrough} = \rho_{mercury} \cdot g \cdot h_{mercury} \tag{3.1}$$

Here we assume the difference of mercury density $\rho_{mercury}$ at different pressure is negligible, because liquids, in general, are very incompressible. We use $\rho_{mercury} = 13.6\ g/cm^3$. If the mercury reservoir is vented to the atmosphere ($1\ atm$ or 101325 Pa), we can get $h_{mercury} = 745mm$. The mercury cell is designed in a way that the distance between the liquid level in the reservoir and the Hg cell port inside the chamber is higher than $745mm$. If the reservoir is accidentally exposed to the air, the mercury will not be pumped and spilled into the chamber. This is an important safety feature.

During normal operations, however, we vent the reservoir with high-pressure nitrogen gas, $h_{mercury}$ can go higher than $745mm$. If the mercury level is too high, the mercury will pour into the MBE chamber, which would contaminate the chamber and should be avoided. To monitor the mercury level inside the feedthrough closely to avoid mercury being poured into the chamber, we added a glass tube to the feedthrough (Figure 27 and Figure 28). Using the physics of communicating vessels, we can monitor the mercury level inside the feedthrough up to the cell port by checking the mercury level inside the glass tube.

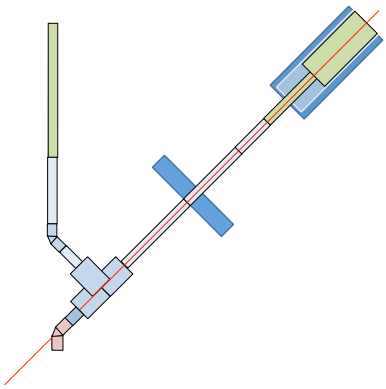

Figure 27 The upper part of the Hg cell. The feedthrough is connected to the cell port inside the chamber. And a glass tube is connected to the feedthrough to monitor the mercury level inside the cell port closely.

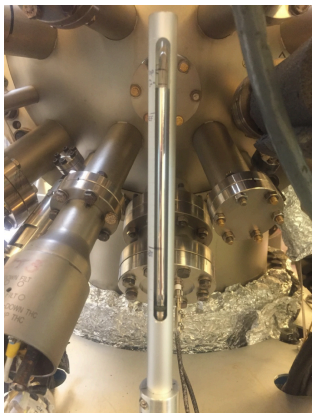

Figure 28 The glass tube used to monitor the mercury level

This mechanism is crucial for the safety reason mentioned above and also essential to the run-to-run flux stability. We make sure the mercury is at the same level for every MBE growth. It turns out that this is quite maneuverable by controlling the pressure inside the reservoir. To test the run-to-run flux stability, we did flux calibration twice, on two different days, to measure the relationship between the mercury cell flux and the cell port temperature (Figure 29). During the two flux calibrations, the mercury is raised to the same level. We can see that the flux is very stable in a broad temperature range (131-149 ºC). During normal operations, the cell temperature remains below 140 ºC.

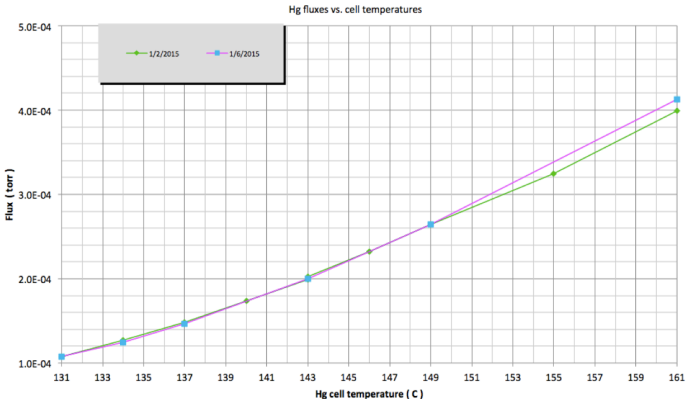

Figure 29 Mercury cell flux calibration on two different days showing good run-to-run flux stability

Another significant benefit of this mercury design is that the mercury cell can be flushed and cleaned. During each growth, many other sources other than mercury cell is emitting molecules into the chamber. Some of these molecules will condense on the mercury cell port or even inside. Most of these can be removed by outgassing the cell at a high temperature, and we make sure it is even cleaner by flushing the cell port using mercury a few times. Mercury will bring down most of these impurities into the mercury reservoir. These impurities will float on top of mercury and will not affect future growths.

Stable mercury flux during each MBE growth is also critical. The mercury cell port inside the MBE chamber (Figure 27) has a heating mechanism attached. A welded stainless-steel tubing is holding the mercury. A graphite sleeve wraps the tube. And the graphite sleeve is surrounded by a tantalum heating assembly covered by another layer of graphite sleeve (Figure 30). This enables even heating on the mercury. Besides, the mercury level is close to the end of the cell port during the growth. These mercury cell design characters warrant stable mercury flux for hours during each MBE growth.

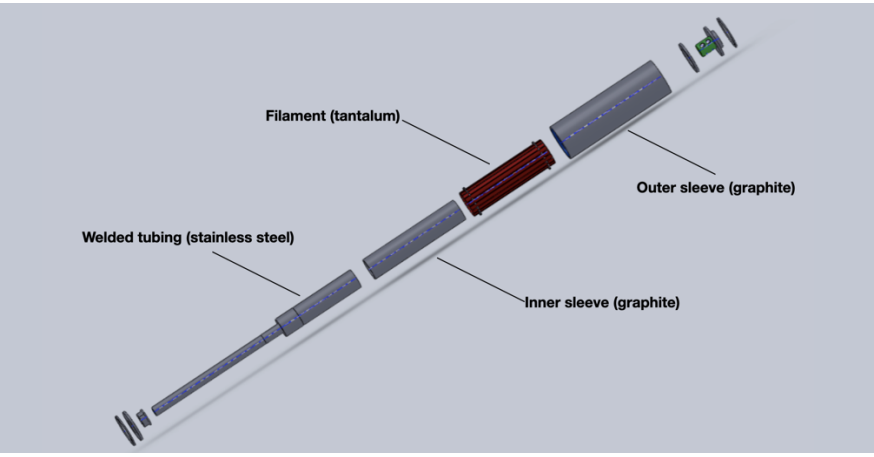

Figure 30 A sketch of mercury cell port.

Mercury consumes very fast during MBE growths. We want to have a large mercury reservoir to hold as much mercury as possible, and also a safe and straightforward way to refill mercury into the Hg cell in practice. One of the motivations to build a customized Hg cell is to reduce the effort to replenish mercury. We have a valved glass tube for refilling attached to a 2000cc capacity reservoir in this new design. It is a big reservoir and can be easily refilled even when the chamber and the reservoir are both under vacuum.

In summary, as a significant part of successful MBE growth, we designed and built a customized mercury cell that warrants stable, pure, and high mercury flux during each growth and excellent run-to-run flux stability. Moreover, it is easy to use, clean, and refill.

3.4 MBE Temperature Control

During an MBE growth, there are several temperatures that need monitoring. The cell temperatures need to be controlled to provide stable and desired fluxes, and the substrate temperature is crucial to successful MBE growth. A set of proportional–integral–derivative (PID) controller is used to control the cells' temperatures and the substrate individually. The major components in a PID control system are shown in Figure 31. The temperatures of the cells and substrate holder are measured with thermocouples. The thermocouples send temperature input to the PID control unit. The unit generates an output signal to the power supply based on the current temperature and the set temperature. The power supply heats the heating elements in the cells as well as those behind the substrate holder; one temperature control loop is complete.

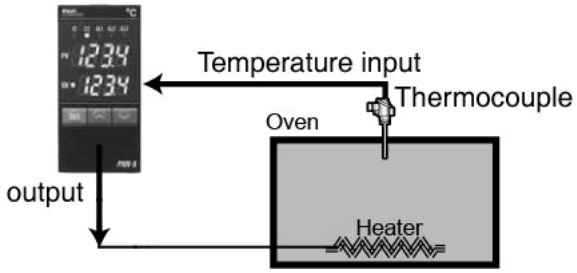

Figure 31 An illustration of PID control loop

PID control is excellent at confining the temperature within a minimal range and ramping the temperature smoothly. Figure 32 shows a temperature ramping profile using PID control. PID control can prevent overshoot when rapidly changing the temperature settings. Moreover, it can keep the temperature stable around the set temperature without too much fluctuation.

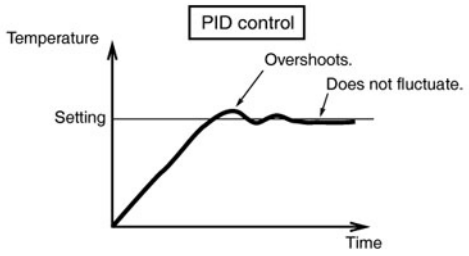

Figure 32 A temperature ramping profile using PID control

As we mentioned in section 3.1, the growth window, which is the substrate's optimized temperature range, is extremely small. This means two things: 1) The temperature has to be within this growth window to achieve high-quality growths; 2) Once the temperature hits the window, it needs to stay in the window stably. The second thing is solved by PID control. However, the first one is not that easy to deal with. There are several factors that make it difficult to hit the growth window:

1. The thermocouple is connected to the back of the substrate holder, and there is a temperature difference between the back of the holder and the surface of the substrate.

2. The quality of the thermal contact between the substrate and the moly block introduces inconsistency in temperature.

3. As the sample becomes thicker during the growth, the temperature of the sample surface drops due to thermal radiation and poor thermal conductivity of II-VI materials.

4. The size of the substrate affects thermal radiation and hence affects the temperature.

Factor 1 & 2 is solved by introducing good thermal contact between the substrate and the moly holder. We use Isopropanol based Colloidal Graphite to mount the substrate. It provides thermal contact and acts as a good adhesive to attach the substrate so it will not drop during the growth. It is easy to apply but dries fast. To improve the applying speed and quality simultaneously, we recently designed a customized stencil with a "waterfall" inner edge to prevent capillary action due to surface tension. Colloidal Graphite is growth-temperature tested and can hold the substrate at $210°C$ for more than 40 hours.

Factor 3 can be handled with *in-situ* characterization techniques like RHEED and SE. These tools can help us monitor the real-time sample surface during the growth. We will discuss RHEED and SE in the next chapter.

Factor 4 is eliminated by *ex-situ* characterization. Many other complicated factors, like the condition of the chamber, cells, pumps, and substrate surface morphology, are hard to adapt to. *Ex-situ* characterization like microscope and Nomarski can give us information on the surface so that the growers can adjust the temperatures for the next growth accordingly.

To tackle the uncertainties and unseen factors that affect the growth temperature, a new machine learning approach is used. We want to use a few critical MBE growth parameters as input and build a machine learning model with Neural Network Architecture. Some promising preliminary result has been achieved. The majority of this project will remain as part of future work.

3.5 Growing T3SL Using MBE

Cadmium telluride and mercury telluride have similar lattice constants, 6.4815 and 6.4618˚A, respectively. This minimal mismatch (0.3%) makes them good candidates for growth of heterostructures and multilayers as the strain is small.

Both Normal and Inverted band structure HgTe/CdTe superlattices are grown using MBE. The growth temperature of these samples ranges from $191 - 202°C$, no noticeable effect of the growth temperature is observed.

The inverted band structure superlattices are the earlier attempts to grow T3SL to study absorption characteristics and optimize SL growth conditions. These samples were grown on CdTe (211)B on Si substrates and employ a simple SL structure followed by a CdTe cap layer. These layers are n-type doped with a doping level of low 10^{15}. The designed HgTe well layer thicknesses of these samples range from 67 Å to 360 Å, and the CdTe barrier thicknesses range

from 44 Å to 88 Å. The structure of the inverted band SL samples is shown in Figure 33. And the number of periods, well thickness, and barrier thickness of these samples are shown in Table 4.

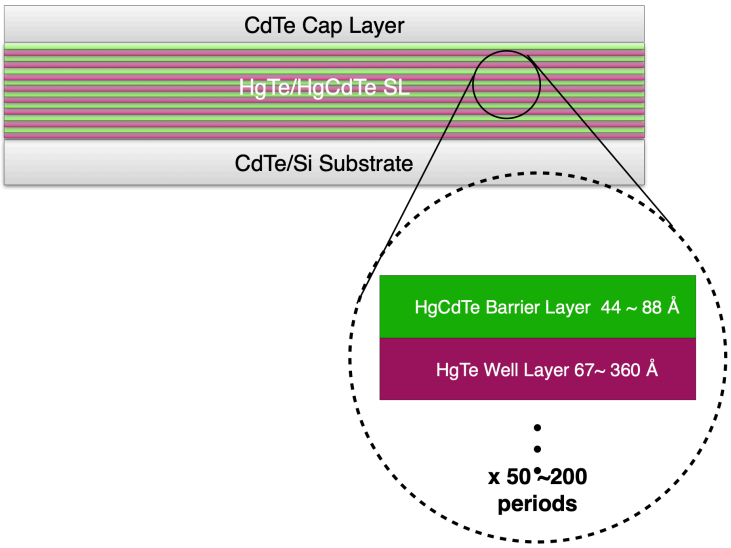

Figure 33 The structure of the inverted band SL samples. The insert shows one period of the SL layer.

Sample	# of Periods	Well thickness (Å)	Barrier thickness (Å)
hct15048	100	180	44
hct15049	120	180	44
hct15051	80	180	44
hct15052	100	225	44
hct15053	50	360	88
hct15054	80	270	44
hct15055	200	67	44
hct15056	80	180	88
hct16001	200	180	44
hct16002	160	180	88
hct16003	160	88	88

Table 4 The designed number of periods, HgTe well layer thickness, and CdTe barrier layer thickness of the inverted band structure superlattice samples

The normal band structure SLs are grown on two different substrates, namely CdZnTe (211)B and CdTe (211)B on Si. The structure of these SLs is significantly different from the inverted band samples (Figure 34). First, we have a SWIR HgCdTe bottom contact layer, which also acts as a buffer layer for the SL growth. The second is that we have an MWIR top contact layer right below the CdTe cap layer. The bottom and top contact layers are added to form a device structure.

Doping is also handled differently in these samples. Doping could potentially introduce defect levels, which would reduce Shockley-Read-Hall lifetime. As we mentioned before, the electrons and holes are confined inside the HgTe well layer in the HgTe/CdTe superlattices. By doping the CdTe barrier layers only, the defects are formed inside the CdTe cap layer and are separated from the carriers. The carrier lifetime is expected to be longer.

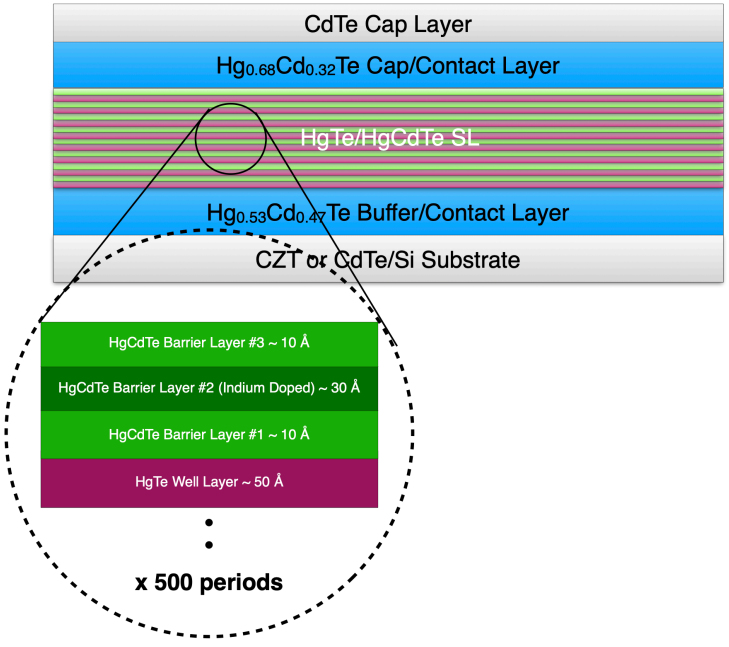

Figure 34 The structure of the normal band SL samples. The insert shows one period of the SL layer.

These samples have 500 periods, and HgTe well and CdTe barrier thicknesses are in the range of 50Å to 60Å, which are designed based on our modeling result. The cutoff wavelength of these samples is in the VLWIR range. The designed number of periods, HgTe well layer thickness, and CdTe barrier layer thickness of three representing normal band structure superlattice samples are given in Table 5. To avoid confusion and help the reader remember the difference between these samples, the samples' names are omitted and replaced by nicknames with their substrate included.

Sample nickname	# of Periods	Well thickness (Å)	Barrier thickness (Å)
SL_CZT	500	50	50
SL_CdTe/Si_1	500	52	54
SL_CdTe/Si_2	500	50	52

Table 5 The designed number of periods, HgTe well layer thickness, and CdTe barrier layer thickness of three representing normal band structure superlattice samples.

It is worth mentioning that the thickness of the CdTe barrier is picked so that a reduced tunneling current can be achieved while maintaining a sufficiently large vertical transport. It has been shown that SL designs with d_{CdTe}~50 Å can meet this requirement and the perpendicular effective mass is about ten times larger than the in-plane effective mass [68].

4 CHARACTERIZATION

4.1 MBE *In-situ* Growth Characterization

4.1.1 Reflection High Energy Electron Diffraction

4.1.1.1 Overview

Reflection High Energy Electron Diffraction (RHEED) is one of the most critical *in-situ* characterization tools for molecular beam epitaxy. It provides real-time information on sample surface morphology and assists in finding the optimum growing condition.

The RHEED system is installed directly on the MBE growth chamber. A beam of electrons accelerated to 10keV is focused and directed to the sample mounted on the manipulator with deflection and focus plates, then the electrons are diffracted at a very small angle ($1 - 5°$). The diffracted beam containing sample surface information then hits a phosphor screen mounted on a vacuum quartz window, showing an RHEED pattern that can be observed. An illustration of an RHEED system is shown in Figure 35. Because the electrons are directed onto a sample's surface at a shallow incident angle, the electrons have a small normal momentum component so they can only penetrate to a few atomic monolayers. This makes RHEED an excellent real-time surface monitor.

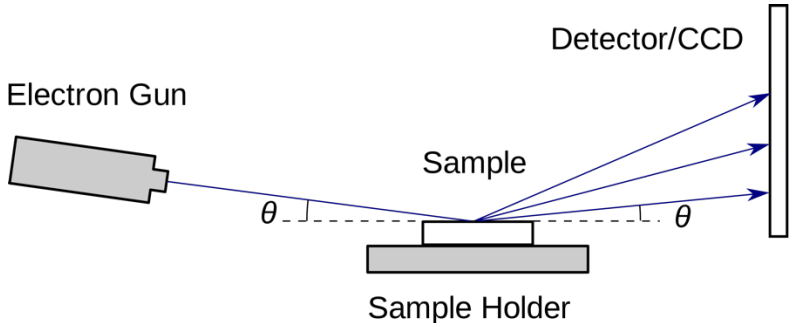

Figure 35 An illustration of an RHEED system. (https://en.wikipedia.org/wiki/Reflection_high-energy_electron_diffraction)

Because RHEED only touches the samples surface, the lattice structure it interacts with can be described as a 2D surface. The reciprocal net points of a 2D periodic net are a series of infinite rods perpendicular to the sample's surface. The Ewald's sphere has a radius equal to the incident electrons wavevectors' magnitude and is center on the sample surface with :

$$k_0 = \frac{2\pi}{\lambda} \tag{4.1}$$

where λ is the electron's de Broglie wavelength. The different between incident beam wavevectors k_0 and diffracted beam wavevector k' defines the possible reflection conditions:

$$k' - k_0 = G \tag{4.2}$$

And for elastic scattering

$$|k_0| = |k'| \tag{4.3}$$

This diffraction condition is illustrated in Figure 36. Diffraction conditions are satisfied where the rods of reciprocal lattice intersect the Ewald's sphere. The RHEED electrons typically have energies in the 10–40KeV range and de Broglie wavelengths of 0.17–0.06 Å, which is much smaller than the crystal lattice constant. As a result, Ewald's sphere is much larger than the sample's reciprocal lattice, which produces an almost straight cut through the reciprocal lattice Brillouin zones that can be observed in the RHEED patterns.

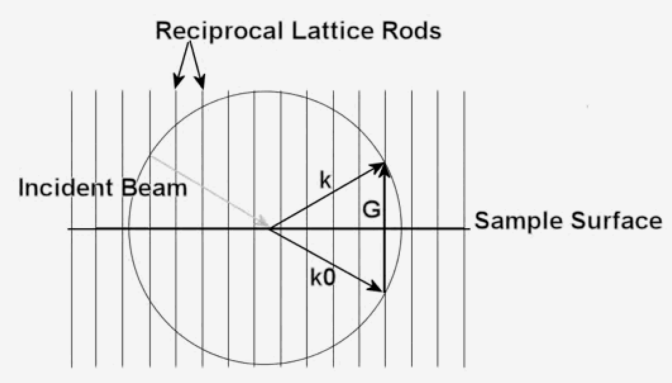

Figure 36 This diffraction condition of RHEED

4.1.1.2 RHEED Patterns of T3SL samples

RHEED image of a typical HgTe/CdTe SL growth is shown in Figure 37., The RHEED diffraction pattern observed during planar 2D growth appears as a series of vertical streaks, which we call 2D streaks. They are an indication of good growing conditions and a smooth sample surface. More, thinner and longer streaks mean better quality of the growth.

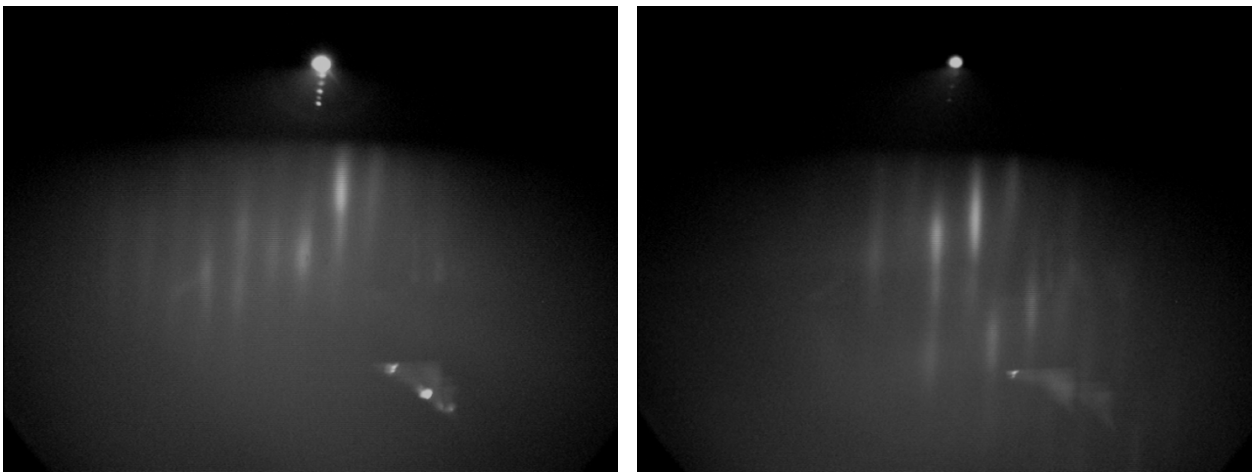

Figure 37 RHEED images of a typical HgTe/CdTe SL growth. (Left) HgTe well (Right) CdTe barrier

RHEED can be used to extract quantitative information from the surface. The spacing of the streaks is related to the lattice spacing, and the widths of the streaks are related to in-plane grain size. Oscillations in the intensity of observed RHEED patterns have been widely reported [79], and the periodicity of the oscillation is associated with individual atom layer growth. A bright RHEED pattern is observed when a flat atomic layer is grown. Then the RHEED pattern decreases in brightness until the full formation of the next layer. Each oscillation period can be used to calculate and calibrate the growth rates *in-situ*, therefore allowing precise layer thickness control. These oscillations are often used to calibrate growth rates in real-time and allow more precise layer thicknesses to be attained. However, these oscillations are not observed in our lab due to the nature of the step-flow growth mode of (211) growths [80].

In reality, RHEED is not suitable for extracting quantitative information from the surface because the substrate holder is rotating to allow uniform deposition on the substrate. The RHEED pattern changes rapidly, and it is challenging to take the best RHEED image and analyze it on the go. Besides that, the RHEED beam contains high energy electrons; focusing the beam on the same area of the sample for too long can result in localized and uneven heating on the surface, which generates defects. To take RHEED images without stopping the rotation, A Python program is written to take 16 consecutive burst images in about 1second so that the user can pick the best one for comparison with other images taken during the growth.

During our routine growth of HgCdTe alloy or HgTe/CdTe superlattices, RHEED is used primarily as a qualitative tool to verify single crystal growth conditions and monitor the surface defects. Especially during the nucleation, though primarily based on experience, the RHEED pattern transformation gives much information on the growth conditions. Figure 38 shows two

RHEED patterns associated with problems during MBE growth. These patterns are rarely seen during SL growth but are very common during HgCdTe alloy growth. “Grow window” does not exist for a SL growth. Unless the growth condition is quite off, 2D streak patterns should be seen throughout the SL growth. However, in a HgCdTe growth, these patterns in Figure 38 showing up during the early stage of the growth are usually associated with incorrect growth temperatures. Usually, we adjust the growth temperature immediately when there are signs of these patterns, and the surface can be flattened out. However, if these patterns show up and the growth condition is not corrected, then the defects are formed, and it is impossible to recover a flat high-quality single crystal layer.

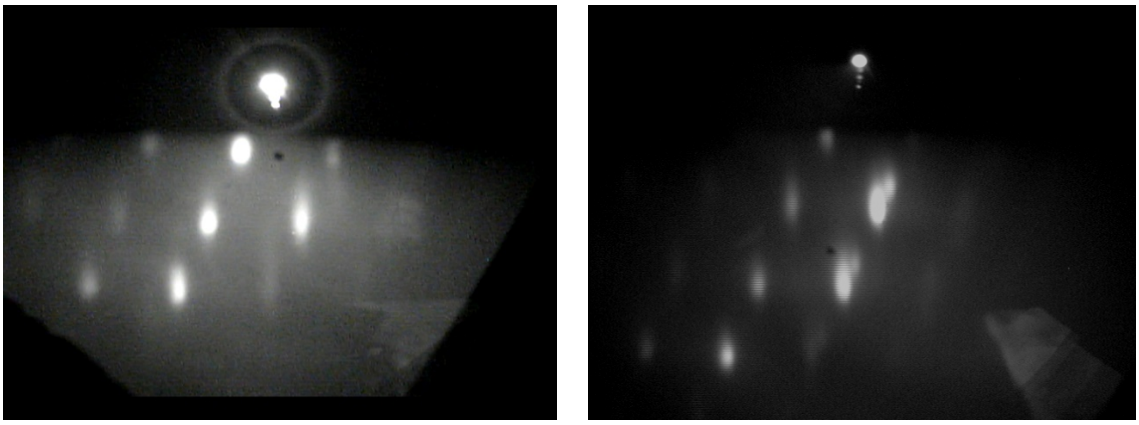

Figure 38 RHEED patterns associated with problems during the growth. (Left) 3D growth on the samples surface usually resulting from multiple crystalline phases; (Right) Twinning dots due to short streaks from (111) twin plane adjacent to the primary reflection.

4.1.2 Ellipsometry

4.1.2.1 Overview

Ellipsometry or Spectroscopic ellipsometry (SE) is another important *in-situ* characterization tool for molecular beam epitaxy. It provides real-time information on sample surface roughness, sample surface temperature, and composition for HgCdTe. Compared to RHEED, it is much easier to quantify the surface of the sample.

The Ellipsometry system is installed directly on the MBE growth chamber. A light source produces unpolarized light which is then sent through a polarizer. The polarizer axis is oriented between the p- polarized and s- polarized planes, such that both s- and p-polarized light arrive at the sample surface. The elliptically polarized light reflects from the sample surface goes through a continuously rotating polarizer (analyzer) and reaches the detector, where the light is converted into an electronic. The electronic signal carries polarization information, and is compared to the model build with a known input polarization. An illustration of an Ellipsometry system is shown in Figure 39.

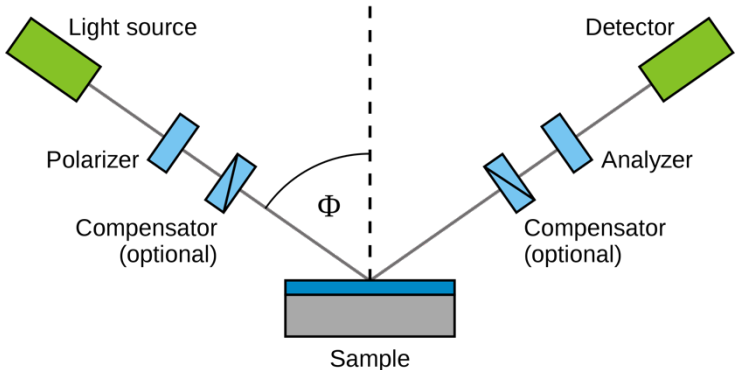

Figure 39 An illustration of an Ellipsometry system (https://en.wikipedia.org/wiki/Ellipsometry)

When a light beam shines on a HgCdTe/CdTe/Si multilayer or HgTe/CdTe SL structure, multiple reflections and refractions result in an infinite series for the transmitted and reflected light. After many reflections and refractions from the interfaces among the layers, the light travels to the detector with rich information about the sample. Compared to RHEED, Ellipsometry light goes deeper into the surface but still carries information of the top layer instead of the whole sample. So, Ellipsometry also provides real-time information about the sample surface.

The ellipsometry model build with known input polarization requires two ellipsometry parameters. The ratio of the Fresnel reflection coefficients of p-polarized light and s-polarized light is

$$\rho = \frac{r_p}{r_s} = \frac{|r_p|}{|r_s|}\exp\left(i\delta_p - i\delta_s\right) = tan\psi e^{i\Delta} \tag{4.4}$$

where ψ and Δ are the two ellipsometry parameters. ψ represents the ratio of the amplitude diminutions, and Δ is the phase difference induced by the reflection from the sample. The ellipsometry emits light with an energy range from 1.5eV to 3.5eV. ψ and Δ as a function of energy is plotted. The data is fitted using regression analysis where hundreds of experimental data are used. The unknown parameters are determined until the minimum of an estimator, the Mean Squared Error (MSE) for instance, is reached. An example of fitted data is shown in Figure 40. ψ and Δ are plotted as a function of light energy. The data is from a singletimestampp during the HgTe/CdTe superlattice growth, and the fitted model is a HgTe model based on experimental data.

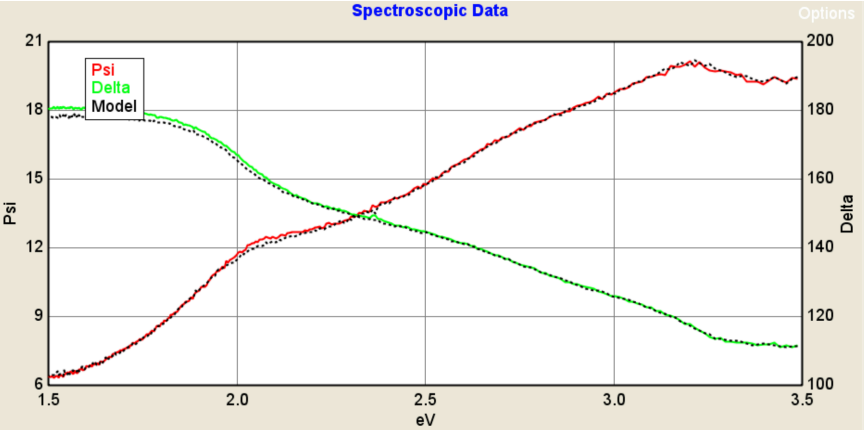

Figure 40 An example of fitted ellipsometry data. ψ and Δ are plotted as a function of light energy. The data is from a single timestamp during the HgTe/CdTe superlattice growth, and the fitted model is a HgTe model based on experimental data.

Ellipsometry can extract various information during different phases of MBE growth. We can get CdZnTe or CdTe on Si substrate temperature along with its surface roughness during the substrate outgassing process. During a HgCdTe alloy growth, we can extract the composition x and the surface roughness. The most grown HgCdTe heterostructure in our lab is MWIR Double-layer planar heterostructure (DLPH). This device structure contains a SWIR buffer layer, an MWIR absorber layer, and an MWIR HgCdTe cap layer followed by a CdTe cap layer. The whole growth is monitored by ellipsometry. Figure 41 shows the Ellipsometry data during one MWIR DLPH growth. Surface roughness and $Hg_{1-x}Cd_xTe$ composition are plotted as a function of time into the growth process. SWIR buffer layer, MWIR absorber layer, and the HgCdTe cap layer corresponds to different regions on the composition vs. time curve.

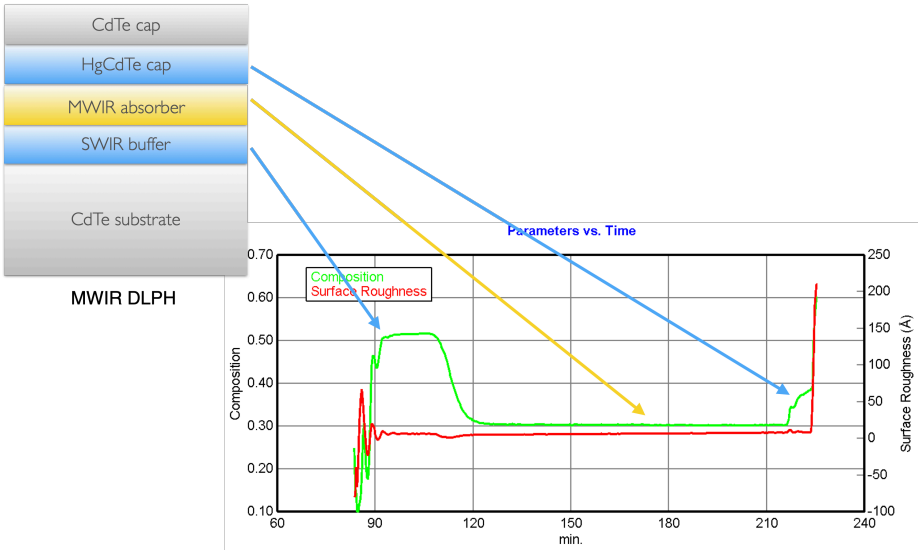

Figure 41 Ellipsometry data during one MWIR DLPH growth. Surface roughness and Hg1-xCdxTe composition are plotted as a function of time into the growth process. SWIR buffer layer, MWIR absorber layer, and the HgCdTe cap layer corresponds to different regions on the composition vs. time curve.

It can be observed in Figure 41 that there are some noticeable oscillations at the beginning of the growth, then the fluctuations slowly disappear after about 10min into growth. This is due to the interference of the reflecting light [81], majorly between the light reflected from the vacuum-epilayer and epilayer-substrate interfaces. As the layer thickness increases continuously during the MBE growth, the constructive /destructive interference wavelength changes, which causes fluctuations in the light intensity, and hence the model fitting is incomplete. Note that the ellipsometry light has energy higher than the bandgap of the semiconductor materials that we are growing. Eventually, the reflected lights inside the layer are fully absorbed, and the interference effect disappears.

4.1.2.2 Ellipsometry data of T3SL samples

Despite it holds ellipsometry from being used as a tool to monitor the growth from the beginning, the interference effect that we mentioned in 4.1.2.1 can be used to calculate and

calibrate the growth rate. The ellipsometry parameters' oscillations are due to interference, and interference condition depends on the layer thickness. By subtracting the time between two peaks on the oscillation curve, combining the change of layer thickness calculated from the interference condition, the growth rate can be extracted. Figure 42 shows ellipsometry parameter ψ as a function of time for light sampled at different energies. The curves oscillate at the beginning of the growth due to interference between reflected lights. The effect totally disappears after 30min into the growth. The data is fitted using interference theory. Note that the time starts at a non-zero position because ellipsometry and the growth were started at different times. Figure 43 shows ellipsometry being used to calibrate the HgTe growth rate. A HgTe layer is grown on CdTe on Si sample for 15 minutes. The thickness of the layer as a function of time is plotted using the fitted data. The growth rate can then be extracted from the slope of the linear fit.

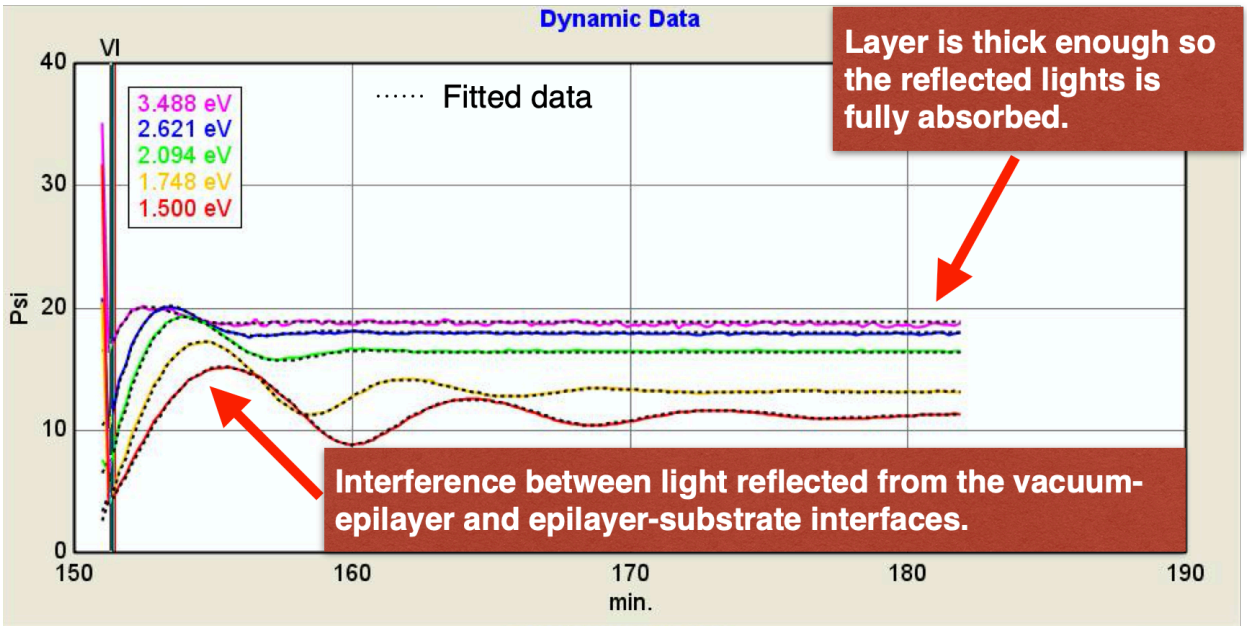

Figure 42 Ellipsometry parameter ψ as a function of time for light sampled at different energies. The curves oscillate at the beginning of the growth due to interference between reflected lights. The effect disappears after 30min into the growth. The data is fitted using interference theory. Note that the time starts at a non-zero position because ellipsometry and the growth were started at different times.

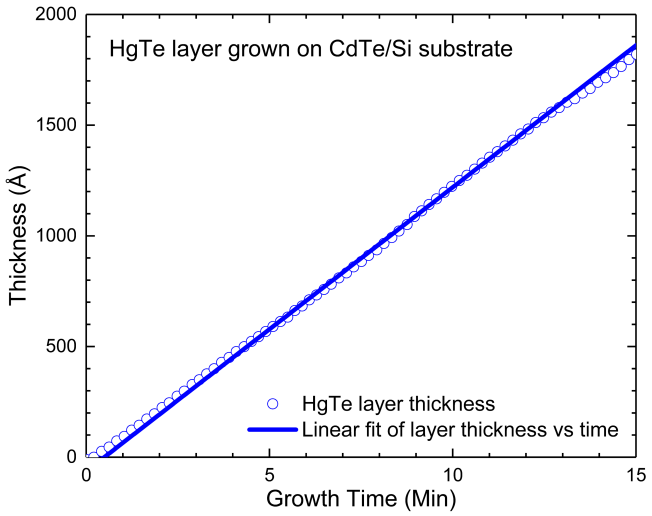

Figure 43 Ellipsometry being used to calibrate HgTe growth rate. A HgTe layer is grown on CdTe on Si sample for 15 minutes. The thickness of the layer as a function of time is plotted using the fitted data. The growth rate can then be extracted from the slope of the linear fit.

The surface roughness obtained from ellipsometry is also proved useful. It is evident that high quality layers have relatively low surface roughness. We have found a strong correlation between the ellipsometry surface roughness and RHEED patterns. Figure 44 gives a few examples of the RHEED pattern and the ellipsometry surface roughness of MWIR single layer HgCdTe samples.

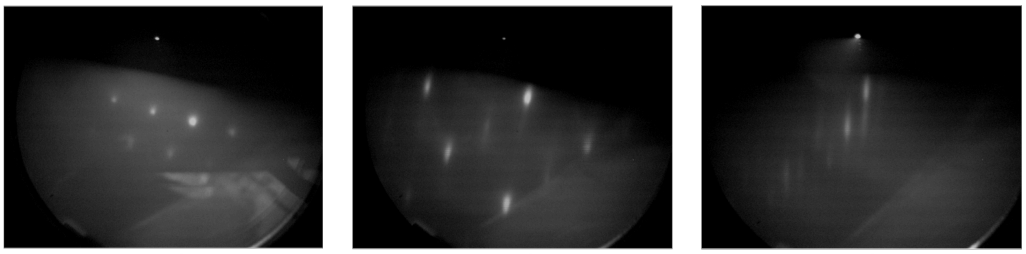

Figure 44 A few examples of the RHEED pattern and the ellipsometry surface roughness of MWIR single layer HgCdTe samples. A strong correlation between the ellipsometry surface roughness and RHEED patterns can be observed.

Unfortunately, ellipsometry is not quite useful for superlattice growths. Because the HgTe well and barrier layers are relatively thin, ellipsometry does not have enough layer thickness to build up stable polarization information (Figure 45). So ellipsometry is majorly used for SL growth rate calibration and monitoring HgCdTe growths.

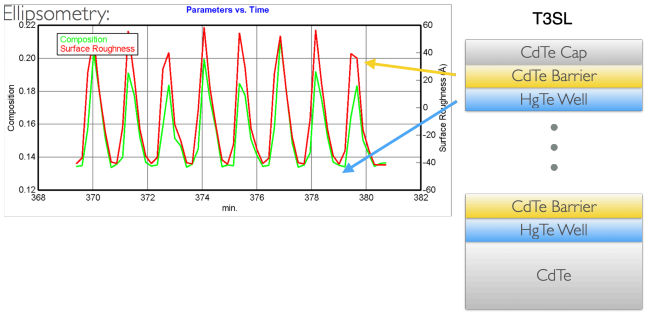

Figure 45 An example of ellipsometry data got from superlattice growth. Because the HgTe well and barrier layers are relatively thin, ellipsometry does not have enough layer thickness to build up stable polarization information.

4.2 MBE *Ex-situ* Growth Characterization

4.2.1 Overview

Molecular beam epitaxy growth optimization relies heavily on accurate *ex-situ* characterization. Characterization result on previous samples is used to improve subsequent growths.

Ex-situ characterization starts from taking pictures of the sample surface. A strong flashlight is used to illuminate the sample surface at different angles. This can give us some preliminary yet useful information about the growth quality. Good growth usually ends with shining surface, while unsuccessful growth can result in haze and visible point defect. Based on our experience, the sample surface color reflects the growth temperature condition during the growth. The purplish surface is what we are expecting for a sample with optimized growth

temperature, while pale gray or yellowish color is associated with high temperature or low-temperature growth. A picture of an as-grown 25mmx25mm HgTe/CdTe superlattice sample on CdZnTe (211)B substrate is shown in Figure 46.

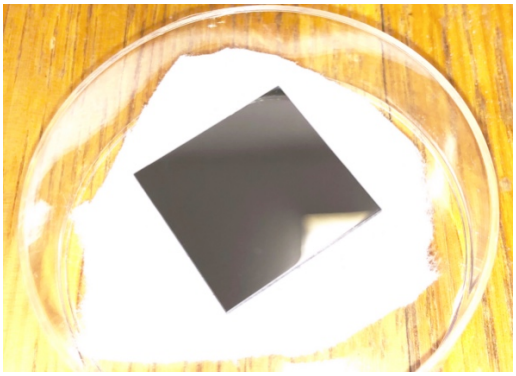

Figure 46 A picture of as-grown HgTe/CdTe superlattice sample on CdZnTe (211)B substrate

A whole wafer imaging system is occasionally used to identify any significant macro defect or scratch on the sample surface. A digital single-lens reflex camera (DSLR) with a Microlens is used within a dark tunnel. The sample is illuminated with the flashlight mounted on the side. A black sample surface with no white dots would be ideal. Any kinds of void defects caused by dust particles left on the surface by the substrate cleaning process, chamber flakes dropping, substrate transferring and mounting, or from the Hg or other cells will be revealed. A picture taken with a whole wafer imaging system of as-grown 25mmx25mm HgTe/CdTe superlattice sample on CdZnTe (211)B substrate is shown in Figure 47.

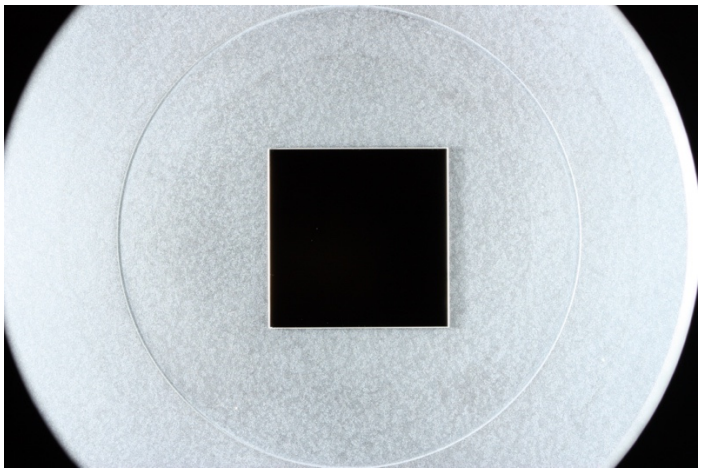

Figure 47 A picture taken with a whole wafer imaging system of as-grown 25mmx25mm HgTe/CdTe superlattice sample on CdZnTe (211)B substrate

More sophisticated methods are used to characterize HgTe/CdTe superlattice growths. Microscope (4.2.2) and Fourier-transform Infrared Spectroscopy (Chapter 0) are used as routine. Some preliminary imaging results utilizing Scanning Electron Microscopy (4.2.3) and Transmission Electron Microscopy (4.2.4) are presented to verify the superlattice structures. X-ray diffraction (4.2.5) is used to characterize SL periods thickness and lattice constant.

4.2.2 Microscope and Nomarski

The sample's structural quality almost always limits infrared device performance. The fastest and most direct way to characterize the sample's quality is to use a microscope. Optical microscopy was used to evaluate grown samples' surface morphology, which reveals information about the crystallization mechanism prevalent during MBE growth. Figure 48 shows microscope imaging of the surface of three HgTe/CdTe superlattice samples. A defect-free surface looks smooth and free of dark dots, which is usually an indication of good sample quality. Triangle void defects are usually associated with high-temperature growth or insufficient Hg flux. The formation of these void defects from the viewpoint of crystallography and nucleation is still

unclear, though it is very likely that the origin of void defects is bundles of screw defects [60]. On the other hand, if the growth temperature is low and the growth condition cannot offer enough surface relaxation time for atoms to relocate to a global energy minimum, high-density micro-defects with twins will form on the surface.

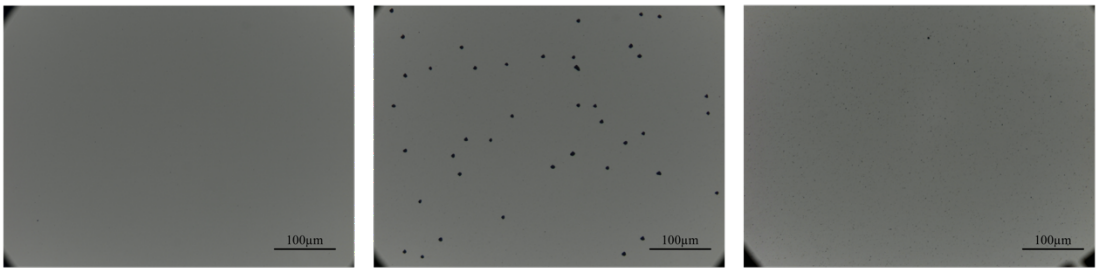

Figure 48 Microscope imaging of the surface of three HgTe/CdTe superlattice samples: (a) a defect-free surface (b) a surface full of triangle void defects (c)a micro-defects rich surface.

Nomarski microscopy is a phase imaging technique that utilizes differential interference contrast (DIC). It is named after its inventor, Polish and naturalized-French physicist, Georges Nomarski [82]. A polarized light source is separated into two orthogonally polarized mutually coherent parts, which recombine before observation. Their optical path difference induces interference. The contrast is then produced due to the path length gradient along the shear direction on the sample, and a 3D image corresponding to the sample surface optical densities is generated. Hence, Nomarski images emphasizes defects, lines, and edges on the sample surface.

A Nomarski microscopic image of an as-grown HgTe/CdTe superlattice sample on CdTe (211)B on Si substrate is shown in Figure 49. Crossed lines with 44 deg to 45 deg angles forming a crosshatched pattern are usually found on the MBE-grown HgCdTe or HgTe/CdTe superlattice epilayers of relatively high quality and without large densities of micro- or macro-

defects [83], [84]. This pattern can only be seen using a Nomarski microscope, which reveals the surface morphology. We did not observe this pattern using a regular microscope.

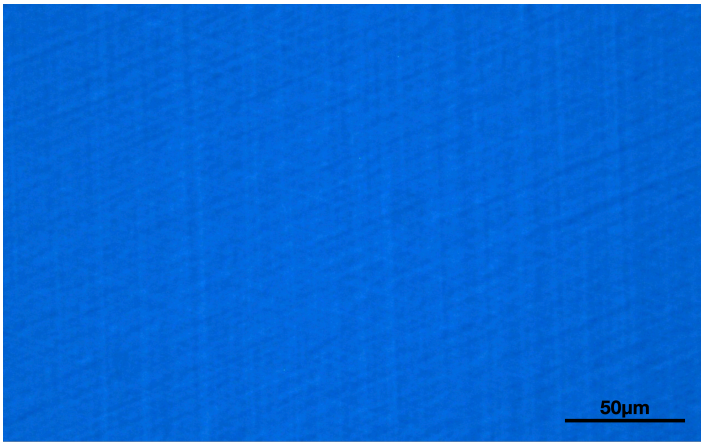

Figure 49 A Nomarski microscopic image of an as-grown HgTe/CdTe superlattice sample on CdTe (211)B on Si substrate.

For a heterostructure that is approximately 10µm thick, the peak-to-valley distance of a crosshatched pattern on the surface is of 5 ~ 20 nm. This pattern is usually more visible for samples grown CdTe on Si substrates than those on CdZnTe bulk substrates. The orientations of these lines follow either the $[\bar{2}13]$ or $[\bar{2}31]$directions, which corresponds to the intersection of a (211) surface plane with $(1\bar{1}1)$and $(11\bar{1})$ slip planes, respectively [60]. The primary cause of these crosshatches is slippage along these planes and consequently misfit dislocation formation. Another cause is the amplification of already existing crosshatches from the CdTe on Si substrates. Smaller height crosshatches (~around 0.4 nm) are likely caused by surface strain relief [83], [85] where misfit dislocations may not be present.

Nomarski microscopy emphasizes and shows the morphological structure of defects on the surface. Figure 50 (a) shows a Nomarski image of a void defect under 1000x magnification.

The triangle void defect is sitting on a crater, which can only be seen using Nomarski. Figure 50 (b) shows a Nomarski image of needle defects on the surface under 500x magnification. Twins (craters) can coexist with needle defects at non-ideal low (high) growth temperatures. Sometimes needle defects may even be induced by rough or damaged substrate, which favors the formation of clusters.

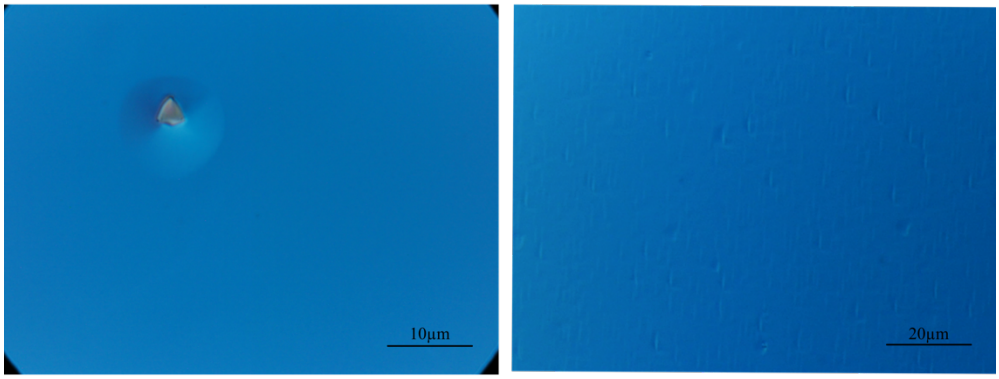

Figure 50 Nomarski imaging of (a) a void defect under 1000x magnification. The triangle void defect sits on a crater (b) a needle defects rich surface under 500x magnification.

4.2.3 Scanning Electron Microscopy

4.2.3.1 Overview

While the sample surface provides essential information, we want to look inside the T3SL samples to learn more. A cross-section view should reveal the heterostructure of the SL samples. Scanning Electron Microscopy (SEM) and Transmission Electron Microscopy (TEM) are two electron microscopes that are widely used for this purpose. SEM scans the sample with a focused beam of electrons. The signals are produced through the interaction between electrons and atoms in the sample, where information regarding the surface topography and composition

of the sample is revealed. Very often SEM is operated in the mode that the image is formed using the secondary electrons emitted by atoms excited by the electron beam. An image is created by scanning the sample and collecting the secondary electrons which contains information about the sample surface topography. An illustration of SEM is shown in Figure 51. In this work, a Raith eLine SEM operating at 10kV was used.

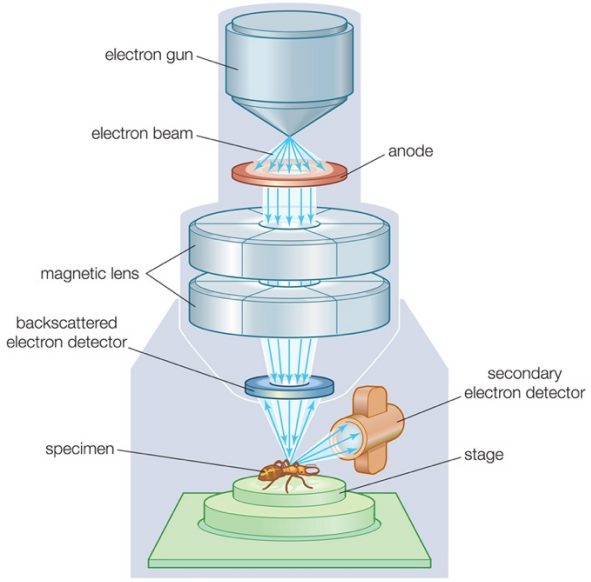

Figure 51 An illustration of a Scanning electron microscope. (Source: Encyclopædia Britannica, https://www.britannica.com/technology/scanning-electron-microscope)

4.2.3.2 Characterization Result

Our goal is to observe SL patterns and measure layer thicknesses using SEM. SEM is more accessible than TEM, and the sample is much easier to prepare, so the feedback cycle is much shorter. However, we did not observe SL patterns in the SEM images (Figure 52). The sample we used in the SEM characterization is a HgTe/CdTe superlattice sample with 200 periods. The HgTe well layer's designed thickness is 67 Å, and the designed thickness of the

CdTe barrier layer is 44 Å. The SL layer is grown on a CdTe (211)B on Si substrate, where the CdTe layer is usually around 10 μm thick, and the Si base layer is a few hundred microns thick. The SL layer, the CdTe layer, and the Si layer can be clearly distinguished from the TEM images, even though the SL periodic pattern is not observed. The HgTe wells in the SL layer dominate the SL layer's color, resulting in the apparent color difference between the SL layer and the CdTe bulk layer.

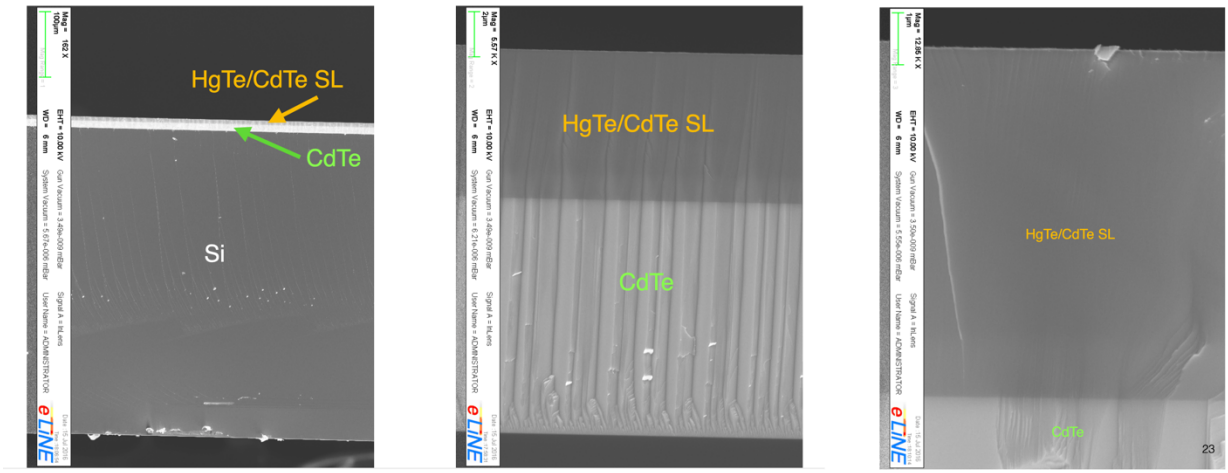

Figure 52 SEM imaging of the cross-section of a HgTe/CdTe superlattice sample grown on CdTe (211)B on Si substrate at (a) 162× magnification (b) 5570× magnification (c) 12850× magnification

The primary reason why the SL pattern is not observed with SEM is still unclear. A possible explanation is that the SL well/barrier layers are too thin, and SEM does not have enough resolution to reveal them. However, the subtle textures/lines on Figure 52 (b) and (c) seems to be on a smaller scale than the SL well/barrier layers. Another possible explanation is that the color difference between HgTe and CdTe layers is small, so that they cannot be distinguished when clustered. This theory is also suspicious because the interface between the SL layer and the CdTe substrate looks sharp and clear. The third possible explanation is that the SL

layer interdiffuse too much during the growth, and it eventually becomes HgCdTe alloy. This is proved wrong with FTIR measurement (section 5.2.3.3), where these HgTe/CdTe superlattices display SL absorption behavior that cannot be mistaken.

Though SEM failed to provide the thicknesses of individual layers in the SL, we can still get the SL layer's total thickness to calibrate the growth rate. The designed thickness of this specific SL sample is 2.22 μm. The thickness calculated from SEM is ~6 μm, which is much bigger than the designed thickness. We later found out that the thicknesses of this batch of SL samples are off due to the rapidly increasing CdTe flux from growth to growth. The CdTe flux changes a lot after the calibration growth we did at the beginning of this batch. The cause of this increase in flux is that the CdTe ingot is close to the end of its life.

The superlattice sample is hand cleaved along the <111> direction to reveal the cross-section. Initially, we tried using a dicing saw to expose the cross-section, it turns out that the saw blade would damage the edge and makes the cross-section useless (Figure 53). Saw blade marks are present everywhere on the Si substrate. The SL layer and the CdTe layer are cracked. Surprisingly, hand cleaving along the <111> direction would give a much smoother cross-section, and cracking at the edge is avoided.

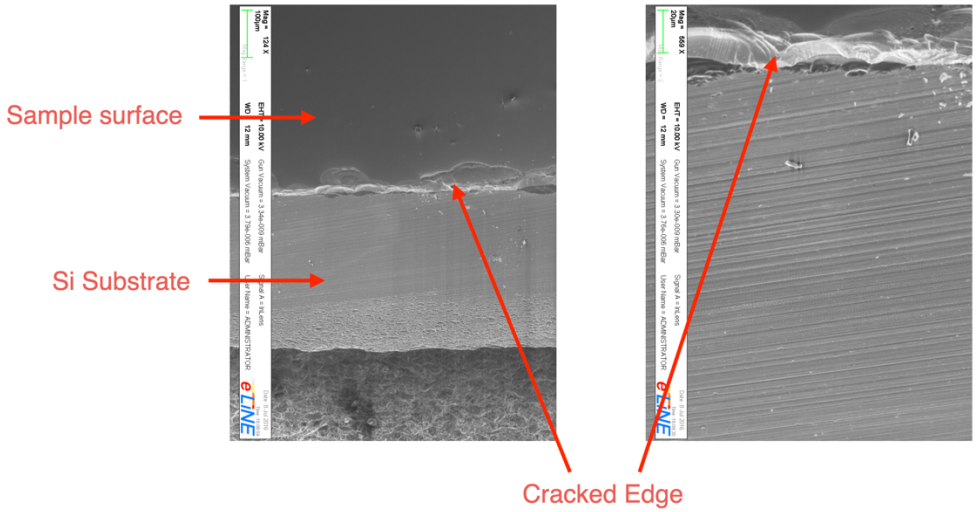

Figure 53 SEM imaging of the cross-section of a HgTe/CdTe superlattice sample grown on CdTe (211)B on Si substrate made with a dicing saw.

4.2.4 Transmission Electron Microscopy

4.2.4.1 Overview

Transmission Electron Microscopy (TEM) is a microscopy technique in which a beam of electrons is transmitted through a specimen to form an image. It is a superior technique for imagining at nanometer dimensions compared to SEM. An illustration of TEM is shown in Figure 54. It consists of three essential part: (1) an electron gun and a condenser system to focus the electron beam, (2) the image-producing system, which focuses the electrons passing through the specimen to form a real, highly magnified image, consisting of the movable specimen stage, objective lens, intermediate lens and projector lens (3) the image-recording system, which converts the information carried by electrons into some visual images. Besides, TEM must operate under vacuum, so a vacuum system including pump and valves is involved. In this work, the TEM characterization is done at Prof. David Smith's research group at Arizona State University with a Philips-FEI CM200 FEG-TEM operated at 200 keV.

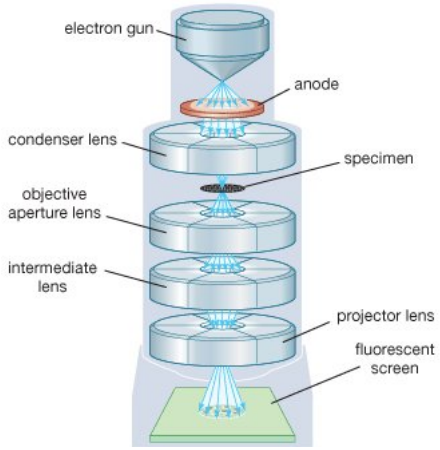

Figure 54 An illustration of transmission electron microscope

TEM is considered a destructive characterization method because TEM samples need special preparation where the sample is micro-machined to a thickness of 100 nm or less under a milling or polishing process. The challenges met in producing suitable TEM samples limit the studies of HgTe/CdTe superlattices using TEM compared to other semiconductor materials. HgTe/CdTe superlattices are mechanically weak, making it challenging to prepare, and defect analysis can be erroneous due to the likely possibility of defect creation from the sample preparation process. This precludes the use of TEM as a routine form of characterization for T3SL. Still, it remains the only microscopy to image the superlattice layers at sufficient magnification. In this work, we use TEM as an accurate tool to determine the individual layer thicknesses and gain preliminary information on HgTe/CdTe interface.

Two types of TEM sample preparation techniques were used in this work, namely Focused Ion Beam (FIB) and Ar-ion milling at liquid N2 temperature. The nanometer-scale resolution of FIB gives it the advantage to precisely mill and polish the sample, with the drawback of creating more damage to the sample compared to Ar-ion milling. To minimize the

damage, low beam voltage FIB was used. Ar-ion-milling was done at liquid N2 temperature to reduce the heat, while FIB is done at room temperature.

4.2.4.2 Characterization Result

TEM characterization was performed on three HgTe/CdTe superlattice samples. The designed number of periods and well/barrier thicknesses are shown in Table 6.

Sample hct16003 is prepared using FIB at 20kV and 0.21nA with ionized Gallium (Ga^+). A thin film of Platinum was deposited on top of the superlattice sample before the FIB process. The SEM image of the cross-section of the FIB lift-out sample is shown in Figure 55. The vertical stripes present on all layers are due to the FIB milling process, which are often referred to as "curtaining." FIB inevitably causes damage to the cross-section, which we need to keep in mind when analyzing defects. Similar to the SEM images we showed in section 4.2.3, we did not observe any superlattice periodic patterns. Note that two different SEM systems were used, which confirms that superlattice patterns cannot be seen using SEM.

	# of Periods	Designed well thickness d_w (Å)	Designed barrier thickness d_b (Å)	Estimated total thickness d_{total} (μm)
hct15048	100	180	44	2.24
hct15052	100	225	44	2.69
hct16003	125	88	88	2.20

Table 6 The designed number of periods and well/barrier thicknesses of three T3SL samples used in TEM characterization

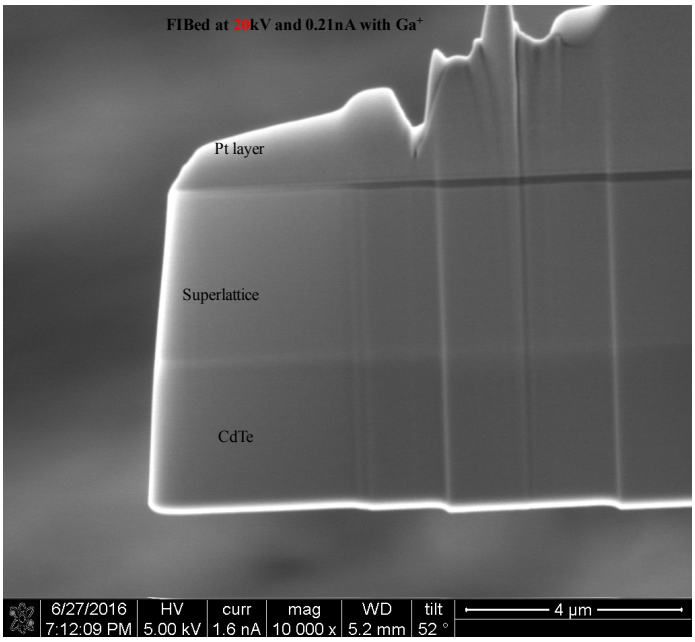

Figure 55 SEM Imaging of the cross-section of the FIB lift-out sample

A low magnification TEM image of the cross-section (also known as XTEM) is shown in Figure 56. The sample is rotated to <110>. The sample is much thicker than the design thickness, which is 2.2 µm. This confirms that this batch of SL sample has an issue with thickness overshot. We do not know whether the overshooting is in the HgTe well layer or the CdTe barrier layer yet. Counting from the top to the bottom of the SL layers gives us 125 periods, which agrees with our expectation. Some short threading defect segments are present in the superlattice layer. Note that none of these threading defect segments go across the whole SL layer. There are a few started in the substrate and terminated after about 10 SL periods. HgTe/CdTe superlattice has been used as an interfacial layer to block the dislocations to propagate from the substrate to the HgCdTe absorber layer [13], [60]. It is believed that abrupt interfaces interposed between HgTe and CdTe layers might help block the propagation of substrate-related defects.

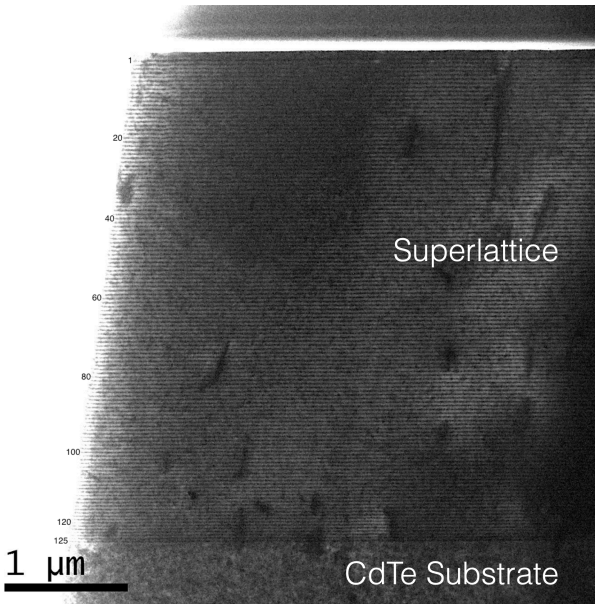

Figure 56 A low magnification (10k×) XTEM image of sample hct16003

The small black patches in CdTe substrates shown in Figure 56 are most likely due to Ga-implantation introduced during the FIB milling process. These small patches are further investigated with medium magnification XTEM. The result is shown in Figure 57. HgTe appears a darker color compared to CdTe. As a result, the small black patches in the CdTe layer looks like HgTe. This is not much of an issue for the substrate layer since we know the substrate is just CdTe bulk grown on Si. However, these small black patches are also visible in the SL layer, makes it hard to distinguish between a Hg bulge defect and Ga-implantation induced by FIB.

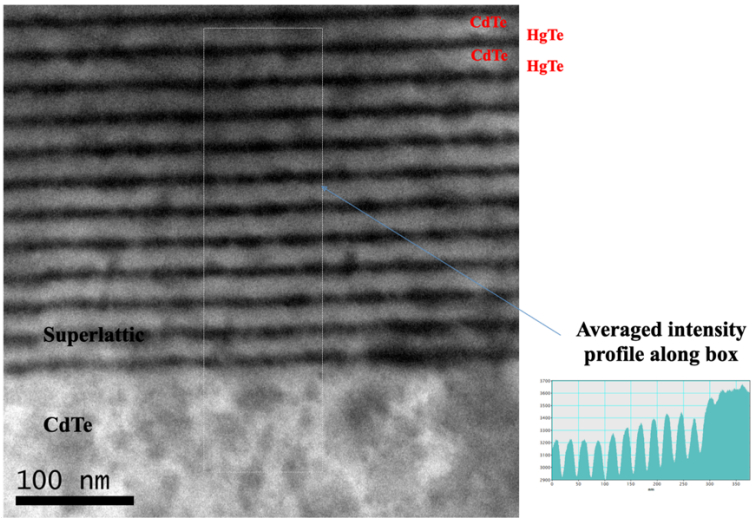

Figure 57 A medium magnification XTEM image of sample hct16003

A high magnification XTEM image of sample hct16003 prepared with FIB is shown in Figure 58 (a). The interfaces of HgTe and CdTe layers are vague. There are two possible explanations: (1) The superlattice layers interdiffused; (2) FIB damaged the sample. In order to find the answer, another sample is prepared using Ar-ion milling at 2.5 keV at liquid nitrogen temperature, followed by a 2.0 keV finish for cleaning. The high magnification XTEM image of this new TEM sample is shown in Figure 58 (b). It is evident that the new TEM sample prepared with Ar-ion milling has much sharper and straighter interfaces than the one prepared with FIB. Since these two TEM specimens came from the same SL sample, we concluded that FIB damaged the HgTe/CdTe superlattice cross-section. The damage is likely due to the heat from high energy Gallium. The heat cannot dissipate fast enough due to the poor thermal conductivity of II-VI materials, and some areas of the cross-section are heated fast, so interdiffusion happens. The quality of the image could be improved by cleaning the sample surface after FIB process. The explanation of FIB induced damage is backed up by the fact that Ar-ion milling, which was done at liquid nitrogen temperature, causes less damage. However, the Ar-ion milled sample

looks more defective, where quite a few sharp lines are visible on the cross-section. These defects most likely came from the Ar-ion milling process since similar defects are not observed in the FIB TEM sample. The TEM sample preparation technique needs to be further improved, considering both FIB and Ar-ion milling causes damage to the HgTe/CdTe superlattice sample, which makes it almost impossible to do defect analysis using TEM.

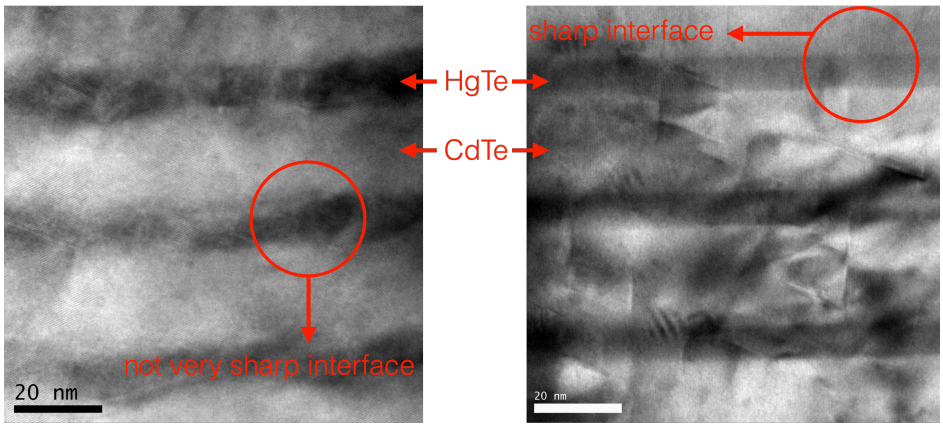

(a) FIB (b) Ar-ion milling under 77K

Figure 58 high magnification XTEM images of sample hct16003 prepared with (a) FIB (b) Ar-ion milling at liquid nitrogen temperature.

The sample thickness can be calibrated using XTEM. As we mentioned before, the sample thickness overshoot due to an unexpected run-to-run jump in CdTe flux. As a result, we expect to see thicker CdTe barrier layers. The insert in Figure 57 shows the average intensity profile along the superlattice growth direction. The intensity periodicity corresponds to the periodicity of the superlattice. The thickness of one SL period can be obtained by taking the average of several intensity periods. The result shows that the thickness of one SL period is 26.5 nm, and the total thickness of the SL layer is 3.31 μm.

A higher magnification XTEM image is needed to acquire the thicknesses of the individual HgTe/CdTe layer. Figure 59 shows the high magnification XTEM images of all three

samples we mentioned in Table 6. The HgTe thicknesses for all three samples are slightly smaller than the designed value, with a 5-15% error; The CdTe thicknesses overshot more than 80% of the designed value. Thicknesses are related to growth rate, and growth rate is directly related to cell flux. To check the regularity of flux change, HgTe error percentage and CdTe error percentage as a function of sample index since the start of this batch is plotted in Figure 60. Te flux drops gradually over time, while CdTe flux increases dramatically. The issue was fixed by refill the CdTe cell with a new ingot and slightly increase Te cell temperature from run-to-run.

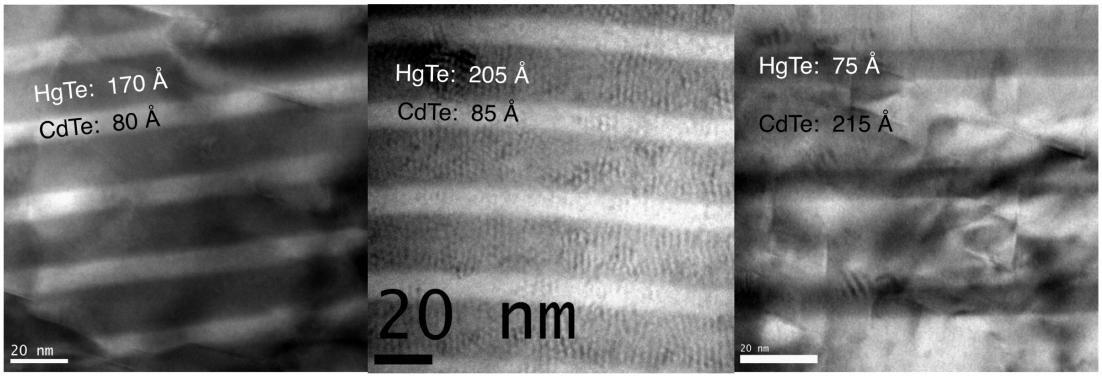

Figure 59 High magnification XTEM images of all three samples mentioned in Table 6. The average thicknesses of HgTe well layers and CdTe barrier layers are also given on the images.

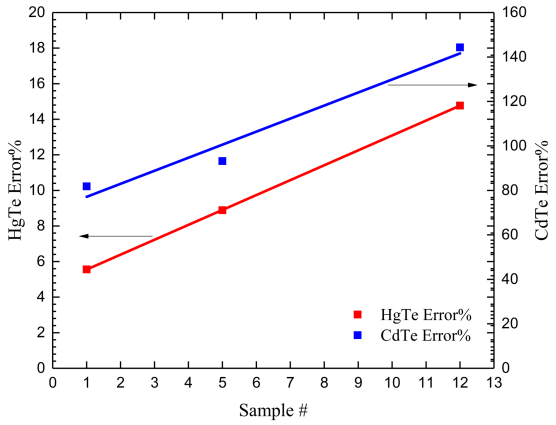

Figure 60 HgTe error percentage (left) and CdTe error percentage (right) as a function of sample index since the start of this batch of HgTe/CdTe superlattice growths. The blue and red straight lines are the linear fit of the three TEM characterized samples.

Some other sample characteristics can be obtained from XTEM images. Two examples of irregularity observed from XTEM are shown in Figure 61. Figure 61 (a) shows a wavy pattern that has previously been reported on HgCdTe bulk material [60]. This wavy pattern shows up in the region near the top of the SL layer and is likely due to twins formed on the exposed {111}-type planes of needle defects. Figure 61(b) shows an extra thick CdTe barrier layer created due to Tellurium shutter malfunction that happened shortly after the SL growth started.

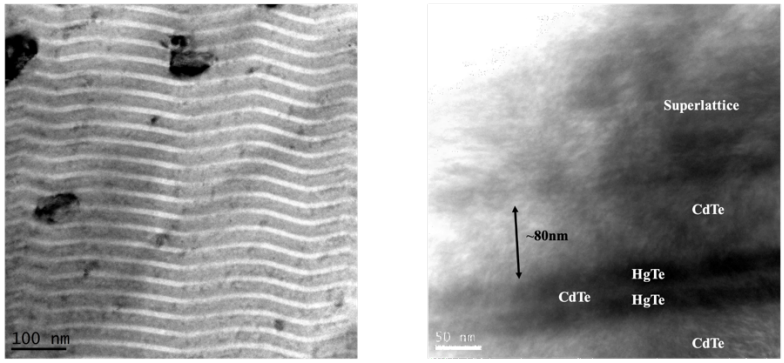

(a) (b)

Figure 61 Examples of irregularity observed from XTEM. (a) Superlattice pattern becomes wavy near the sample surface, and Te Precipitates are observed. (b) An extra thick CdTe barrier layer was created shortly after the SL growth started due to Tellurium shutter malfunction.

4.2.5 X-ray Diffraction

4.2.5.1 Experiment setup

X-ray diffraction (XRD) allows for a thorough structural analysis of the grown crystal, making it one of the most important tools for the MBE-grown sample characterization. X-ray has a strong interaction with the crystal lattice because the x-ray wavelengths are comparable to the crystal lattice spacing. As a result, information-carrying crystal structure is revealed through the scattering process. Lattice spacing itself can be extracted, which can then be used to determine the composition of ternary materials, provided the lattice constants of the constituent binaries follow the empirical Vegard's law.

The source of x-rays is a copper x-ray tube. Electrons are accelerated into a copper target with 40kV, and the associated emission current is 40mA. This interaction generates x-ray photons with a wavelength peaked at $\lambda_{xray} = 1.5406$ Å, which is in the same order as the crystal lattice of II-VI materials. The x-ray beam is then narrowed by x-ray mirrors and focused on a monochromator containing four high purity germanium crystals, which further reduces the angular divergence. Then the x-ray pass through a vertical slit of various size (0.1~2 mm) to adjust the lateral size of the output beam. The sample is mounted on a stage with six degrees of freedom, namely the three cartesian directions xyz, y-direction rotation ω, z-direction rotation ϕ, and x-direction rotation χ. 2θ corresponds to the angle between the detector and the plane of the sample surface, and it shares the same rotating axis as ω. $\omega/2\theta$ axis is used for XRD measurement, while ϕ and χ are used for alignment of the sample to the plane of the incident x-ray. The three rotation angles are illustrated in Figure 62.

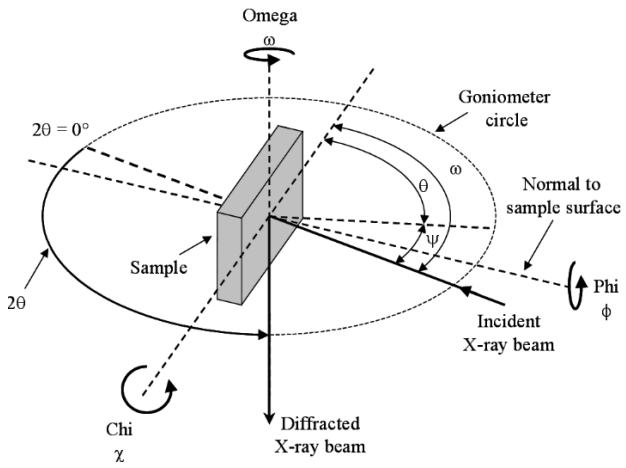

Figure 62 Rotation angles of the XRD sample stage. (https://www.semanticscholar.org/paper/Determination-of-residual-stresses-by-X-ray-Fitzpatrick-Fry/ecbaba17e7e95806ab701cefab1fd50781adc2b6#paper-header)

Rocking curve XRD measurements are used in this work. The samples are 'rocked' over a small range of ω about a diffraction peak. Rocking curve measurement is quick and commonly used on single-crystal sample characterizations. The quality of the growth, the periodicity of the superlattice layer can be obtained. Two major types of rocking curve measurements are used, namely ω scan and $\omega - 2\theta$ scan. For ω scan, the ω-axis is scanned about the reflection peak while 2θ is fixed at $2\theta = 2\omega$. ω scan is majorly used to do sample alignment along with z-scan. Once the alignment is done, we use the $\omega - 2\theta$ scan to expand the scan range, which is essential for superlattice XRD measurements. For $\omega - 2\theta$ scan, 2θ is coupled with ω. 2θ and ω change at the same time for each step of the scan. The change amount of 2θ and the change amount of ω satisfy $\Delta 2\theta = 2\Delta\omega$.

A Bruker D8 XRD system is used in this work. A picture of the XRD system at Microphysics Laboratory of the University of Illinois at Chicago is shown in Figure 63.

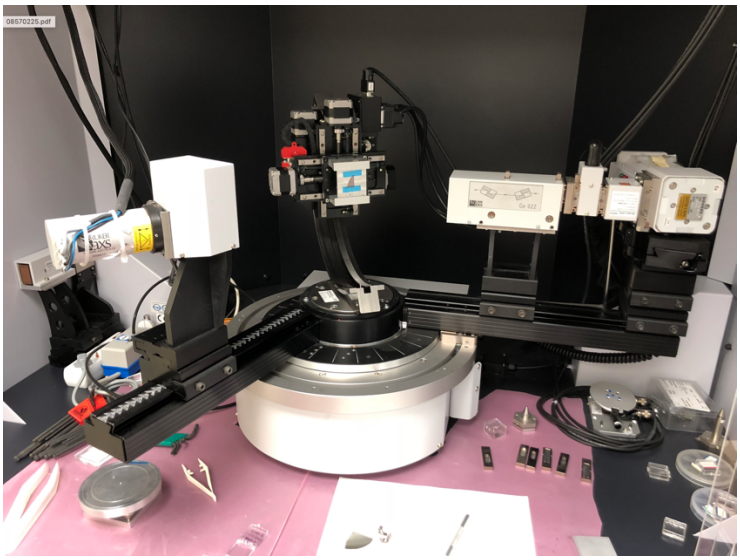

Figure 63 The basic setup of the XRD system at Microphysics Laboratory of the University of Illinois at Chicago

4.2.5.1 Bragg's law

X-ray diffraction is based on Bragg's law, which gives the angles for coherent and incoherent scattering from a crystal lattice. The x-ray beam approaches the crystal lattice, and the photons are scattered off different atoms within the crystal. The difference in the optical path of these photons leads to constructive or destructive interference. Bragg's law describes the condition of constructive interference between the x-ray radiation with wavelength λ_{xray} and the crystal plane (hkl) as:

$$n\lambda_{xray} = 2d_{hkl}sin\theta \tag{4.5}$$

where n is an integer, θ is the angle between the incident x-ray beam and the plane of the sample surface, d_{hkl} is the distance between planes inside a periodic lattice and is a function of lattice constant a:

$$d_{hkl} = \frac{a}{\sqrt{h^2 + k^2 + l^2}} \tag{4.6}$$

An illustration of Bragg diffraction is shown in Figure 64.

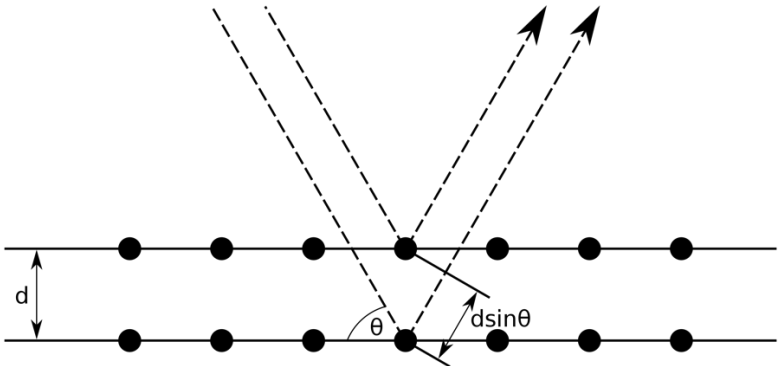

Figure 64 Two beams scattered off atoms in two different planes in a Bragg diffraction situation. (https://en.wikipedia.org/wiki/Bragg%27s_law)

For the (211)B HgTe/CdTe superlattice samples that we are considering here, the only symmetric reflection of interest is (422). So d_{hkl} becomes:

$$d_{hkl} = \frac{a}{\sqrt{4^2 + 2^2 + 2^2}} = \frac{a}{2\sqrt{6}} \tag{4.7}$$

The lattice constant of HgTe at room temperature is 6.462 Å, and that of CdTe is 6.482 Å. Plug these two numbers into Equation (4.7) and then back to Equation (4.5) gives us:

$$\theta_{HgTe} = \arcsin\left(\frac{\lambda_{xray}}{2d_{hkl}}\right) = 35.73° \tag{4.8}$$

$$\theta_{CdTe} = \arcsin\left(\frac{\lambda_{xray}}{2d_{hkl}}\right) = 35.60° \tag{4.9}$$

Note that n=1 is used in the equation above because any n>1 does not have a solution in the real space. Usually, we are more interested in 2θ value because the intensity is plotted as a function of 2θ in a $\omega - 2\theta$ scan. Doubling the values in Equation 4.8 and Equation 4.9 gives us:

$$2\theta_{HgTe} = 71.46° \tag{4.10}$$

$$2\theta_{CdTe} = 71.20° \tag{4.11}$$

$Hg_{1-x}Cd_xTe$ with any composition has a lattice constant between 6.462 Å and 6.482 Å. Assuming that the lattice constants of $Hg_{1-x}Cd_xTe$ follow the empirical Vegard's law, we have

$$a_{Hg_{1-x}Cd_xTe} = 6.462(1 - x) + 6.482x \tag{4.12}$$

Then the constructive interference angle θ of HgCdTe alloy can be obtained using the method shown in Equation (4.5-4.9), and the calculated 2θ value will lie between the two numbers in Equation (4.10) and (4.11). If the 2θ value of the HgCdTe alloy peak is known from XRD measurement, then the HgCdTe alloy composition can be calculated. Note that for a HgCdTe sample grown on either CdTe/Si or CdZnTe substrate, the major HgCdTe peak should be present as well as a substrate peak. However, HgCdTe based materials have an extinction depth of the order of 10μm [86], so there will not be a substrate peak if the HgCdTe layer is too thick. Besides, the major HgCdTe peak could overlap with the substrate peak, in which case the substrate peak is also not present.

The interference induced peaks in a superlattice layer are more complicated than HgCdTe alloy. Primary superlattice peaks represent an average bilayer composition instead of a direct

measurement of the makeup of the individual layers. The individual layers are strained, and the resulting lattice spacing is different from either of the superlattice constituents. To estimate the superlattice lattice spacing, the superlattice is thought of as a $Hg_{1-x}Cd_xTe$ layer with an x value given by the thickness-weighted x values of well and barrier:

$$x = \frac{d_w}{d_{bilayer}} x_w + \frac{d_b}{d_{bilayer}} x_b \tag{4.13}$$

where

$$d_{bilayer} = d_w + d_b \tag{4.14}$$

For HgTe/CdTe superlattices, $x_w = 0$ and $x_b = 1$. Plug these two numbers along with Equation (4.14) back to Equation (4.13) gives us the simplified form of pseudo x value of SL:

$$x = \frac{d_b}{d_w + d_b} \tag{4.15}$$

However, due to the continuing Hg flux background during the MBE growth, the barrier usually has a small Hg mode fraction of about 0.05 for (211) orientated samples, making the barrier $Hg_{0.05}Cd_{0.95}Te$. The pseudo x value can still be calculated with Equation (4.13). The expected 2θ value corresponding to the superlattice's main peak can be calculated using Equation (4.5-4.12).

Other than the main SL peaks, there are satellite peaks observed on rocking curve XRD measurements. The satellite peaks, also called satellite fringes, are due to the new periodicity introduced by the superlattice. Now other than the d-spacing between planes in the crystal lattice,

the superlattice period d_{SL} also creates interference conditions based on Bragg's law. Because d_{SL} is much larger than the crystal lattice, the spacing or the angle difference between interference peaks are much smaller according to Equation (4.5). The superlattice period d_{SL} can be calculated using the positions of satellite peaks. Consider two adjacent satellite peaks i and j, according to Equation (4.5), we have:

$$n_i\lambda_{xray} = 2d_{SL}sin\theta_i \tag{4.16}$$

$$n_j\lambda_{xray} = 2d_{SL}sin\theta_j \tag{4.17}$$

(4.16) - (4.17) gives:

$$(n_i - n_j)\lambda_{xray} = 2d_{SL}(sin\theta_i - sin\theta_j) \tag{4.18}$$

Since satellite peaks i and j are adjacent, $n_i - n_j = 1$. Then we have

$$d_{SL} = \frac{\lambda_{xray}}{2(sin\theta_i - sin\theta_j)} \tag{4.19}$$

4.2.5.2 Characterization result

For convenience, the information on the samples that we will present XRD data here is summarized in Table 7. Two superlattice samples, hct15048 and hct15051, have an inverted

band structure and the other three have a normal band structure. Sample SL_CZT was grown on CdZnTe substrate, while the other four were grown on CdTe (211)B on Si substrate.

	# of Periods	Designed well thickness d_w (Å)	Designed barrier thickness d_b (Å)	Estimated SL period d_{SL} (Å)
hct15048	100	180	44	224
hct15051	80	180	44	224
SL_CdTe/Si_1	500	52	54	106
SL_CdTe/Si_2	500	50	52	102
SL_CZT	500	50	50	100

Table 7 The designed number of periods, well thicknesses $\mathrm{d_w}$, barrier thicknesses $\mathrm{d_b}$, and SL period $\mathrm{d_{SL}}$ ($\mathrm{d_{SL}} = \mathrm{d_w} + \mathrm{d_b}$) of selected T3SL samples used in XRD characterization.

The result of a ω-2θ scan of the (422) reflection of two SL samples with inverted band structure, hct15048 and hc15051, is shown in Figure 65. Both of these samples have diffraction peaks associated with the substrate (S), superlattice (L), and satellite fringes (F). Recall from Equation (4.10) and Equation (4.11) that 2θ of HgTe is $71.46°$ and 2θ of CdTe is $71.20°$. Both samples are grown on CdTe substrate, so a CdTe substrate peak is observed around $71.20°$. The small error is likely due to sample alignment precision and sample tilting. A superlattice main peak is present on the right-hand side of the substrate peak, with a 2θ value lies in the range of $(71.20°, 71.46°)$.

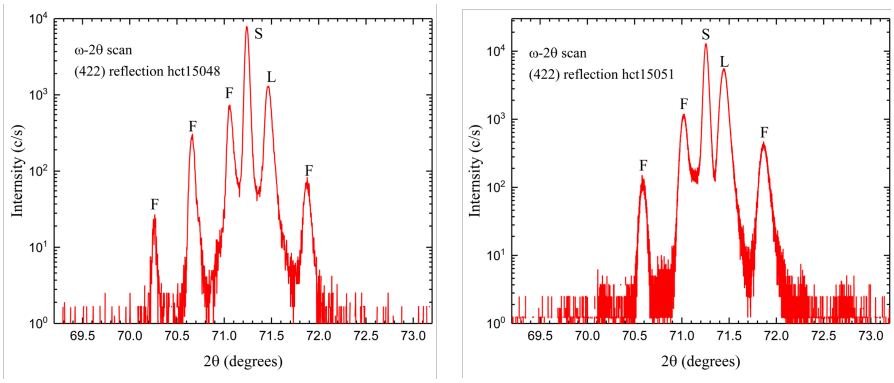

Figure 65 A ω-2θ scan of the (422) reflection of two SL samples with inverted band structure, hct15048 (left) and hc15051(right). Diffraction peaks associated with the substrate (S), superlattice (L), and satellite fringes (F) are labeled on the figure.

The superlattice pseudo x value can be calculated using Equation (4.5-4.12), and then the thickness ratio of the well and barrier layer can be extracted using Equation (4.13). The SL period d_{SL} can be calculated using Equation (4.19), taking the average value between all satellite peaks. The result is shown in Table 8. The calculated SL periods are bigger than the designed values, which agrees well with TEM data and can be explained by CdTe flux overshoot. However, the ratio of well and barrier thicknesses calculated from SL pseudo x is inaccurate. While the calculated well and barrier thicknesses of sample hct15051 meet our expectation, the calculated barrier thickness of sample hct15048 undershoots, which contradicts our previous conclusion. This inaccuracy is likely due to alignment induced error in 2θ. Another explanation is that XRD takes measurements on a tiny area on the sample, which may have irregular HgTe/CdTe layers that do not represent the whole sample.

	Calculated SL pseudo x	Calculated d_w (Å)	Calculated d_b (Å)	Calculated SL period d_{SL} (Å)
hct15048	0.105	238.9	28.0	266.9
hct15051	0.283	182.0	71.9	253.9

Table 8 Calculated pseudo x value, well thickness d_w, barrier thickness d_b and SL period d_{SL} of sample hct15048 and hct15051 from XRD ω-2θ scan.

The result of a ω-2θ scan of the (422) reflection of three SL samples with normal band structure is shown in Figure 66. Both of these samples have diffraction peaks associated with the substrate (S), superlattice (L), HgCdTe cap layer (C), and satellite fringes (F). For all three samples, the superlattice layer was grown on a $Hg_{0.53}Cd_{0.47}Te$ SWIR buffer layer, about 0.5 µm thick. And a 0.5µm $Hg_{0.68}Cd_{0.32}Te$ cap layer is grown right after the superlattice layer is done. The $Hg_{0.53}Cd_{0.47}Te$ SWIR buffer layer has a composition too close to the superlattice pseudo x, which is about 0.49~0.5. Hence a peak corresponding to the buffer layer is not observed. A peak associated with the $Hg_{0.68}Cd_{0.32}Te$ cap layer can be seen for the two samples grown on CdTe on Si substrate, though it is more obvious for sample SL_CdTe/Si_2 than SL_CdTe/Si_1. The peak associated with the HgCdTe cap layer for sample SL_CZT is merged into the substrate peak because the CdZnTe is lattice matched to low composition HgCdTe.

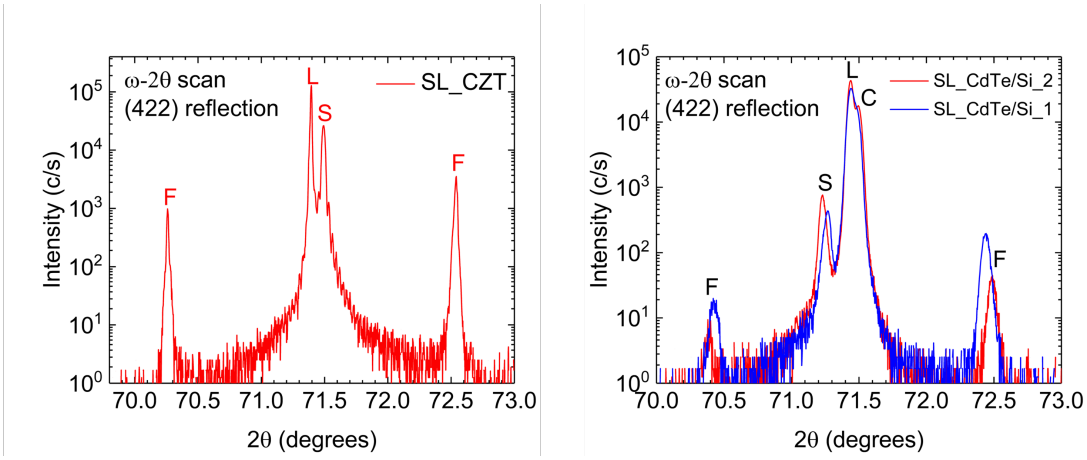

Figure 66 ω-2θ scan of the (422) reflection of sample SL_CZT (left), sample SL_CdTe/Si_1 and SL_CdTe/Si_2 (right). Diffraction peaks associated with the substrate (S), superlattice (L), HgCdTe cap layer (C), and satellite fringes (F) are labeled on the figure.

The substrate peak is on different sides of the SL main peak for samples grown on different substrates. CdZnTe substrates are usually lattice matched to low composition HgCdTe, so the substrate's peak is on the right side of the SL main peak. For all three samples, the

substrate peak has a smaller intensity compared to the SL main peak. It is likely due to the total layer thickness is comparable to the x-ray extinction depth, so the substrate peak starts to disappear. This also explains why SL_CZT has a relatively higher substrate peak than the other two samples because the designed thickness of SL_CZT is 0.2~0.6 μm thinner. Directly comparing SL_CdTe/Si_1 and SL_CdTe/Si_2, SL_CdTe/Si_1 has a lower substrate peak because it has a thicker SL layer.

The SL period d_{SL} can be calculated using Equation (4.19), taking the average value between all satellite peaks and the main SL peak. The calculated SL period d_{SL}, along with the designed layer thicknesses are given in Table 9. It can be seen that the calculated d_{SL} of all three samples are close to the designed values, indicating reasonable growth rate control. We do not see a similar growth rate overshoot issue of the samples in Table 8.

	Designed d_w (Å)	Designed d_b (Å)	Designed d_{SL} (Å)	Calculated d_{SL} (Å)	FWHM (arcsec)
SL_CZT	50	50	100	97.92	30.9
SL_CdTe/Si_1	52	54	106	107.76	157.4
SL_CdTe/Si_2	50	52	102	103.31	158.0

Table 9 The designed and calculated thicknesses, along with FWHM of the peak associated with superlattice of the three selected samples for XRD measurement

The last column in Table 9 is the full width at half maximum (FWHM) of the main SL peaks. FWHM has long been a widely quoted metric of crystal quality. Generally speaking, the HgCdTe based samples grown on CdZnTe have a higher quality than those grown on CdTe/Si. The substrate directly limits the quality of the sample. It is meaningful to compare the FWHM of the SL peak to the FWHM of the substrate peak. The result is shown in Table 10. For sample SL_CZT, because the peak associated with the HgCdTe cap is merged into the substrate peak, the substrate peak is broadened; hence it is meaningless to compare the FWHM of substrate peak and SL peak. For the two samples grown on CdTe/Si, we see a reasonable low increase of FWHM from the substrate to the SL layer, indicating quality single crystal growth.

	Substrate Peak FWHM (arcsec)	SL Peak FWHM (arcsec)	Increased %
SL_CZT	92.6	30.9	N/A
SL_CdTe/Si_1	132.4	157.4	18.9%
SL_CdTe/Si_2	136.6	158.0	15.7%

Table 10 A comparison between the substrate peak FWHM and SL Peak FWHM of the selected three samples.

5 ABSORPTION STUDY

5.1 Absorption and Absorption Coefficient

One cannot talk about infrared photodetectors without mentioning photon absorption. The study of the optical absorption behavior is vitally important to the design and characterization of infrared detectors. It is also key to understanding the optical properties and the band structure of infrared materials.

As mentioned in section 1.1.3, photodetectors are based on the conversion of photons of light directly into free current carriers. Electrons are photo-excited across the energy gap from the valence band to the conduction band, only when an incident photon has energy larger than the energy gap E_g is absorbed:

$$E_{photon} = \frac{hc}{\lambda} > E_g \tag{5.1}$$

The absorption coefficient represents how far into a material that light of a particular wavelength can penetrate before it is fully absorbed. Assume the initial intensity of the incident light is I_0, then the light intensity I as a function of depth x into the material is:

$$I(x) = I_0(1 - R)\exp(-\alpha x) \tag{5.2}$$

where R is the reflection at the material surface and α is the absorption coefficient. The absorption coefficient depends on the material properties and also on the wavelength of light that is under consideration.

From Equation (5.2), we can see that the bigger the x value, i.e., the thicker the material, the bigger portion of the light is absorbed into the material. However, in reality, thicker material means more cost, and high-quality layers are more difficult to make. Hence infrared materials with high absorption coefficient are favored because similar absorption performance can be achieved with thinner materials. II-VI materials have high absorption coefficients due to their direct bandgap absorption. This is one of the most significant advantages of HgCdTe as an infrared material. The rule of thumb of how thick the HgCdTe material should be to absorb most of the infrared light is, the thickness of the layer should roughly equal to the wavelength of the infrared light that it is designed to detect. For example, MBE-grown HgCdTe heterostructures designed for the MWIR region ($\lambda = 3{\sim}5$ μm) usually have an absorber thickness of 5 μm. However, when this rule of thumb is applied to the VLWIR region, a high-quality HgCdTe absorber that is thicker than 15μm embedding in a complex device structure is needed and is almost impractical to achieve. T3SL, on the other hand, has an even higher absorption coefficient onset than HgCdTe, due to its large density of state near the band edge. This can be seen from the modeling result of electric band structures in chapter 2.

The inter-subband absorption behavior of HgTe/CdTe superlattices was first predicted by Schulman and McGill [11] when they proposed HgTe/CdTe superlattices as new infrared material. Now we are capable of producing high-quality MBE-grown superlattices; with the help of the sophisticated 14-band k·p method to model the electric band structures, we can have a detailed and meaningful discussion on the absorption behavior of HgTe/CdTe superlattices. The superlattice samples' absorption is extracted from the transmission measurements performed with Fourier-transform Infrared Spectroscopy (FTIR). The absorption coefficients are calculated using a multi-thin-layer model. Then the experimental absorption coefficients are compared with

theoretical absorption coefficients obtained from the electric band structures. The temperature dependence of the transition energies is also studied.

5.2 Fourier-transform Infrared Spectroscopy

5.2.1 Overview

Fourier-transform Infrared Spectroscopy (FTIR) is a technique that is used to obtain the transmission, reflection, or absorption infrared spectrum of a sample. In our application, we use FTIR measurement to obtain the transmission spectrum of II-VI infrared materials.

Compared to dispersive spectroscopy, where a selection of monochromatic light beam interacts with the sample one by one, FTIR collects high spectral resolution data over a wide spectral range. A beam of light containing many frequencies shines at the sample, then the transmission of the sample is measured. Next, another beam of light containing a different combination of frequencies interacts with the sample, giving a second data point. This process repeats over and over again in a short period of time, so a raw dataset called interferogram is generated. The interferogram is Fourier transformed to the wavenumber domain, so now we have the transmission as a function of wavenumber. Wavenumbers $\tilde{\nu}$ has a simple relationship with the wavelength λ:

$$\tilde{\nu} = \frac{1}{\lambda} \tag{5.3}$$

Wavenumbers have a unit of cm^{-1}.

The frequency selection of FTIR is made through a setup called Michelson interferometer, which is a particular configuration of mirrors. One of the mirrors is moving, so the frequency of light is selected, owning to constructive and destructive interference. Because the mirror is moving during the FTIR measurement, the light coming out of the interferometer has a different spectrum at every moment. A schematic diagram of a FTIR Michelson interferometer is shown in Figure 67.

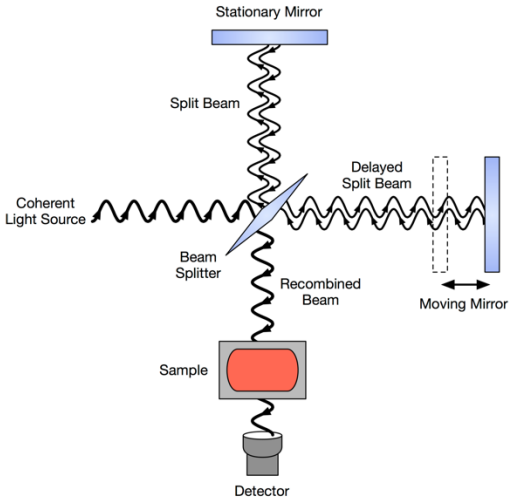

Figure 67 A schematic diagram of a Michelson interferometer configured for FTIR (https://en.wikipedia.org/wiki/Fourier-transform_infrared_spectroscopy)

5.2.2 FTIR Analysis of MCT Samples

The transmission spectrum of HgCdTe has been well studied. However, A careful investigation of the transmission behavior of HgCdTe can help us understand that of T3SL. Besides, we are going to model the transmission and compare it to the experiment data. Having a wide range of data available for HgCdTe can help us evaluate the model, then the model can be adjusted and applied to superlattices.

An example of the transmission spectrum of a HgCdTe MWIR DLPH heterostructure obtained from FTIR measurement is shown in Figure 68. The wavenumber is sampled from 400 cm^{-1} to 4000 cm^{-1}, which corresponds to a wavelength range of 2.5~25 μm. Type-III superlattices have very similar transmission spectra as HgCdTe.

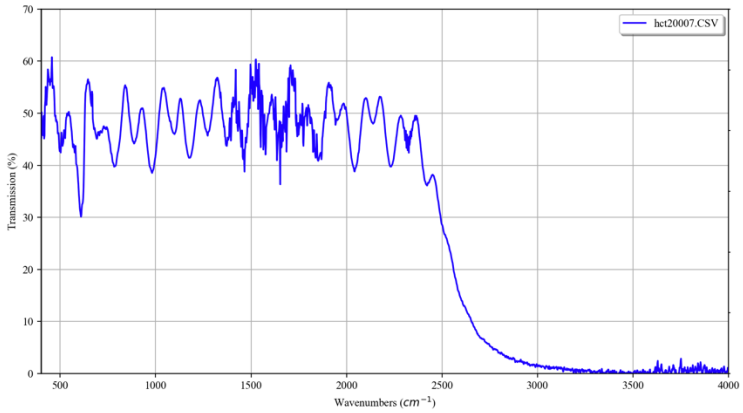

Figure 68 An example of the transmission spectrum of a HgCdTe MWIR DLPH heterostructure obtained from FTIR measurement.

The transmission curve can be interpreted as three regions.

Frist region is 400 - 2400 cm^{-1}. This region corresponds to incident light with energy less than the band gap, so the absorbing condition described in Equation (5.1) is not satisfied. The light beam will transmit through the material without any loss. Note that the maximum transmission value is not 100% without any absorption. This is because a big portion of the light is reflected at the sample surface and inside the sample. For HgCdTe based materials, the reflection is usually about 40%, making the maximum transmission in the range of 50-70%.

The second region is 2400 - 3000 cm^{-1}. This region is where the absorption starts to happen. At some point on the curve, the photon energy becomes bigger than the energy band

gap. Photons are absorbed, and electrons are excited from the valence band to the conduction band. The curve did not drop as a vertical line but rather present as an absorption cut-off edge. The reason is that the density of states is limited at the conduction band edge; as the energy increases in the conduction band, there are more states for electrons to occupy. Hence more photons can be absorbed.

The third region is 3000 - 4000 cm^{-1}. In this region, the light is almost fully absorbed by the material, so the transmission reaches 0.

There are two other things worth mentioning for region 400 - 2400 cm^{-1}. The transmission curve has a periodic wave pattern with peaks and troughs, which are called interference fringes. As the name suggested, interference fringes formed due to the interference between the transmitting and reflecting lights inside the sample. A device structure usually has more than one layer; hence there are multiple boundaries inside the sample. Various interferences can happen, and a complicated interference pattern is formed. It turns out that we can make use of these interference fringes to calculate the thicknesses of the layers because the interference conditions are directly related to the layer thicknesses. The second thing worth mentioning is the strong Si absorption peak near 600 cm^{-1} wavenumbers, which shows as a trough in the transmission curve. This character of the transmission curve can only be seen for samples grown on CdTe on Si substrates and is not observed for those grown on CdZnTe substrates.

5.2.3 FTIR Data Analysis Using Multi-Layer Thin-film Model

In this section, a multi-layer thin-film (MLTF) model is introduced. This model is extensively used for fitting FTIR transmission data, extracting layer thicknesses, and calculating absorption coefficient. The MLTF model will be first discussed in the scenario of HgCdTe heterostructures; then, we will apply what we have learned to T3SLs. The technique used to derive the absorption coefficient of T3SL based on the transmission data is discussed. The result will be given in the next section.

5.2.3.1 Theory

This section briefly covers the basic theory necessary for modeling the transmission and absorption of multi-layer thin films. A major part of this section is adapted from the book "*Thin Film Optical Filters*" by H. A. Macleod [87].

The refractive index of a material is defined as the ratio of the velocity of light in free space c to the velocity of light in the medium v. A complex refractive index N of a material can be written as:

$$N = n - ik \tag{5.4}$$

where n is the real refractive index, and k is the extinction coefficient. k is directly related to the absorption coefficient of the material by:

$$\alpha = 4\pi k/\lambda \tag{5.5}$$

The complex refractive index is always a function of wavelength λ. Electromagnetic light waves may be represented by:

$$\boldsymbol{E} = \mathcal{E} \exp\left[i\omega t - \left(\frac{2\pi N}{\lambda}\right)x + \varphi\right] \tag{5.6}$$

$$\boldsymbol{H} = \mathcal{H} \exp\left[i\omega t - \left(\frac{2\pi N}{\lambda}\right)x + \varphi'\right] \tag{5.7}$$

Where **E** is the electric field, $\mathcal{E}$ is the electric amplitude, **H** is the magnetic field, $\mathcal{H}$ is the magnetic amplitude, and φ and φ' are arbitrary phases. φ, φ' and N are not independent. The $-\left(\frac{2\pi N}{\lambda}\right)x$ term present the lost or the phase change by the wave on traversing a distance x in the media, and can be written as:

$$-\left(\frac{2\pi N}{\lambda}\right)x = -\left(\frac{2\pi n}{\lambda}\right)x + i\left(\frac{2\pi k}{\lambda}\right)x \tag{5.8}$$

The imaginary part of Equation (5.8) can be interpreted as a reduction in amplitude. We define the ratio of the magnetic and electric fields as optical admittance, which is denoted by y:

$$y = H/E \tag{5.9}$$

and y is usually a complex number. In free space, optical admittance is real and is denoted by $\mathcal{Y}$:

$$\mathcal{Y} = 2.6544 \times 10^{-3}\ \text{S.} \tag{5.10}$$

And they are connected with the refractive index by

$$y = N\mathcal{Y} \tag{5.11}$$

The irradiance of the light, defined as the mean rate of flow of energy per unit area carried by the wave, is given by

$$I = \frac{1}{2} Re(EH^*) = \frac{1}{2} n\mathcal{Y} EE^* \tag{5.12}$$

When a normal incident beam is split into a reflected beam and a transmitted beam at the boundary of two media 0 and 1, we have

$$\rho = \frac{\mathcal{E}_r}{\mathcal{E}_i} = \frac{y_0 - y_1}{y_0 + y_1} \tag{5.13}$$

$$\tau = \frac{\mathcal{E}_t}{\mathcal{E}_i} = \frac{2y_0}{y_0 + y_1} \tag{5.14}$$

where ρ and τ denote the amplitude reflection coefficient and amplitude transmission coefficient, respectively. Plug Equation (5.11) into Equation (5.13) and (5.14) gives us

$$\rho = \frac{(n_0 - n_1) - i(k_0 - k_1)}{(n_0 + n_1) - i((k_0 + k_1)} \tag{5.15}$$

$$\tau = \frac{2(n_0 - ik_0)}{(n_0 + n_1) - i((k_0 + k_1)} \tag{5.16}$$

Assume the incident medium is absorption-free, N_0 and y_0 are real, the reflection R and transmission T can be written as:

$$R = \rho\rho^* = \left(\frac{y_0 - y_1}{y_0 + y_1}\right)\left(\frac{y_0 - y_1}{y_0 + y_1}\right)^* \tag{5.17}$$

$$T = \frac{4y_0 Re(y_1)}{(y_0 + y_1)(y_0 + y_1)^*} \tag{5.18}$$

Up to this point, we only considered normal incidence. For oblique incidence, it is simpler to split the wave into two plane-polarized components, namely s-polarized and p-polarized. The propagation of each of these two waves can be treated independently. Introduce the idea of tilted optical admittance η, which is different for s-polarized and p-polarized waves:

$$\eta_s = N\mathcal{Y}cos\theta \tag{5.19}$$

$$\eta_p = \frac{N\mathcal{Y}}{cos\theta} \tag{5.20}$$

N and θ denote different values for different layers. For a multi thin layer structure, N and θ values satisfy Snell's law:

$$N_0 sin\theta_0 = N_1 sin\theta_1 = \cdots = N_q sin\theta_q \tag{5.21}$$

η_s and η_p in Equation (5.19) and (5.20) can be used to replace y in Equation (5.13-5.18) when s-polarized and p-polarized light is considered. However, Equation (5.13-5.18) are based on the assumption that there is only one boundary with two media 0 and 1. For an assembly of thin films, we replace the multiplayer with a single layer with an admittance Y, defined as the ratio of the total tangential magnetic and electric fields:

$$Y = C/B \tag{5.22}$$

and

$$\begin{bmatrix} B \\ C \end{bmatrix} = \left\{ \prod_{r=1}^{q} \begin{bmatrix} cos\delta_r & (isin\delta_r)/\eta_r \\ i\eta_r sin\delta_r & cos\delta_r \end{bmatrix} \right\} \begin{bmatrix} 1 \\ \eta_{q+1} \end{bmatrix} \tag{5.23}$$

where

$$\delta_r = \frac{2\pi}{\lambda} N d cos\theta \tag{5.24}$$

We define the transfer matrix of layer r as:

$$M_r = \begin{bmatrix} cos\delta_r & (isin\delta_r)/\eta_r \\ i\eta_r sin\delta_r & cos\delta_r \end{bmatrix} \tag{5.25}$$

then we have

$$\begin{bmatrix} B \\ C \end{bmatrix} = [M_1][M_2] \dots [M_q] \begin{bmatrix} 1 \\ \eta_{q+1} \end{bmatrix} \tag{5.26}$$

Note that the order of multiplication is important. Using the definition of N in Equation (5.4), and Snell's law in Equation (5.21), we can rewrite Equation (5.19) and (5.20) for multi thin layers as:

$$\eta_{0_s} = n_0 cos\theta_0 \tag{5.27}$$

$$\eta_{0_p} = \frac{n_0}{cos\theta_0} \tag{5.28}$$

$$\eta_{r_s} = \sqrt{(n_r - ik_r)^2 - {n_0}^2 sin^2\theta_0} \qquad r = 1, \dots, q \tag{5.29}$$

$$\eta_{r_p} = \frac{(n_r - ik_r)^2}{\eta_{r_s}} \qquad r = 1, \dots, q \tag{5.30}$$

Now once we have B and C, we can finally give the expression for reflection R, transmission T, and absorption A for an assembly of thin films:

$$R = \left(\frac{\eta_0 B - C}{\eta_0 B + C}\right)\left(\frac{\eta_0 B - C}{\eta_0 B + C}\right)^* \tag{5.31}$$

$$T = \frac{4\eta_0 Re(\eta_{q+1})}{(\eta_0 B + C)(\eta_0 B + C)^*} \tag{5.32}$$

$$A = \frac{4\eta_0 Re(BC^* - \eta_{q+1})}{(\eta_0 B + C)(\eta_0 B + C)^*} \tag{5.33}$$

And R, T, and A satisfy

$$R + T + A = 1 \tag{5.34}$$

Note that the complex refraction index $N = n - ik$ is a function of wavelength λ. As a result, reflection R, transmission T, and absorption A are all wavelength dependent.

n and k values of T3SLs are not widely available, especially considering the design degrees of freedom of superlattices. For HgTe/CdTe superlattices, we treat the whole SL layer as

a single $Hg_{1-x}Cd_xTe$ bulk layer with a pseudo composition x so that the cutoff wavelength is comparable to $Hg_{1-x}Cd_xTe$ with the same x. Note that this is fundamentally different from what we did in Equation (4.13), where the pseudo composition x is given by thickness-weighted x values of well and barrier. The reason is that the method used in Equation (4.13) is for XRD measurement, where the physical lattice constant is needed. Here we care about SL's optical characteristics, so the cutoff wavelength is used as the standard to pick x.

Many results have been published on the refractive index measurements of HgCdTe [88]–[91]. The refractive index of HgCdTe is a function of composition x, temperature T, and wavelength λ. An empirical formula can describe the dispersion of the refractive index:

$$n(\lambda,T)^2 = A + \frac{B}{\left[1-\left(\frac{C}{\lambda}\right)^2\right]} + D\lambda^2 \tag{5.35}$$

where A, B, C, and D are fitting parameters, and they vary with x and T:

$$A = 13.173 - 9.852x + 2.909x^2 + 10^{-3}(300 - T)$$

$$B = 0.83 - 0.246x - 0.0961x^2 + 8 \times 10^{-4}(300 - T)$$

$$C = 6.706 - 14.437x + 8.531x^2 + 7 \times 10^{-4}(300 - T)$$

$$D = 1.953 \times 10^{-4} - 0.00128x + 1.853 \times 10^{-4}x^2 \tag{5.36}$$

5.2.3.2 Fitting transmission data using MLTF model

Now let us discuss more on the transmission spectrum in Figure 68. For the first region (400 - 2400 cm^{-1}), there is almost no absorption, so the absorption coefficient is a negligible value. Based on Equation (5.5), extinction coefficient k is also negligible. With n given by Equation (5.35), the transmission spectrum can be calculated from Equation (5.32). Note that the optical transfer matrix (5.25) varies with the thickness of each layer. By comparing the multi-layer thin-film model calculated transmission spectrum with the experimental data obtained from FTIR, one can acquire each layer's correct thicknesses. MBE growers often use this method as a routine sample characterization method.

For the second region (2400 - 3000 cm^{-1}), absorption happens, and the absorption coefficient is nontrivial. The extinction coefficient k has a finite value. The absorption behavior of HgCdTe has been well studied [52], [88], [89], [92]. A set of typical intrinsic absorption spectra of $Hg_{1-x}Cd_xTe$ with x=0.0030 at various temperatures is shown in Figure 69.

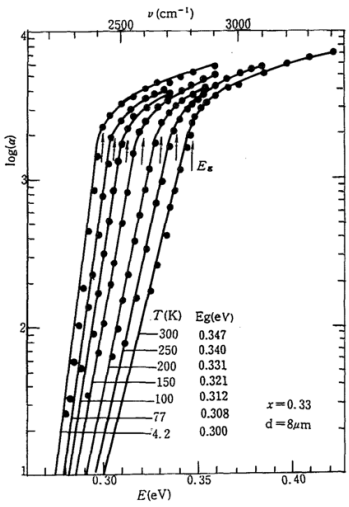

Figure 69 Typical intrinsic absorption spectra of $Hg_{1-x}Cd_xTe$ with x=0.0030 at temperatures from 4.2 to 300K [92].

The parts of absorption spectra shown in Figure 69 are called the absorption edge, where the rapid rising of absorption coefficient happens. The absorption edge can be divided into two regions with the energy band gap E_g as the middle point, namely the intrinsic region (Kane region) and the Urbach tail region. The intrinsic region majorly includes the intrinsic transitions of electrons from the valence band to the conduction band. The expression of the absorption coefficient for the intrinsic region [89] is derived from fitting to the experimental data and can be written as:

$$\alpha = \alpha_g \exp\left[\beta\left(E - E_g\right)\right]^{1/2} \tag{5.37}$$

where α_g stands for the absorption coefficient at the band gap energy E_g. β is a fitting parameter to match the experimental data. α_g, β and E_g are all functions of composition x and temperature T:

$$\alpha_g = -65 + 1.88T + (8694 - 10.31T)x \tag{5.38}$$

$$\beta = -1 + 0.083T + (21 - 0.13T)x \tag{5.39}$$

$$E_g = -0.295 + 1.87x - 0.28x^2 + (6 - 14x + 3x^2)(10^{-4})T + 0.35x^4 \tag{5.40}$$

Note that Equation (5.40) is slightly different from Equation (1.2) given by Hansen[9].

The Urbach tail, an exponential absorption edge, was first found by Urbach [93] and resulted from interactions other than intrinsic band-to-band transitions, such as impurity induced

transitions, electron-phonon, and electron-hole interactions. The empirical expression of Urbach tail can be written as:

$$\alpha = \alpha_0 \exp\left[\delta(E - E_0)/kT\right] \tag{5.41}$$

where

$$\alpha_0 = \exp(-18.5 + 48.65x) \tag{5.42}$$

$$E_0 = -0.355 + 1.77x \tag{5.43}$$

$$\delta/kT = (ln a_g - ln\alpha_0)/(E_g - E_0) \tag{5.44}$$

A more precise empirical expression for the HgCdTe absorption edge can be found in the paper by Chang [49].

The turning point where the Urbach tail and the Kane plateau region meet on the absorption curve can be defined as 'cutoff' energy, which corresponds to the cutoff wavelength. However, when we are doing transmission data analysis, $\alpha = 500\ \text{cm}^{-1}$ or $\alpha = 1000\ \text{cm}^{-1}$ is often used as the cutoff point on the absorption spectra for convenience.

The extinction coefficient k can now be calculated from Equation (5.5), (5.37), and (5.41). Now we have n and k values ready, the transmission spectrum for the whole 400 cm^{-1}~ 4000 cm^{-1} range can be calculated. The calculated transmission spectrum agrees with the experimental data very well and is shown in Figure 70.

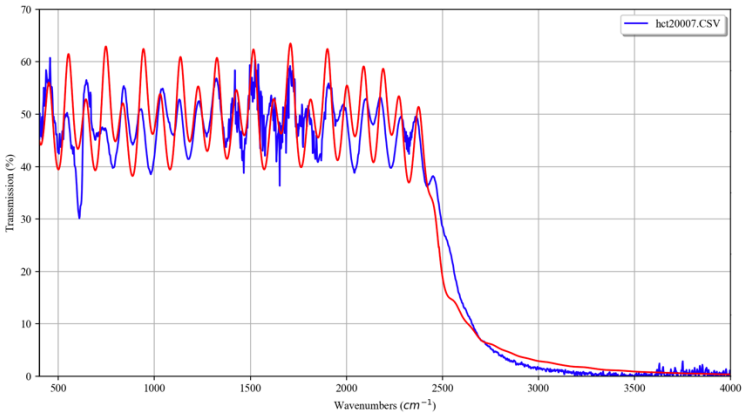

Figure 70 The experimental (blue) and fitted (red) transmission spectrum of an MBE-grown HgCdTe MWIR DPLH layer.

Fitting the whole transmission spectrum of a HgTe/CdTe superlattice is challenging because the value of k is unknown. However, we can still fit the first region of the transmission curve, where the value of k is small and negligible. The SL layer total thickness and the SL period d_{SL} can be obtained. The transmission cut-off edge gives us information on SL bandgap energy, which can then be compared to the theoretical band gap energy values given by the 14-band k·p method. We can get the HgTe well thickness d_w in this way. And the CdTe barrier thickness d_b can be acquired by subtracting the well thickness from the d_{SL}.

5.2.3.3 Calculating Absorption Coefficient of T3SL using MLTF model

The absorption coefficient α of T3SLs can be calculated from the FTIR transmission data using the MLTF model. As we mentioned in section 5.2.3.2, transmission can be calculated using Equation (5.32) if n, k and thicknesses of the layers are known. The only thing that we do not know is k. Hence, we can use a recursion method to find k. We fix the value of λ, and then we recursively pick values of k and calculate the transmission based on Equation (5.32). The calculated transmission is compared to the experimental data. A new k value is picked, and the

calculation is repeated until the difference between the calculated transmission and the experimental transmission data is within a certain level of tolerance. Then we move to the next λ value and repeat the recursion process again. When the calculation is all done, we have k as a function of wavelength λ. With some help from Equation (5.5), we can obtain the absorption spectrum of T3SLs.

Note that there are a few necessary conditions to meet to calculate the absorption coefficients of T3SLs. First, the thicknesses of all layers are required so the MLTF model can be used. Second, for all T3SL samples under consideration here, we can only have one layer with unknown k values, the SL layer. Both conditions are met in our case because layers other than the SL layer are either HgCdTe or CdTe, which have known n and k values given in Equation (5.35), (5.37), and (5.41).

5.3 Absorption Behavior of T3SL

The transmission and the absorption coefficient of two HgTe/CdTe superlattice samples as a function of wavenumber at room temperature are shown in Figure 71. The two samples are inverted and normal band structure T3SLs separately. Sample hct15055 on the left was designed to have 200 periods consists of 67 Å HgTe well and 44 Å CdTe barrier. Sample SL_CZT on the right has 500 periods, and each period is made up of 50 Å HgTe/50 Å CdTe. The solid blue lines on both graphs are the transmission spectra measured by FTIR. The solid red lines are the absorption coefficient calculated from the MLTF model using the method described in 5.2.3.3. The dashed red lines represent the absorption coefficient computed using the density of states near the band edges, calculated from the 14-band k·p method. The theoretically modeled

absorption coefficient is used along with the MLTF model to calculate the theoretical transmission shown as the dashed blue line. The transmission and the absorption coefficient measured from FTIR agrees reasonably well with the theoretical modeling result. The two major transition peaks on the absorption curve, namely HH1-C1 and LH1-C1, are marked in the figure.

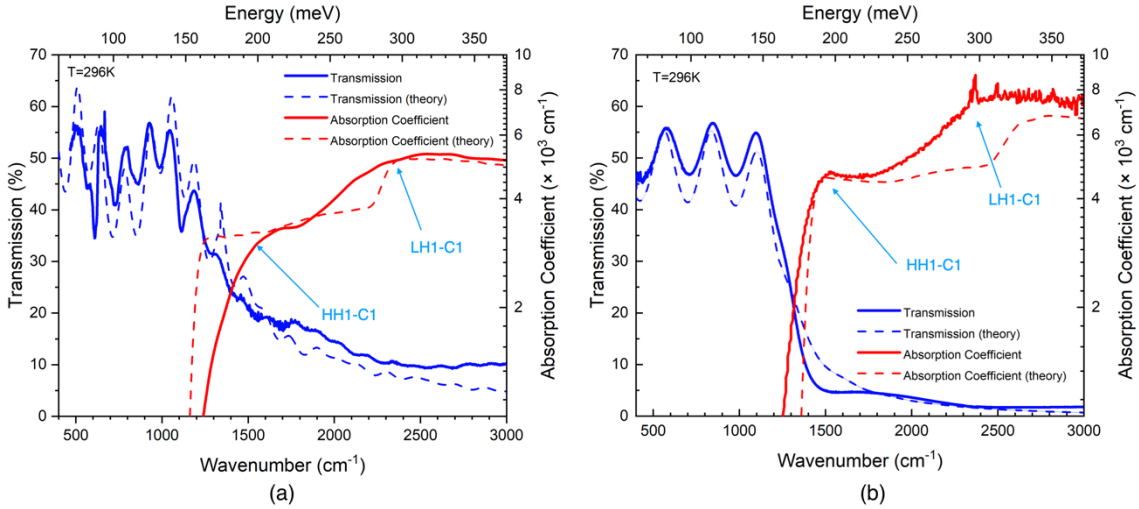

Figure 71 The transmission and the absorption coefficient of two HgTe/CdTe superlattice samples as a function of wavenumber at room temperature. The two samples are (a)sample hct15055 with inverted band structure, 200 periods of 67 Å HgTe/44 Å CdTe (b)sample SL_CZT with normal band structure, 500 periods of 50 Å HgTe/50 Å CdTe. The transmission (solid blue line), the absorption (solid red line), the theoretical transmission (dashed blue line), and the theoretical absorption (dashed red line) are shown.

The two samples have a similar cutoff wavelength, which is around 8 μm at room temperature. We noticed that the sample SL_CZT with normal band structure has a sharper and higher absorption onset than sample hct15055 with an inverted band structure. It is noticeable that sample hct15055 has a soft transmission edge. The transmission value never becomes close to zero even at high wavenumbers, which results from relatively thin layer thickness providing insufficient absorption. The influence of layer thickness on transmission edge is verified by growing a layer SL_CdTe/Si_0, which has the same well/barrier thicknesses as SL_CdTe/Si_1, but with only 150 periods instead of 500 periods. The transmission spectra of the two samples

are shown in Figure 72. The two samples were both designed to have 52 Å HgTe well and 54 Å CdTe barrier, with a normal band structure. The designed total thickness of SL_CdTe/Si_0 is 1.5 μm, while that of SL_CdTe/Si_1 is 5.3 μm. It can be observed that the transmission curve of sample SL_CdTe/Si_0 is less steep. It is worth mentioning that the absorption coefficient depends on the material band structure and is independent of layer thickness. As a result, the absorption coefficient spectra of sample SL_CdTe/Si_0 and SL_CdTe/Si_1 should be very close, which can be proved by computing the absorption coefficients using the MLTF model.

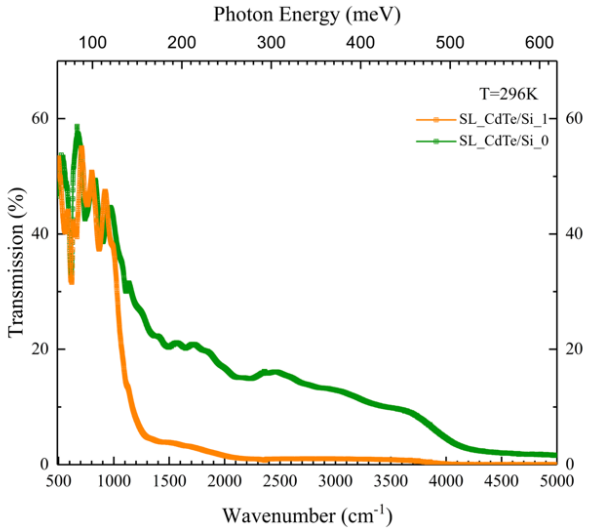

Figure 72 The transmission spectra of two HgTe/CdTe superlattice samples SL_CdTe/Si_0 (green) and SL_CdTe/Si_1 (orange) as a function of wavenumber at room temperature. The two samples were both designed to have 52 Å HgTe well and 54 Å CdTe barrier.The difference is that SL_CdTe/Si_0 has 150 periods while SL_CdTe/Si_1 has 500 periods.

As we have mentioned in chapter 1, inverted band structure HgTe/CdTe superlattices were once thought to be great IR absorbers, considering their great bandgap control at larger HgTe well thickness. However, the H2-H1 electric gap precludes the use of them as an infrared photodetector. As a result, we will focus on using normal band structure superlattices ($d_w < d_c = 6.3\ nm$) for VLWIR applications. Three samples are taken under consideration,

namely SL_CZT, SL_CdTe/Si_1 and SL_CdTe/Si_2. The details of their structures are given in Table 5.

The room temperature transmission spectra of the three samples as a function of wavenumber and photon energy are shown in Figure 73. A sharp absorption edge can be seen for all three samples, and two prominent absorption stages corresponding to HH1-C1 and LH1-C1 transitions are observed and labeled on the full spectral range graph. A sharp absorption peak associated with Si is labeled on the "Zoom in for the 1st transition" graph. We do not see this peak on sample SL_CZT, which is grown on CdZnTe. This proves that this absorption character is associated with Si substrates. The interference fringes of sample SL_CZT are clearly different from those of sample SL_CdTe/Si_1 and SL_CdTe/Si_2 because the structure and thicknesses of the substrates are quite different. Also, note that sample SL_CdTe/Si_1 has a cutoff at longer wavelength/lower energy compared to SL_CZT and SL_CdTe/Si_2, because it is designed to have a thicker HgTe well thickness; hence the bandgap energy is smaller.

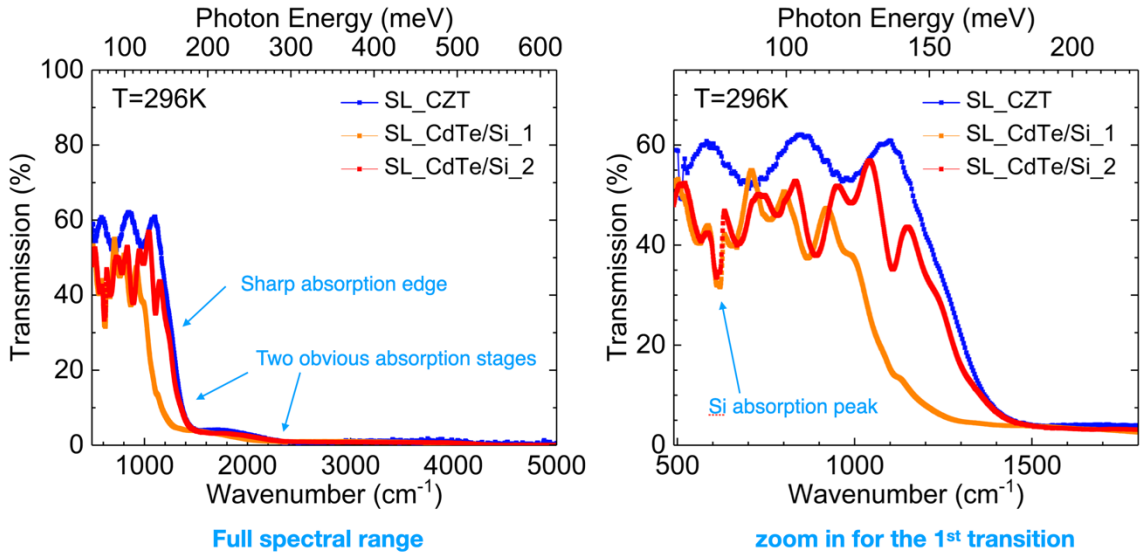

Figure 73 The room temperature transmission spectra of SL_CZT (blue), SL_CdTe/Si_1(orange) and SL_CdTe/Si_2 (red) as a function of wavenumber and photon energy. The sharp absorption

edge, two obvious absorption stages are labeled on the full spectral range graph (left). The absorption peak associated with Si is labeled on the "Zoom in for the 1st transition" graph(right).

It is worth comparing the absorption coefficients of SL_CZT and SL_CdTe/Si_2, considering they have almost identical designs, similar band gap and cutoff wavelength, and grown on different substrates. The calculated absorption coefficients are shown in Figure 74. Sample SL_CdTe/Si_2 has a stronger absorption onset than SL_CZT, even though SL_CZT has a higher crystal quality provided the XRD data given in Table 9. This is likely due to the slightly thicker CdTe barrier in SL_CdTe/Si_2 results in a higher density of states at the band edge. Note that a drop-down in absorption coefficient after the sharp absorption edge for both samples is observed and is most likely due to the high joint density of states at the transition edge.

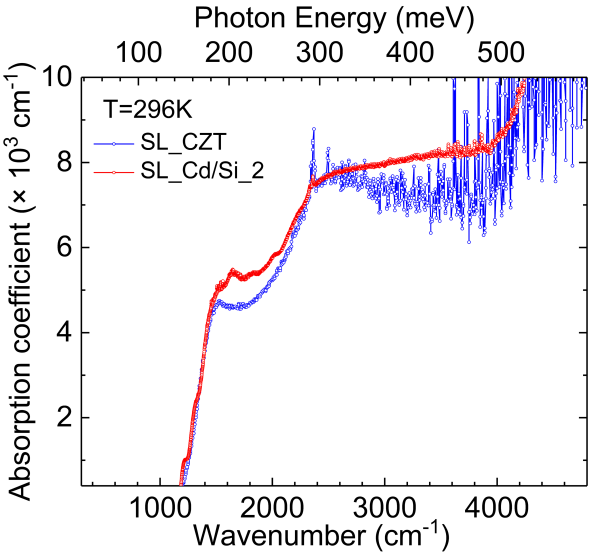

Figure 74 The calculated absorption coefficients of SL_CZT (blue) and SL_CdTe/Si_2 (red).

5.4 Temperature-dependent Absorption Study of T3SL

Temperature-dependent transmission measurements were performed on an FTIR spectrometer with a continuous-flow liquid helium cryostat, which ensures a uniform and stable

temperature distribution in the T3SL sample over a wide temperature range. The temperature-dependent transmission curves of sample SL_CZT is shown in Figure 75. A sharp absorption edge is observed at all temperatures. The transmission cut-off edge shifts to a smaller wavelength at a lower temperature due to the unusual positive temperature-dependent band gap of HgTe [94]. The cutoff wavelength can be roughly calculated taking 50% of maximum transmission. At 40 K, the 50% of the maximum transmission is at 613 cm-1, which corresponding to 76 meV in energy and 16 μm in wavelength.

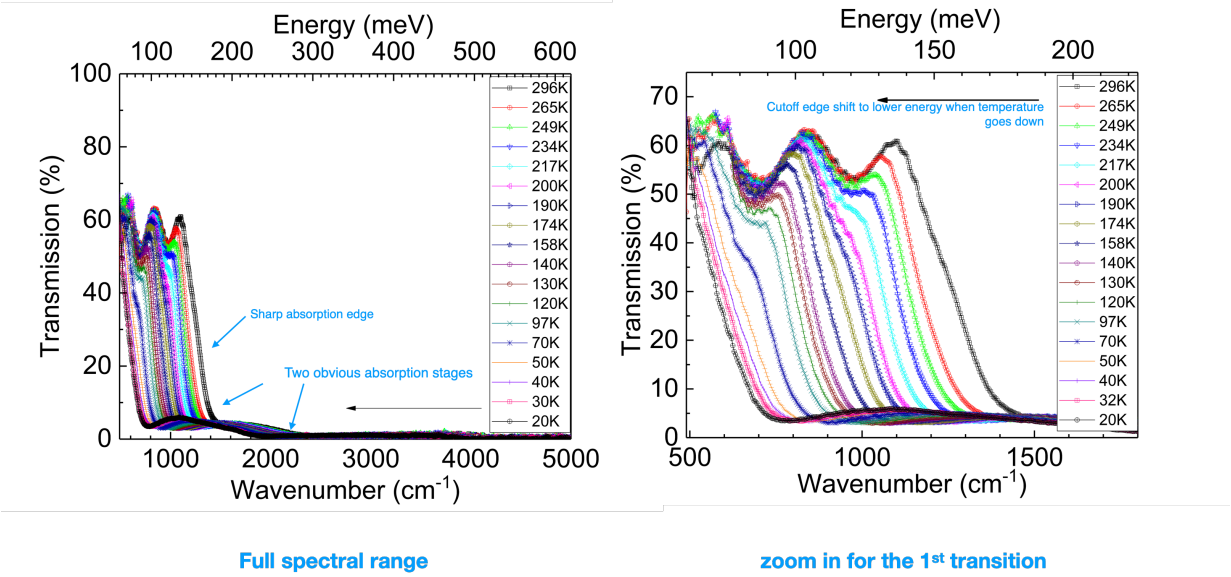

Figure 75 20 to 296 K transmission curves of a 50Å HgTe/50Å CdTe HgTe/CdTe superlattice sample measured using FTIR. At 40 K, 50% of the maximum transmission is at 613 cm-1, which corresponds to 76 meV in energy and 16 μm in wavelength.

Absorption coefficients α were then extracted employing the MLTF model and plotted as a function of infrared photon wavenumber in Figure 76. The absorption cutoff onset shifts to higher wavenumbers, i.e., higher energy and lower cutoff wavelength, as the temperature increases. The two major transition peaks on the absorption curve, namely HH1-C1 and LH1-C1 are marked in the figure. As we mentioned in 5.2.3.2, $\alpha = 500\ \mathrm{cm}^{-1}$ or $\alpha = 1000\ \mathrm{cm}^{-1}$ is often

used as the cutoff point on the absorption spectra when we are doing transmission data analysis. At 40 K, the cut-off defined using the 500 cm-1 absorption coefficient is 555 cm-1 (68.76 meV and 18 μm). If we define the cut-off using the 1000 cm-1 absorption coefficient, the cut-off at 40 K is 617 cm-1 (76.4 meV and 16.2 μm).

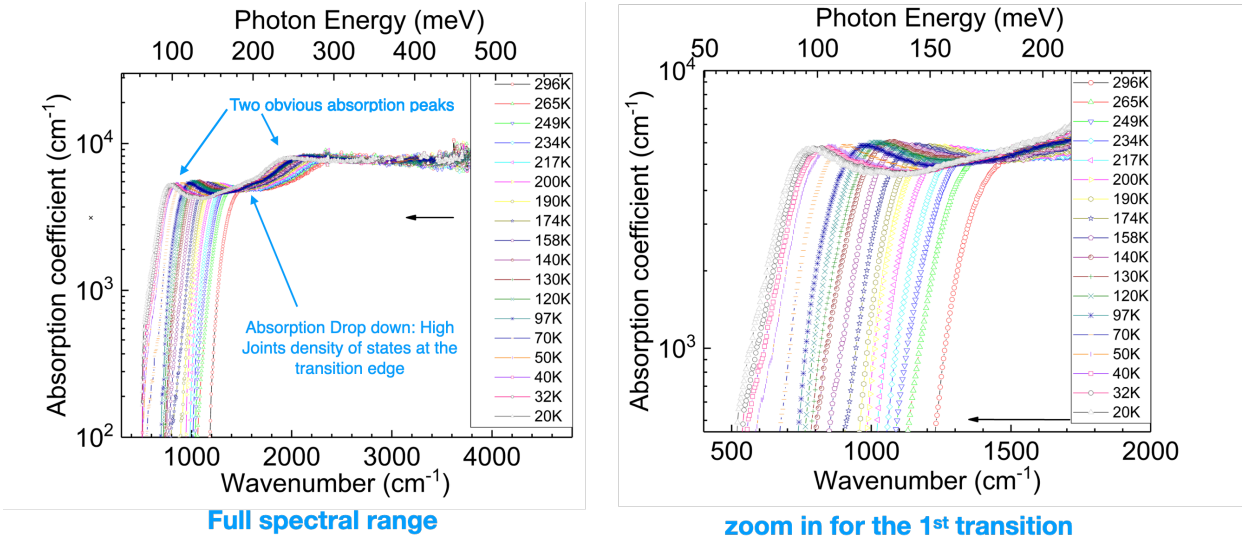

Figure 76 20 to 296 K temperature-dependent absorption coefficients extracted from transmission measurements of sample SL_CZT. They are plotted as a function of infrared photon wavenumbers and energies.

The experimentally extracted absorption coefficients are compared with theoretical results at various doping levels in Figure 77. 40K and 300K are selected to represent the full temperature-dependent absorption spectra. The theory agrees reasonably well with experiments at various temperatures. Three theoretical curves of different doping levels, namely intrinsic (non-doped), 5×10^{14} n-type doping and 1×10^{16} n-type doping, are plotted. The fact that the theoretical curves do not change much for different doping levels indicates the Burstein-Moss shifts are small in the T3SLs due to the high density of states near the band edge.

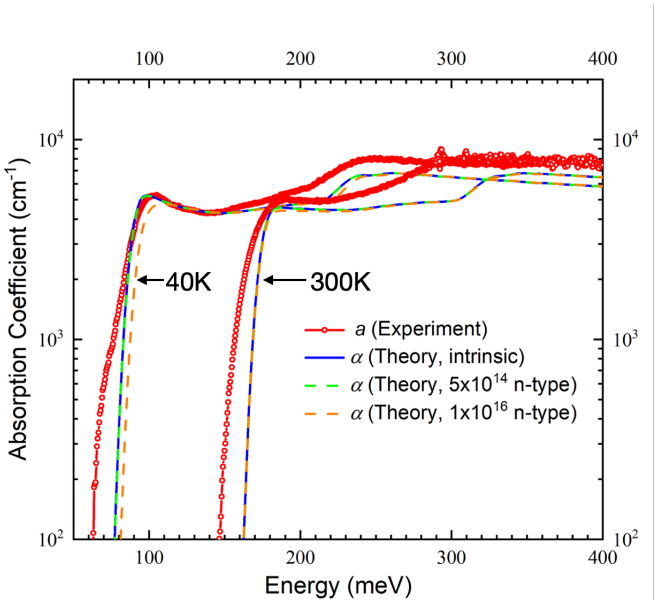

Figure 77 The experimentally extracted absorption coefficients of sample SL_CZT compared with theoretical predictions at three doping levels, at two temperatures, 40K and 296K (indicated by arrows in the figure).

To compare the absorption characteristic of T3SL with other state-of-the-art infrared materials, we plotted the absorption spectrum of SL_CZT along with the calculated absorption spectrum of a HgCdTe alloy with a similar cut-off at 40K from two well-known sources, one is Chu[89], and the other one is Schacham and Finkman [88], [95]. The result is shown in Figure 78. It can be seen that T3SL has a sharp absorption onset, and it is 2~4 times higher than that of HgCdTe given by Chu (notice that Figure 78 is using log scale on the y axis). This is again due to T3SL's high joint density of state at the band edge, which can be justified by comparing the band structure of HgCdTe (Figure 16) and T3SL (Figure 17) modeled by the 14-band k·p method in chapter 2. Similar result has been demonstrated by C. Becker [17]. Comparing our T3SL absorption coefficients with Schacham and Finkman's result, it seems that T3SL has higher absorption coefficients only at the band edge. However, Schacham and Finkman's empirical Equation of the absorption coefficients [95] at the intrinsic absorption region has an unrealistic negative temperature dependency, where the absorption coefficients are overestimated

at low temperatures. Hence, here we draw our comparison conclusion using Chu's absorption curve.

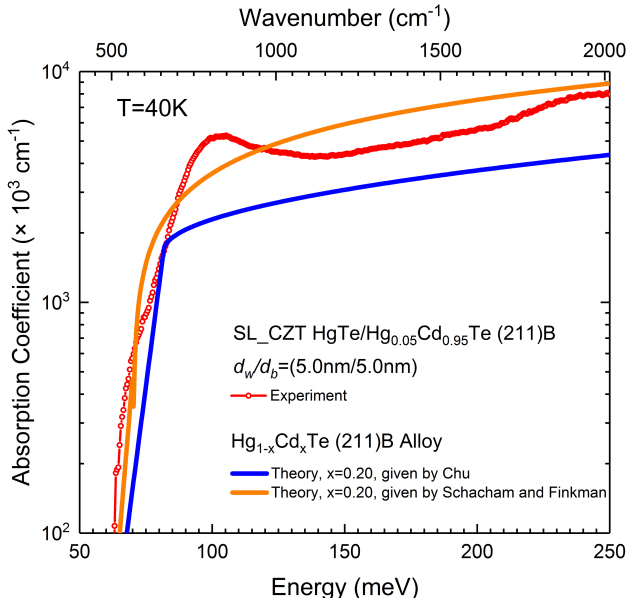

Figure 78 Comparing the measured absorption coefficient of sample SL_CZT with the calculated absorption spectrum of a HgCdTe alloy with a similar cut-off at 40K.

The absorption characteristic of T3SL shown in Figure 77 can also be compared to that of T2SL with similar cutoff in the VLWIR region (Figure 79) which is given by G. Brown et al. [23]. T3SL shows sharper absorption onset and more than two times bigger absorption coefficients at and near the cutoff edge, due to the electrons and holes confining in the same layer in a Type-III band alignment. This the most important advantage of T3SL as a VLWIR absorber.

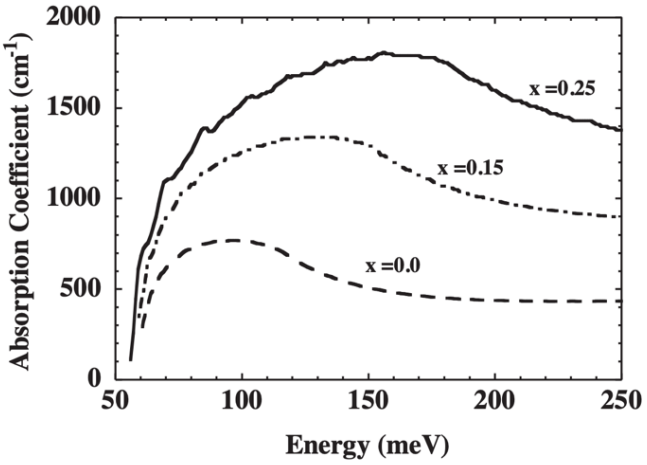

Figure 79 The calculated absorption spectra for InAs/$In_xGa_{1-x}Sb$ SLs with various indium content.

5.5 Determination of T3SL Interband Transition Energies

Other than the $\alpha = 500\ \text{cm}^{-1}$ or $\alpha = 1000\ \text{cm}^{-1}$ method that we used to determine the cutoff point on the absorption spectra when we are doing transmission data analysis, there are several other techniques to calculate the interband transition energies like E_{H1-E1} (HH1-C1) and E_{L1-E1} (LH1-C1). One obvious technique is to use the maxima of the first derivative of the absorption spectra as the interband transition energies. This method is based on the fact that SLs have a high density of states right at the band edge. The second method is based on the fact that the difference between two transmittance spectra measured at slightly different temperatures is proportional to the change in the absorption coefficient [96]:

$$\frac{\Delta \mathbf{T}}{\mathbf{T}} = \frac{\mathbf{T}_2}{\mathbf{T}_1} - 1 \approx d\Delta\alpha \tag{5.45}$$

where d is the sample thickness, and **T** is the transmission.

Here we take the 40K transmission data of sample SL_CZT as an example. Temperature $\mathbf{T}_1$ and $\mathbf{T}_2$ in Equation (5.45) are taken as 20K and 60K, respectively. The absorption coefficient extracted from the transmission spectrum and its first derivative, the theoretically calculated absorption coefficient and its first derivative, the ratio of transmission at 60K and 20K are shown in Figure 80. The two major peaks shown in the first derivatives and the transmission ratio curve are fitted using the Gaussian function. The Physics meaning of the two peaks is marked with arrows. The first major peak corresponds to the E_{H1-E1} transition, with calculated transition energy of 88 meV. The second peak, which has a lower height, corresponds to the E_{L1-E1} transition with transition energy of 222meV.

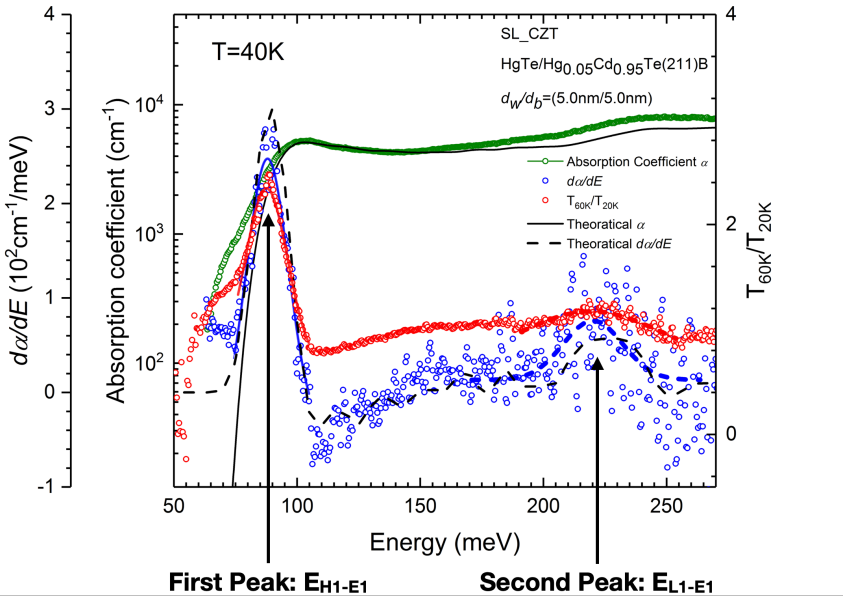

Figure 80 The absorption coefficient extracted from transmission spectrum(solid green line) and its first derivative(blue circles), the theoretically calculated absorption coefficient(solid black line) and its first derivative (dashed black line), the ratio of transmission at 60K and 20K (red circles) are shown in Figure 84. The two major peaks shown in the first derivatives and the transmission ratio curve are fitted using the Gaussian function. The Physics meaning of the two peaks is marked with arrows.

We repeated our calculation for all the transmission spectra at all temperatures. The result is shown in Figure 81. The transition energies change linearly with temperature. It can be seen that both E_{H1-E1} and E_{L1-E1} increases with temperature due to the positive temperature dependence of HgTe.

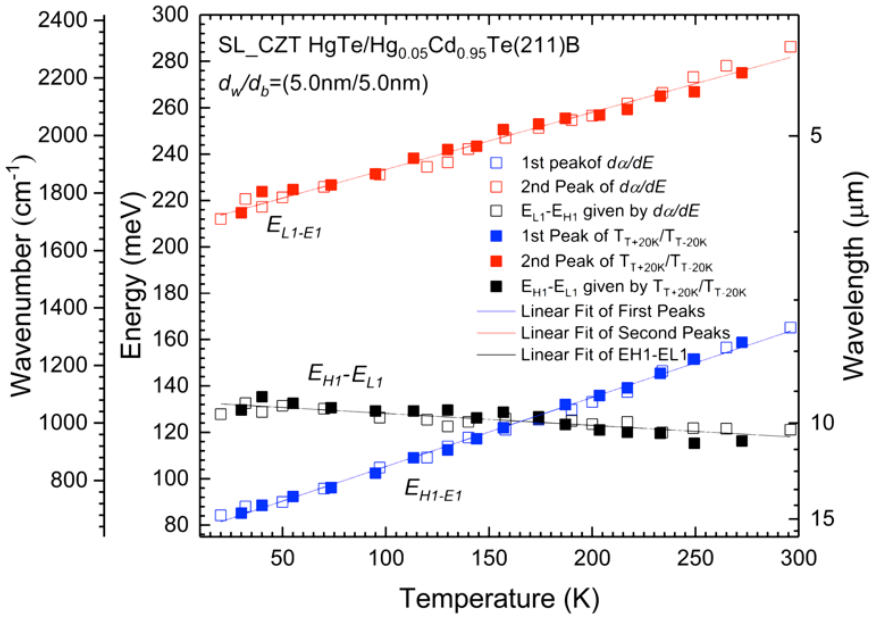

Figure 81 Experimental HH1-C1 and LH1-C1 intersubband transition energies and their difference (H1-L1) are plotted as a function of temperature. Two methods are used to determine these energies, namely dα/dE (empty squares) and the transmission ratio (filled squares).

A detailed comparison of the first transition energy, i.e., the "cutoff" energy, computed using a different method as a function of temperature is shown in Figure 82. The HgTe/CdTe superlattice's first transition energy is also compared to that of HgCdTe with similar cutoff wavelengths. It can be observed that HgTe/CdTe superlattices and HgCdTe alloys have similar temperature dependence on transition energies. This conclusion can be used to estimate the transition energy of any HgTe/CdTe superlattice at low temperatures without taking low-temperature FTIR measurement, which is a beneficial technique for MBE growers to determine the layer structures quickly.

However, the reason of HgTe/CdTe superlattices have the same temperature dependence as HgCdTe with similar bandgap energy is unknown. It has been previous reported that the bandgap energy is reduced (increased) due to intra (inter)-band transitions [94], and the energy is also affected by the temperature-dependent dilatation of the lattice and electron lattice interaction [97]. “The intra-valence (-conduction) band interactions push the valence (conduction) band edge up (down), thus reducing the gap; Similarly, the valence-conduction band interactions increase the gap. Hence, one might expect the gap to increase in small-gap semiconductors” [94]. HgTe/CdTe superlattices and HgCdTe consists of the same substances, namely HgTe and CdTe, but their band structure is fundamentally different. Compared to HgCdTe with similar bandgap energies, HgTe/CdTe superlattices have much bigger valence band effective mass and surprising smaller conduction band effective mass based on our 14-band k·p modeling result. It is difficult to compare the intraband and interband interactions in HgTe/CdTe superlattices to that of HgCdTe directly. Further inspection needs to be done to reveal the reason behind HgTe/CdTe superlattices’ bandgap energy temperature dependence.

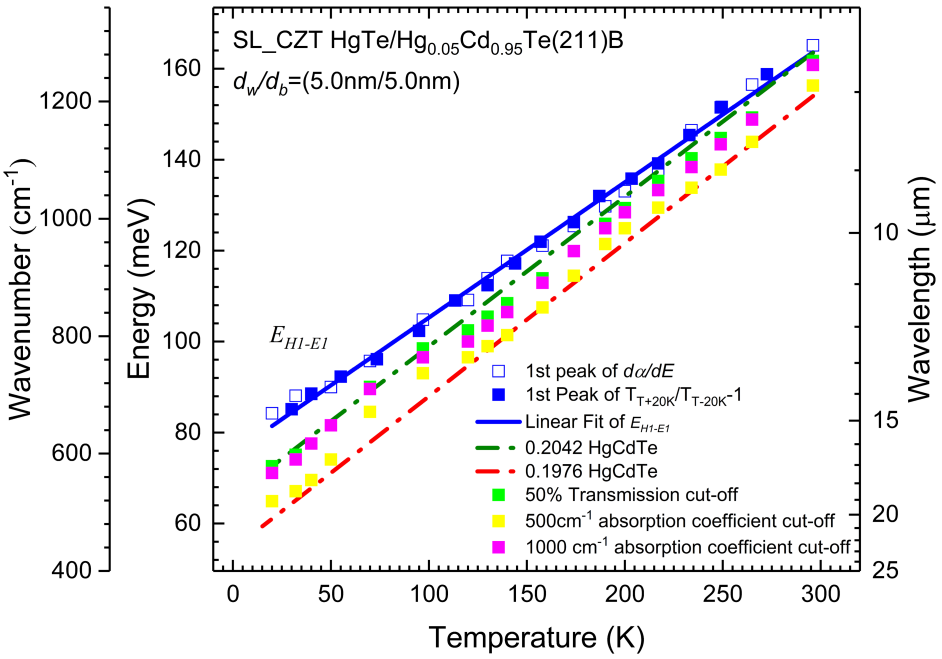

Figure 82 The first transition energy of sample SL_CZT as a function of temperature computed using dα/dE (empty blue square), the ratio of transmission (solid blue square), 50% transmission cut-off (green square), 500cm^{-1} absorption coefficient cutoff (yellow square) and 1000cm^{-1} absorption coefficient cutoff (pink square). The first transition energy of two HgCdTe alloys with similar cutoff wavelength as a function of temperature is also shown (green and red dashed line).

6 SUMMARY AND ISSUES WITH T3SL

6.1 Summary

In Part I of this thesis, we focused on designing, modeling, growth, and characterizing Type-III superlattices.

The lack of high-performance intrinsic photodetectors working in the VLWIR region motivates us to find the best candidate for VLWIR absorption. Type III Superlattice has many advantages over HgCdTe alloy, namely longer Auger lifetime, lower tunneling currents, sharper absorption onset, and more uniform and easier-to-control cutoff wavelength, especially in the VLWIR region. T3SL has many advantages over T2SL, namely stronger absorption coefficient, tunable band gap energy in a wider range, and longer Shockley-Read-Hall lifetimes.

The band structures of HgTe/CdTe superlattices can be engineered utilizing various well/barrier thicknesses and were calculated using semi-empirical 14-band k·p method. The absorption spectra calculated using the band structures given by 14-band k·p method shows good agreement with the experiment data.

HgTe/CdTe superlattices with both normal and inverted band structure were grown using Molecular Beam Epitaxy (MBE). Growth condition controlling techniques are discussed and a newly designed Hg cell was built in house to provide stable and reliable Hg flux. RHEED and Ellipsometry shows good sample quality and well-controlled growth condition.

Ex-situ characterization like Nomarski Microscope provides information about the sample surface and the sample's overall quality. SEM and TEM are used to observe the cross-section of superlattices. While SEM failed to reveal the superlattice periods, TEM shows sharp

HgTe/CdTe interfaces, and the thicknesses are extracted. XRD measurement is also taken to provide information on the layer quality and superlattice period thickness. The calculated SL period thicknesses from XRD agree very well with the designed values.

Optical characteristics of T3SLs are extensively studied utilizing FTIR transmission measurement. A multi-layer thin-film model is used to fit the transmission data and compute absorption coefficients. A good agreement is found between experimental absorption coefficients and absorption coefficients computed from the density of states obtained from the 14-band k·p method. Temperature-dependent FTIR measurement is also done, and a sharp absorption onset, which is much higher than that of HgCdTe alloy, is observed at all measured temperatures.

Various methods of calculating the first and second transition energies of HgTe/CdTe superlattices are present and compared. The temperature-dependent absorption cutoff of the HgTe/CdTe superlattice is discussed. We found a surprisingly good agreement between the transition energy temperature-dependence of T3SL and HgCdTe.

6.2 The Major Challenge of T3SL Infrared Photodetectors

Advantages possessed by type-III superlattices in theory were not realized in practice, despite relatively comprehensive research efforts in the 1980s and early 1990s. At that time, MBE itself was a rather new technologies at that time and growing HgCdTe-based infrared materials was immature. Nowadays, high-quality substrates, mature MBE growth technology, and widely available sophisticated characterization techniques enable us to finally realize the advantages of superlattices in the lab. Our optical characterization results have proved the excellent absorption behavior of T3SLs in the VLWIR region.

However, there is minimal published data on T3SL photodetectors, especially in the VLWIR range. One of the main reasons is that T3SL's significant interdiffusion under elevated temperatures during the annealing process could shift the absorption edge to higher energies and even make the SL characters disappear. Several studies have been undertaken to examine the extent of the interdiffusion in HgTe/CdTe superlattices [98]–[104]. It has been shown by Zhou et al. [105] that annealing at a temperature as low as 225℃ would significantly reduce the mobility and carrier concentration. Figure 83 shows the effect of annealing on the absorption spectrum of a HgTe/HgCdTe (112)B SL [105]. With higher annealing temperatures and longer annealing times, the absorption edges shift to higher energies or even show an absorption edge similar to that of the corresponding alloy. Figure 84 shows the cross-sectional TEM images illustrating the effect of annealing [105]. Significant interdiffusion is observed at 250℃.

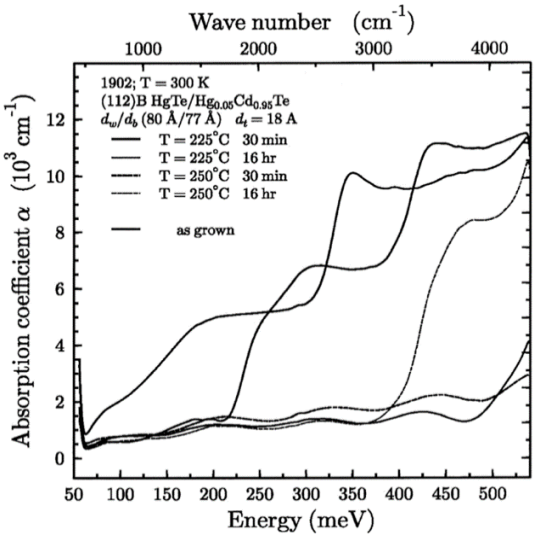

Figure 83 Annealing process shifts the cutoff edge of T3SL samples [105].

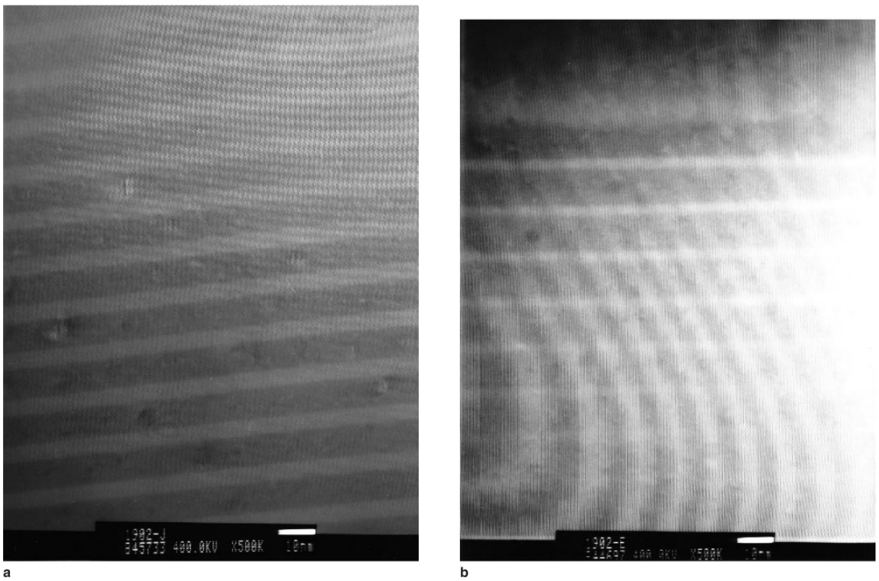

Figure 84 XTEM images of T3SL sample annealed (a) 30 min at 225°C and (b) 30 min at 250°C [105].

Unfortunately, the annealing process is inevitable in the photovoltaic device fabrication process. p-type doping is usually achieved through ion implantation on top of an n-type MBE-grown layer to form a p-n junction, which is the essential part of a photovoltaic device. Annealing at elevated temperatures is required to activate Arsenic doping in the p-n junction, which will likely increase the interdiffusion between SL layers. This precludes the use of T3SL in a photovoltaic device. Interdiffusion at high temperatures is the primary reason why there is very limited published work on T3SL photodetectors. Hence, a photoconductive device structure that works for T3SL that does not require p-type doping and annealing at elevated temperatures is highly needed.

There are limited data published on the performance of devices fabricated on HgTe/CdTe superlattices, despite significant efforts to model and grow the material. The first device is a MOS structure reported by Goodwin et al. [106], with a cut-off of 4.5 μm and 30% quantum

efficiency. Later Harris et al. [107] and Shin et al. [108] have fabricated photovoltaic HgTe/CdTe superlattice devices. Harris demonstrated a peak quantum efficiency was 66% at 140 K, with an average over the 3–5 μm waveband of 55%. Y. Selamet et al. [68] fabricated p^+-n^--n^+ device working in MWIR region at 80K. Au diffusion is used to create p-type doping at low temperature, which is a possible solution to achieve p-type doping without high temperature annealing.

Hatch [16] has shown some promising results of photoconductor devices using HgTe/CdTe superlattices as the LWIR/VLWIR absorber. However, the photoconductor devices reported are all literal type. The applied field is in the plane of the sample's surface, so that carrier transport occurs predominately within the plane of the superlattice layers. We want a design that utilizes T3SL in a vertical configuration instead of an in-plane configuration, where vertical transport properties of minority carriers determine the device operation.

In part II of this thesis, a photoconductive device using an nBn architecture is proposed to solve the dilemma of putting a T3SL layer in a device structure without p-type doping and high-temperature annealing.

PART II:
nBn Devices using Type III Superlattices

7 INTRODUCTION TO NBN DEVICES

7.1 Overview

The unipolar nBn photodetector structure was first reported by Maimon and Wicks[109]. The nBn is proposed as a concept that can be implemented in different semiconductor materials. As an example, an InAs-based nBn structure is shown in Figure 85. The name of nBn comes from the three layers it consists of: an MWIR-absorbing n-type InAs absorption layer, a large band gap undoped AlAsSb barrier layer, and a second thin n-type InAs contact layer. The barrier layer is thick enough so that electron tunneling is negligible, i.e., 50 or 100 nm. The barrier also needs to be high enough so the thermal excitation of the majority carriers over it can be neglected. The absorbing layer is the same as those in a photovoltaic device, with a thickness of roughly one or two absorption length. The second n-type contact layer can be as thin as a few tens of nanometer. nBn layers can be grown on a latticed matched substrate using MBE. The concept of nBn was later demonstrated using T2SL based materials with better control of band edge alignments[110], [111].

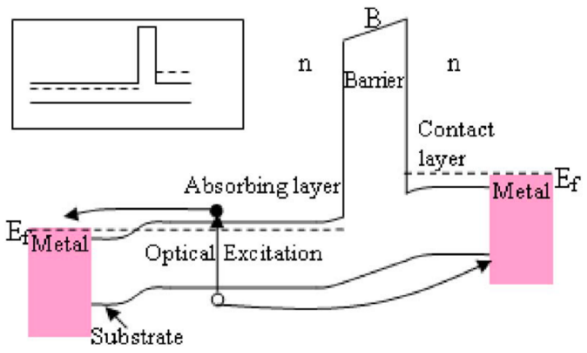

Figure 85 Band diagram of an InAs-based nBn structure [109].

The unique character of the nBn structure is that the barrier layer acts as a barrier in the conduction band to block the electrons flow from the contact region to the absorption region while being no barrier to minority carrier holes in the valence band. nBn devices work under a certain bias. The thermally and optically generated holes in the absorber can move from the absorber region to the contact layer under the bias. The generated electrons in the absorber move from the absorber to the contact on the left. However, thermally generated electrons in the contact layer will be blocked by the barrier.

For the past decade, there has been strong interest in designing unipolar nBn devices [110]–[112] since it was first reported by Maimon and Wicks [109]. Applying the same concept to II-VI materials, especially HgCdTe, seems appealing because it eliminates the requirements for *p*-type material in traditional p-n junctions and thus avoids defects generated due to ion implantation [113]–[115]. Besides, the device fabrication process is simplified by removing the additional implantation and annealing steps.

Surprisingly, a HgCdTe implemented nBn structure was first proposed back in 1983 [116]. However, this concept has not been pursued possibly due to the limitation of MBE and lack of high-quality materials at that time, until Maimon and Wicks brings it to sight by implementing III-V materials. The major challenge of using HgCdTe in nBn structures will be discussed in section 7.3.

7.2 Dark Current Suppression in nBn Devices

Dark current is the residual electric current flowing in a photoelectric device when there is no incident illumination, which generates noise that limits device performance. There are three significant contributions to dark current in narrow bandgap semiconductor photo devices:

1. The generation current associated with Shockley-Reed- Hall (SRH) process from traps created by dopant or defects.

2. The diffusion current associated with Auger and radiative process.

3. The surface current associated with traps at or near the surface formed due to dangling bonds.

The generation current associated with the SRH process is the most dominant dark current components in MWIR photodiodes at low temperatures[117], [118]. The SRH generation process is significant in the depletion region where the SRH generated carriers can be quickly separated by the electric field. Assuming the SRH lifetime of minority carriers are similar in the nBn structure and photodiodes, which depends on the material quality, the SRH process is significantly suppressed in nBn structure because the n-type layers are in a flat band with little to no depletion. The photo generated carriers in the absorber region can still be collected with the help of the small electric field and also diffusion. From Figure 85 one can see that a major portion of the applied voltage is dropped across the undoped barrier layer. There is usually only a very smaller part of the absorber that is depleted, the part which is close to the barrier. Hence the barrier layer in an nBn structure not only does not produce SRH dark current because of the large band gap but also blocks the flow of majority carriers like the built-in barrier of a p-n junction.

SRH generation currents are nearly eliminated, which translates into a reduction in dark current. A lower dark current means less noise and better performance, or the same performance can be achieved at a higher device operating temperature.

7.3 Valence Band Offset

The key to a successful nBn device is close-to-zero valence band offset (VBO) ΔE_v. Valence band offset is the energy difference between the undoped barrier and the n-type absorber. The barrier must also act as a minimum energy barrier (i.e., small VBO) to holes in the valence band so the optically generated carriers can be moved from the absorber to the contact region and collected. nBn structure was first proposed for III-V materials because of their nearly zero valence band offset.

However, nBn photodetectors cannot be easily realized using II-VI materials because of the substantial VBO present in HgCdTe-based heterostructures. The absorption and barrier layers are made of HgCdTe with significantly different compositions. Because the VBO between HgTe and CdTe is quite large (~540meV), the difference in composition creates substantial VBO between absorption and barrier layers. We will discuss this in more detail in Section 8.1.1 when we present the band alignment of HgCdTe-based nBn structures. This challenge is particularly difficult to overcome if one is developing LWIR and VLWIR HgCdTe-based nBn detectors, where the band gap of the absorber is very small and a large VBO may be comparable to the bandgap energy.

The existence of the VBO limits the performance of HgCdTe-based nBn photodetectors because the energy barrier in the valence band inhibits the flow of holes [119]. This is illustrated in Figure 86 (a). Depending on the operation wavelength, a "turn-on" voltage, which is a relatively high bias, must be applied to the device to improve the efficiency of collecting photogenerated minority carriers. Ideally, the VBO energy ΔE_v encountered by minority carrier holes should be comparable to the average carrier thermal energy so the carriers can step over the barrier without the need of a high turn-on voltage[54]:

$$\Delta E_v \sim f\frac{1}{2}kT \tag{7.1}$$

Where f is the degrees of freedom, k is the Boltzmann constant, and T is the temperature. For carriers moving in the bulk material, we take $f = 3$. Using this equation, one can get ΔE_v should be approximately 15 meV at around 100K.

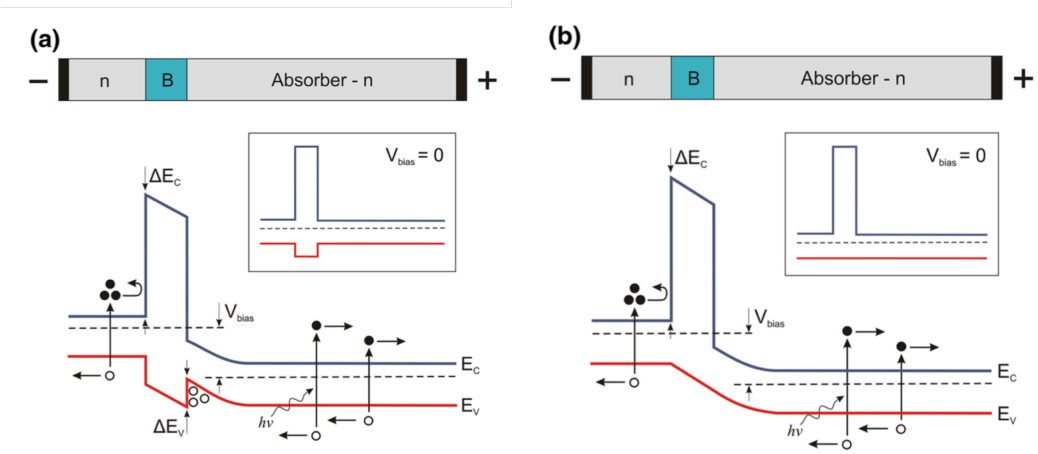

Figure 86 Band alignment for nBn detectors under reverse bias: (a) with significant VBO (b) zero VBO [54].

Further development of nBn photodetector technology using II-VI materials requires effort to minimize the VBO to realize the optimum nBn detector structure depicted in Figure 86

(b). In chapter 8, we will focus on various designs of the barrier layer to minimize the valence band barrier. The advantages and disadvantages of these designs will be discussed.

8 DESIGN AND MODELING OF NBN DEVICE

8.1 nBn Device with Bulk (n and p-type) Barrier

8.1.1 nBn Device with n-type Barrier

The barrier layer in most nBn structure designs is undoped or lightly n-doped. By eliminating requirements for p-type doped material, one can avoid implantation-induced defects and, at the same time, simplify the device fabrication process. nBn devices designed with n-type barrier has previously been reported[54], [120], [121]. HgCdTe nBn devices utilizing a n-type barrier have been experimentally demonstrated by Itsuno et al. [122], and bias-dependent photoresponse is observed and a MWIR cut-off wavelength around 5.7 μm is extracted.

Here we contribute our design of nBn structure with a n-type doped barrier. The nBn structure is designed to work in the MWIR region. The HgCdTe absorber with a composition $x = 0.31$ has a thickness of 5 μm, thick enough to provide full absorption. The cap layer has the same composition as the absorber, but with a thickness of only 0.3 μm. The absorber and the cap layer are both n-type doped, with a doping level of 5×10^{15} cm^{-3} and 5×10^{16} cm^{-3}, respectively. The barrier layer has a thickness of 0.2 μm and is background doped ($N_D = 5 \times 10^{14}$ cm^{-3}). Given that the barrier layer is sufficiently thick, tunneling can be neglected. There is a contradiction when it comes to adjusting the composition of the barrier. The composition controls the barrier height. On one side, the barrier needs to be high enough to block majority carriers. Otherwise, the electrons are not blocked sufficiently from the cap region so that the dark current density would increase; On the other side, a high barrier will increase VBO and the turn-on voltage. So, the barrier height has to be chosen carefully. In this work, we used a barrier with a composition of 0.6.

Another contact layer below the absorber layer is added to provide bottom contact for mesa device structure. The full cross-sectional device structure and structural parameters are illustrated in Figure 87.

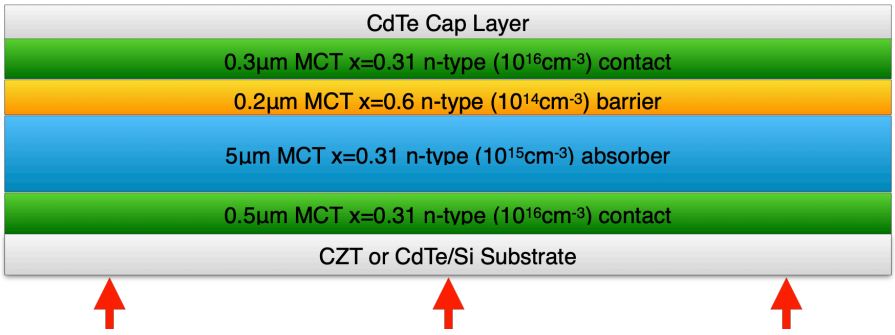

Figure 87 The cross-sectional device structure and structural parameters of an nBn device with a n-type barrier. The red arrows indicate the light incident direction.

The modeled energy band diagrams of HgCdTe nBn photodetector with an n-type barrier under different bias at 300K is shown in Figure 88. An apparent valence band offset is observed and is about 100 meV. This barrier height is too big to satisfy the upper bound associated with the thermal energy in Equation (7.1). Hence a high turn-on voltage, i.e., a high voltage reverse bias, is needed to move the photogenerated minority holes from the absorber to the contact layer. The barrier is background doped, which is the lowest doping level that we believe can be achieved in MBE growth. Suppose the barrier's doping level went higher than the background level, the VBO energy ΔE_V would increase to a more significant value. In conclusion, HgCdTe nBn photodetector with n-type barriers cannot achieve a small enough VBO that the barrier is "invisible" to the holes.

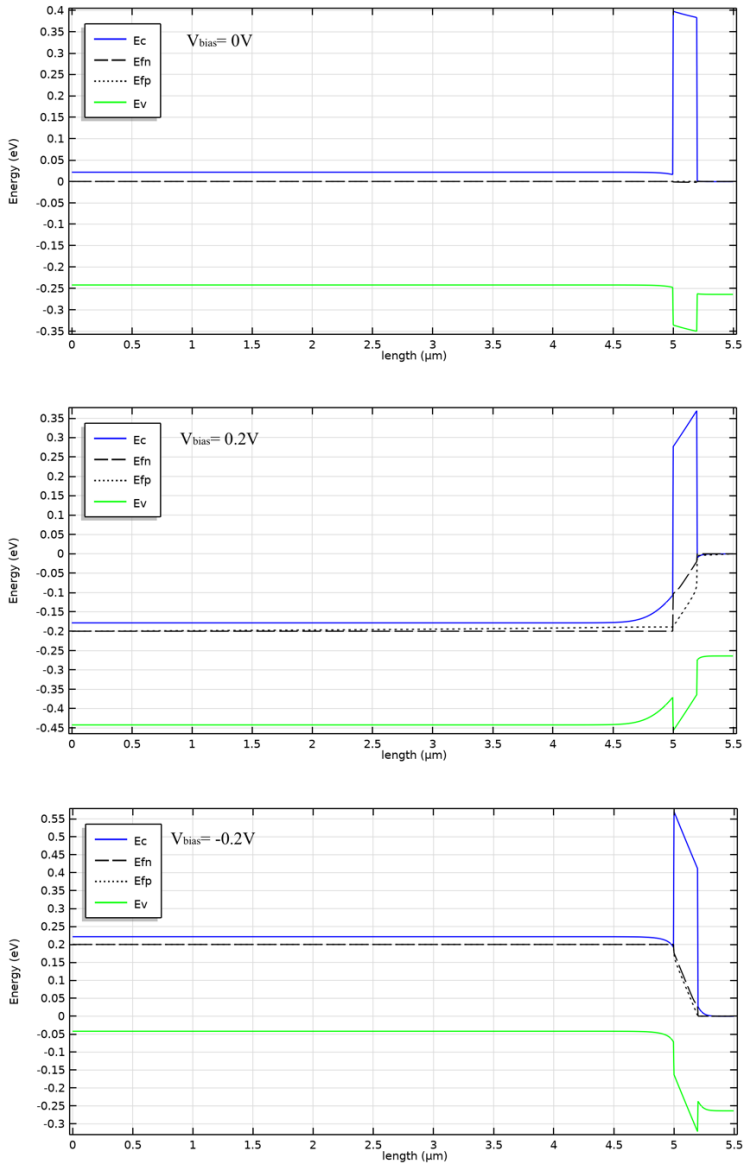

Figure 88 Modeled energy band diagrams of HgCdTe nBn photodetector with an n-type barrier (a) at equilibrium (b) under 600mV reverse bias (c) under 600 mV forward bias.

8.1.2 nBn Device with *p*-type Barrier

It was previously reported that zero VBO could be achieved using a p-type doped HgCdTe alloy barrier[123]. Since HgCdTe nBn photodetector with n-type doped barrier cannot achieve small enough VBO, it is worthwhile to investigate p-type doped barrier.

The nBn structure with a p-type doped barrier is designed to work in the MWIR region. The HgCdTe absorber with a composition $x = 0.31$ has a thickness of 5 µm. The cap layer has the same composition as the absorber, but with a thickness of 0.3 µm. The absorber and the cap layer are both n-type doped, with a doping level of 5×10^{15} cm^{-3} and 5×10^{16} cm^{-3}, respectively. The barrier layer has a thickness of 0.2 µm and a composition of 0.6 and is p-type doped ($N_A = 5 \times 10^{16}$ cm^{-3}). Given that the barrier layer is sufficiently thick, tunneling can be neglected. Another contact layer below the absorber layer is added to provide bottom contact for mesa device structure. The full cross-sectional device structure and structural parameters are illustrated in Figure 89.

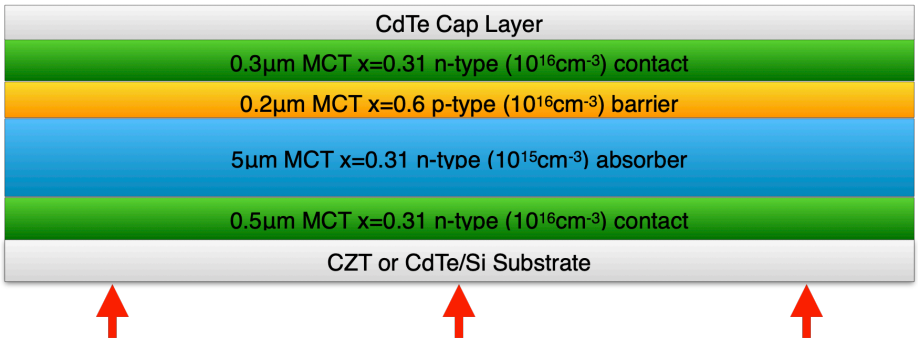

Figure 89 The cross-sectional device structure and structural parameters of an nBn device with a p-type barrier. The red arrows indicate the light incident direction.

The modeled energy band diagrams of HgCdTe nBn photodetector with a p-type barrier at 300K is shown in Figure 90. The valence band offset substantially decreased from ~100 meV to ~50meV compared to a n-type barrier. A closer look at the valence band offset shows that the thickness of the energy barrier in the valence band is very thin (~10 nm) so that the holes can tunnel through the energy barrier. This enables the nBn devices with p-type doped barriers to operate at near zero-bias voltage.

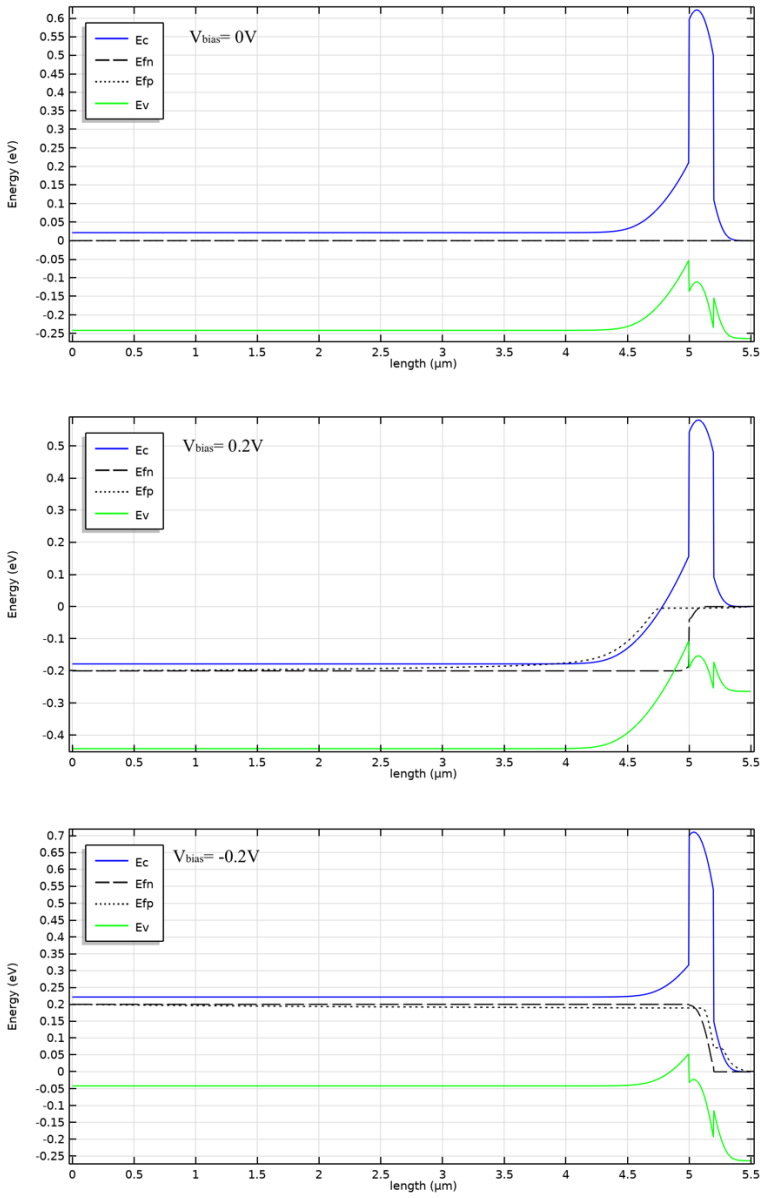

Figure 90 Modeled energy band diagrams of HgCdTe nBn photodetector with an p-type barrier (a) at equilibrium (b) under 600mV reverse bias (c) under 600 mV forward bias.

However, *p*-type doping introduces an extra layer of complexity in MBE growth, and the dopant activation after MBE growth is a problem. The *ex-situ* thermal annealing process required for Arsenic activation may destroy the doping and composition profile of the structure, considering the fast interdiffusion rate of II-VI materials. Besides, a depleted space-charge

region is formed in the vicinity of the barrier layer. The calculated space charge profile is shown in Figure 91. This space charge region and its associated electric field can help move and collect generated holes from the absorber region. However, it also potentially gives rise to enhanced trap assisted SRH thermal generation due to relatively high electric fields and, consequently, higher dark current. This drawback of nBn with p-type doped barrier hinders the primary advantage of nBn structure, which is suppressing the SRH generation current. Hence, we need to find an alternative approach to reduce the effective valence band offset while circumventing p-type doping.

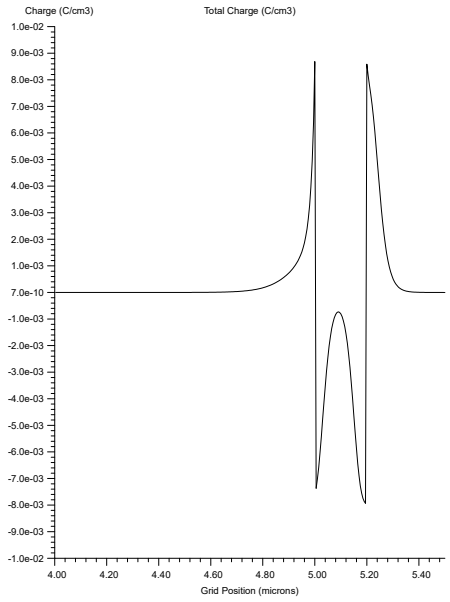

Figure 91 Calculated space-charge regions in an MWIR HgCdTe nBn detector with a p-type barrier.

8.2 nBn Device with T3SL Barrier

Other than n-type and p-type doped HgCdTe with various composition being considered as the barrier for nBn structure, there is another approach which uses doping modulation

technique[124]. The material composition and doping concentration of the barrier layer are graded simultaneously, which potentially leads to the elimination of the valence band discontinuity in HgCdTe-based nBn detectors. However, this method still needs to be verified by experiment, and the complicated composition and doping profile is relatively hard to achieve with MBE.

An alternative approach is to use T3SL, specifically HgTe/CdTe superlattices, as the barrier[54], [121]. The conduction band and the valence band in a normal band structure HgTe/CdTe superlattice are the C1 band and the HH1 band, respectively. As we have discussed in 2.1, the energies of the C1 band and the HH1 band in the SL are decided by quantum confinement and can be controlled by the thicknesses of the HgTe well layer thickness. The design degrees of freedom, like the HgTe well thickness, the CdTe barrier thickness, and the doping level, provides a big possibility that zero VBO can be achieved with a HgTe/CdTe superlattice barrier. Besides, modeling using the 14-band k·p method has shown that the effective masses of electrons and holes in a T3SL are expected to be much higher than that in HgCdTe alloys. As a result, a T3SL barrier could potentially suppress band-to-band and trap-assisted tunneling and reduce the dark current. And additionally a thinner barrier can be used to block the majority carriers.

Here we adopt the design by M. Kopytko et al.[54], where a HgTe/CdTe superlattice barrier layer is used in a HgCdTe-based MWIR nBn detector. The HgCdTe absorber with a composition $x = 0.315$ has a thickness of 5 μm. The cap layer has the same composition as the absorber, but with a thickness of 1 μm. The absorber and the cap layer are both n-type doped, with a doping level of 1×10^{15} cm^{-3}. The HgTe/CdTe superlattice barrier layer has a total

thickness of 0.2 µm and is non-intentionally doped. Given that the barrier layer is sufficiently thick, tunneling can be neglected. The full cross-sectional device structure and structural parameters are illustrated in Figure 92.

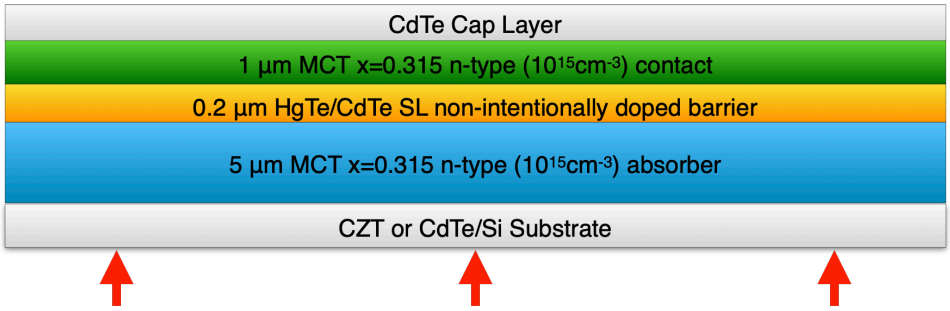

Figure 92 The cross-sectional device structure and structural parameters of an nBn device with HgTe/CdTe SL barrier. The red arrows indicate the light incident direction.

Each HgTe/CdTe superlattice period consists of 5 monolayers (ML) of HgTe and 28 MLs of CdTe, which corresponds to 16 Å HgTe/90 Å CdTe. Our computational methodology to obtain SL band structures employs a 14-band k·p method, which we discussed in great detail in chapter 2. The energy band gap can be tailored by varying the layer thicknesses of the well and barrier layers in SL.

The modeled energy band diagrams of HgCdTe nBn photodetector with HgTe/CdTe superlattice barrier at 80K is shown in Figure 93. The valence band offset is minimal, which is about 10 meV. Hence the valence band offset can be neglected, which results in a close-to-zero turn-on voltage. This concludes the HgCdTe-based nBn structure's optimized design, where a HgTe/CdTe superlattice barrier layer overcomes the problems associated with the relatively high valence band energy barriers formed by the use of abrupt HgCdTe alloy designs.

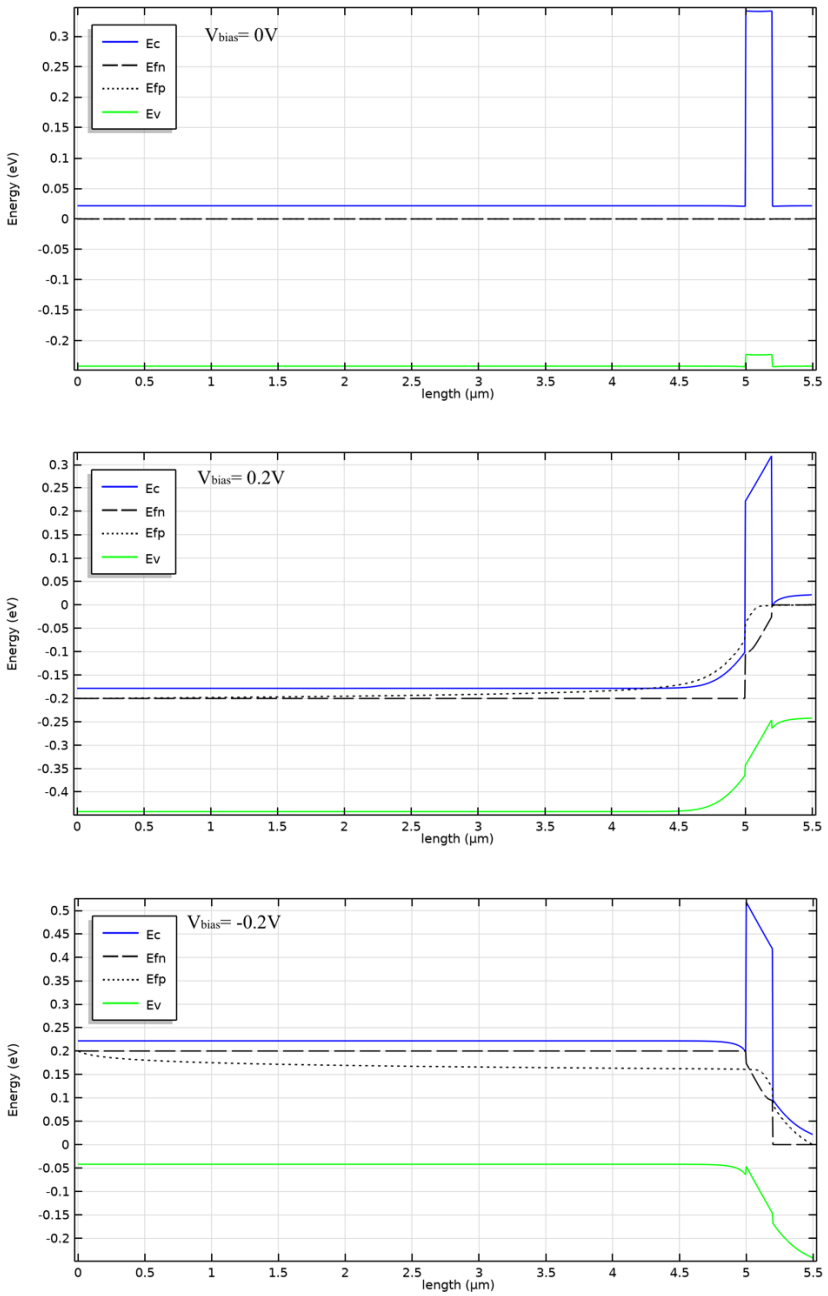

Figure 93 Modeled energy band diagrams of HgCdTe nBn photodetector with HgTe/CdTe superlattice barrier at equilibrium.

9 MBE GROWTH AND CHARACTERIZATION OF NBN DEVICE

9.1 nBn Samples Grown with MBE and Their Characterization Results

Four HgCdTe-based nBn samples with HgTe/CdTe superlattice barriers, including a calibration sample, are grown using Molecular Beam Epitaxy. Our goal is to prove that high quality nBn layers with SL barrier can be grown. Ideally, these samples should be fabricated into devices, and the I-V characteristics should be tested. Ultimately, we want to grow T3SL-based nBn structures and fabricate devices. However, due to limitations at the time of this work, we could only grow HgCdTe-based nBn heterostructures. The preliminary experiment result discussed in this chapter will serve as the foundation of future lab work.

All four samples grown using MBE employ a similar device structure to the one discussed in section 8.2. The samples are grown on CdTe (211)B on Si substrates. Before growth, the substrates were treated by sequential degreasing, Te desorption, and Te annealing. The growth of a nucleation layer and a SWIR HgCdTe alloy buffer layer was performed to lattice match with the substrate and smooth out the substrate surface. The nucleation and buffer layers are thin enough so they do not affect the optical properties of the sample. Then a HgCdTe absorber layer with a composition of either 0.310 or 0.315 is grown. The layer is 5 μm thick and is grown with a growth rate of 3 μm/h to ensure high-quality single crystal growth. A HgTe/CdTe SL buffer layer was then grown. During the CdTe layer's growth, the Hg source remains open to provide a constant Hg flux background, which leads to 5-10% Hg unintentionally incorporated into the CdTe layers [81], [125]. A contact layer with the same composition and the same growth rate is then grown on top of the SL barrier layer. The absorber layer and the contact layer are n-type doped, while the SL barrier is background doped. Each layer's composition and growth rate are calibrated with Ellipsometry and FTIR data from

previous calibration samples. The growth temperature, absorber composition, absorber thickness, superlattice barrier thicknesses, and the growth time of each superlattice period are summed up in Table 11.

Sample #	Growth Temp.	Absorber Comp. x	Absorber Thickness	SL Barrier thicknesses	SL Barrier Growth time(Well/Barrier)
hct17027	199.0℃	0.310	5 µm	6/28 ML	3.7s/37.1s
hct17028	199.5℃	0.315	5 µm	5/28 ML	3.1s/37.1s
hct18001	199.5℃	0.315	5 µm	5/28 ML	3.1s/37.1s

Table 11 The growth temperatures, absorber compositions, absorber thicknesses, superlattice barrier thicknesses, and the growth time of each superlattice period of the three HgCdTe-based nBn structure with HgTe/CdTe superlattice barrier.

In-situ reflection-high-energy electron diffraction (RHEED), an infrared pyrometer, and in-situ spectroscopic ellipsometry (SE) were used for growth control. Screenshots of the RHEED pattern at different stages of the MBE growth are shown in Figure 94. More detail on RHEED has been given in section 4.1.1. The RHEED images show a 2D streaks pattern throughout the growth, indicating the layer's good quality. There is a relatively large lattice match between the SL layer and the MWIR absorber layer. However, we do not see any RHEED characteristics associated with layer quality degrading. A possible explanation is that the SL layer's well/barrier layers are relatively thin, so the SL layer is strained and latticed matched to the absorber layer. It is the same with the SL barrier/contact layer interface, where we do not see any significant change in the RHEED pattern.

It is worth mentioning that the absorber's quality is more important than that of the contact layer and the SL barrier layer. Trap-assisted SRH generates a current in the contact layer that is blocked by the SL barrier. Moreover, the SL barrier has a relatively big band gap, so the thermally generated current is minimal. As a result, a bad-quality barrier or contact layer will not

significantly affect the device's performance. Growing the absorber before the SL barrier layer and the contact layer helps with the absorber layer quality because defects generated during earlier stages of the growth could “propagate” to the sample surface.

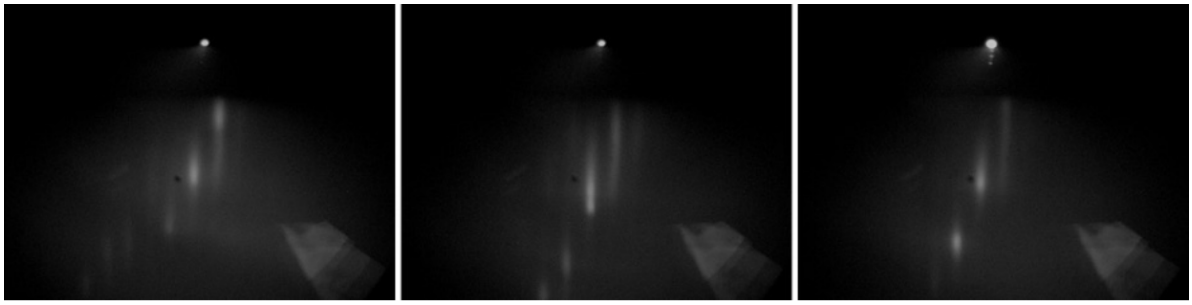

Figure 94 Screenshots of RHEED pattern at different stages of the MBE growth of an nBn structure with HgTe/CdTe superlattice barrier. (a) Absorber (b) CdTe barrier in SL (c) HgTe well in SL

As we mentioned in section 4.1.2, ellipsometry has its limitations when it comes to *in-situ* monitoring superlattice growths. Because the HgTe well and barrier layers are relatively thin, ellipsometry does not have enough layer thickness to build up stable polarization information. Nevertheless, ellipsometry is still useful to monitor the absorber layer's growth and contact layer in an nBn heterostructure. The ellipsometry data of one full MBE growth is shown in Figure 95. Composition (green) and surface roughness (red) as a function of time are plotted. An Ellipsometry HgCdTe model is used throughout the growth. The absorber and the contact layer show stable and nearly zero surface roughness, which indicates good quality growth. Note that the surface roughness did not increase before and after the growth of SL barrier, which agrees with our observations from RHEED. The irregular fluctuations of composition and roughness during barrier layer growth do not reflect the real growth condition; it only shows the model's struggle to fit HgTe/CdTe superlattice real-time data. The average composition of the

absorber is ~0.325, which is close to our target x=0.315. We will verify the composition using FTIR.

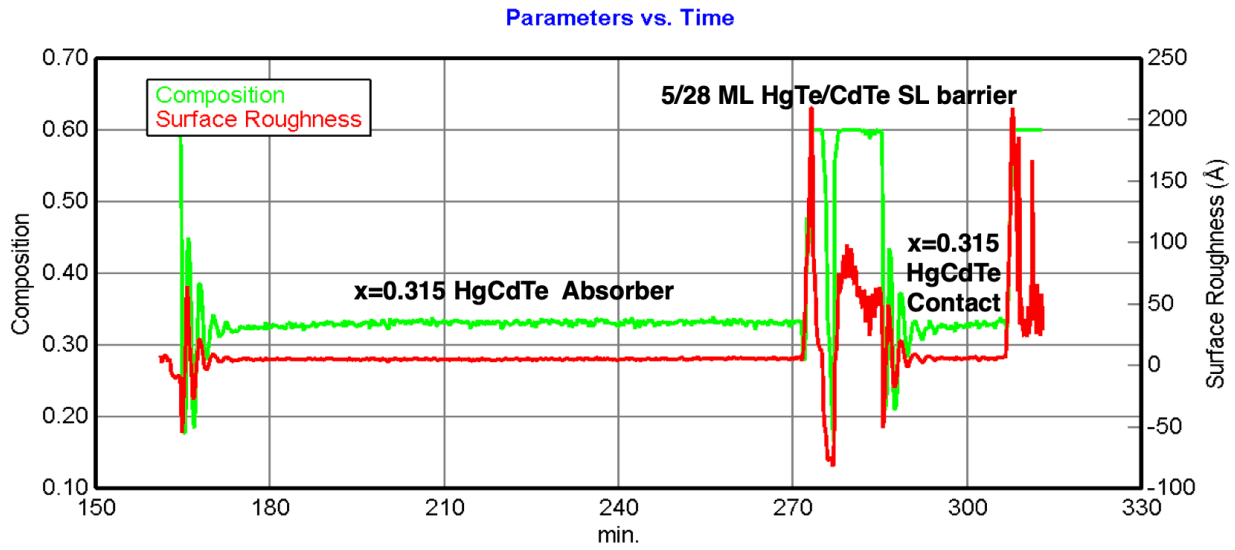

Figure 95 The ellipsometry data of one full MBE growth of nBn structure with HgTe/CdTe superlattice barrier. Composition (green) and surface roughness (red) as a function of time are plotted.

The transmission spectra as a function of the wavenumber of the three nBn samples mentioned in Table 11 are shown in Figure 96. The three samples show similar absorption behavior. Since the SL barrier layer has a bigger band gap than the absorber, the transmission curve only represents the absorber's absorption. The absorption layer is thick enough so that the transmissions at higher energies become zero. Fitting the transmission cutoff edges with $500\ \mathrm{cm}^{-1}$ gives the composition of the three layers, which are 0.315, 0.319, and 0.311 for sample hct17027, hct17028, and hct18001, respectively. The interference fringes are fitted using the MLTF model given in section 5.2.3 and layer thicknesses are extracted. The thicknesses agreed very well with the designed value, though the individual well/barrier thickness cannot be obtained from FTIR fitting.

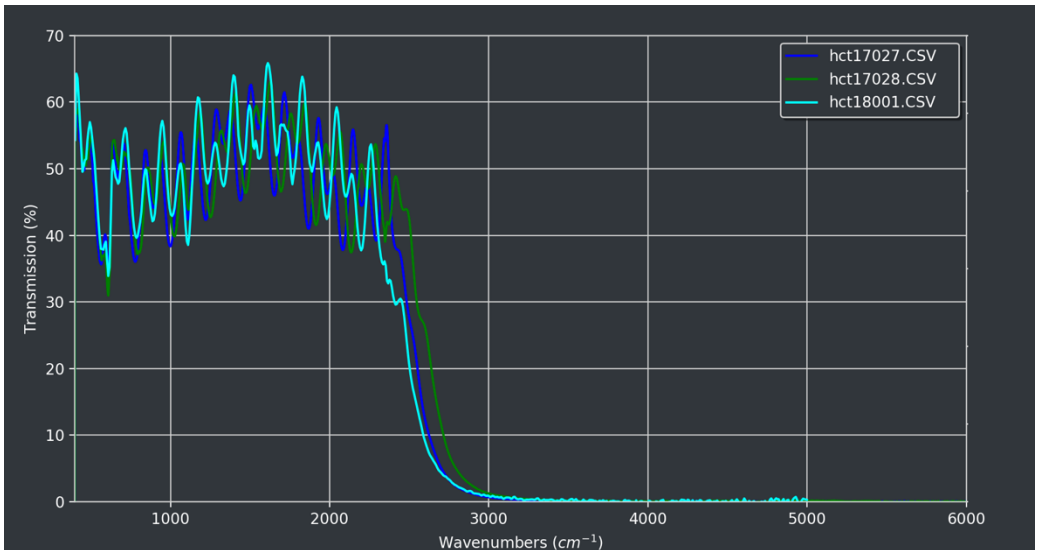

Figure 96 The transmission spectra as a function of the wavenumber of the three nBn samples mentioned in Table 11.

The Nomarski image of as-grown nBn sample hct18001 is shown in Figure 97. Crosshatch pattern is clearly visible on the sample surface, caused by surface strain relief associated with slight lattice deformation. Few micro-defects can be seen on the surface, indicating optimized growth temperature was achieved. The shadowed circles in Figure 97 (b) are due to dust on the microscope lens (which was cleaned later with a nitrogen gun).

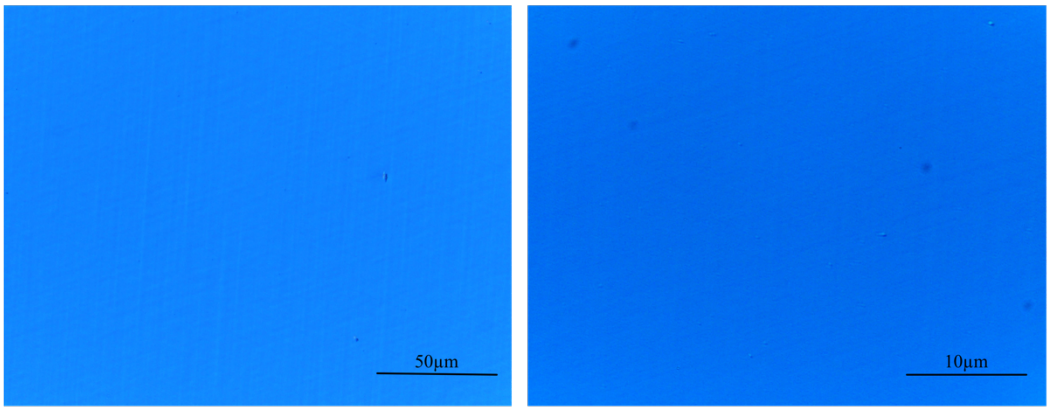

(a) (b)

Figure 97 Nomarski imaging of nBn sample hct18001 at (a) 100x magnification (b) 500x magnification

XRD measurement is also taken on one of the nBn samples. However, the peak of the substrate, the peak of the absorber, and the peak of the SL barrier overlap with each other so that the peak positions and FWHMs cannot be obtained; hence here we omit the XRD result analysis.

9.2 Methods to Measure Valence Band Offset

Valence band offset, an essential parameter of an nBn device, can be evaluated after the device fabrication is done. Due to limitations and situations at the time of this work, device fabrication and device characterization using the nBn layers grown with MBE are beyond this thesis's scope. Nevertheless, here we propose two methods that can potentially measure the VBO.

The first method is to measure the I-V curve of the nBn device and see if a turn-on voltage can be observed. The turn-on voltage is directly related to the valence band offset because the minority carrier holes need a turn-on voltage to overcome the valence band energy barrier and transport from the absorber to the contact layer. This is probably the fastest way to examine if a VBO is present. However, this method cannot quantitively decide the value of VBO.

The second method proposed is to use internal photoemission (IPE) spectroscopy [126]–[128]. The transition energies can be determined by IPE through the fitting of the near-threshold quantum yield spectra. This method has previously been reported by Lao et al. [127] that the band offsets in a type-II pBp photodetector were successfully determined. Moreover, a study of

IPE applied to an n-type HgCdTe heterojunction shows the possibility to detect if an energy barrier exists [128]. Hence IPE could be the best method to decide the band offset in an nBn structure quantitively.

10 NBN DEVICE WITH T3SL ABSORBER AND 2-COLOR NBN

10.1 Introduction

It has been shown in section 8.2 that near-zero valence band offset can be achieved with HgTe/CdTe superlattice barrier, which is the key to a successful nBn structure design. If one still remembers, HgTe/CdTe superlattice has been discussed as the best candidate for the VLWIR absorber layer in Part I of this thesis, not a barrier in an nBn device. Despite its great potential in the VLWIR region, it has one major drawback that hinders the possibility of a HgTe/CdTe superlattice based photodetector: The significant interdiffusion under elevated temperatures during the annealing process could make the SL characters disappear. Unfortunately, the annealing process is inevitable because p-type ion implantation is necessary to form a p-n junction. Hence the most critical question is: How do we get rid of p-type ion implantation?

The answer is to use a photoconductor device structure, especially an nBn device structure. An nBn photoconductive device with HgTe/CdTe superlattice absorber working in the VLWIR region does not need p-type doping, and the VBO can be potentially lowered to a small value by using a HgTe/CdTe superlattice barrier. The nBn structure helps HgTe/CdTe superlattice absorber eliminate the need for p-type doping, and the HgTe/CdTe superlattice barrier helps the nBn structure to solve the problem with VBO. They complement each other. Ultimately, we need a design with HgTe/CdTe superlattices used as both the absorber and the barrier, but with different well/barrier thicknesses to achieve different bandgap energies. This is utilizing the design degrees of freedom of superlattices to the best.

To fully exploit the advantages of nBn architecture, we take the design a step further and propose a 2-color (dual-band) nBn device. Multispectral detection is highly desirable for

advanced infrared (IR) systems because it improves the sensitivity and provides a new dimension of contrast by gathering data in separate IR spectral bands. Two-color infrared focal plane arrays (IRFPAs) show much potential in the rapid and efficient identification of objects in a scene by subtracting background clutter and sunlight using two wavebands. The signal-to-noise ratio of two-color IR detectors greatly exceeds that of single-color photodetectors [129]. Unlike many dual-band IRFPAs that use simultaneous readout architectures, which require an additional electrical contact to a recessed layer in each unit cell, dual-band IRFPAs using nBn structures can achieve sequential two-color detection by simply changing the polarity of the bias voltage, which simplifies optical design and reduces device size, weight and power consumption.

This idea has been demonstrated with HgCdTe-based 2-color nBn by Grein et al. [123] The specific layers of the device from the top down (for back-illumination) are 8 μm VLWIR $Hg_{0.79}Cd_{0.21}Te$ absorber doped to n=1×10^{15} cm^{-3}, which has a cutoff wavelength of 14 μm at 40K; 1 μm $Hg_{0.55}Cd_{0.45}Te$ barrier doped to p=8×10^{17} cm^{-3}; and 8 μm LWIR $Hg_{0.764}Cd_{0.236}Te$ absorber doped to n=1×10^{15} cm^{-3}, which has a cutoff wavelength of 9 μm at 40K. The computed band profiles is shown in Figure 98. Depends on the applied bias, different absorption region is activated. Under positive bias (Figure 98 (a)), the LWIR region is activated, the photogenerated holes in the LWIR region can move freely across the barrier and produce a large photocurrent, and vice versa for reverse bias (Figure 98 (b)). Hence, the photodetector is sensitive to LWIR (VLWIR) radiation under forward (reverse) bias. The barrier prevents electrons from traveling between the two absorbers under any conditions.

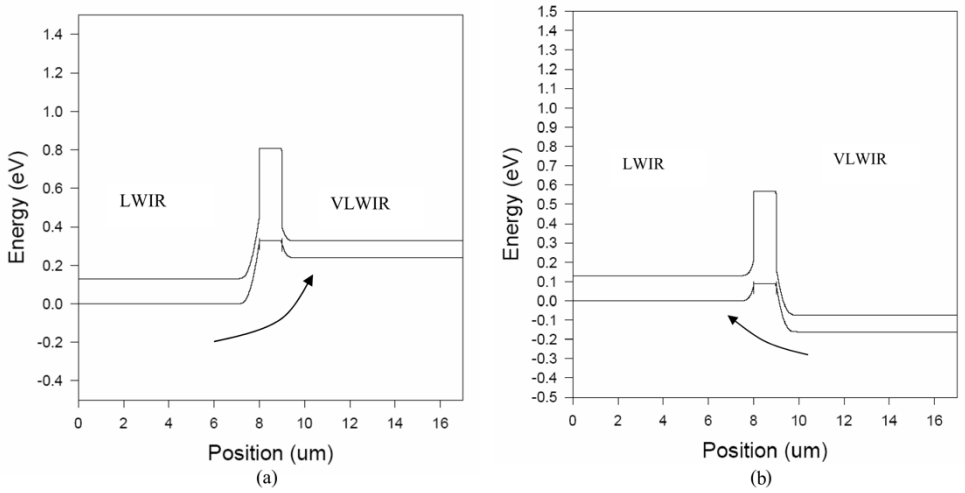

Figure 98 The computed HgCdTe alloy detector band profiles with the LWIR layer under (a) +0.2 V (b) -0.2V bias relative to the VLWIR layer. The arrow shows the motion of photo holes generated in the activate absorber region [123].

Additional to the HgCdTe-based nBn, a 2-color nBn device with LWIR and VLWIR superlattice absorbers is also proposed in this paper. However, the barrier layer is heavily p-type doped HgCdTe alloy to remove the potential barrier, which introduces an extra layer of complexity in MBE growth, and also potentially gives rise to enhanced trap-assisted Shockley–Read–Hall thermal generation due to relatively high electric fields in depletion regions at the barrier interfaces.

On the other hand, another paper by Lao et al. [127] reported a two-color type-II InAs/GaSb superlattice photodetector based on a pBp architecture (Figure 99). T2SL is used in both the absorbers and the barrier. A near-zero conduction band offset (CBO) is measured using IPE, the method of which was briefly discussed in section 9.2. This paper proves that an all-superlattice barrier structure can achieve a near-zero band offset, and the band offset can be measured. However, the paper is using T2SL, which consists of III-V materials, and the material is p-type doped. It would be interesting to employ a similar idea to an n-type doped nBn

structure with T3SLs, where holes instead of electrons become minority carriers and VBO matters.

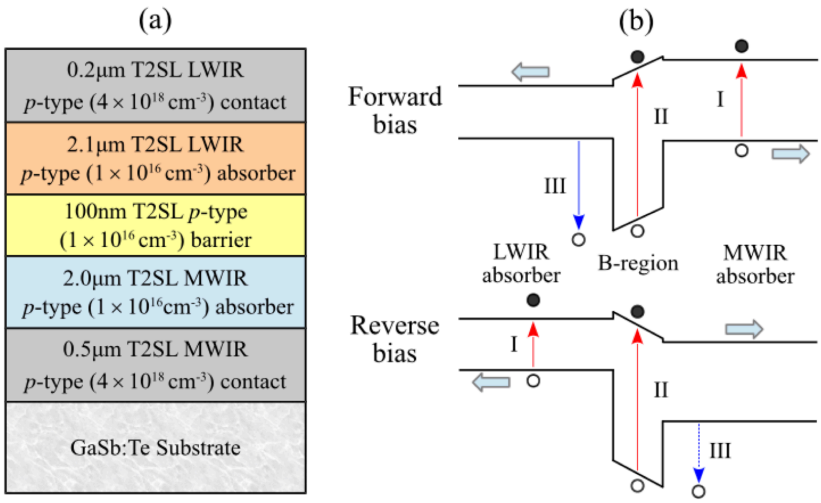

Figure 99 (a) Schematic of a two-color type-II InAs/GaSb superlattice-based pBp photodetector. (b) Band alignment under forward and reverse biases, where the bias is applied on the top electrode of the detector [127].

In summary, we want to design and model an nBn structure using HgTe/CdTe superlattices as both the absorber and the barrier, and ultimately extend the design to a 2-color nBn setup where two superlattice absorbers are present. The key to these designs is to keep VBO to a low value so that the minority carrier holes do not see a large potential barrier and a low turn-on voltage can be used. The design and modeling details will be given in section 10.2 and the modeling result will be discussed in 10.3.

10.2 Design and Modeling

Here we propose an nBn architecture designed for the VLWIR region, using HgTe/CdTe superlattices as both the absorber and the barrier. The band structures of all HgTe/CdTe superlattices used in this work are calculated using the 14-band k·p method (detailed in section 2.3). A 55 Å HgTe/55 Å CdTe (17ML/17ML) superlattice is used as the VLWIR absorber. The calculated band structure of this superlattice at 100K is shown in Figure 100 (a). The bandgap energy of this HgTe/CdTe superlattice is 91.7 meV, which corresponds to a cutoff wavelength of 13.6 μm. Longer cutoff wavelength can be achieved at lower operating temperature. This absorber's thickness is chosen to be 5 μm, which provides enough photon absorption due to T3SL's large absorption coefficients that we have demonstrated in section 5.4. A 26 Å HgTe/90 Å CdTe (8ML/28ML) superlattice is used as the barrier. The calculated band structure of this superlattice at 100K is shown in Figure 100 (b). The bandgap energy of this HgTe/CdTe superlattice is 337.1 meV, which corresponds to a cutoff wavelength of 3.68 μm and about three times higher than the absorber bandgap energy. While the HgTe well thickness of the barrier superlattice controls its band gap, the CdTe barrier thickness is used to adjust the superlattice period thickness so that it is similar to the period in the absorber. The doping levels of all layers are parameters subject to change. By adjusting the doping level in each layer, we can potentially achieve a low valence band offset. The full device structure is shown in Figure 101.

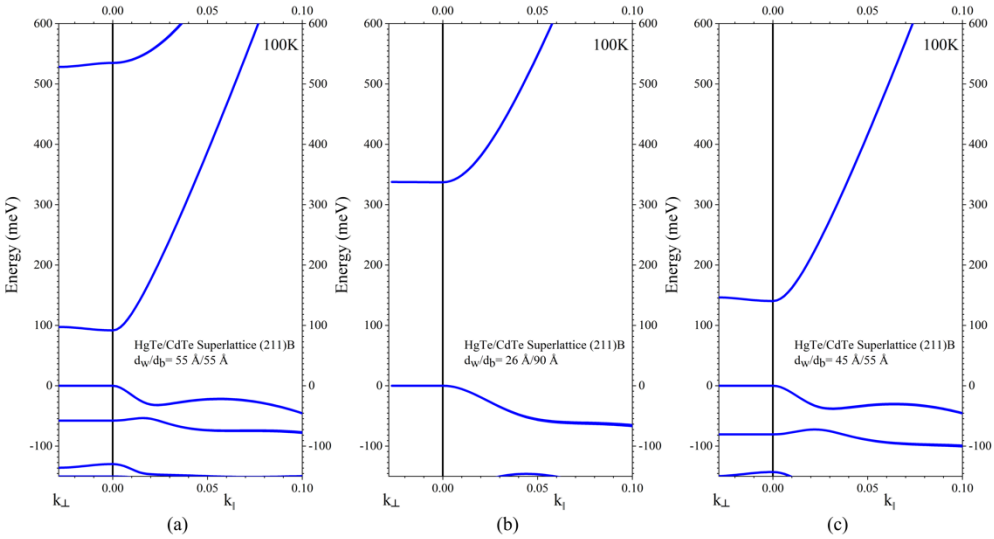

Figure 100 Calculated band structure of HgTe/CdTe superlattices at 100K. (a) 55 Å HgTe/55 Å CdTe SL. (b) 26 Å HgTe/90 Å CdTe SL (c) 45 Å HgTe/55 Å CdTe SL.

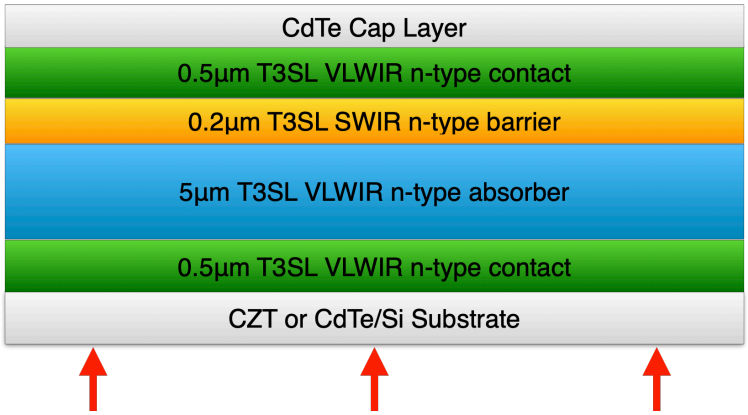

Figure 101 The cross-sectional device structure and structural parameters of an nBn device designed for the VLWIR region with all superlattice layers except the substrate. The red arrows indicate the light incident direction.

As a step further, we propose another nBn architecture, which is designed for VLWIR/LWIR dual-band absorption, using HgTe/CdTe superlattices as both the two absorbers and the barrier. The same VLWIR absorber layer and the barrier layer as the previous design is used, but we replace the VLWIR cap layer in Figure 101 with an LWIR absorber. A 45 Å HgTe/55 Å CdTe (17ML/17ML) superlattice is used as the LWIR absorber. The calculated band structure of this superlattice at 100K is shown in Figure 100 (c). The bandgap energy of this

HgTe/CdTe superlattice is 140.4 meV, which corresponds to a cutoff wavelength of 8.84μm. The thickness of this LWIR absorber layer is chosen to be 5 μm, which is the same as the VLWIR absorber. We did not test the absorption behavior of LWIR HgTe/CdTe superlattices. However, based on the experience, a thinner absorber layer is needed for a shorter wavelength. As such, 5 μm should be more than enough. The doping levels of all layers are parameters subject to change so that a low valence band offset can be achieved. The full device structure is shown in Figure 102. Note that we consider the usual employment of back illumination in our design so that the LWIR absorber is grown epitaxially before the barrier layer and VLWIR absorber. In this way, the LWIR absorption layer act as a long-wavelength-pass filter for the VLWIR layer.

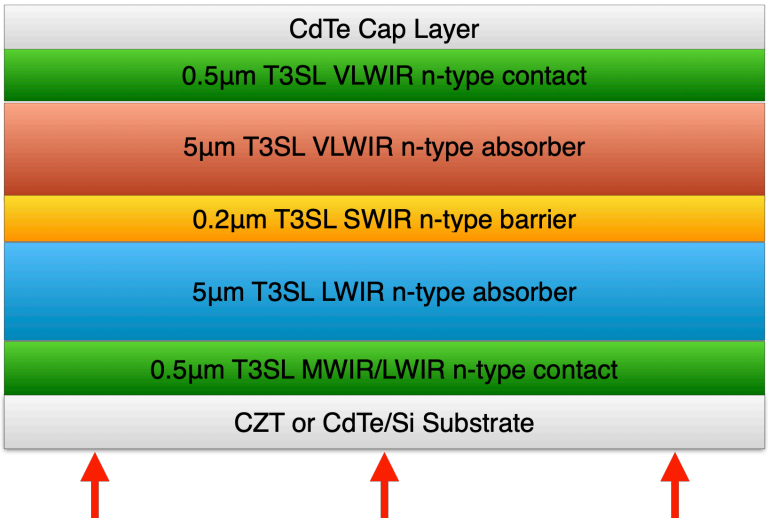

Figure 102 The cross-sectional device structure and structural parameters of a 2-color nBn device designed for VLWIR and LWIR absorption with all superlattice layers except the substrate. The red arrows indicate the light incident direction.

The expected device band alignment is shown in Figure 103. Depends on the applied bias, either LWIR or VLWIR absorber region is activated. Under positive bias (Figure 103 (a)), the LWIR region is activated, the photogenerated holes in the LWIR region can move freely across the barrier and produce a large photocurrent. Under reverse bias (Figure 103 (b)), the

VLWIR region is activated, the photogenerated holes in the VLWIR region can move freely across the barrier and produce a large photocurrent. Ideally, only transition #1 in Figure 103 happens. The barrier prevents electrons from traveling between the two absorbers under any conditions. However, if the photon energy is big enough, transition #2 would happen. Transition #3 may also happen due to free-carrier absorption [130], [131], an intra-band absorption process in which a charge carrier absorbs light and excites itself to another higher level in that same band. Phonons are usually involved in conserving momentum; thus, this process can be ignored unless the absorber layer is heavily doped or highly defective.

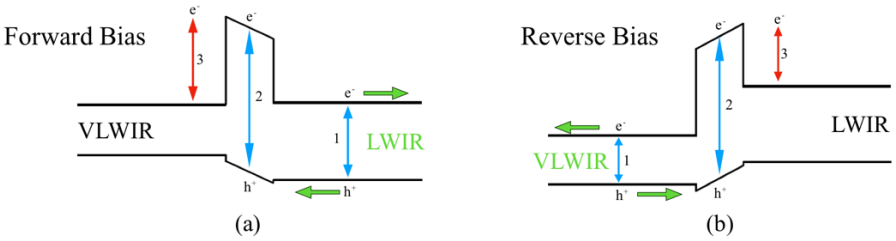

Figure 103 Schematic illustration of the predicted band alignment under (a) forward and (b) reverse biases for a 2-color nBn device designed for VLWIR and LWIR absorption. The forward bias means a positive polarity applied on the LWIR absorber side (bottom side) of the detector. The optical transitions contributing to photocurrents are also shown in the figure.

The modeling of the nBn structures' band alignment and the calculations on their I-V characteristics are done using COMSOL Multiphysics™. The semiconductor module is used, which is based on the drift-diffusion equations. Fermi-Dirac statistics is used to deal with the case of degenerate semiconductors with relatively high doping levels. The nBn device is set up as a 1D geometry shape along the growth direction with a 4 μm^2 cross-section area. Different generation/recombination mechanisms, namely radiation, Shockley-Read-Hall and auger, are considered. Poisson equation is solved to extract the spatial distribution of the band structure. The modeling result will be discussed in the next section.

10.3 Result and Discussion

The calculated energy band diagrams of an nBn device designed for the VLWIR region with HgTe/CdTe superlattice absorber and barrier (device structure shown in Figure 101) is shown in Figure 104. The absorber and the contact layer are the same except for the thickness. Both layers are lightly n-type doped to $n = 2.46 \times 10^{15}$ cm^{-3}. The barrier layer is non-intentionally n-type doped.

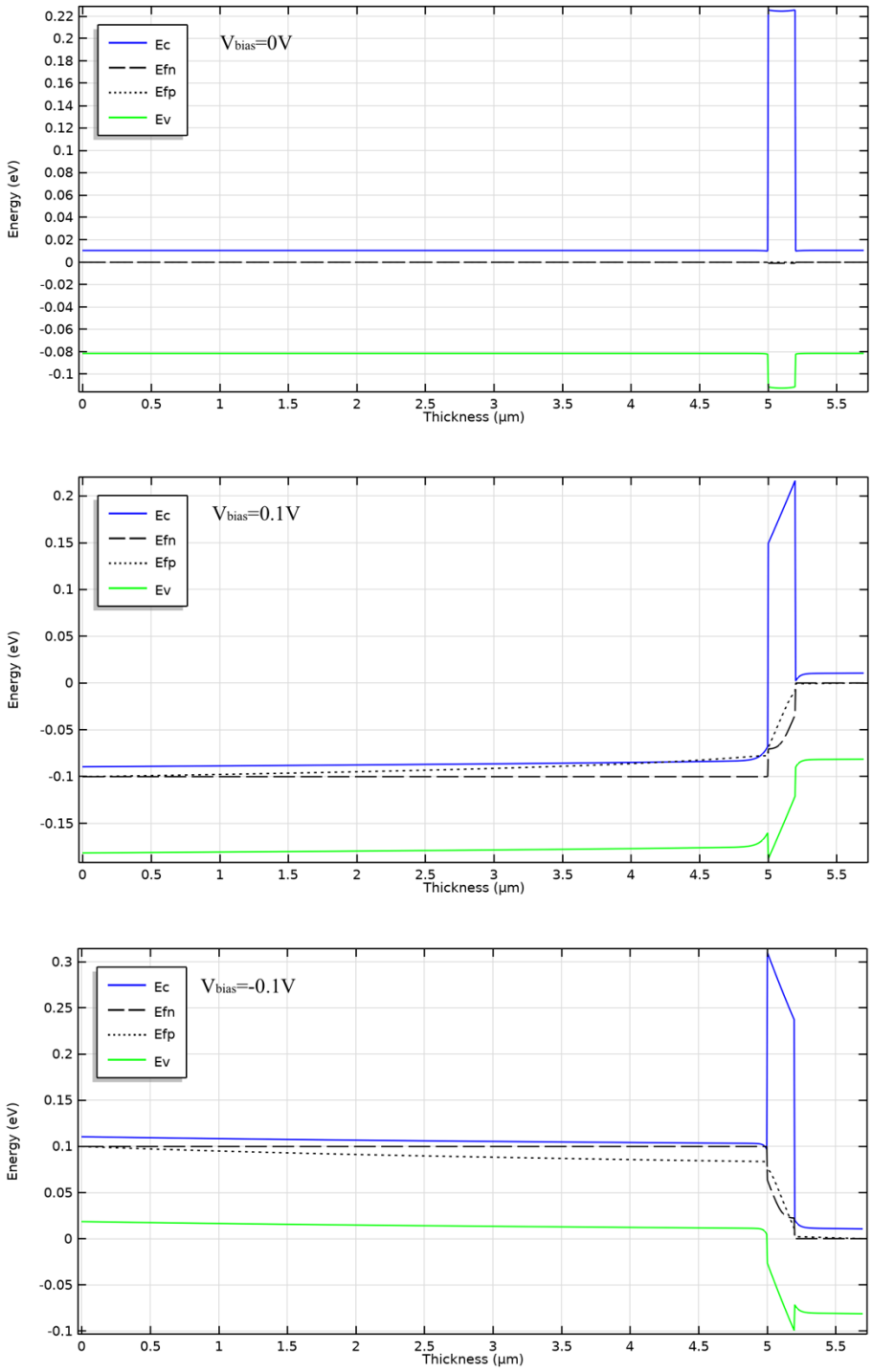

Figure 104 The calculated energy band diagrams of an nBn device designed for the VLWIR region with HgTe/CdTe superlattice absorber and barrier (device structure shown in Figure 101) (top) at equilibrium (middle) under forward bias $V_{bias} = 0.1V$ (bottom) under reverse bias $V_{bias} = -0.1V$.

The band diagram at equilibrium shows a high conduction band barrier and a small valence band barrier. The valence band offset is ~30meV, which is very close to the average carrier thermal energy given in Equation (7.1). The energy barrier encountered by minority carrier holes is minimal, and the carriers can easily step over the barrier with a small turn-on voltage.

For this nBn device with one VLWIR absorber, a slight forward bias is needed to reduce the obstruction of hole carriers diffusing into the contact region. The band diagram gives in Figure 104 shows that a forward/reverse bias can even reduce the VBO. The VBO between the VLWIR absorber and the barrier is reduced to ~20meV under forward bias. With the help of the bias voltage, the minority carrier holes can move freely from the absorber to the contact layer.

It is worth mentioning that only a tiny bias-induced depletion region in the barrier layer's vicinity is observed when an operating voltage is applied. The voltage drop through the majority of the absorber layer is minimal. The SRH generation process is significant in the depletion region. Assuming the SRH lifetime of minority carriers are similar in the nBn structure and photodiodes, which depends on the material quality, the SRH process is significantly suppressed in the nBn structure because the n-type layers are in a flat band with little to no depletion.

The simulated I-V characteristics of this VLWIR nBn structure is shown in Figure 105. The device is limited by intrinsic Auger generation processes dominating the saturation current. Note that a turn-on voltage usually can be seen in the I-V curve of nBn structures, reflected as a kink in the current for a given bias. However, we do not observe a visible turn-on voltage characteristic in Figure 105, indicating the valence band energy barrier is minimal and

can be neglected; thus, the flow of hole current arising from minority carrier generation in the absorber layer is unrestricted.

To evaluate the contact layer's contribution to the dark current, we extended the contact layer's thickness to 5μm, which is the same thickness as the absorber. The I-V characteristics are shown as the dashed red line in Figure 105, which is identical to the I-V curve before. This has proven that transition #3 in Figure 103 can be neglected.

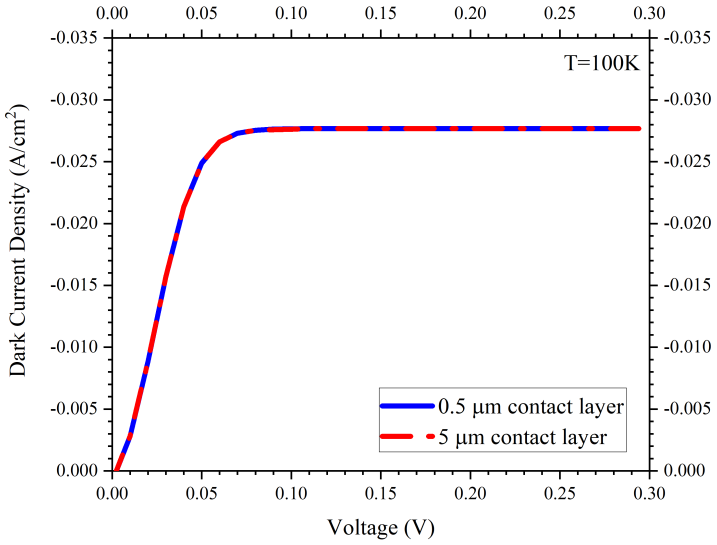

Figure 105 The simulated I-V characteristics of an nBn device designed for the VLWIR region with HgTe/CdTe superlattice absorber and barrier (device structure shown in Figure 101). 0.5μm (solid blue line) or 5 μm (dashed red line) contact layer is used in the simulation.

The calculated energy band diagrams of a two-color nBn device working in the VLWIR/LWIR region with HgTe/CdTe superlattice absorbers and barrier (device structure shown in Figure 102) is shown in Figure 106. There are two absorbers, one for VLWIR and one for LWIR. Both absorber layers are 5 μm thick and lightly n-type doped to $n = 2.46 \times 10^{15}$ cm^{-3}. The barrier layer is non-intentionally n-type doped.

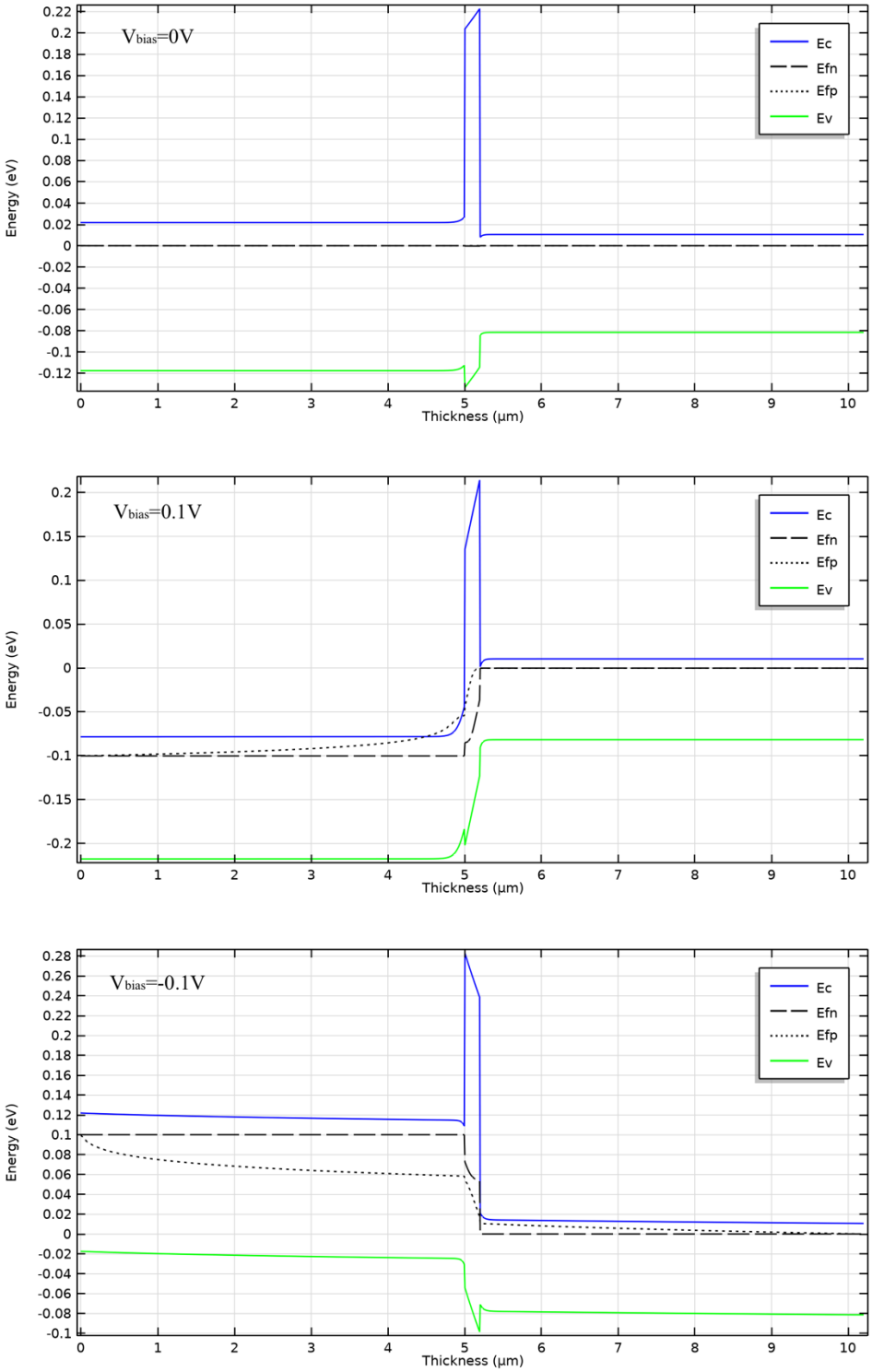

Figure 106 The calculated energy band diagrams of a two-color nBn device designed for VLWIR/LWIR region with HgTe/CdTe superlattice absorbers and barrier (device structure

shown in Figure 102) (top) at equilibrium (middle) under forward bias $V_{bias} = 0.1V$ (bottom) under reverse bias $V_{bias} = -0.1V$.

The band diagram at equilibrium shows a high conduction band barrier and a small valence band barrier. The valence band offset is ~30meV for the VLWIR absorber side and ~20mev for the LWIR absorber side. Each side has a small value of VBO that is very close to the average carrier thermal energy given in Equation (7.1). Same as single color nBn, a forward/reverse bias can reduce the VBO. The VBO between the VLWIR absorber and the barrier is reduced to ~25meV under reverse bias, and the VBO between the LWIR absorber and the barrier is reduced to ~15meV under forward bias. With the help of the bias voltage, the minority carrier holes can move freely from the absorber to the contact layer. A very small bias-induced depletion region is observed on both sides of the barrier when an operating voltage is applied. The SRH generation process is significantly suppressed because the voltage drop through the major portions of the two absorber layers is minimal.

The simulated I-V characteristics of this two-color nBn structure are shown in Figure 107. Under reverse bias, the VLWIR absorber is activated; Under forward bias, the LWIR absorber is activated. The device is limited by intrinsic Auger generation processes dominating the saturation current under both forward and reverse bias. The VLWIR absorber shows higher current density compared to the LWIR side due to its smaller band gap. The dark current on either side of the I-V curve is majorly from either the VLWIR or LWIR absorber.

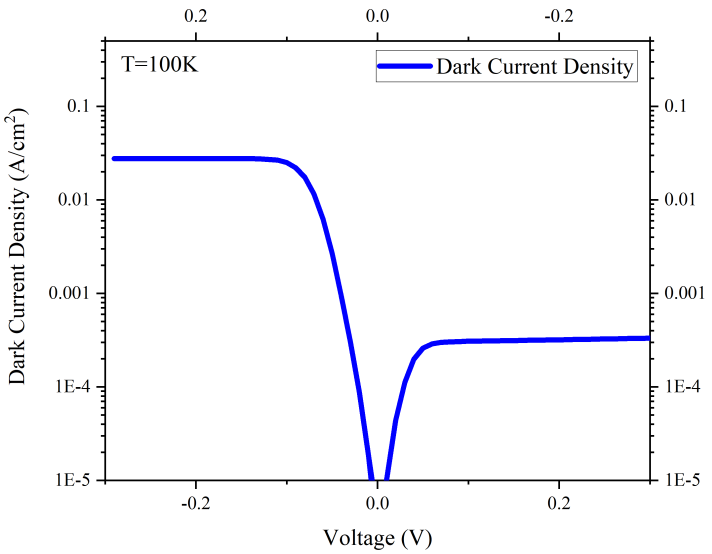

Figure 107 The simulated I-V characteristics of a two-color nBn device designed for VLWIR/LWIR region with HgTe/CdTe superlattice absorbers and barrier (device structure is shown in Figure 102).

To have a better idea of the dark current density values, we compare the dark current density of our modeled 2-color nBn device to the famous "Rule 07" [132], [133], which is believed to be the lowest dark current that can be achieved in a p-n HgCdTe photodiode performance. The result is shown in Figure 108. Note that Rule 07 values are quite different at different temperatures and different cutoff wavelengths. Through some calculations, we have Rule-07 dark current $I_{dark} = 0.0539\ \mathrm{A/cm^2}$ at 14 μm, 100K and $I_{dark} = 0.0001\ \mathrm{A/cm^2}$ at 9 μm, 100K. The dark currents of the activated VLWIR absorber and LWIR absorber are comparable to the Rule-07 dark currents. They are slightly higher, likely due to the high density of states near superlattices' band edge.

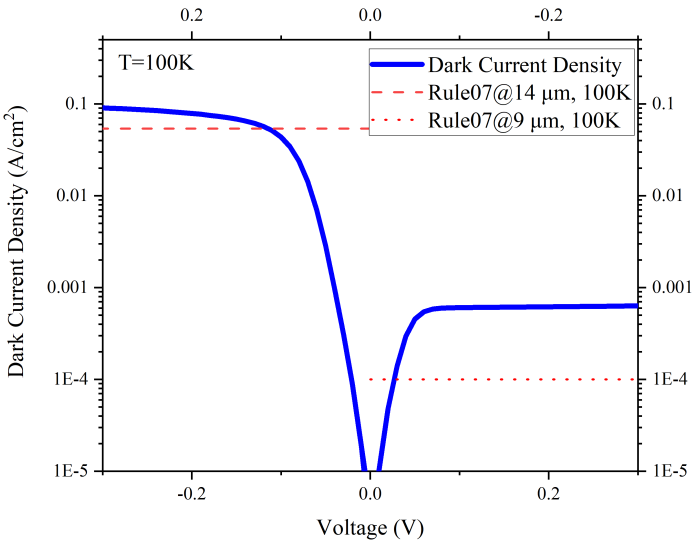

Figure 108 The simulated I-V characteristics of a two-color nBn device with increased absorber thicknesses (15 µm of VLWIR absorber and 10 µm of LWIR absorber) compared to Rule 07.

There is a small concern about the calculated band diagram at equilibrium shown in Figure 106. A visible VBO between the two absorbers is observed. There is no prominent I-V characteristic associated with this VBO. However, we decided to try a second design with different VLWIR absorber doping levels to examine if a smaller VBO between the two absorbers can be achieved. We want to bring down the valence band of the VLWIR absorber, so the doping level should be increased. A high doping level is relatively hard to achieve and could introduce more defects into the material, so moderate n-type doping of 2.4×10^{16} cm^{-3} is used in this new design. The calculated energy band diagrams of the second design are shown in Figure 109. The VBO between the two absorbers is reduced while keeping the VBO between the absorbers and the barrier about the same.

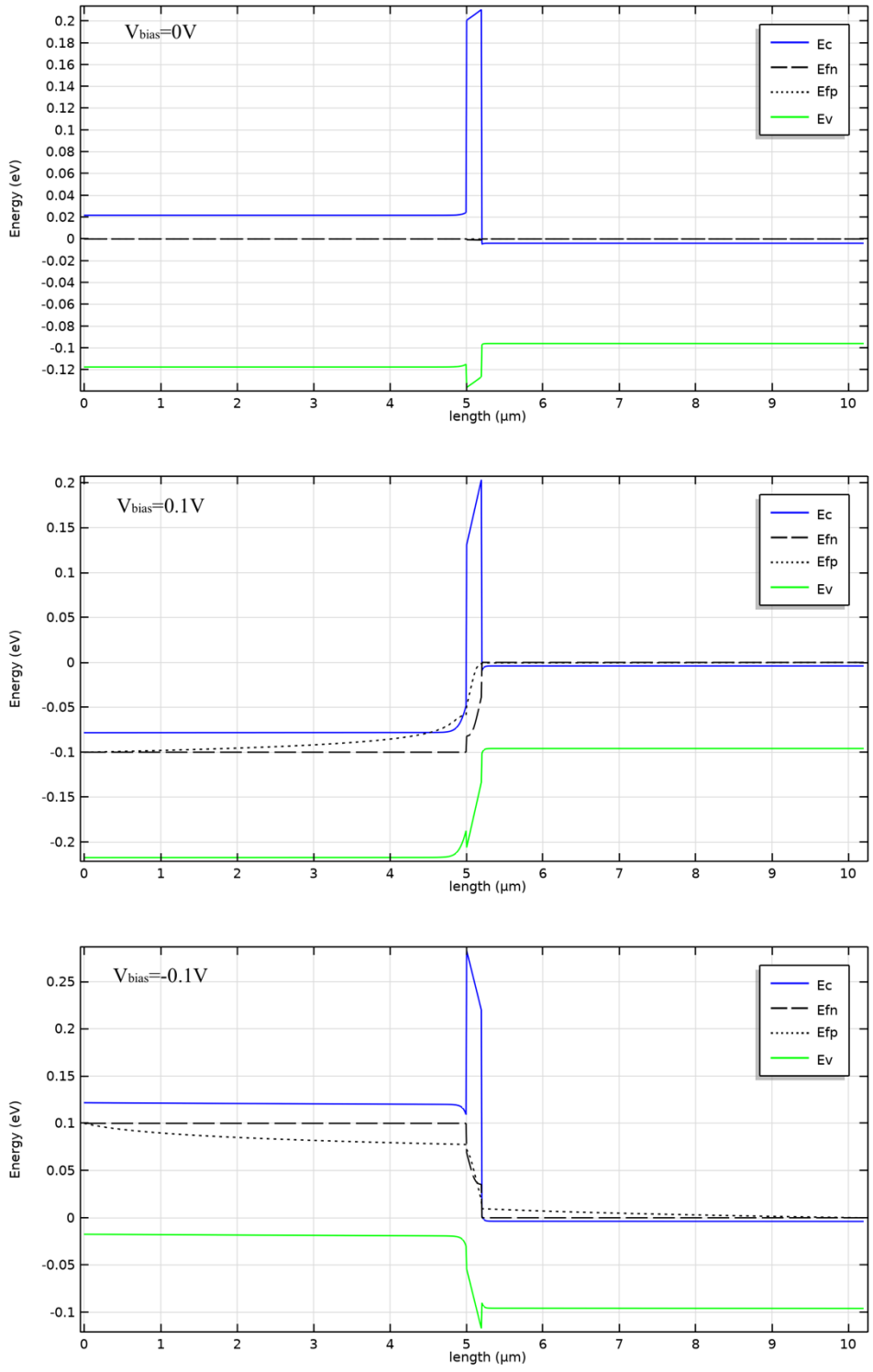

Figure 109 The calculated energy band diagrams of a two-color nBn device with the VLWIR absorber doped at a higher level (8×10^{16} cm^{-3}) (top) at equilibrium (middle) under forward bias $\mathrm{V_{bias}} = 0.1\mathrm{V}$ (bottom) under reverse bias $\mathrm{V_{bias}} = -0.1\mathrm{V}$.

The simulated I-V characteristics of this new design are shown in Figure 110. The maximum dark current density on either side is slightly reduced. Similar to the previous design, we compare the dark current density of our modeled 2-color nBn device to Rule 07 dark currents (Figure 111). The dark currents of the activated absorbers are comparable to the Rule-07 dark currents.

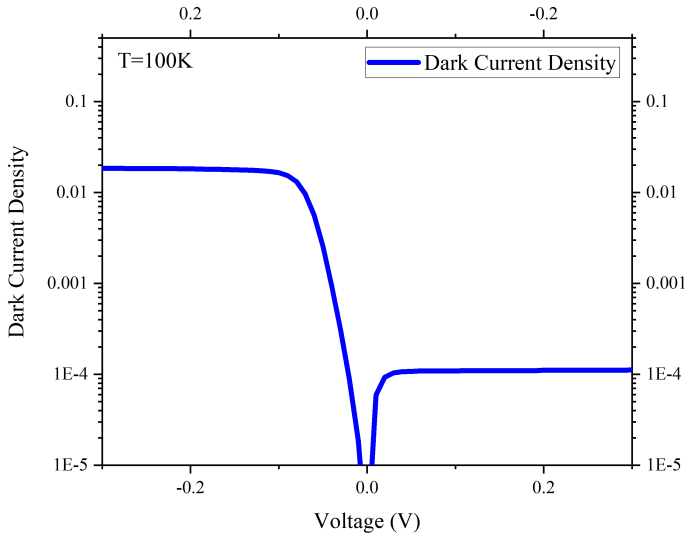

Figure 110 The simulated I-V characteristics of the second design of two-color VLWIR/LWIR nBn.

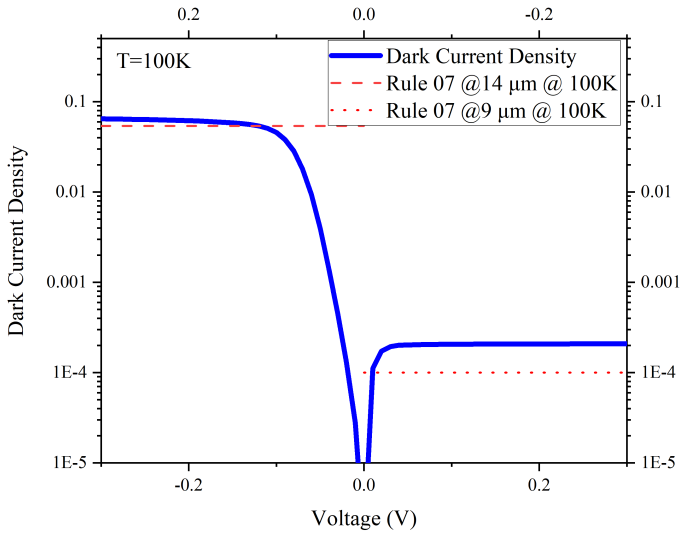

Figure 111 The simulated I-V characteristics of the second design of two-color VLWIR/LWIR nBn with increased absorber thicknesses (15 µm of VLWIR absorber and 10 µm of LWIR absorber) compared to Rule 07.

It is worth mentioning that a "zero" valence band offset can be achieved with a p-type doped superlattice barrier. Despite the disadvantages of the p-type barrier we discussed in section 8.1.2, here we provide the calculated band diagrams of such an nB_pn structure for reference (Figure 112).

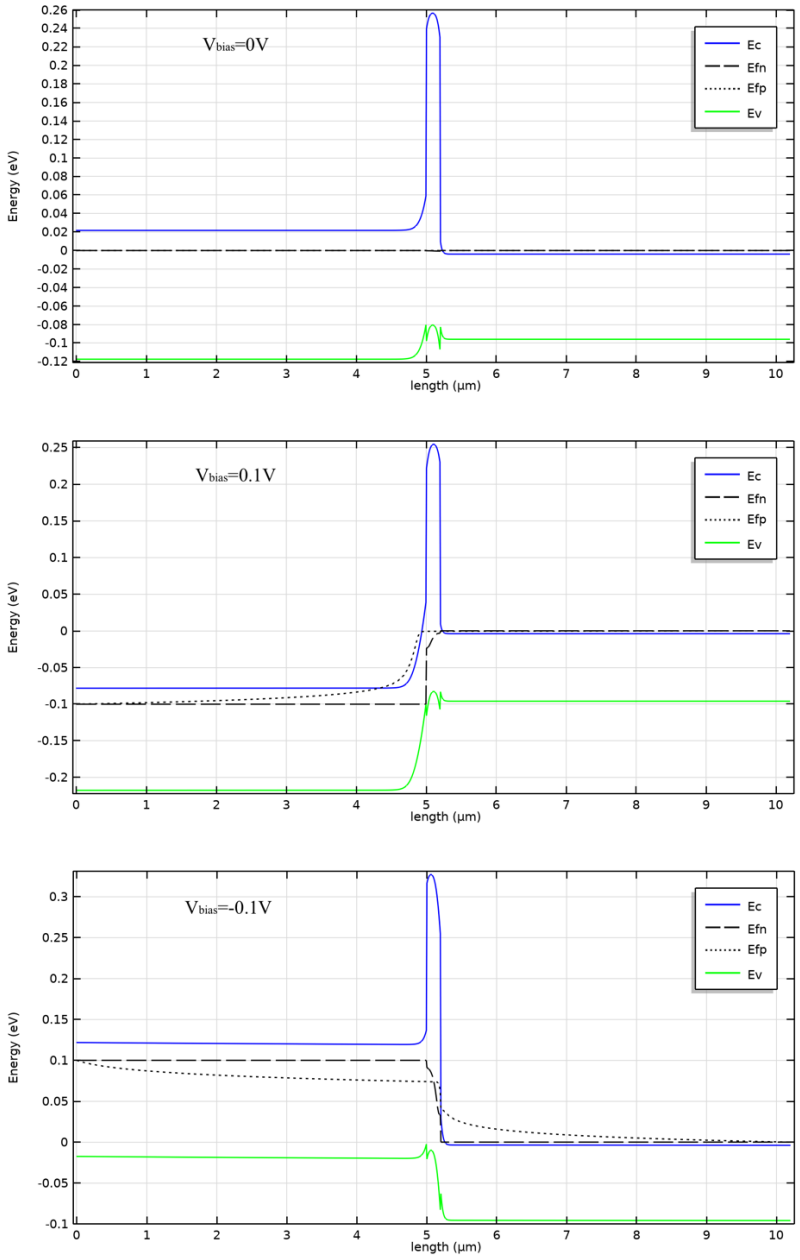

Figure 112 The calculated energy band diagrams of a two-color nB_pn device with 1×10^{16} cm^{-3} p-type doped barrier (top) at equilibrium (middle) under forward bias $V_{bias} = 0.1V$ (bottom) under reverse bias $V_{bias} = -0.1V$.

The I-V characteristics shown in Figure 107 and Figure 110 are also compared to those of T2SLs working in VLWIR region. H. Mohseni et al. has reported the measured and modeled dark current density of a type-II $InAs/Ga_{1-x}In_xSb$ SL photodiode working in VLWIR region at

T=80 K [134]. The dark current under -0.4V reverse bias at 80K is 4.5 $\mathrm{A/cm^2}$, which is substantially larger than the value we predicted here for T3SL at 100K of about 3×10^{-2} $\mathrm{A/cm^2}$. Y. Wei et al. later reported a dark current density of a type-II InAs/GaSb SL of about 3 $\mathrm{A/cm^2}$ under -0.6V reverse bias at 80K [135]. A. Hoang et al. reported a similar dark current of about 2 $\mathrm{A/cm^2}$ under -0.9V reverse bias at 77K [136]. B.-M Nguyen et al. has reported the I-V characteristics of a unipolar photodetector based on T2SL working in VLWIR region [25]. The I-V characteristics at 77 K shows a promising dark current density of 2×10^{-2} $\mathrm{A/cm^2}$, which is comparable to the values we got for T3SL nBn detectors. In conclusion, the dark current density we predicted for T3SL nBn structures working in VLWIR region is either comparable or smaller than those reported for T2SL-based photodetectors.

11 SUMMARY AND FUTURE WORK

In Part II of the thesis, we propose an nBn device structure that can potentially get around the p-type doping and annealing necessity for a photodetector made with T3SL. nBn structure blocks the majority carriers while the minority carriers can flow with no impedance, reducing dark current and noise without impeding photocurrent flow, with the essential condition of a near-zero VBO. While n-type or p-type bulk barrier has its disadvantages, it has been shown that HgTe/CdTe superlattice barrier can eliminate the VBO. We followed this path and modeled the HgCdTe-based nBn device with HgTe/CdTe superlattice barrier, which works in the MWIR region. Three nBn layers with this design are grown and characterized, and the preliminary results show promising layer quality.

An nBn architecture utilizing HgTe/CdTe superlattice as both the absorber and the barrier is proposed. The absorber is doped to $n = 2.46 \times 10^{15}$ cm^{-3} while the barrier is non-intentionally doped. The band diagram at equilibrium shows a high conduction band barrier and a small valence band barrier. The valence band offset is ~30meV, which is very close to the average carrier thermal energy. The minority carrier holes can flow from the absorber to the contact with no impedance.

We took a step further and designed a two-color nBn photodetector for sequential detection in LWIR and VLWIR region. The bias-selectivity of the nBn structure enables nBn photodetectors to achieve two-color detection. By switching the bias voltage polarity applied to the device, different absorption regions of the nBn bias-selectable detector are activated. The nBn device architecture being proposed exploits the T3SL's ability to provide near-zero VBO and absorb in the LWIR and VLWIR regions. Due to HgTe/CdTe SL's large absorption

coefficient near the cutoff wavelength, the absorber regions' thickness can be significantly less than what is required for alloy-based devices. The two absorption layers and the barrier layers are all HgTe/CdTe SLs, but with different well/barrier thicknesses. We have identified a 26 Å/90 Å HgTe/CdTe SL as a promising candidate to provide a high enough conduction band barrier with minimal VBO, and two SL absorber layers employ 45 Å/55 Å HgTe/CdTe and 55 Å/55 Å HgTe/CdTe designs to achieve photodetection in LWIR and VLWIR regions, respectively. At 100 K, we employ a doping level of 2.46×10^{15} cm^{-3} n-type for LWIR absorber, and either 2.46×10^{15} cm^{-3} or 2.4×10^{16} cm^{-3} for two different designs of VLWIR absorber. We predict near-zero VBO can be achieved with the help of these doping levels. The current-voltage characteristics of our designs are simulated, and the dark current densities are comparable to those given by "Rule 07", which is a rule of thumb for HgCdTe-based photodetector dark currents. The dark current densities we predicted are also compared to those of T2SL-based photodetectors, and T3SL-based nBn detectors show either comparable or smaller dark current densities.

Continuing from the idea of implementing a T3SL absorber into nBn structures, it would be interesting to combine a T3SL absorber with a HgCdTe absorber to achieve a different dual-band photoresponse than VLWIR/LWIR, for example, VLWIR/MWIR or LIWR/MWIR. As part of the future work, we would like to model these nBn structures and compare their I-V characteristics to state-of-the-art HgCdTe-based photodetectors and other dual-band detector solutions.

The next step is to grow the designed structures using Molecular Beam Epitaxy. The layers will be characterized using various techniques that we have mentioned, and then device

fabrication and device testing will take place. The feedback from device testing will help us to tune and polish our design. Ultimately, the potential promised by T3SL and nBn can be fully realized.

REFERENCES

[1] A. Rogalski, *Infrared Detectors, Second Edition*. 2011.

[2] P. W. Kruse, "A comparison of the limits to the performance of thermal and photon detector imaging arrays," *Infrared Phys. Technol.*, vol. 36, no. 5, pp. 869–882, Aug. 1995, doi: 10.1016/1350-4495(95)00014-P.

[3] C. L. Tan and H. Mohseni, "Emerging technologies for high performance infrared detectors," *Nanophotonics*, vol. 7, no. 1, pp. 169–197, Jan. 2018, doi: 10.1515/nanoph-2017-0061.

[4] W. Jiang *et al.*, "A versatile photodetector assisted by photovoltaic and bolometric effects," *Light Sci. Appl.*, vol. 9, no. 1, p. 160, Dec. 2020, doi: 10.1038/s41377-020-00396-3.

[5] A. Rogalski, J. Antoszewski, and L. Faraone, "Third-generation infrared photodetector arrays," *J. Appl. Phys.*, vol. 105, no. 9, p. 091101, May 2009, doi: 10.1063/1.3099572.

[6] A. Rogalski, "HgCdTe infrared detector material: history, status and outlook," *Reports Prog. Phys.*, vol. 68, no. 10, pp. 2267–2336, Oct. 2005, doi: 10.1088/0034-4885/68/10/R01.

[7] A. Rogalski, P. Martyniuk, and M. Kopytko, "InAs/GaSb type-II superlattice infrared detectors: Future prospect," *Appl. Phys. Rev.*, vol. 4, no. 3, p. 031304, Sep. 2017, doi: 10.1063/1.4999077.

[8] A. Rogalski, "Infrared Detectors 2nd Edition," CRC Press, Boca Raton, 2020.

[9] G. L. Hansen, J. L. Schmidt, and T. N. Casselman, "Energy gap versus alloy composition and temperature in Hg1-xCdxTe," *J. Appl. Phys.*, vol. 53, p. 7099, 1982, doi: 10.1063/1.94237.

[10] S. Zhang, "Public Lecture: Electron Superhighway: A Quantum Leap for Computing," 2017.

[11] J. N. Schulman and T. C. McGill, “The CdTe/HgTe superlattice: Proposal for a new infrared material,” *Appl. Phys. Lett.*, vol. 34, no. 10, pp. 663–665, 1979, doi: 10.1063/1.90629.

[12] J. P. Faurie, A. Million, and J. Piaguet, “CHARACTERIZATION OF CdxHgl _ ~ Te p-TYPE LAYERS G R O W N BY MBE,” vol. 59, pp. 10–14, 1982.

[13] J. Zhao *et al.*, “Correlation of CdZnTe(211)B substrate surface morphology and HgCdTe(211)B epilayer defects,” *J. Electron. Mater.*, vol. 33, no. 8, pp. 881–885, 2004, [Online]. Available: http://www.scopus.com/scopus/inward/record.url?eid=2-s2.0-4043111191&partnerID=40&rel=R6.5.0.

[14] A.-B. Chen and A. Sher, *Semiconductor Alloys*. Boston, MA: Springer US, 1996.

[15] B. Bernevig, T. Hughes, and S. Zhang, “Quantum spin Hall effect and topological phase transition in HgTe quantum wells.,” *Science*, vol. 314, no. 2006, p. 1757, 2006, doi: 10.1126/science.1133734.

[16] S. Hatch, “Investigation of HgTe-CdTe superlattices grown by molecular beam epitaxy,” *Ph.D. Thesis*, 2010.

[17] C. R. Becker, “MBE growth and characterization of HgTe based Heterostructures; in situ n and p type doping of HgCdTe alloys and HgTe/HgCdTe Heterostructures.” p. Talk at University of Illinois at Chicago, 2007.

[18] C. H. Grein, J. Garland, and M. E. Flatté, “Strained and unstrained layer superlattices for infrared detection,” *J. Electron. Mater.*, vol. 38, no. 8, pp. 1800–1804, 2009, doi: 10.1007/s11664-009-0757-8.

[19] K. A. Harris, “Properties of (211)B HgTe–CdTe superlattices grown by photon assisted molecular-beam epitaxy,” *J. Vac. Sci. Technol. B Microelectron. Nanom. Struct.*, vol. 10, no. 4, p. 1574, Jul. 1992, doi: 10.1116/1.586251.

[20] Y. Aytac *et al.*, “Effects of layer thickness and alloy composition on carrier lifetimes in mid-wave infrared InAs/InAsSb superlattices,” *Appl. Phys. Lett.*, vol. 105, no. 2, p.

022107, 2014, doi: 10.1063/1.4890578.

[21] A. Hood, D. Hoffman, B. M. Nguyen, P. Y. Delaunay, E. Michel, and M. Razeghi, “High differential resistance type-II InAs/GaSb superlattice photodiodes for the long-wavelength infrared,” *Appl. Phys. Lett.*, vol. 89, no. 9, p. 093506, 2006, doi: 10.1063/1.2345020.

[22] C. H. Grein, P. M. Young, M. E. Flatte, and H. Ehrenreich, “Long wavelength InAs/InGaSb infrared detectors: Optimization of carrier lifetimes,” *J. Appl. Phys.*, vol. 78, no. 12, pp. 7143–7152, 1995, doi: 10.1063/1.360422.

[23] G. J. Brown, S. Houston, and F. Szmulowicz, “Type-II InAs/GaSb superlattices for very long wavelength infrared detectors,” *Phys. E Low-Dimensional Syst. Nanostructures*, vol. 20, no. 3–4, pp. 471–474, 2004, doi: 10.1016/j.physe.2003.08.061.

[24] A. Hood, M. Razeghi, E. H. Aifer, and G. J. Brown, “On the performance and surface passivation of type II InAs⁄GaSb superlattice photodiodes for the very-long-wavelength infrared,” *Appl. Phys. Lett.*, vol. 87, no. 15, p. 151113, Oct. 2005, doi: 10.1063/1.2089170.

[25] B. M. Nguyen, S. Bogdanov, S. A. Pour, and M. Razeghi, “Minority electron unipolar photodetectors based on type II InAs/GaSb/AlSb superlattices for very long wavelength infrared detection,” *Appl. Phys. Lett.*, vol. 95, no. 18, pp. 2007–2010, 2009, doi: 10.1063/1.3258489.

[26] C. R. Becker, V. Latussek, M. Li, A. Pfeuffer-Jeschke, and G. Landwehr, “Valence band offset in HgTe/Hg1-xCdxTe superlattices,” *J. Electron. Mater.*, vol. 28, no. 6, pp. 826–829, 1999, doi: 10.1007/s11664-999-0078-y.

[27] C. R. Becker, V. Latussek, G. Landwehr, and L. W. Molenkamp, “Band structure and its temperature dependence for type-III HgTeÕHg1ÀxCdxTe superlattices and their semimetal constituent,” *Phys. Rev. B*, vol. 62, no. 15, pp. 1–7, 2000, doi: 10.1103/PhysRevB.62.10353.

[28] B. F. Levine, “Quantum-well infrared photodetectors,” *J. Appl. Phys.*, vol. 74, no. 8, pp. R1–R81, Oct. 1993, doi: 10.1063/1.354252.

[29] E. H. Sargent, “Infrared Quantum Dots,” *Adv. Mater.*, vol. 17, no. 5, pp. 515–522, Mar. 2005, doi: 10.1002/adma.200401552.

[30] J. Tang and E. H. Sargent, “Infrared Colloidal Quantum Dots for Photovoltaics: Fundamentals and Recent Progress,” *Adv. Mater.*, vol. 23, no. 1, pp. 12–29, Jan. 2011, doi: 10.1002/adma.201001491.

[31] K. K. N. Simon M. Sze, *Physics of Semiconductor Devices,3rd Edition*. 2006.

[32] M. J. Deen and P. K. Basu, “Appendix A: k.p Method,” in *Silicon Photonics*, Chichester, UK: John Wiley & Sons, Ltd, 2012, pp. 403–420.

[33] L. C. L. Y. Voon and M. Willatzen, *The k p Method: Electronic Properties of Semiconductors*. 2009.

[34] E. O. Kane, “Energy band structure in p-type germanium and silicon,” *J. Phys. Chem. Solids*, vol. 1, no. 1–2, pp. 82–99, 1956, doi: 10.1016/0022-3697(56)90014-2.

[35] E. O. Kane, “Band structure of indium antimonide,” *J. Phys. Chem. Solids*, vol. 1, no. 4, pp. 249–261, 1957, doi: 10.1016/0022-3697(57)90013-6.

[36] G. Bastard, *Wave mechanics applied to semiconductor heterostructures*. New York: Halsted Press, 1988.

[37] G. Bastard, “Superlattice band structure in the envelope-function approximation,” *Phys. Rev. B*, vol. 24, no. 10, pp. 5693–5697, 1981, doi: 10.1103/PhysRevB.24.5693.

[38] C. R. Becker, V. Latussek, G. Landwehr, and L. W. Molenkamp, “Inverted band structure of type-III HgTe Õ Hg 1 À x Cd x Te superlattices and its temperature dependence,” *Phys. Rev. B*, vol. 68, no. 15, p. 035202, 2003, doi: 10.1103/PhysRevB.68.035202.

[39] S. H. Groves, R. N. Brown, and C. R. Pidgeon, “Interband magnetoreflection and band structure of HgTe,” *Phys. Rev.*, vol. 161, no. 3, pp. 779–793, 1967, doi: 10.1103/PhysRev.161.779.

[40] J. M. Luttinger and W. Kohn, “Motion of Electrons and Holes in Perturbed Periodic

Fields," *Phys. Rev.*, vol. 97, no. 4, pp. 869–883, Feb. 1955, doi: 10.1103/PhysRev.97.869.

[41] L. R. Ram-Mohan, K. H. Yoo, and R. L. Aggarwal, "Transfer-matrix algorithm for the calculation of the band structure of semiconductor superlattices," *Phys. Rev. B*, vol. 38, no. 9, pp. 6151–6159, Sep. 1988, doi: 10.1103/PhysRevB.38.6151.

[42] M. Flatté, P. Young, L. H. Peng, and H. Ehrenreich, "Generalized superlattice K·p theory and intersubband optical transitions," *Phys. Rev. B - Condens. Matter Mater. Phys.*, vol. 53, no. 4, pp. 1963–1978, 1996, doi: 10.1103/PhysRevB.53.1963.

[43] R. Winkler and U. Rössler, "General approach to the envelope-function approximation based on a quadrature method," *Phys. Rev. B*, vol. 48, no. 12, pp. 8918–8927, Sep. 1993, doi: 10.1103/PhysRevB.48.8918.

[44] J. R. Meyer, C. A. Hoffman, and F. J. Bartoli, "Narrow-gap II-VI superlattices: correlation of theory with experiment," *Semicond. Sci. Technol.*, vol. 5, no. 3S, pp. S90–S99, Mar. 1990, doi: 10.1088/0268-1242/5/3S/020.

[45] N. F. Johnson, H. Ehrenreich, P. M. Hui, and P. M. Young, "Electronic and optical properties of III-V and II-VI semiconductor superlattices," *Phys. Rev. B*, vol. 41, no. 6, pp. 3655–3669, Feb. 1990, doi: 10.1103/PhysRevB.41.3655.

[46] A. Simon, D. Bertho, D. Boiron, and C. Jouanin, "Effects of interdiffusion on the electronic properties of HgTe-CdTe superlattices," *Phys. Rev. B*, vol. 42, no. 8, pp. 5221–5228, Sep. 1990, doi: 10.1103/PhysRevB.42.5221.

[47] W. H. Lau, J. T. Olesberg, and M. E. Flatte', "Electronic structures and electron spin decoherence in (001)-grown layered zincblende semiconductors," no. 001, Jun. 2004, [Online]. Available: http://arxiv.org/abs/cond-mat/0406201.

[48] Y. Guldner, G. Bastard, J. P. Vieren, M. Voos, J. P. Faurie, and A. Million, "Magneto-optical investigations of a novel superlattice: HgTe-CdTe," *Phys. Rev. Lett.*, vol. 51, no. 10, pp. 907–910, 1983, doi: 10.1103/PhysRevLett.51.907.

[49] Y. Chang *et al.*, "Absorption of narrow-gap HgCdTe near the band edge including

nonparabolicity and the urbach tail," *J. Electron. Mater.*, vol. 36, no. 8, pp. 1000–1006, 2007, doi: 10.1007/s11664-007-0162-0.

[50] J. Chu, Z. Mi, and D. Tang, "Band-to-band optical absorption in narrow-gap Hg 1− x Cd x Te semiconductors," *J. Appl. Phys.*, vol. 71, no. 8, pp. 3955–3961, Apr. 1992, doi: 10.1063/1.350867.

[51] W. W. Anderson, "Absorption constant of Pb1−xSnxTe and Hg1−xCdxTe alloys," *Infrared Phys.*, vol. 20, no. 6, pp. 363–372, Nov. 1980, doi: 10.1016/0020-0891(80)90053-6.

[52] Y. Chang, C. H. Grein, S. Sivananthan, M. E. Flatte, V. Nathan, and S. Guha, "Narrow gap HgCdTe absorption behavior near the band edge including nonparabolicity and the Urbach tail," *Appl. Phys. Lett.*, vol. 89, no. 6, p. 062109, Aug. 2006, doi: 10.1063/1.2245220.

[53] D. L. Smith, T. C. McGill, and J. N. Schulman, "Advantages of the HgTe-CdTe superlattice as an infrared detector material," *Appl. Phys. Lett.*, vol. 43, no. 2, pp. 180–182, 1983, doi: 10.1063/1.94272.

[54] M. Kopytko *et al.*, "Engineering the Bandgap of Unipolar HgCdTe-Based nBn Infrared Photodetectors," *J. Electron. Mater.*, vol. 44, no. 1, pp. 158–166, 2015, doi: 10.1007/s11664-014-3511-9.

[55] M. A. Herman, "Physical problems concerning effusion processes of semiconductors in molecular beam epitaxy," *Vacuum*, vol. 32, no. 9, pp. 555–565, 1982, doi: 10.1016/0042-207X(82)93785-X.

[56] P. E. Luscher and D. M. Collins, "Design considerations for molecular beam epitaxy systems," *Prog. Cryst. Growth Charact. Mater.*, vol. 2, pp. 15–32, 1979, doi: 10.1016/0146-3535(81)90023-X.

[57] J. P. Faurie, "Molecular beam epitaxy of alloys and superlattices involving mercury," *J. Vac. Sci. Technol. A Vacuum, Surfaces, Film.*, vol. 3, no. 1, p. 55, 1985, doi: 10.1116/1.573245.

[58] G. Biasiol and L. Sorba, “Molecular beam epitaxy: principles and applications,” *... Energy Prod. Energy-Saving Appl.*, pp. 66–83, 2001, [Online]. Available: http://www.tasc.infm.it/research/amd/file/school.pdf.

[59] F. Bassani *et al.*, “Indium doping of CdTe and Cd1-xZnxTe by molecular-beam epitaxy: Uniformly and planar-doped layers, quantum wells, and superlattices,” *J. Appl. Phys.*, vol. 72, no. 7, pp. 2927–2940, 1992, doi: 10.1063/1.351496.

[60] Y. Chang *et al.*, “Surface morphology and defect formation mechanisms for HgCdTe (211)B grown by molecular beam epitaxy,” *J. Electron. Mater.*, vol. 37, no. 9, pp. 1171–1183, 2008, doi: 10.1007/s11664-008-0477-5.

[61] K. A. Harris, “Growth of HgCdTe and other Hg-based films and multilayers by molecular beam epitaxy,” *J. Vac. Sci. Technol. A Vacuum, Surfaces, Film.*, vol. 4, no. 4, p. 2061, 1986, doi: 10.1116/1.574027.

[62] D. L. Smith and V. Y. Pickhardt, “Molecular beam epitaxy of II-VI compounds,” *J. Appl. Phys.*, vol. 46, no. 6, pp. 2366–2374, 1975, doi: 10.1063/1.321915.

[63] J. A. Curless, “Molecular beam epitaxy beam flux modeling,” *J. Vac. Sci. Technol. B*, vol. 3, no. 2, pp. 531–534, 1985, doi: 10.1116/1.583169.

[64] Y. Chang *et al.*, “Performance and reproducibility enhancement of HgCdTe molecular beam epitaxy growth on CdZnTe substrates using interfacial HgTeCdTe superlattice layers,” *Appl. Phys. Lett.*, vol. 86, no. 13, pp. 1–3, 2005, doi: 10.1063/1.1890471.

[65] J. P. Faurie, “CdTe-HgTe multilayers grown by molecular beam epitaxy,” *Appl. Phys. Lett.*, vol. 41, no. 8, p. 713, 1982, doi: 10.1063/1.93644.

[66] Y. Chang *et al.*, “Improve molecular beam epitaxy growth of HgCdTe on CdZnTe (211)B substrates using interfacial layers of HgTe/CdTe superlattices,” *J. Appl. Phys.*, vol. 100, no. 11, pp. 1–7, 2006, doi: 10.1063/1.2399890.

[67] M. Boukerche, J. Reno, I. K. Sou, C. Hsu, and J. P. Faurie, “Indium doping of HgCdTe layers during growth by molecular beam epitaxy,” *Appl. Phys. Lett.*, vol. 48, no. 25, pp.

1733–1735, 1986, doi: 10.1063/1.96818.

[68] Y. Selamet *et al.*, “HgTe/HgCdTe superlattices grown on CdTe/Si by molecular beam epitaxy for infrared detection,” *J. Electron. Mater.*, vol. 33, no. 6, pp. 503–508, 2004, doi: 10.1007/s11664-004-0038-5.

[69] W. S. Knodle and R. Chow, “10 - Molecular Beam Epitaxy: Equipment and Practice,” *Handb. Thin Film Depos. Process. Tech. (Second Ed.*, pp. 381–461, 2001, doi: http://dx.doi.org/10.1016/B978-081551442-8.50015-8.

[70] Y. Chang, C. Fulk, J. Zhao, C. H. Grein, and S. Sivananthan, “Molecular beam epitaxy growth of HgCdTe for high performance infrared photon detectors,” *Infrared Phys. Technol.*, vol. 50, no. 2–3, pp. 284–290, 2007, doi: 10.1016/j.infrared.2006.10.017.

[71] K. Ploog, “EPITAXY OF III-V COMPOUNDS : Technology and Growth Process,” *Annu. Rev. Mater. Sci.*, vol. 11, pp. 171–210, 1981, doi: 10.1146/annurev.ms.11.080181.001131.

[72] P. P. Chow, “Growth and characterization of MBE grown HgTe–CdTe superlattices,” *J. Vac. Sci. Technol. A Vacuum, Surfaces, Film.*, vol. 3, no. May 2013, p. 67, 1985, doi: 10.1116/1.573247.

[73] K. Ploog and a. Fischer, “In situ characterization of MBE grown GaAs and Al x Ga1−x As films using RHEED, SIMS, and AES techniques,” *Appl. Phys.*, vol. 13, no. 2, pp. 111–121, 1977, doi: 10.1007/BF00882468.

[74] P. Ballet *et al.*, “MBE Growth of Strained HgTe / CdTe Topological Insulator Structures,” *J. Electron. Mater.*, vol. 43, no. 8, pp. 2955–2962, 2014, doi: 10.1007/s11664-014-3160-z.

[75] G. Brill *et al.*, “MBE growth and device processing of MWIR HgCdTe on large area Si substrates,” *J. Electron. Mater.*, vol. 30, no. 6, pp. 717–722, 2001, doi: 10.1007/BF02665861.

[76] C. R. Becker *et al.*, “MBE growth and characterization of Hg based compounds and heterostructures,” *Thin Solid Films*, vol. 412, no. 1–2, pp. 129–138, 2002, doi: 10.1016/S0040-6090(02)00324-3.

[77] K. D. Mynbaev *et al.*, “Photoluminescence of Hg1 − x Cd x Te based heterostructures grown by molecular-beam epitaxy,” *Semiconductors*, vol. 45, no. 7, pp. 872–879, 2011, doi: 10.1134/S1063782611070153.

[78] D. J. Friedman, G. P. Carey, I. Lindau, and W. E. Spicer, “Effect of different cation-anion bond strengths on metal – ternary-semiconductor interface formation: Cu/ Hg 0.75 Cd 0.25 Te and Cu/CdTe,” *Phys. Rev. B*, vol. 34, no. 8, pp. 5329–5342, Oct. 1986, doi: 10.1103/PhysRevB.34.5329.

[79] W. Braun, *Applied RHEED Reflection High-Energy Electron Diffraction During Crystal Growth*. 1999.

[80] T. Byrappa, Kullaiah, Ohachi, *Crystal Growth Technology*. 2003.

[81] R. H. Hartley *et al.*, “Ellipsometry: a technique for real time monitoring and analysis of MBE-grown CdHgTe and CdTe/HgTe superlattices,” *J. Cryst. Growth*, vol. 117, no. 1–4, pp. 166–170, 1992, doi: 10.1016/0022-0248(92)90738-5.

[82] R. D. Allen, G. B. David, and G. Nomarski, “The zeiss-Nomarski differential interference equipment for transmitted-light microscopy.,” *Z. Wiss. Mikrosk.*, vol. 69, no. 4, pp. 193–221, Nov. 1969, [Online]. Available: http://www.ncbi.nlm.nih.gov/pubmed/5361069.

[83] J. D. Benson *et al.*, “Surface Structure of Molecular Beam Epitaxy (211)B HgCdTe,” *J. Electron. Mater.*, vol. 36, no. 8, pp. 949–957, Aug. 2007, doi: 10.1007/s11664-007-0143-3.

[84] T. R. Hanlon, R. J. Koestner, and H. -Y. Liu, “Misfit accommodation in a lattice-mismatched HgTe-CdTe superlattice/HgCdTe heterostructure grown by molecular beam epitaxy,” *Appl. Phys. Lett.*, vol. 55, no. 15, pp. 1513–1515, Oct. 1989, doi: 10.1063/1.101592.

[85] M. Carmody, D. Lee, M. Zandian, J. Phillips, and J. Arias, “Threading and misfit-dislocation motion in molecular-beam epitaxy-grown HgCdTe epilayers,” *J. Electron. Mater.*, vol. 32, no. 7, pp. 710–716, Jul. 2003, doi: 10.1007/s11664-003-0057-7.

[86] Z. Yang, Y. Lansari, J. W. Han, Z. Yu, and J. F. Schetzina, “Temperature-Dependent Infrared Absorption of Hg-Based II-VI Semiconductor Superlattices,” *MRS Proc.*, vol. 161, p. 257, Feb. 1989, doi: 10.1557/PROC-161-257.

[87] H. A. MacLeod, “Thin-Film Optical Filters,” *Thin-Film Opt. Filters*, 2001, doi: 10.1201/9781420033236.

[88] E. Finkman and S. E. Schacham, “EXPONENTIAL OPTICAL ABSORPTION BAND TAIL OF Hg//1// minus //xCd//xTe.,” *J. Appl. Phys.*, vol. 56, no. 10, pp. 2896–2900, 1984, doi: 10.1063/1.333828.

[89] J. Chu, B. Li, K. Liu, and D. Tang, “Empirical rule of intrinsic absorption spectroscopy in Hg 1-xCdxTe,” *Journal of Applied Physics*, vol. 75, no. 2. pp. 1234–1235, 1994, doi: 10.1063/1.356464.

[90] K. Liu, J. H. Chu, and D. Y. Tang, “Composition and temperature dependence of the refractive index in Hg 1− x Cd x Te,” *J. Appl. Phys.*, vol. 75, no. 8, pp. 4176–4179, Apr. 1994, doi: 10.1063/1.356001.

[91] B. Jensen and A. Torabi, “Linear and nonlinear intensity dependent refractive index of Hg 1− x Cd x Te,” *J. Appl. Phys.*, vol. 54, no. 10, pp. 5945–5949, Oct. 1983, doi: 10.1063/1.331770.

[92] J. Chu, Z. Mi, and D. Tang, “Band-to-band optical absorption in narrow-gap Hg1−xCdxTe semiconductors,” *J. Appl. Phys.*, vol. 71, no. 8, p. 3955, 1992, doi: 10.1063/1.350867.

[93] F. Urbach, “The long-wavelength edge of photographic sensitivity and of the electronic Absorption of Solids [8],” *Phys. Rev.*, vol. 92, no. 5, p. 1324, 1953, doi: 10.1103/PhysRev.92.1324.

[94] S. Krishnamurthy, A. B. Chen, A. Sher, and M. Van Schilfgaarde, “Temperature dependence of band gaps in HgCdTe and other semiconductors,” *J. Electron. Mater.*, vol. 24, no. 9, pp. 1121–1125, 1995, doi: 10.1007/BF02653063.

[95] S. E. Schacham and E. Finkman, “Recombination mechanisms in p-type HgCdTe: Freezeout and background flux effects,” *J. Appl. Phys.*, vol. 57, no. 6, pp. 2001–2009, 1985, doi: 10.1063/1.334386.

[96] D. Fasold, K. Hehl, and S. Jetschke, “Optical reflection and transmission through a flat system with a thick fluctuating layer,” *Phys. Status Solidi*, vol. 86, no. 1, pp. 125–131, Nov. 1984, doi: 10.1002/pssa.2210860112.

[97] Y. P. Varshni, “Temperature dependence of the energy gap in semiconductors,” *Physica*, vol. 34, no. 1, pp. 149–154, 1967, doi: 10.1016/0031-8914(67)90062-6.

[98] M. S. Han *et al.*, “Interdiffusion behavior of Hg in HgTe/CdTe superlattices grown on Cd0.96Zn0.04 Te (211)B substrates by molecular beam epitaxy,” *J. Electron. Mater.*, vol. 27, no. 6, pp. 680–683, Jun. 1998, doi: 10.1007/s11664-998-0035-1.

[99] A. Tardot, A. Hamoudi, N. Magnea, P. Gentile, and J. L. Pautrat, “Interdiffusion studies in CdTe/HgTe superlattices,” *Semicond. Sci. Technol.*, vol. 8, no. 1S, pp. S276–S280, Jan. 1993, doi: 10.1088/0268-1242/8/1S/060.

[100] Y. Kim, A. Ourmazd, M. Bode, and R. D. Feldman, “Nonlinear diffusion in multilayered semiconductor systems,” *Phys. Rev. Lett.*, vol. 63, no. 6, pp. 636–639, Aug. 1989, doi: 10.1103/PhysRevLett.63.636.

[101] J. G. A. Wehner, R. H. Sewell, C. A. Musca, J. M. Dell, and L. Faraone, “Optical and Structural Properties of CdTe Grown by Molecular Beam Epitaxy at Low Temperature for Resonant-Cavity-Enhanced HgCdTe Detectors,” *J. Electron. Mater.*, vol. 36, no. 8, pp. 877–883, Aug. 2007, doi: 10.1007/s11664-007-0115-7.

[102] D. K. Arch, J. L. Staudenmann, and J. P. Faurie, “Layer intermixing in HgTe-CdTe superlattices,” *Appl. Phys. Lett.*, vol. 48, no. 23, pp. 1588–1590, Jun. 1986, doi: 10.1063/1.96877.

[103] N. Otsuka, Y. E. Ihm, K. A. Harris, J. W. Cook, and J. F. Schetzina, “Transmission electron microscope study of Hg-based multilayer structures,” *J. Vac. Sci. Technol. A Vacuum, Surfaces, Film.*, vol. 5, no. 5, pp. 3129–3132, Sep. 1987, doi: 10.1116/1.574231.

[104] K. Zanio and T. Massopust, “Interdiffusion in HgCdTe/CdTe Structures,” *J. Electron. Mater.*, vol. 15, no. 2, pp. 103–109, Mar. 1986, doi: 10.1007/BF02649911.

[105] Y. D. Zhou *et al.*, “Far-infrared detector based on HgTe/HgCdTe superlattices,” *J. Electron. Mater.*, vol. 32, no. 7, pp. 608–614, 2003, doi: 10.1007/s11664-003-0040-3.

[106] M. W. Goodwin, M. A. Kinch, and R. J. Koestner, “Metal–insulator–semiconductor properties of HgTe–CdTe superlattices,” *J. Vac. Sci. Technol. A Vacuum, Surfaces, Film.*, vol. 6, no. 4, pp. 2685–2692, Jul. 1988, doi: 10.1116/1.575531.

[107] K. A. Harris, “A high quantum efficiency in situ doped mid-wavelength infrared p-on-n homojunction superlattice detector grown by photoassisted molecular-beam epitaxy,” *J. Vac. Sci. Technol. B Microelectron. Nanom. Struct.*, vol. 9, no. 3, p. 1752, May 1991, doi: 10.1116/1.585411.

[108] S. H. Shin, J. M. Arias, M. Zandian, J. G. Pasko, J. Bajaj, and R. E. DeWames, “Minority carrier lifetime and diffusion length in HgTe/CdTe superlattices by molecular beam epitaxy,” *Appl. Phys. Lett.*, vol. 61, no. 10, pp. 1196–1198, Sep. 1992, doi: 10.1063/1.107592.

[109] S. Maimon and G. W. Wicks, “nBn detector, an infrared detector with reduced dark current and higher operating temperature,” *Appl. Phys. Lett.*, vol. 89, no. 15, 2006, doi: 10.1063/1.2360235.

[110] J. B. Rodriguez *et al.*, “nBn structure based on InAs⁄GaSb type-II strained layer superlattices,” *Appl. Phys. Lett.*, vol. 91, no. 4, p. 043514, Jul. 2007, doi: 10.1063/1.2760153.

[111] G. Bishop *et al.*, “nBn detectors based on InAs⁄GaSb type-II strain layer superlattice,” *J. Vac. Sci. Technol. B Microelectron. Nanom. Struct.*, vol. 26, no. 3, p. 1145, 2008, doi: 10.1116/1.2830627.

[112] J. R. Pedrazzani, S. Maimon, and G. W. Wicks, “Use of nBn structures to suppress surface leakage currents in unpassivated InAs infrared photodetectors,” *Electron. Lett.*, vol. 44, no. 25, p. 1487, 2008, doi: 10.1049/el:20082925.

[113] L. O. Bubulac, “Defects, diffusion and activation in ion implanted HgCdTe,” *J. Cryst. Growth*, vol. 86, no. 1–4, pp. 723–734, Jan. 1988, doi: 10.1016/0022-0248(90)90799-Q.

[114] H. F. Schaake, “Ion implantation damage in Hg 0.8 Cd 0.2 Te,” *J. Vac. Sci. Technol. A Vacuum, Surfaces, Film.*, vol. 4, no. 4, pp. 2174–2176, Jul. 1986, doi: 10.1116/1.574050.

[115] G. L. Destéfanis, “Electrical doping of HgCdTe by ion implantation and heat treatment,” *J. Cryst. Growth*, vol. 86, no. 1–4, pp. 700–722, Jan. 1988, doi: 10.1016/0022-0248(90)90798-P.

[116] A. White, “U.S. Patent,” *No. 4,679,063, (1983).*

[117] A. Rogalski, “Analysis of the R0A product in n+-p Hg1−xCdxTe photodiodes,” *Infrared Phys.*, vol. 28, no. 3, pp. 139–153, May 1988, doi: 10.1016/0020-0891(88)90002-4.

[118] F. K. Hopkins and J. T. Boyd, “Dark current analysis of InSb photodiodes,” *Infrared Phys.*, vol. 24, no. 4, pp. 391–395, Jul. 1984, doi: 10.1016/0020-0891(84)90031-9.

[119] P. Martyniuk and A. Rogalski, “Modelling of MWIR HgCdTe complementary barrier HOT detector,” *Solid. State. Electron.*, vol. 80, pp. 96–104, Feb. 2013, doi: 10.1016/j.sse.2012.10.021.

[120] A. M. Itsuno, J. D. Phillips, and S. Velicu, “Design and modeling of HgCdTe nBn detectors,” *J. Electron. Mater.*, vol. 40, no. 8, pp. 1624–1629, 2011, doi: 10.1007/s11664-011-1614-0.

[121] D. Benyahia *et al.*, “nBn HgCdTe infrared detector with HgTe(HgCdTe)/CdTe SLs barrier,” *Opt. Quantum Electron.*, vol. 48, no. 3, p. 215, 2016, doi: 10.1007/s11082-016-0439-8.

[122] A. M. Itsuno, J. D. Phillips, and S. Velicu, “Mid-wave infrared HgCdTe nBn photodetector,” *Appl. Phys. Lett.*, vol. 100, no. 16, pp. 1–4, 2012, doi: 10.1063/1.4704359.

[123] C. H. Grein, P. Boieriu, and M. E. Flatté, “Single- and two-color HgTe/CdTe superlattice based infrared detectors,” *Proc. SPIE*, vol. 6127, p. 61270W1, 2006, doi:

10.1117/12.640090.

[124] N. D. Akhavan, G. A. Umana-Membreno, G. Jolley, J. Antoszewski, and L. Faraone, “A method of removing the valence band discontinuity in HgCdTe-based nBn detectors,” *Appl. Phys. Lett.*, vol. 105, no. 12, 2014, doi: 10.1063/1.4896577.

[125] J. Reno, R. Sporken, Y. J. Kim, C. Hsu, and J. P. Faurie, “Hg incorporation in CdTe during the growth of HgTe-CdTe superlattices by molecular beam epitaxy,” *Appl. Phys. Lett.*, vol. 51, no. 19, pp. 1545–1547, 1987, doi: 10.1063/1.98630.

[126] Y. F. Lao and A. G. U. Perera, “Temperature-dependent internal photoemission probe for band parameters,” *Phys. Rev. B - Condens. Matter Mater. Phys.*, vol. 86, no. 19, pp. 1–9, 2012, doi: 10.1103/PhysRevB.86.195315.

[127] Y. F. Lao, P. K. D. D. P. Pitigala, A. G. Unil Perera, E. Plis, S. S. Krishna, and P. S. Wijewarnasuriya, “Band offsets and carrier dynamics of type-II InAs/GaSb superlattice photodetectors studied by internal photoemission spectroscopy,” *Appl. Phys. Lett.*, vol. 103, no. 18, 2013, doi: 10.1063/1.4827881.

[128] Y. F. Lao, A. G. Unil Perera, and P. S. Wijewarnasuriya, “Optical study of HgCdTe infrared photodetectors using internal photoemission spectroscopy,” *Appl. Phys. Lett.*, vol. 104, no. 13, pp. 10–13, 2014, doi: 10.1063/1.4870479.

[129] A. Rogalski, “Quantum well photoconductors in infrared detector technology,” *J. Appl. Phys.*, vol. 93, no. 8, pp. 4355–4391, Apr. 2003, doi: 10.1063/1.1558224.

[130] D. K. Schroder, R. N. Thomas, and J. C. Swartz, “Free carrier absorption in silicon,” *IEEE Trans. Electron Devices*, vol. 25, no. 2, pp. 254–261, Feb. 1978, doi: 10.1109/T-ED.1978.19066.

[131] C. M. Horwitz and R. M. Swanson, “The optical (free-carrier) absorption of a hole-electron plasma in silicon,” *Solid. State. Electron.*, vol. 23, no. 12, pp. 1191–1194, Dec. 1980, doi: 10.1016/0038-1101(80)90111-2.

[132] W. E. Tennant, D. Lee, M. Zandian, E. Piquette, and M. Carmody, “MBE HgCdTe

technology: A very general solution to IR detection, described by ‘rule 07’, a very convenient heuristic,” *J. Electron. Mater.*, vol. 37, no. 9, pp. 1406–1410, 2008, doi: 10.1007/s11664-008-0426-3.

[133] W. E. Tennant, “‘Rule 07’’ revisited: Still a good heuristic predictor of p/n HgCdTe photodiode performance?,” *J. Electron. Mater.*, vol. 39, no. 7, pp. 1030–1035, 2010, doi: 10.1007/s11664-010-1084-9.

[134] H. Mohseni, M. Razeghi, G. J. Brown, and Y. S. Park, “High-performance InAs/GaSb superlattice photodiodes for the very long wavelength infrared range,” *Appl. Phys. Lett.*, vol. 78, no. 15, pp. 2107–2109, 2001, doi: 10.1063/1.1362179.

[135] Y. Wei, A. Gin, M. Razeghi, and G. J. Brown, “Advanced InAs/GaSb superlattice photovoltaic detectors for very long wavelength infrared applications,” *Appl. Phys. Lett.*, vol. 80, no. 18, pp. 3262–3264, 2002, doi: 10.1063/1.1476395.

[136] A. M. Hoang, G. Chen, R. Chevallier, A. Haddadi, and M. Razeghi, “High performance photodiodes based on InAs/lnAsSb type-ll superlattices for very long wavelength infrared detection,” *Appl. Phys. Lett.*, vol. 104, no. 25, pp. 1–5, 2014, doi: 10.1063/1.4884947.

VITA

Peihong Man

Department of Physics · University of Illinois at Chicago
845 W Taylor St, M/C 273 · Chicago, IL 60607, United States
Tel: +1 (312)-888-6351 · Email: pman3@uic.edu

EDUCATION

Ph.D. in Physics, University of Illinois at Chicago, IL, USA *05/2021*
Thesis: "The Study of MBE-grown Type-III Superlattices for Very Long Wavelength Infrared nBn Detectors"
Advisors: Dr. Sivalingam Sivananthan

Master of Computer Science, University of Illinois at Chicago, IL, USA *05/2020*
Master of Science in Physics, University of Illinois at Chicago, IL, USA *05/2014*
Bachelor of Science in Physics, Nanjing University, Jiangsu, China *06/2012*

PROFESSIONAL EXPERIENCE

Research as Ph.D. student *08/2013 – 05/2021*
Microphysics Laboratory, Department of Physics, University of Illinois at Chicago

- Independent Molecular Beam Epitaxy (MBE) growth of more than 200 layers.
- Substrate preparation including etching and mounting; MBE chamber maintenance and cleaning.
- Successful growth of layer structures including SWIR, MWIR, LWIR device structures on Si and CZT substrates; Type III superlattices with various layer thicknesses and periods; nBn structure with LWIR/MWIR absorber and superlattice barriers.
- Participation in the setup and assemble of new designed Hg cell.
- Operation and maintenance of Fourier-transform infrared spectroscopy measurement, microscope including Nomarski and X-ray Diffraction measurement.
- Theoretical modeling of nBn structures with HgCdTe barriers/ superlattice barriers, with superlattice absorbers.
- Training more than 5 people on MBE, 3 of them are trained to the level of being able to operating MBE system independently.
- Software development for more than ten lab equipment to enhance data analysis and experiment automation.

Internship *05/2015 – 08/2015*
EPIR Technologies.

- Participation in the single detector project.
- More than 10 MBE growth of SWIR epilayers used for single detector project. Device made with these SWIR samples show very good performance.
- Growth temperature control /defect formation study using pyrometer and RHEED.

Internship *07/2016 – 08/2016*

EPIR Technologies.

- Characterization of HgCdTe and superlattice samples including Scanning Electron Microscopy and Atomic Force Microscopy.
- Transmission and absorption study of HgCdTe and Type III superlattices.

Internship *06/2017 – 05/2021*

EPIR Technologies.

- MBE growth of MWIR DPLH structures, VLWIR superlattice detector structures, nBn with superlattice barrier.
- FTIR, microscope and XRD measurements of various MBE grown samples including HgCdTe epilayers, Type III superlattices and nBn.
- Cleanroom design and initial setup.
- Construction of predictive models using deep learning to aid MBE growth temperature control /defect formation analysis utilizing database and data visualization.

Teaching Assistant Coordinator *08/2015 – 05/2021*

Department of Physics, University of Illinois at Chicago.

- Lead teaching assistant (TA) team perform TA jobs related to undergraduate Physics classes evolving more than ten TAs and three hundred students each semester.
- Coordinate between TAs and professors, also TAs and students, to provide the best learning experience for the students.

PUBLICATIONS

Manuscripts in Preparation

- "Two-Color nBn Infrared Detectors Based on Type-III Superlattices", P. Man, C.H. Grein, S. Krishnamurthy and S. Sivananthan.
- "Temperature-dependent Absorption Characteristics of Very Long Wavelength Infrared Type-III Superlattices", P. Man, Y. Chang, C.H. Grein and S. Sivananthan.

CONFERENCE PRESENTATIONS

II-VI Workshop

- "Absorption Characteristics of Very Long Wavelength Infrared Type-III Superlattices", US Workshop of Physics and Chemistry of II-VI materials, Nov 2017.
- "Two-Color nBn Infrared Detectors Based on Type-III Superlattices", US Workshop of Physics and Chemistry of II-VI materials, Nov 2019.